GHENT UNIVERSITY

FACULTY OF MEDICINE AND HEALTH SCIENCES

EXTRACELLULAR RNA IN LIQUID BIOPSIES: ENTERING A NEW ERA FOR CANCER TREATMENT MONITORING?

Jill Deleu

supervisor: prof. dr. Bram De Wilde
co-supervisors: prof. dr. Tom Van Maerken and prof. dr. ir. Jo Vandesompele

thesis submitted to fulfill the requirements for the degree of Doctor in Health Sciences
2023

thesis submitted to fulfill the requirements for the degree of Doctor in Health Sciences

Supervisor

Prof. dr. Bram De Wilde
Department of Internal Medicine and Pediatrics, Ghent University (Ghent, Belgium)
Department of Biomolecular Medicine, Ghent University (Ghent, Belgium)
Department of Paediatric Haematology Oncology and Stem Cell Transplantation, Ghent University Hospital (Ghent, Belgium)

Co-supervisors

Prof. dr. Tom Van Maerken
Department of Biomolecular Medicine, Ghent University (Ghent, Belgium)
Department of Laboratory Medicine, AZ Groeninge (Kortrijk, Belgium)

Prof. dr. ir. Jo Vandesompele
Department of Biomolecular Medicine, Ghent University (Ghent, Belgium)

Doctoral advisory committee

Prof. dr. Tim Lammens
Department of Internal Medicine and Pediatrics, Ghent University (Ghent, Belgium)

Prof. dr. David Creytens
Department of Diagnostic Sciences, Ghent University Hospital (Ghent, Belgium)

Examination committee

Prof. dr. Björn Heindryckx (chairman)
Department for reproductive medicine, Ghent University Hospital (Ghent, Belgium)

Prof. dr. Nadine Van Roy
Department of Biomolecular Medicine, Ghent University (Ghent, Belgium)

Prof. dr. Ward De Spiegelaere
Laboratory of Veterinary Morphology, Ghent University (Ghent, Belgium)

Prof. dr. Katrien Remaut
Laboratory for General Biochemistry and Physical Pharmacy, Ghent University (Ghent, Belgium)

Prof. dr. Lieve Tytgat
Princess Máxima Center for Pediatric Oncology/Hematology (Utrecht, the Netherlands)

Prof. dr. Hedwig Deubzer
Charité – Universitätsmedizin Berlin, Deubzer lab (Berlin, Germany)

The research in this thesis was conducted at the Center for Medical Genetics Ghent (Ghent University, Ghent, Belgium). This work was supported by Kom op tegen Kanker (Stand up to Cancer) and the Ghent University Special Research Fund (BOF22/CDV/077).

Fout! Gebruik het tabblad Start om Heading 1 toe te passen op de tekst die u hier wilt weergeven.

Table of contents

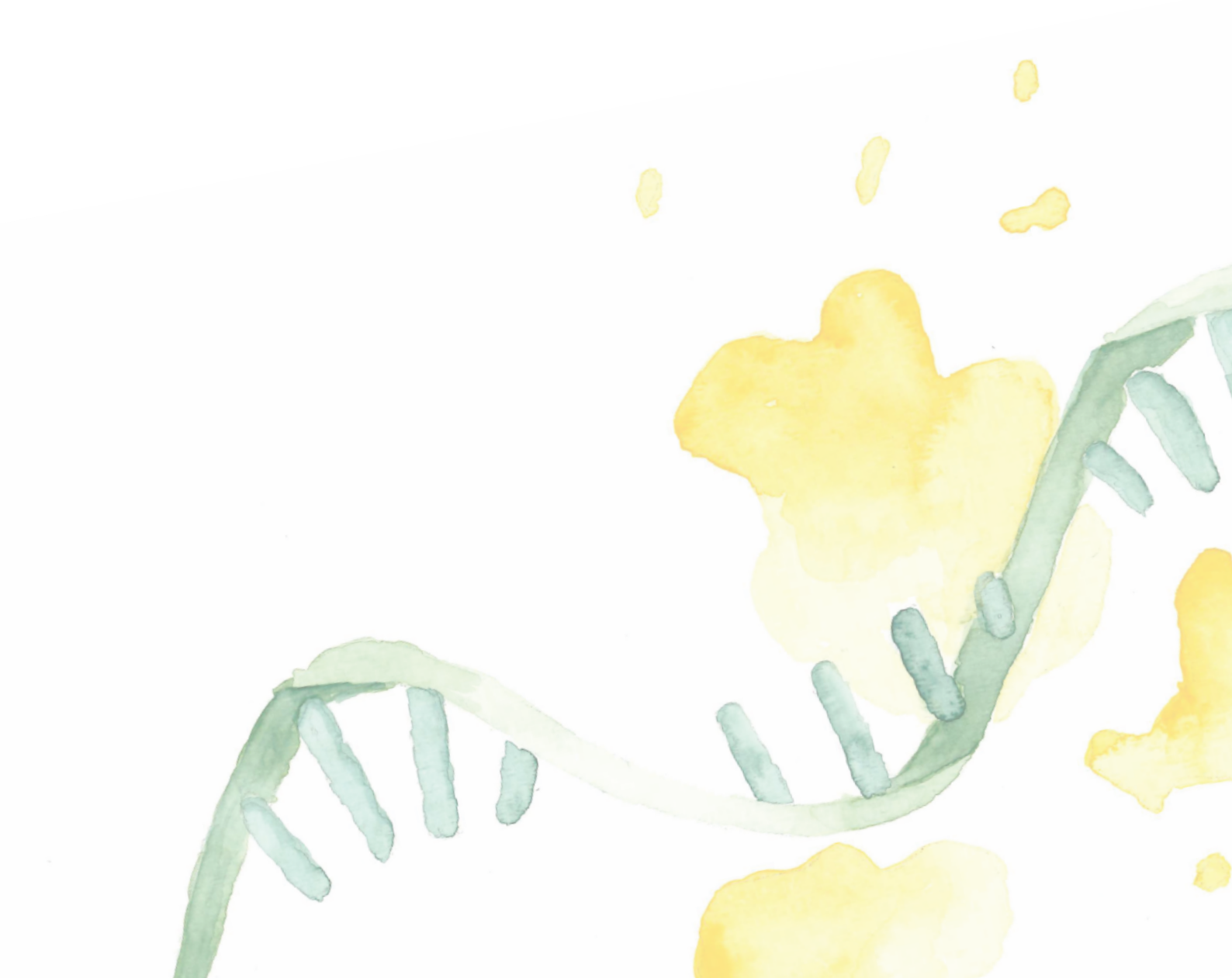

Table of contents

Table of contents

Abbreviations

ALK	anaplastic lymphoma kinase
ALT	alternative lengthening of telomeres
ASCR	autologous stem cell rescue
BMP(s)	bone morphogenetic protein(s)
Bu-Mel	busalfan/melphalan
CDK4	cyclin-dependent kinase 4
CDK6	cyclin-dependent kinase 6
CEA	carcino-embryonic antigen
CEM	carboplatin/etoposide/melphalan
cfDNA	cell-free DNA
circRNA	circular RNA
CNA	copy number alterations
COG	Children's Oncology Group
CPC(s)	connecting progenitor cell(s)
CTC(s)	circulating tumor cell(s)
ctDNA	cell-free circulating tumor DNA
EMT	epithelial-to-mesenchymal transformation
exRNA	extracellular RNA
EV(s)	extracellular vesicle(s)
exoRNA	exosomal RNA
FDA	U.S. Food and Drug Administration
FFPE	formalin-fixed paraffin-embedded
FGFR1	fibroblast growth factor receptor 1
GPOH	Society of Paediatric Oncology and Haematology
HDC	high-dose chemotherapy
HR-NB	high-risk neuroblastoma
H&E	hematoxylin and eosin
IDRF	image-defined risk factor
INPC	International Neuroblastoma Pathology Classification
INRG	International Neuroblastoma Risk Group
INRGSS	International Neuroblastoma Risk Group Staging System
INSS	International Neuroblastoma Staging System
ISTH	International Society on Thrombosis and Haemostasis

LINES	Low and Intermediate Risk Neuroblastoma European Study
lncRNA	long non-coding RNA
MAF	mutant allele fraction
mRNA	messenger RNA
miRNA	microRNA
MKI	mitosis-karyorrhexis index
MSKCC	Memorial Sloan Kettering Cancer Center
NB	neuroblastoma
NCC(s)	neural crest cell(s)
NSCLC	non-small cell lung cancer
qPCR	quantitative polymerase chain reaction
RT-qPCR	reverse transcription - quantitative polymerase chain reaction
SA	sympathoadrenal
SCP(s)	Schwann cell precursor(s)
SIOPEN	International Society of Paediatric Oncology Europe Neuroblastoma Group
SNPC(s)	sympathetic neural progenitor cell(s)
SNV	single nucleotide variants
SRG	suprarenal sympathetic ganglia
TEP(s)	tumor-educated platelet(s)
TKIs	tyrosine kinase inhibitors
TVD	topotecan, vincristine, doxorubicine
VEGF	vascular endothelial growth factor
^{131}I-MIBG	iodine-131 meta-iodobenzylguanidine

Summary

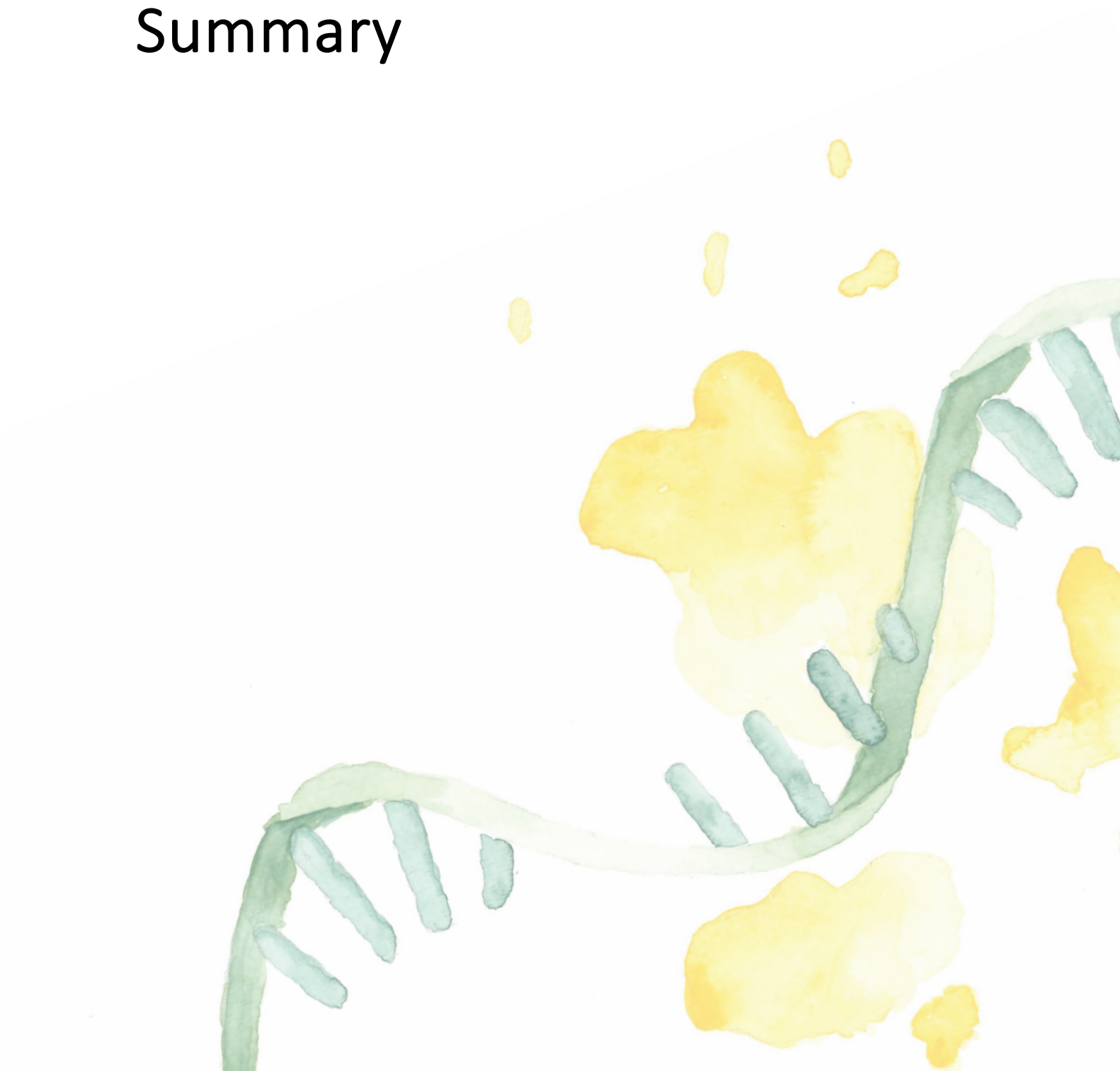

Summary

Neuroblastoma is the most frequently occurring extracranial childhood tumor, accounting for 15% of pediatric cancer-related deaths. While five-year survival rates have improved overall, a discrepancy exists between the less harmful low-risk variants and the high-risk neuroblastoma groups. Cure rate improvements in high-risk neuroblastoma patients are disappointingly low despite intensive multimodal therapies, with more than half of cases leading to disease progression and a fatal outcome. Pediatric oncologists still face a major challenge in treating neuroblastoma, and there is an urgent need for early detection of therapy non-response and to understand why some patients respond to therapy while others do not.

Monitoring a tumor's response can be aided by a thorough analysis of transcriptomic changes that occur during treatment. Yet, obtaining multiple samples of the tumor tissue is impractical because it is invasive and requires prior sedation of the patient. Additionally, tissue biopsies often involve a needle biopsy, which only captures a small portion of the primary tumor. Therefore, temporal and spatial tumor heterogeneity is not adequately captured with tissue biopsies. Alternatively, liquid biopsies have emerged as a promising approach for monitoring treatment responses. Liquid biopsies contain various biomarkers, such as cell-free DNA, extracellular RNA (e.g., microRNA, messenger RNA, long non-coding RNA and circular RNA), proteins, extracellular vesicles and tumor-educated platelets. In this thesis, my goal was to assess the potential of using circulating extracellular RNA found in serum and plasma as a means of monitoring treatment responses. Due to the difficulty in obtaining patient samples and differentiating between tumor and host responses in human samples, my research concentrated on improving xenograft models to investigate a tumor's reaction to treatment using liquid biopsies. To be more precise, by injecting a human tumor into mice, it is possible to distinguish between the tumor and host response to treatment since they originate from two different species, namely humans and mice, respectively.

The study conducted by Van Goethem et al. illustrated that serum microRNAs obtained from orthotopically engrafted neuroblastoma xenograft models can indicate the level of tumor burden as well as the pharmacodynamic response to idasanutlin therapy (**paper in addendum**). To assess the potential of the total extracellular RNA as a biomarker in xenograft models, a computational pipeline was optimized to distinguish between murine (host) and human (tumoral) reads. The pipeline was then applied to various plasma fractions and platelets, revealing that the tumoral signal in blood-based liquid biopsies is not mainly present in platelets. Instead, the platelets have a high content of host-derived extracellular RNA. To reduce the background host signal, I put forward platelet-depleted plasma for monitoring the treatment response of a tumor (**paper 1**). During my initial endeavor to assess the extracellular RNA response to idasanutlin treatment, I was unable to observe any tumoral

responses due to the low amount of tumoral extracellular RNA present in the bloodstream. However, I was able to identify a definite correlation between the size of the tumor at the time of sacrifice and the level of tumoral extracellular RNA present in the bloodstream. Moreover, while searching for additional factors that could influence the extracellular RNA load in circulation, I discovered significant variations among the models that were injected with different cell lines. Additionally, the injection site also played a potential role in the quantity of tumoral extracellular RNA in circulation (**manuscript under review**).

Relying solely on extracellular RNA as a biomarker for predicting and monitoring treatment responses may not be the most effective approach. The field of extracellular RNA is less explored than cell-free DNA because extracellular RNA is more susceptible to degradation and therefore sensitive to pre-analytical factors. However, extracellular RNA has the advantage of being more dynamic, allowing for real-time monitoring of treatment responses and the identification of highly expressed genes, even when the tumor has low levels of DNA shedding into circulation. To analyze both cell-free DNA and extracellular RNA in limited volumes of murine plasma, it is highly desirable to co-purify both types of nucleic acids from the same sample. In **paper 2**, I compared the performance of different extracellular RNA/cell-free DNA co-purification kits and demonstrated that the combined quantification can result in increased analytical sensitivity.

In conclusion, the findings from this thesis have opened new avenues for further assessment of the transcriptomic and genomic responses in biofluids obtained from xenograft models after therapy. These findings could have a crucial role in assessing the effectiveness of treatments for neuroblastoma patients.

Samenvatting

Neuroblastoom is de meest voorkomende vorm van kanker buiten de hersenen bij kinderen, verantwoordelijk voor 15% van de sterfgevallen door kinderkanker. Hoewel de vijfjaarsoverleving in de loop der tijd is verbeterd, bestaat er een discrepantie tussen de minder schadelijke laag-risico varianten en de hoog-risico neuroblastoom groepen. Ondanks intensieve therapieën is het genezingspercentage van hoog-risico neuroblastoom patiënten teleurstellend laag en leidt meer dan de helft van de gevallen tot ziekteprogressie en een fatale afloop. Kinderoncologen staan voor een grote uitdaging bij de behandeling van neuroblastoom, en het is belangrijk om zo vroeg mogelijk te detecteren wanneer een patient niet reageert op therapie en om te begrijpen waarom sommige patiënten op therapie reageren en andere niet.

Een grondige analyse van het tumorweefsel tijdens de behandeling kan waardevol zijn voor het opvolgen van de respons van een tumor. Het verkrijgen van meerdere biopten van tumorweefsel doorheen de tijd is echter niet evident. Het is een invasieve procedure, waarbij voorafgaande sedatie van de patiënt vereist is. Daarenboven wordt slechts een kleine fractie van de tumor gecollecteerd, waardoor de tumor heterogeniteit niet weerspiegeld wordt bij analyse van één enkel (naald)biopt. Als alternatief zijn vloeibare biopsieën veelbelovend gebleken voor het opvolgen van behandelingsresponsen. Vloeibare biopsieën bevatten namelijk biomerkers, waaronder celvrij DNA, extracellulair RNA (zoals microRNA, messenger RNA, long non-coding RNA en circulair RNA), eiwitten, extracellulaire vesikels en bloedplaatjes. Mijn doel was om het potentieel van extracellulair RNA in serum en plasma te evalueren om het antwoord op therapie op te volgen. Aangezien het moeilijk is om voldoende plasmastalen te verkrijgen van patiënten met een zeldzame ziekte als neuroblastoom, en het uitdagend is een onderscheid te maken tussen het antwoord van de tumor en dat van het gezond weefsel (gastheer) op behandelingen, heb ik me voornamelijk geconcentreerd op het optimaliseren van een preklinisch model. Door menselijke tumoren in muizen te injecteren (xenograft modellen), kan een onderscheid worden gemaakt tussen de tumor- en gastheerreactie op behandeling omdat ze afkomstig zijn van twee verschillende organismen.

We toonden aan dat microRNAs in het serum van muizen die orthotoop werden geïmplanteerd met neuroblastoom cellen de tumoromvang kunnen reflecteren, evenals de farmacodynamische respons op idasanutlin therapie (**paper in addendum**). Om het potentieel van extracellulair RNA als biomerker in muismodellen te beoordelen, werd een computationele pijplijn geoptimaliseerd om onderscheid te maken tussen exRNA afkomstig van de gastheer (muis) en de tumor (mens). De pijplijn werd vervolgens toegepast op verschillende plasmafracties en bloedplaatjes van xenograft modellen, waarbij werd aangetoond dat het tumorsignaal niet hoofdzakelijk aanwezig is in bloedplaatjes. De bloedplaatjes bezitten daarentegen een hoog gehalte aan extracellulair RNA afkomstig van

de gastheer. Om het achtergrondsignaal van de gastheer te verminderen, stel ik plasma zonder bloedplaatjes voor om het antwoord van de tumor op therapieën op te volgen (**paper 1**). Tijdens mijn eerste poging om de extracellulaire RNA-respons op idasanutlin therapie te beoordelen, kon ik geen tumorreacties waarnemen vanwege de lage hoeveelheid tumor-extracellulair RNA in de bloedbaan. Wel kon ik een duidelijke correlatie aantonen tussen de grootte van de tumor op het moment van opoffering en de hoeveelheid extracellulair tumor-RNA in de bloedbaan. Bovendien ontdekte ik bij het zoeken naar aanvullende factoren die de extracellulaire tumor-RNA hoeveelheden in circulatie konden beïnvloeden, significante variaties tussen de modellen die met verschillende cellijnen werden geïnjecteerd. Ook speelde de injectieplaats een potentiële rol in de hoeveelheid extracellulair tumor-RNA in circulatie (**manuscript under review**).

Uitsluitend vertrouwen op extracellulair RNA als biomerker voor het voorspellen en monitoren van behandelingsresponsen is wellicht niet het meest doeltreffend. Het veld van extracellulair RNA is minder onderzocht dan celvrij DNA omdat extracellulair RNA gevoeliger is voor afbraak en daarom ook meer onderhevig is aan pre-analytische factoren. Extracellulair RNA heeft echter het voordeel dat het meer dynamisch is, waardoor nauwe opvolging van behandelingsresponsen en de identificatie van sterk tot expressie gebrachte genen mogelijk is, zelfs wanneer de tumor weinig DNA in het bloed afscheidt. Om zowel celvrij DNA als extracellulair RNA te analyseren in beperkte volumes muizenplasma, is het wenselijk om beide soorten nucleïnezuren uit hetzelfde staal te co-purificeren. In **paper 2** vergeleek ik verschillende celvrij DNA/RNA co-purificatiekits en toonde ik aan dat de analytische sensitiviteit hoger kan zijn bij een gecombineerde analyse.

Concluderend hebben de bevindingen uit deze thesis nieuwe wegen geopend voor verdere beoordeling van de antwoorden op therapie in vloeibare biopten, verkregen uit muismodellen. Deze bevindingen kunnen een cruciale rol spelen bij het beoordelen van de effectiviteit van behandelingen voor neuroblastoompatiënten.

Introduction

"Extracellular RNA in liquid biopsies: entering a new era for cancer treatment monitoring?" This is the million-dollar question I tried to answer during my PhD trajectory. In this thesis introduction, I will first guide you through the concept of liquid biopsies and give an overview of which useful markers they contain to improve cancer detection and treatment follow-up. Then, I will introduce you to the childhood cancer neuroblastoma, which has been the main disease focus of my research. Curing patients with neuroblastoma is one of the current challenges for pediatric oncologists. Despite treatment with intensive multimodal therapies in some patients, disease progression is often observed, leading to fatal outcomes. I will explain how liquid biopsies potentially aid in improving the outcomes of these children by monitoring the responses to treatment more carefully.

1. Liquid biopsies: minimal invasion to unlock the mysteries of the human body

The human body contains an estimated 37 trillion (37×10^{12}) cells (1). These cells both actively and passively release their content into the extracellular environment (2). In this way, molecules from the parental cells, either cancerous or non-cancerous, end up in biofluids, such as blood, cerebrospinal fluid, urine, sweat, tears and saliva (3). The ability to detect these analytes in fluids, has opened unprecedented opportunities for accessing tumor-derived molecules without the need to perform an invasive tissue biopsy. Moreover, the lower invasiveness of the sampling procedure of liquids enables serial collection to follow-up on treatment responses. Liquid biopsies may also provide a more comprehensive picture of the genomic make-up of the entire cancer as they are not restricted to a specific local tumor sampling site, which may not be representative (4). Taken together, these advantages predict an important role for liquid biopsies in the emerging era of precision oncology, thereby tailoring treatments to the specific requirements of individuals based on the molecular characteristics of their tumor (5–7). Detecting biomarkers, enabling estimation of prognosis, prediction of sensitivity or resistance to a specific therapy, and guiding the selection of treatment through the characterization of genetic aberrations involved in tumor progression, poses a major challenge to implement precision oncology into the clinic (8).

1.1. Blood-based biofluids: storage of biomarkers

Liquid biopsies refer to any collectable liquid in the human body, such as urine, saliva, sweat, tears, seminal plasma and many more. My thesis focuses on blood-based biofluids, such as plasma or serum, being the most studied liquid biopsies. They contain a repertoire of promising cancer biomarkers (**Figure 1**). These markers include proteins, circulating tumor cells (CTCs), cell-free DNA (cfDNA), extracellular RNA (exRNA), and extracellular vesicles (EVs) (9). Recently, also tumor-educated platelets (TEPs) have emerged as a promising biomarker.

The different types of biomarkers and their (potential) applications in precision oncology will be discussed in more detail in this section.

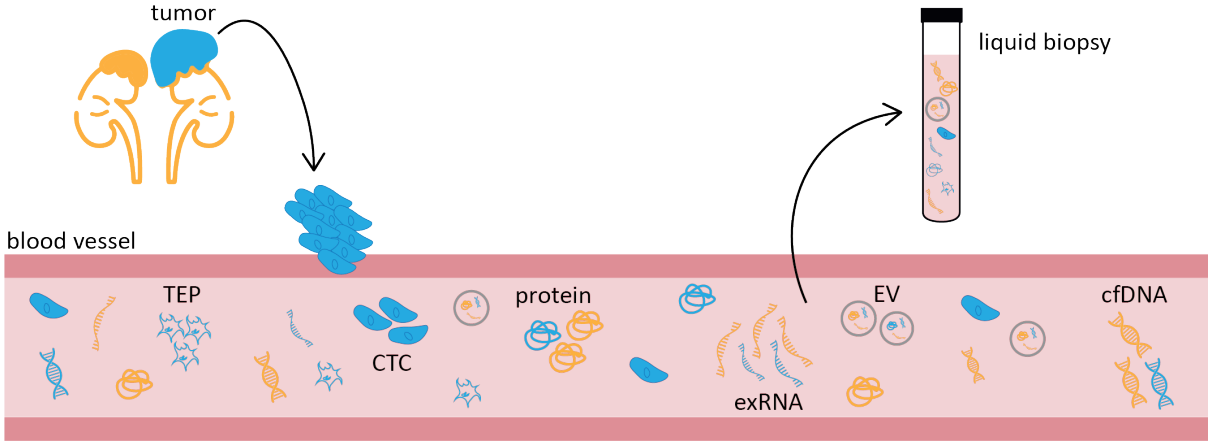

Figure 1 Overview of potential cancer biomarkers in the blood stream. cfDNA: cell-free DNA; CTC: circulating tumor cell; exRNA: extracellular RNA; EV: extracellular vesicle; TEP: tumor educated platelet. Figure created with Adobe Illustrator 2022.

1.1.1. Proteins

The first serum biomarker, currently still used in clinical practice, was approved in 1985 by the U.S. Food and Drug Administration (FDA), being carcino-embryonic antigen (CEA) (10,11). CEA is the most used marker in the clinical diagnosis of colorectal cancer, despite being non-specific (12). For instance, CEA has also shown to be elevated in other malignancies but also in benign conditions (i.e., cirrhosis, ulcerative colitis), and even smoking can increase the levels to almost the double (13). Another example is cancer antigen 125, a serum-based biomarker for the detection of early-stage ovarian tumors. Together with human epididymis protein 4, it belongs to the best two available protein biomarkers for ovarian cancer (14). However, their sensitivity and specificity has shown to be insufficient, especially to detect early-stage disease, even when combining multiple protein markers (14–16). Prostate-specific antigen (PSA) is commonly used to detect prostate cancer, and is showing high sensitivity in symptomatic patients, but it has low specificity in the screening setting (17). Most diagnostic tests are immunoassay kits, requiring low volumes of serum depending on the specific kit, i.e. approximately 50 µL (18).

Clearly, serum or plasma protein biomarkers are insufficiently sensitive or specific, although they are widely used in clinical practice. The combined analysis of multiple proteins, characterized by high-throughput mass spectrometry, can slightly improve sensitivity and specificity; however, combining different types of biomarkers might be better suited for cancer diagnosis and follow-up (11,19).

1.1.2. Circulating tumor cells

Circulating tumor cells (CTCs) are cancer cells that have detached from a primary tumor and entered the bloodstream. In this way, CTCs serve as precursors for metastatic disease. Once the cancer has metastasized, the tumor cells detected in the blood stream also reflect cell populations in metastatic sites. In 2004, the FDA approved the first and only method for CTC enumeration used to predict cancer patient outcome, the CellSearch system, requiring 7.5 mL of blood (20,21). It has been cleared by the FDA for clinical use in breast, colorectal and prostate cancer patients (20). If cells are detected by this method, a worse cancer prognosis is expected, and it is generally considered that increased CTC counts are correlated with a higher likelihood of metastasis and cancer aggressiveness (20,22). The number of CTCs in a patient's blood is extremely small (<10 cells/mL of blood): one CTC is thought to be surrounded by approximately one million white blood cells and one billion red blood cells per milliliter of peripheral blood (22–24). This poses a great challenge to specifically isolate CTCs from the blood cells. Due to the rarity of CTCs in the blood, other techniques are being evaluated to analyze CTCs in larger volumes of blood (25).

1.1.3. Cell-free DNA

cfDNA is shed in circulation mainly passively by apoptosis or necrosis, but also by active secretion of EVs. However, some controversies exist about the EVs carrying cfDNA in their lumen, or the cfDNA being attached to the surface of EVs (26). The total plasma cfDNA concentration in healthy individuals is on average 30 ng/mL, which increases to a mean concentration of 180 ng/mL in cancer patients (8). In high-risk neuroblastoma (HR-NB) patients, the plasma at diagnosis contains on average 1034 ng cfDNA per mL (ranging from 26 to 13,533 ng/mL) (27). As DNA is enzymatically cleaved during apoptosis, the cfDNA fragments are still wrapped around single nucleosomes, resulting in a length of 120 to 220 bp or multiples thereof (oligonucleosomes), with a maximum peak at 167 bp (length of cfDNA wrapped around a single nucleosome plus a short stretch of approximately 20 bp, the linker DNA) (28). The mono- or oligonucleosome structure protects the cfDNA from cleavage by DNase I. The half-time of cfDNA in the blood circulation ranges from 16 minutes to 2.5 hours (8). Circulating tumor DNA (ctDNA) represents only a fraction of the circulating cell-free DNA, depending on the tumor type, tumor burden, size and vascularity of the tumor, cancer stage, cellular turnover and response to therapy leading to a difference in ctDNA levels from 0.01 to 90% (8). In HR-NB patients, a high mean ctDNA fraction of 60% was observed (ranging between 3% and 99%) (27).

cfDNA is widely being investigated in the cancer field. Multiple diagnostic tests have reached the market, such as the FoundationOne Liquid CDx and the Cobas *EGFR* Mutation Test v2. The

FoundationOne Liquid CDx identifies patients with non-small cell lung cancer (NSCLC) of whom the tumors have epidermal growth factor receptor (*EGFR*) exon 19 deletions or exon 21 (L858R) substitution mutations and are suitable for treatment with a tyrosine kinase inhibitor approved by FDA for that indication (i.e. erlotinib, osimertinib and gefitinib) (29). This test requires 2 blood tubes, each filled with 8.5 mL of blood. Mutation analysis is later performed on the cfDNA extracted from the plasma. The Cobas *EGFR* Mutation Test v2 is a quantitative polymerase chain reaction (qPCR) test for the detection of defined mutations of the *EGFR* gene. This test was initially approved for use on formalin-fixed paraffin-embedded (FFPE) tissue specimens. Subsequently, the test received approval for identifying exon 19 deletions or exon 21 (L858R) substitution mutations on plasma samples as well. This was the first liquid biopsy test approved by the FDA in 2016 as companion diagnostic test to identify NSCLC patients eligible for specific targeted treatments (i.e. osimertinib, gefitinib and erlotinib) and requires 2 mL of plasma as input (30). However, this test only achieves a sensitivity of 58.4% and a specificity of 80.4%, indicating that ctDNA biomarkers could also benefit from a combined analysis with other types of biomarkers. For instance, Krug et al. showed that combining exosomal RNA (exoRNA) and ctDNA increased the sensitivity for *EGFR* mutation detection in plasma (29,31).

In addition to measuring cfDNA levels and identifying somatic mutations and copy number changes, cfDNA can also be used for epigenomic profiling, such as the examination of cfDNA fragmentation patterns and cfDNA methylation. Exploring the fragmentation patterns of cfDNA is an actively pursued domain within biomarker research. For instance, by examining the sizes of these fragments, it becomes possible to differentiate between cfDNA derived from tumors and that from normal tissues (32). More specifically, fragments originating from tumors typically exhibit a smaller size distribution compared to the larger size distribution seen in healthy background fragments (32). Moreover, the end signature of fragments could also hint at the presence of cancer, as the preferred sites of cleavage might differ (32). Furthermore, the fragmentation profiles of cfDNA offer insights into gene expression. To be precise, cfDNA originating from active promoters, which are less shielded by nucleosomes, exhibit more randomized cleavage patterns compared to instances where promoters are inactive (33). Through an analysis of the variety in fragment lengths within the promoter region, it becomes feasible to identify highly expressed genes, consequently characterizing the source tissue with potential applications in diagnosis, prognosis, and therapy (33). In contrast to DNA fragmentation patterns, DNA methylation is a well-established epigenetic marker that regulates gene expression. During DNA methylation, a methyl group is added to the fifth carbon of cytosine (5-methylcytosine, 5mC) (34). In somatic cells, 5mC is primarily restricted to CpG dinucleotides, and about 60%–80% of CpGs are

methylated (34). In promoter regions, there is a higher concentration of CpG dinucleotides (CpG islands) when compared to other parts of the genome (35). These CpG islands are predominantly unmethylated across cell types, playing a role in regulating transcription (35). However, in the context of cancer cells, there is a widespread reduction in methylation levels across the genome, along with a specific increase in methylation within CpG islands (36). This phenomenon leads to instability in the genome and disruptions in transcriptional processes. These changes in DNA methylation patterns tend to occur early in the development of tumors, which makes them a promising potential biomarker for the early detection of cancer (37).

1.1.4. Extracellular RNA

ExRNA consists of small RNAs (e.g., microRNA (miRNA)), messenger RNA (mRNA), long non-coding RNA (lncRNA), circular RNA (circRNA) and exogenous RNA, such as bacterial RNA. Compared to cfDNA, exRNA is more dynamic, which makes it more suitable for tracking changes in tumor activity over time. More specifically, the genes themselves will undergo less dynamic alteration over time compared to the dynamic changes seen in gene transcription. Additionally, exRNA serves not only to study abundance differences of relevant target genes, but also to detect mutations in cancer genes, to identify fusion transcripts and alternative splicing events specific to the tumor (38–41). In this thesis, I mainly focused on mRNA, which is more unstable than cfDNA, and has only an estimated half-time of about 15 seconds in plasma if not protected via ribonucleoprotein complexes, lipoprotein complexes, or EVs (8,42). Accurate mRNA quantification is a major challenge, as it is highly dependent on pre-analytical variables, such as the blood tube, the centrifugation protocol, and the RNA extraction kit (43). Also, the concentration is generally very low, and the RNA fragmented. A small part of the thesis focuses on miRNAs, small non-coding RNAs with an average of 22 nucleotides in length. These are released by cells with RNA-binding proteins or packaged inside EVs, which protects them against RNase activity, likely being more stable than naked mRNA (8,44). RNA extraction kits are marketed for plasma or serum input volumes starting from 200 µL. However, companies are starting to focus on optimizing kits that can be applied to higher input volumes, up to 4000 µL, to increase the analytical sensitivity.

The study of exRNAs is underexplored as compared to cfDNA. However, large-scale studies have been set up with the aim to evaluate the potential of exRNA to detect and follow-up cancerous and non-cancerous diseases. Larson et al. performed a transcriptome-wide characterization of plasma exRNA in cancer, i.e. stage III breast (n=46), lung (n=30) and non-cancer (n=89) participants from the Circulating Cell-free Genome Atlas (NCT02889978, a clinical study from Grail) (41). Starting from 8 mL of plasma per patient, they identified tissue- and cancer-specific genes, recurrently detected in individuals with cancer. Moreover, the

levels of these genes correlate with tumor shedding rate and RNA expression in the matched tissue. Hence, exRNAs provide the opportunity to detect cancer in patients with low levels of circulating tumor DNA, by the detection of genes with a high expression in the tumor tissue (41). Some diagnostic companion tests on liquids are marketed. For instance, the Progensa *PCA3* test is a urine-based assay, being the first lncRNA approved by the FDA for the use as biomarker in prostate cancer (45). This test is an aid for the decision-making process regarding the necessity of a tissue biopsy. In addition, the ExoDx Prostate IntelliScore EPI is a urine test for quantitative assessment of three prostate cancer specific, exosome-derived RNA biomarkers (*ERG*, *PCA3* and *SPDEF*) by qPCR (46). This test is intended to assess the risk for high grade prostate cancer in men of 50 years or older, presenting for initial biopsy with a PSA level of 2-10 ng/mL. Furthermore, the biomarker potential of exRNA has also been confirmed in other diseases, such as liver disease, neurodegeneration, and obstetrics (47–50).

1.1.5. Extracellular vesicles

Apart from freely floating nucleic acids (cfDNA and exRNA) in circulation, cfDNA and exRNA are also being encapsulated in EVs, protecting them from the harsh environmental conditions (51). In addition to nucleic acids, EVs also contain a cargo of proteins, lipids, and metabolites within their lipid bilayer (51). EVs can be categorized as exosomes, ectosomes and apoptotic bodies, depending on the mode of biogenesis and release (51). Exosomes originate from endosomes, while ectosomes and apoptotic bodies arise from membrane blebbing of intact and apoptotic cells, respectively (51). EVs are nanometer-sized particles, released into the extracellular space by virtually all eukaryotic cell types (52). EVs are a fingerprint of their parental cell, making them appealing for cancer biomarker studies (52). For instance, Krug et al. showed improved detection sensitivity of *EGFR* mutations in NSCLC patients by a combined exosomal RNA and ctDNA analysis from a median volume of 3 mL plasma (31). The diagnostic prostate cancer test, ExoDx Prostate IntelliScore EPI, described in the previous section, is based on the assessment of exosome-derived RNA.

EV subtypes are very heterogeneous with varying sizes from 40 to over 500 nm, making it challenging to separate them from other extracellular blood-based particles, such as platelets and lipoprotein particles, for EV-based clinical applications (52). In 2012, the issue of platelet removal was recognized by Lacroix et al, by making use of the protocol that was published by the International Society on Thrombosis and Haemostasis (ISTH), i.e., two subsequent centrifugations of 15 min at 2500 g with isolation of the upper phase after each centrifugation step (53). This is the most commonly applied protocol to prepare plasma for the EV research and was adopted by the American Heart Association as the methodological guidelines to study EVs (53). Platelet concentrations in plasma prepared by the ISTH protocol are below the

limit of detection if measured by routine hematology analyzers, while they are still detectable by flow cytometry measurements (53). To effectively remove platelets without affecting the concentration of plasma EVs, a fast, cost-effective, and reproducible filtration step should be introduced (53). Lipoproteins in particular are frequently co-isolated with EVs, leading to confounding results. Separation of both is even harder than the separation of platelets and EVs. To purify EVs, relying solely on density differences is not sufficient, and therefore, a combination of different approaches is suggested, such as liquid chromatography and immunoprecipitation (54).

1.1.6. Tumor-educated platelets

Platelets, originating from megakaryocytes as anucleate cells, assist in thrombosis and hemostasis, conduct immune surveillance and communication, aid vessel remodeling and have a role in inflammation (55). Apart from these functions, an interaction between platelets and cancer has been described back in 1868, when Trousseau noted that spontaneous coagulation is common in patients with cancer (55). Further research on the interaction mechanisms led to new insights: platelets aid in the invasion of tumor cells into the local vasculature, where they protect CTCs from shear stress and from the host's immune response (55). Once the metastatic cell finds its micrometastatic niche, platelets aid in extravasation (55). Furthermore, they assist in building the tumor stroma and neoangiogenesis (55). During this process of interacting with tumor cells, platelets become educated, and their RNA cargo is altered, giving rise to the term TEPs, which is a relatively new concept in the liquid biopsy field (55). Three main processes are responsible for the education of these platelets: sequestration of biomolecules, tumor-specific splice events and megakaryocyte alteration. By sequestration of biomolecules (process 1), platelets continuously exchange circulating nucleic acids and proteins with the tumor and its microenvironment via vesicle-mediated transport. Hence, platelets harbor these tumor-specific elements, such as *KRAS*, *EGFR* and *PIK3CA* variants. Despite being anucleate, platelets harbor many types of RNA, such as precursor messenger RNA, mRNA, ribosomal RNA, small nuclear RNA, small nucleolar RNA, transfer RNA, miRNA, lncRNAs, circRNA, antisense RNA, and mitochondrial DNA, as well as a spliceosome and a ribosome. Specific splice events occur in reaction to stimuli such as platelet activation (process 2). Platelets can also be modified externally, by releasing cytokines or EVs upon tumor-bone marrow communication, thereby altering the megakaryocyte's transcriptional profile. Furthermore, it has been shown that younger platelets are more common than older platelets in cancer patients, bearing a more pro-active, inflammatory, RNA-rich state (process 3) (55).

Hence, the RNA content and RNA splicing patterns of the TEPs are claimed to be cancer-specific, therefore serving as cancer biomarkers. For instance, Jonas et al. showed that *EML4-ALK* fusion transcripts in NSCLC could be identified through reverse transcription-quantitative polymerase chain reaction (RT-qPCR) in circulating blood platelets (sensitivity of 65%) and they have shown to reveal crizotinib resistance two months prior to radiographic disease progression in one patient (56). Apart from RT-qPCR-based approaches, Best et al. optimized an mRNA sequencing-based approach for the analysis of TEPs, called thromboSeq (57,58). With this approach, they were able to distinguish 228 patients with localized and metastasized tumors from 55 healthy individuals with 96% accuracy. Also, *MET* or *HER2* positive, and mutant *KRAS*, *EGFR* or *PIK3CA* tumors were accurately distinguished using surrogate TEP mRNA profiles (57). Furthermore, they showed the potential of performing TEP-based discrimination of early- and late-stage NSCLC from healthy individuals and patients with various non-cancerous inflammatory conditions, as well as the potential to identify three subtypes of breast cancer (57,59). Also, sarcoma patients have been successfully distinguished from healthy controls by Heinhuis et al., and TEPs have proven their value in multiple other cancer entities, such as glioblastoma, prostate cancer, colorectal cancer, pancreatic cancer, hepatobiliary cancer and nasopharyngeal carcinoma (55,60).

Very recently, Liefaard et al. raised some important caveats when applying the wet lab and dry lab (thromboSeq) protocol of Best et al. More precisely, they investigated platelet mRNA from 266 women with stage I-IV breast cancer and 212 female controls from 6 hospitals. First, a classifier was trained according to the tromboSeq protocol on 71% of the multicenter study population. In addition, an alternative classifier was trained using elastic net regression. The performance of both classifiers was assessed using the remaining 29% of the population. Then, the classifier performance was validated on a single-center sample cohort. Initial performance of the classifiers was adequate; however, post hoc analyses revealed the hospital of origin as a confounder. Batch effects could be attributed to the time allowed between blood withdrawal and platelet isolation, as blood can be stored up to 48 hours before platelet isolation according to the protocol of Best et al. Platelet activation has shown to increase with longer time to processing and with higher temperatures. Additionally, the blood tube volumes may influence the TEP profiles, as tube volumes of 4, 6 or 10 mL are allowed to be used in the protocol. Batch effects were also seen within the same hospital, as validation on the single-center sample cohort was unsuccessful. Similar to other biomarkers (e.g. exRNA, EVs and CTCs), the TEP profiles are considered very prone to pre-analytical variables, but also the use of medication or co-morbidities can influence the TEP signal. For instance, chemotherapy suppresses the bone marrow inducing thrombocytopenia, so an effect on the platelet gene expression profile is very probable. Liefaard et al. propose a

thorough revision of the protocol before reconsidering TEP RNA based classifiers in the future. Furthermore, detailed reporting of co-morbidities is crucial for the analysis of TEP signatures (61).

1.2. The bigger picture in oncology: multi-analyte analysis

Even though some protein, cfDNA and CTC biomarkers have been FDA approved, they often suffer from a limited sensitivity and specificity. Detection and follow-up of cancer will benefit from the exploration of additional blood-based biomarkers. Integrating the knowledge of the different fields, such as proteomics, transcriptomics and (epi)genomics, for a combined screening of multiple analytes in a patient's sample will be important to overcome the limitations of each of the biomarkers separately (41). Multi-analyte data can improve early cancer detection, minimal residual disease monitoring and treatment response surveillance (62). For instance, a joint analysis of ctDNA and CTCs has shown to improve outcome prediction and mechanism identification of therapy resistance in metastatic breast cancers (62,63). Putcha et al. demonstrated that combining tumor- and immune-derived signals from cfDNA, epigenetic and protein biomarkers could detect early-stage colorectal cancer with high sensitivity and specificity (62,64). Krug et al. show that an increased sensitivity to detect *EGFR* mutations by the combined analysis of cfDNA and exosomal RNA is obtained (31). Cohen et al. show how combining mutations in ctDNA with protein markers can result in a screening test with improved sensitivity for the earlier detection of pancreatic cancer (65). Furthermore, they developed a multi-analyte test, CancerSeek, simultaneously evaluating the presence of mutations and eight cancer-associated protein biomarkers in the blood (66,67). Multiplex PCR analysis of ctDNA enables the detection of mutations at 2001 genomic positions across 16 genes, whereas levels of the protein biomarkers are assessed using immunoassays (66,67).

2. Neuroblastoma

Neuroblastoma (NB) is an extracranial solid tumor, accounting for up to 15% of pediatric oncology deaths (68). It occurs almost exclusively in early childhood, with a median age at diagnosis of 17-18 months and approximately 40% of the patients younger than 1 year at diagnosis. Less than 5% of the patients are older than 10 years at diagnosis (68). Remarkably, the clinical behavior ranges from an asymptomatic benign, but sometimes metastatic malignancy showing spontaneous regression to very aggressive proliferative tumors that may be widely disseminated and often have a fatal outcome (69).

2.1. The origin of neuroblastoma

NB tumors are derived from neural crest cells (NCCs), a unique population of cells that arise from the dorsal part of the neural tube during embryonic development. As these cells detach

from the neural tube, they undergo an epithelial-to-mesenchymal transformation (EMT) and extensive migration along well-defined pathways (70). Four groups of NCCs are defined, based on their specific regional contributions to structures of the embryo: cranial, vagal, trunk and (lumbo)sacral NCCs (70). NB tumors arise due to an impaired differentiation of the trunk neural crest cells. Trunk neural crest cells follow either a ventral (sympathoadrenal, SA) pathway, or a dorsolateral pathway (**Figure 2**). Neural crest cells following the stream ventrally to the somites, develop into the dorsal root ganglia and the chain ganglia of the sympathetic division of the autonomic nervous system. The neurons that develop in the chain ganglia become the peripheral (postganglionic) neurons of the sympathetic autonomic nervous system. Other NCCs, following the SA pathway, form the neurosecretory chromaffin cells of the adrenal medulla. Apart from forming neurons, NCCs are also capable of forming glia of the peripheral ganglia, non-neural cells supporting and protecting neurons, including Schwann cells and satellite cells. The dorsolateral pathway (between the ectoderm and somites) in its turn results in the formation of melanocytes (70–72). Neuroblastoma is identified as a disease of the ventral, SA lineage, originating from the so-called SA progenitor cells (73). Consequently, neuroblastoma tumors can arise anywhere in the sympathetic nervous system. Approximately 35% of primary neuroblastoma tumors occur in the adrenal medulla. Other common sites include the extra-adrenal retroperitoneum (30%), the neck (5%), posterior mediastinum (20%) and pelvis (5%) (69,73,74).

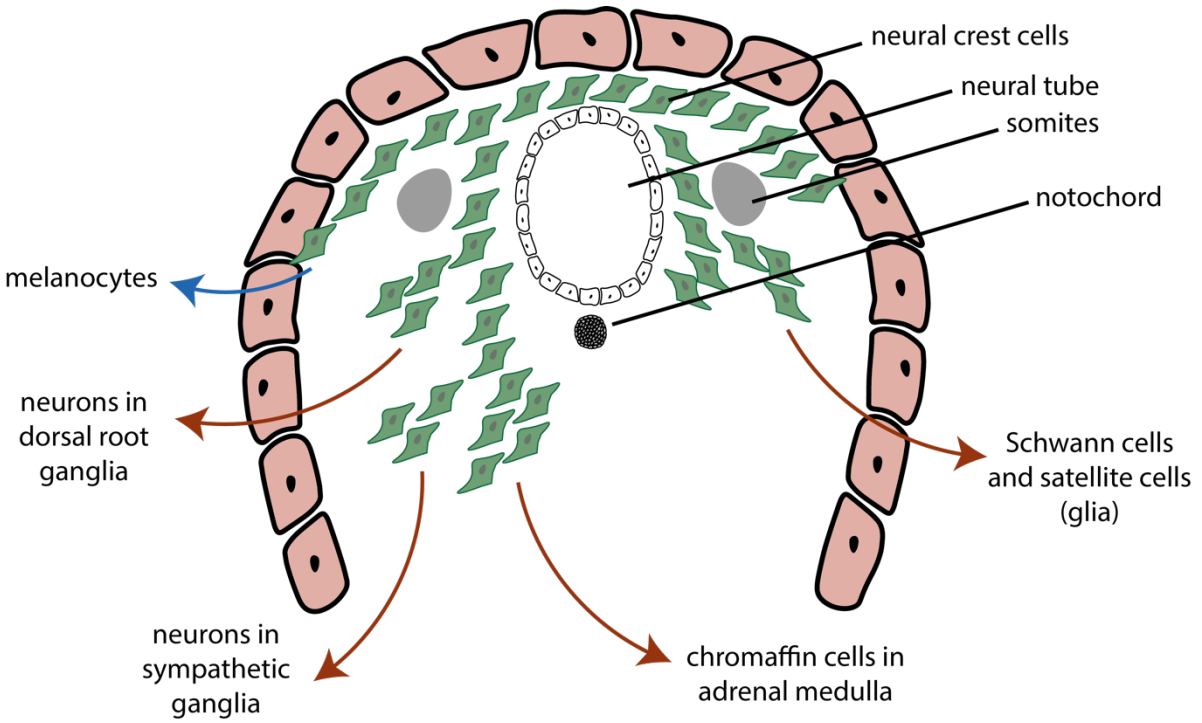

Figure 2. Migration pathways of the trunk neural crest cells. Neural crest cells migrate towards their destined location via a dorsolateral pathway (indicated with a blue arrow) and a ventral pathway (indicated with red arrows). The dorsolateral pathway forms the melanocytes of the skin of the trunk and limbs after invading the surface of the ectoderm. Following the ventral pathway, neurons are formed in the dorsal root ganglia and

sympathetic ganglia, as well as chromaffin cells in the adrenal medulla, non-neuronal Schwann cells and satellite cells as protectors for the neurons. Figure created with Adobe Illustrator 2022.

2.2. From neural crest cells over sympathoadrenal progenitors to committed human cells

As the processes involved in the development of the sympathetic nervous system are very complex, a defective differentiation of NCCs due to genomic and epigenetic impairments is not uncommon (75). Impaired development, differentiation, and migration of NCCs drive oncogenesis of multiple pediatric malignancies, such as NB, peripheral primitive neuroectodermal tumors, malignant peripheral nerve sheath tumors, craniofacial osteosarcoma, as well as adult malignancies such as melanoma (75). As already mentioned, NCCs give rise to specific progenitors diverging into several lineages, and the SA lineage is linked to NB development. The SA lineage will be discussed in more detail in this section (**Figure 3**).

Upon closure of the neural tube, a series of transcription factors activate the EMT machinery and the delamination and formation of NCCs, equipped with migratory properties. The dorsal aorta, expressing bone morphogenetic proteins (BMPs) and therefore producing chemo-attractants SDF1 and NRG1, is key in coordinating NCC migration and guides NCCs through the SA cell lineage, giving rise to sympathetic ganglia and the adrenal medulla. After delamination from the neural plate, NCCs undergo a first split, with a part of the cells ending up in the nervous sensory lineage and another part differentiating to bipotent autonomic-mesenchymal progenitors, co-expressing *PHOX2B* and *PRRX1*. Subsequently the bipotent progenitors undergo a secondary split, separating the mesenchymal lineage (*PRRX1* expression) from the SA lineage (*PHOX2B* expression). Reprogramming between both lineages can occur by NOTCH signaling. The cells entering the SA lineage are called SA progenitors. Other important factors involved in the initial differentiation process to SA progenitors include *ASCL1*, *PHOX2A*, *HAND2*, *MYCN*, *SOX10*, *GATA2* and *GATA3*. SA progenitors differentiate to Schwann cell precursors (SCPs) and sympathetic neural progenitor cells (SNPCs). SNPCs differentiate further to extra-adrenal sympathetic neurons (**Figure 3**, early path), ganglia and suprarenal sympathetic ganglia (SRG). The SCPs show a high differentiation potential and are at the root of the adrenal medulla differentiation hierarchy, next to differentiating to Schwann cells, melanocytes and parasympathetic ganglia. SCPs migrate along the nerve tracks toward the adrenal medulla and differentiate to chromaffin cells and intra-adrenal neuroblasts (forming intrarenal sympathetic neurons, **Figure 3**, late path) via a transient population of bridge cells and connecting progenitor cells (CPCs). Of note, the intra-adrenal early neuroblasts are capable of transitioning to early chromaffin cells, and vice versa, with formation of chromaffin cells being the predominant direction. The discovery

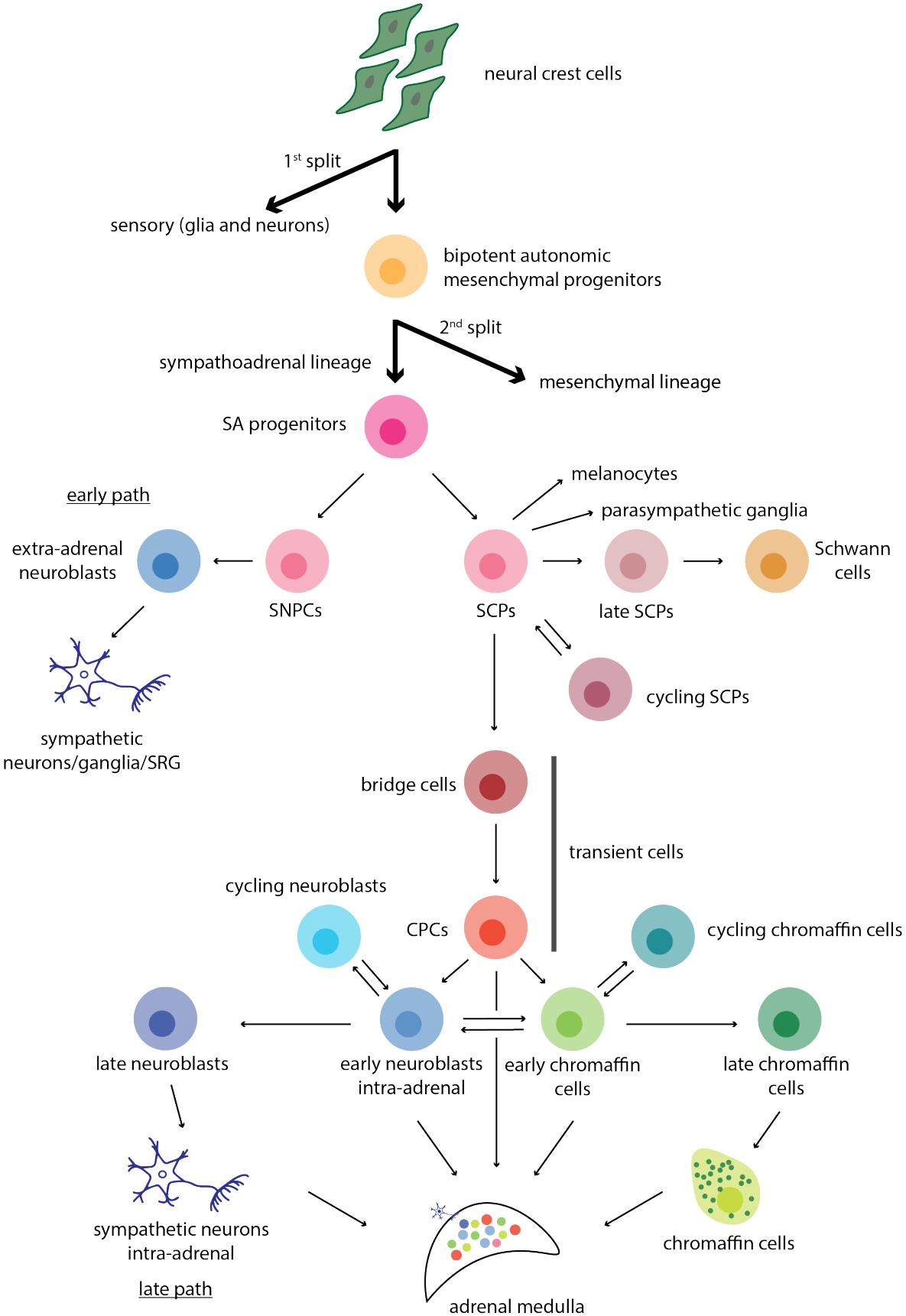

Figure 3. From neural crest cells to committed human cells. Upon closure of the neural tube, the cells from the neural plate delaminate and get migratory properties, resulting in neural crest cells (NCCs). These cells undergo a first split, forming sensory glia and neurons, and bipotent autonomic mesenchymal progenitors. The latter cells undergo a second split, in which part of the cells enter the mesenchymal lineage, and another part enter the SA

lineage as SA progenitors. The SA progenitors on its turn differentiate to sympathetic neurons via sympathetic neural progenitor cells (early phase). Furthermore, SA progenitors form Schwann cell precursors. The Schwann cell precursors differentiate not only to Schwann cells, but also melanocytes and parasympathetic ganglia. Furthermore, they form connecting progenitor cells (CPCs), diverging into chromaffin and neuroblast populations (late path). Of note, intra-adrenal neuroblasts can undergo a transition into local chromaffin cells and vice versa. CPCs: connecting progenitor cells, SA: sympathoadrenal, SCPs: Schwann cell precursors, SNPCs: sympathetic neural progenitor cells, SRG: suprarenal sympathetic ganglion. Figure created with Adobe Illustrator 2022, based on (75).

of two different differentiation pathways (early and late path forming extra-adrenal and intra-adrenal neuroblasts, respectively), and the SCPs being a common progenitor of chromaffin cells and intra-adrenal neuroblasts, and the ability of transition between chromaffin cells and neuroblasts, reveals a remarkable complexity of human adrenal medulla development. The prolonged time of cell transitions observed in the human adrenal medulla development increases the risk for each cell type to acquire genetic alterations, promoting NB formation at different levels. Particularly susceptible to genomic and epigenetic alterations are the neural crest-derived cells with a high transcriptional activity, whereby chromatin is open. These cells include bipotent progenitors and SCPs, bridge cells, CPCs, immature neuroblasts, and chromaffin cells with low degrees of differentiation or with an enhanced proliferative state (cycling cells) that they maintain following malignant transformation (75).

As SA differentiation occurs within the adrenal medulla, it contains a mix of undifferentiated progenitor and differentiated cells. SCPs are located inside nests of neuroblasts with small groups of chromaffin cells clustered around. Most adrenal HR-NB tumors emerge from noradrenergic chromaffin cells, and in general, tumors are correlated with an undifferentiated cell state, explaining the heterogeneous nature of NB tumors, as the undifferentiated population of cells is highly diverse (69,75). Of note, the proportion of differentiated cells is higher in *MYCN*-nonamplified high-risk and low-risk tumors. This suggests that low-risk tumors arise at a later timepoint during development or that a higher degree of dedifferentiation is occurring in *MYCN*-amplified HR-NB tumors (75).

2.3. Disease staging of neuroblastoma tumors

One of the hallmarks of NB is heterogeneity. Because of the tumoral heterogeneity discussed in the previous paragraph, patients' outcomes are also very heterogeneous. To assign the optimal treatment regimen, patients are first staged, categorized to a histology grading system and subsequently assigned to a risk classification group. Many different NB staging systems and risk classifiers have been incorporated worldwide. In 1986, the International Neuroblastoma Staging System (INSS) was described, based on tumor location with respect to midline structures, lymph node status, and extent of upfront surgical resection. Based on this, localized tumors are assigned to INSS stage 1, 2A, 2B or 3. Metastatic patients are subdivided to stage 4 or 4S, depending on the pattern of metastasis. Stage 4S patients include

children under the age of 12 months, with specific metastatic disease pattern including only liver, skin and bone marrow, while stage 4 patients include all metastatic patients, except for these belonging to stage 4S (76,77). Later, in 2005, a staging system independent of surgical resection extent was described, the International Neuroblastoma Risk Group (INRG) staging system (INRGSS, **Table 1**). This system allows for pretreatment staging rather than postsurgical staging, enabling the uniform staging of patients with localized disease who do not require surgical resection including those with perinatally diagnosed disease. Previously these patients could not be properly assigned an INSS stage as surgical resection was required to define stage 1 or 2 disease. In INRGSS, locoregional tumors are defined as L1 (image-defined risk factor (IDRF) absent) or L2 (IDRF present). Furthermore, INRGSS stage M defines metastatic disease, except in children less than 18 months old with metastases restricted to skin, liver, and/or limited marrow involvement (stage MS, metastatic special) (76,77).

Table 1. International Neuroblastoma Risk Group Staging System (INRGSS). Taken from (77).

INRG stage	description
L1	localized tumor with no image-defined risk factors
L2	localized tumor with one or more image-defined risk factors
M	distant metastatic disease
MS	metastatic disease in children under 18 months with metastases limited to skin, liver, and/or bone marrow (<10% involvement)

2.4. Tumor histology grading system

The first tumor histology grading system was developed by Shimada et al. in 1984. Tumors were classified to define groups with either favorable or unfavorable prognosis, by histologic features, including the degree of stroma presence, grade of differentiation, mitosis-karyorrhexis index (MKI), presence of nodules, and age (77). In 1999, this grading system was updated, giving rise to the International Neuroblastoma Pathology Classification (INPC, **Table 2**).

Table 2. International Neuroblastoma Pathology Classification (INPC). MKI: mitosis-karyorrhexis index. Taken from (77).

favorable histology	unfavorable histology
ganglioneuroma mature (stroma-dominant)	ganglioneuroblastoma, nodular (composite; stroma-rich/stroma-dominant and stroma-poor)
ganglioneuroma maturing (stroma-dominant)	neuroblastoma (stroma-poor)—all else not in favorable histology category

ganglioneuroblastoma, intermixed (stroma-rich)	
neuroblastoma (stroma-poor), differentiating or poorly differentiated with low/intermediate MKI in patients <1.5 years at diagnosis	
neuroblastoma (stroma-poor), differentiating with low MKI in patients 1.5–5 years at diagnosis	

2.5. Risk stratification at the basis of an optimal treatment plan

After disease staging and tumor histology grading, a patient is stratified to an appropriate risk group. Through the INRG classification system, as this has been accepted internationally for pre-treatment risk classification, efforts have been made to uniformly define risk groups across collaborative groups. The INRG risk classification system considers the INRG stage, age at diagnosis, tumor histology, tumor cell ploidy, *MYCN* status (amplified and non-amplified) and 11q aberration (**Table 3**) (76,77). In this way, patient outcomes can be compared easily worldwide between clinical trials. This risk system is based on the biomarker and outcome data for over 24,000 patients stored in the INRG Data Commons (78).

Table 3. The INRG risk classification system. GN: ganglioneuroma, GNB: ganglioneuroblastoma, NA: non-amplified, Amp: amplified. Taken from (77).

INRG stage	age (months)	histologic category	grade of tumor differentiation	*MYCN*	11q aberration	ploidy	pretreatment risk group
L1/L2		GN maturing; GNB intermixed					A very low
L1		Any, except GN maturing or GNB intermixed		NA			B very low
				Amp			K high
L2	< 18	Any, except GN maturing or GNB intermixed		NA	No		D Low
					yes		G intermediate
	≥ 18	GNB nodular; neuroblastoma	differentiating	NA	No		E low
					yes		H intermediate
			poorly differentiated or undifferentiated	NA			
				Amp			N High
M	< 18			NA		Hyperploid	F low
	< 12			NA		Diploid	I intermediate

	12 to < 18	NA		diploid	J intermediate
	< 18	Amp			O high
	≥ 18				P high
MS	< 18	NA	No		C very low
			Yes		Q high
		Amp			R high

2.6. The future of patient stratification

Although the INRG Classification System provides a platform for uniformly defining risk, the more recently discovered genomic and molecular biomarkers, including gene expression signatures, mutational profiles, and telomere maintenance mechanisms, were not available during the development of this risk algorithm in 2005 (77,79,80). Furthermore, chromosomal aberrations, the most recurrent genomic alterations found in neuroblastoma, and copy number changes are being studied more into detail. For instance, whole-chromosome imbalances are associated with a more favorable prognosis and usually occur in younger patients (<1 year old), whereas segmental chromosomal gains or losses are associated with poor outcomes and patients harboring these alterations are usually older (81). Common segmental chromosomal alterations include deletions of 1p, 3p, 11q, 4p, 9p and 14q and gains of 1q, 2p and 17q (81). So far, only 11q loss is considered in the INRG risk classification system, however, other segmental chromosomal aberrations have also shown to be associated with poor outcomes, even in the absence of *MYCN* amplification (81,82).

It is anticipated that incorporating these robust prognostic markers in the next-generation INRG Classification System will lead to refined treatment stratification and improved patient outcomes (80). However, applying a revised risk classification system could hamper the comparison of results between research groups and between retrospective and prospective data. Optimizing treatment of individual patients requires close collaboration between the international neuroblastoma community and data scientists to ensure that harmonized criteria are used to define risk and guide therapy (80).

2.7. Treating neuroblastoma: from “wait and see” to intensive multimodal therapy

Therapy will be tailored according to the patient’s risk group, i.e. very low, low, intermediate or high risk. International standardization of risk stratification is pursued by establishing the INRG classification system. In addition, different initiatives emerged to bring countries together to set-up large clinical trials and use the trial outcomes to create standardized treatment protocols. For instance, many European countries were brought together by the establishment of the International Society of Paediatric Oncology Europe Neuroblastoma

Group (SIOPEN) in 1998 (83). Another initiative is the Children's Oncology Group (COG), uniting cancer centers across North America, Australia, New Zealand, and Europe. Germany, Switzerland, and Austria were brought together by the Society of Paediatric Oncology and Haematology (GPOH). As we are following the SIOPEN treatment guidelines in Belgium, further discussion will be focused on this treatment protocol.

Non-high-risk neuroblastoma patients represent nearly half of newly diagnosed cases and have an excellent event-free and overall survival with current therapies. Patients at low risk are either kept under observation or undergo a surgical resection if appropriate. For intermediate-risk patients, treatment consists of multiple courses of chemotherapy, potentially combined with surgical resection and in rare cases radiotherapy. For these groups, the focus over the last decades was to safely reduce treatment intensity, while maintaining the favorable patient outcome. This was achieved by the establishment of several consortium groups performing clinical research trials. One example is the Low and Intermediate Risk Neuroblastoma European Study (LINES) from SIOPEN (83,84).

Next to the LINES trial for low- and intermediate-risk neuroblastoma patients, SIOPEN also has multiple trials either completed or still running, including HR-NB patients. Treating HR-NB patients is complex and involves different phases: (1) initial induction chemotherapy, (2) surgery to remove the primary tumor (3), consolidation with high-dose chemotherapy followed by autologous stem cell rescue (ASCR), (4) radiotherapy to the site of the primary tumor and (5) maintenance therapy with anti-GD2 immunotherapy and retinoic acid (**Figure 4**) (83). The SIOPEN consortium is proposing Rapid COJEC (rCOJEC) in their standard practice for induction chemotherapy (85). rCOJEC is a high-dose rapid schedule of eight cycles, alternating vincristine (O) and carboplatin (J) (course A), vincristine and cisplatin (C) (course B), and vincristine, etoposide (E) and cyclophosphamide (C) (course C) in the sequence ABCBABCB. The interval between courses is 10 days. The Memorial Sloan Kettering Cancer Center (MSKCC) has been using the modified N7 (MSKCC-N5) regimen. This regimen comprised high-dose cyclophosphamide, doxorubicin with vincristine alternating with high-dose cisplatin, etoposide for a total of five courses. In the HR-NBL-1.5/SIOPEN study, the rCOJEC induction regimen was compared to the MSKCC modified N7 (MSKCC-N5) induction regimen and there was no significant difference in outcome observed between both regimens, however the rCOJEC regimen results in less acute toxicity, making it the preferred induction regimen of SIOPEN (86). After the end of induction, ideally after peripheral stem cell harvest, a surgery might be performed to achieve complete excision of the tumor. Additionally, two TVD (topotecan, vincristine, doxorubicine) courses have proven to improve the response rate when no complete or partial metastatic response is observed after rCOJEC, however this addition does not significantly impact the survival rate and thus is no longer

proposed as part of the standard SIOPEN regimen. Patients with a complete or partial response proceed to the consolidation phase (87). After comparing two high-dose chemotherapy (HDC) regimens, busalfan/melphalan (Bu-Mel) and carboplatin/etoposide/melphalan (CEM) in the HR-NBL1 trial, the SIOPEN standard of care during consolidation phase (high dose chemotherapy, HDC) is set to Bu-Mel, followed by autologous stem cell rescue. Bu-Mel improved event-free survival and caused fewer adverse events than did CEM (88). Furthermore, all patients receive radiotherapy (21 Gy) to the primary tumor site after the consolidation phase. To conclude, the maintenance phase within SIOPEN starts with one cycle of 13-cis-retinoic acid (13-cis-RA) and is then followed by 5 cycles of 35 days of dinutuximab beta (anti-GD2 antibody) and 13-cis-RA treatment (89).

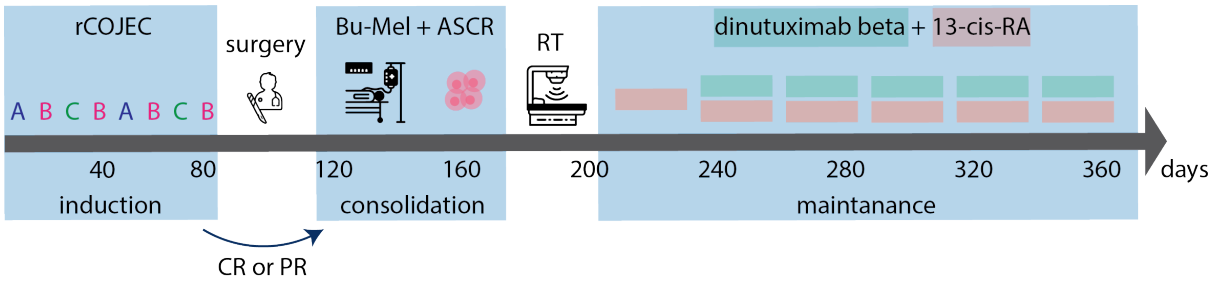

Figure 4. SIOPEN HR-NBL1 (NCT01704716) treatment scheme for HR-NB patients. This figure only includes the selected treatment arms, based on the results of the HR-NBL1 clinical trial. In a first induction phase, the patient is treated in eight cycles (sequence ABCBABCB), consisting of three different courses: vincristine and carboplatin (course A), vincristine and cisplatin (course B), and vincristine, etoposide and cyclophosphamide (course C). Each course takes 10 days to complete. When a patient shows complete or partial response, he proceeds to the consolidation phase with high dose chemotherapy (HDC, Bu-Mel) and ASCR. After the induction phase, ideally after peripheral stem cell harvest, a surgery might be performed to remove primary tumor tissue. Furthermore, after the consolidation phase, all patients will receive radiotherapy and proceed to the maintenance phase starting with one cycle of 13-cis-RA, followed by 5 cycles of 35 days of dinutuximab beta and 13-cis-RA treatment. ASCR: autologous stem cell rescue, Bu-Mel: busalfan/melphalan, CR: complete remission, PR: partial remission, rCOJEC: rapid cisplatin/vincristine/carboplatin/etoposide/cyclophosphamide, RA: retinoic acid, RT: radiotherapy. Figure created with Adobe Illustrator 2022, based on (90).

The treatment of HR-NB patients represents one of the remaining challenges for pediatric oncologists. Despite intensive multimodal therapy, disease progression is observed during therapy in more than half of HR-NB patients, leading to fatal outcome (91). The currently running SIOPEN High Risk Neuroblastoma Study 2 (HR-2) aims to improve the outcome for patients with newly diagnosed HR-NB. In this study, two different induction chemotherapy regimens are compared: rCOJEC and the GPOH regimen. The GPOH regimen consists of three N5 (cisplatin, etoposide, and vindesine) and three N6 cycles (vincristine, dacarbacine, ifosfamide, and doxorubicine) (92). Furthermore, they investigate the impact of giving more intensive consolidation, more specifically, two courses of high dose chemotherapy (Thiotepa followed by Bu-Mel) with each course supported by ASCR, as compared to the standard single course of Bu-Mel. To conclude, they evaluate the benefit of a radiotherapy boost (total of 36 Gy instead of standard 21 Gy dose delivered to the site of the primary tumor) to the

macroscopic residual disease before radiotherapy (ClinicalTrials.gov identifier: NCT04221035).

2.8. Targeted treatments are being integrated in the frontline setting

During the last few years, different omics approaches such as copy number studies, transcriptomic analyses and genome-wide association studies have uncovered genes associated with neuroblastoma susceptibility, aggressiveness, and progression. The identification of such genes opens up the possibility of developing novel targeted therapies or reconsidering already existing drugs by the repositioning of approved drugs (91). Several efforts are ongoing to integrate targeted therapies into the intensive induction regimens, such as the targeted radiopharmaceutical iodine-131 meta-iodobenzylguanidine (^{131}I-MIBG), anaplastic lymphoma kinase (ALK) inhibitors and chemo-immunotherapy including anti-GD2 monoclonal antibodies. These targeted strategies have shown activity in patients with relapsed or refractory disease and are therefore now being studied in the frontline setting. For instance, in an ongoing clinical trial (ClinicalTrials.gov identifier: NCT03126916), patients with a confirmed *ALK* aberration (mutation/amplification) are treated with ALK inhibitors through all phases of treatment. Also, combining anti-GD2 antibodies with chemotherapy is being integrated in the induction phase, as this treatment shows high effectivity in relapse or refractory patients (93).

2.9. Novel potential targeted treatments for neuroblastoma

For patients presenting with relapse or recurrent HR-NB, several treatment options are being evaluated and the SIOPEN consortium has proposed a pragmatic strategy on how to prioritize treatment options available to relapsed HR-NB patients (94). Assignment to clinical trials is often based on the presence or absence of molecular targets for drugging. The proposition is pragmatic in the sense that it is mainly based on the options available to patients via clinical trials. Other options based on genomic alterations are also being proposed (95). The genetic targets can be divided in five main groups, as discussed below.

2.9.1. Mutations

2.9.1.1. *ALK* mutation

The *ALK* gene, which encodes a tyrosine kinase receptor, is mutated in approximately 10% of all diagnostic neuroblastoma cases and in 15% of HR-NB cases (96,97). It is the most common somatically mutated gene in NB, with a higher prevalence of mutations in relapse patients (96). 85% of *ALK* mutations in neuroblastoma occur at three amino acids: R1275 (43%-49%), F1174 (30%-35%) and F1245 (12%). The F1174L mutation is thought to be associated with a more aggressive disease phenotype and resistance to early-generation ALK inhibitors, such as

crizotinib (97). Moreover, co-existence with *MYCN* amplification augments tumor aggressiveness in mouse models as witnessed by a decreased latency to tumor generation and the development of large, bulky tumors as compared to *MYCN* amplified tumors without ALK F1174L mutation (98). Second and third generation ALK inhibitors are being evaluated in clinical trials either in monotherapy or in combination with cyclophosphamide/topotecan (e.g. lorlatinib, ClinicalTrials.gov Identifier: NCT03107988, (93)). Lorlatinib in combination with topotecan and cyclophosphamide is well tolerated, and early data suggest encouraging anti-tumor activity, supporting the current integration of lorlatinib into frontline HR-NB therapy for patients with ALK-driven neuroblastoma (99,100).

2.9.1.2. *FGFR1* mutation

Fibroblast growth factor receptor 1 (*FGFR1*) mutations, more specifically N546K hotspot mutations, have been observed in NB (primary and relapsed tumors), as well as in Ewing sarcoma and brain tumors (101). *FGFR1* is crucial for the expression of genes involved in embryonic stem cell migration and neural crest cell formation (102). By consequence, *FGFR1* can act as a cancer-driver gene in NB and mutations might activate embryonic signaling, promoting disease progression and recurrence. FGFR1 is a tyrosine kinase receptor that, once activated, leads to subsequent activation of downstream cellular signaling pathways such as RAS/MAPK and PI3K/AKT/mTOR (103). Driver mutations in *FGFR1*, altering FGFR1 auto-phosphorylation, resulting in an increase of kinase activity, are a potential target for treating neuroblastoma, for instance by small-molecule tyrosine kinase inhibitors (TKIs) (101).

2.9.1.3. RAS/MAPK pathway mutation

The RAS/MAPK pathway genes have shown to be altered in pre-treated neuroblastoma samples, and these alterations were strongly correlated to poor outcomes (104,105). Interestingly, an mRNA signature for increased RAS-MAPK pathway activity, consisting of 6 genes (i.e. *ETV4*, *ETV5*, *DUSP6*, *MAFF*, *ETV1*, and *DUSP4*), has recently been defined (106). At relapse, an enrichment of RAS-MAPK pathway mutations has been observed by several research groups (106,107). Some examples of mutated genes are *ALK*, *NF1*, *PTPN11*, *FGFR1*, *NRAS*, *KRAS*, *HRAS*, and *BRAF* (105). Despite the multiple targets for treatment contained in this pathway, inhibition is challenging due to the development of resistance, complex feedback-loop regulation, and a large number of interactions with other signaling pathways that can affect the functioning of the RAS-MAPK pathway (105). Inhibition of other pathways, such as PI3K/AKT/mTOR, or processes like the cell cycle, will be vital to achieving effective treatments for NB and avoiding the development of resistance (105).

2.9.1.4. *ATRX* mutation

ATRX mutations are associated with a telomerase-independent telomere maintenance mechanism known as alternative lengthening of telomeres (ALT), which is thought to be suppressed by wild-type *ATRX* in ALT-negative tumors (96). ALT occurs in approximately 25% of HR-NB. Relapse or progression in patients with ALT neuroblastoma during or after front-line therapy is frequent and almost uniformly fatal. Targeting telomere maintenance with ATR inhibitors is being investigated, however, approximately 50% of ALT neuroblastoma lack any known genomic alteration (93,108).

2.9.2. Genomic translocations

2.9.2.1. *TERT* rearrangement

In addition to the telomerase-independent mechanism of ALT through *ATRX* mutations, ALT can also occur by an increased telomerase activity through *TERT* rearrangements. *TERT* rearrangements have been identified in a subset of HR-NB tumors. Targeting telomerase activity represents a novel therapeutic approach, but no clinical candidates are currently available (95). Imetelstat, inhibiting telomerase enzymatic activity, was evaluated in clinical trials, but showed unacceptable toxicity (95). Nucleoside analogue 6-thio-2'-deoxyguanosine (6-thio-dG), is not yet tested in clinical trials, but shows preclinical utility against neuroblastoma. 6-thio-dG is incorporated in *de novo*-synthesized telomeres, which are modified and not functional anymore (95).

2.9.3. Copy number alterations

2.9.3.1. *MYCN* amplification

MYCN is a driver oncogene in NB, confirmed by the fact that overexpression of N-MYC in neural crest progenitor cells of transgenic mice and zebrafish is sufficient to induce NB development. *MYCN* amplification occurs in 20% of cases overall and up to 50% of HR-NB cases, and is associated with advanced, aggressive tumors and frequent disease relapse (96). Given its correlation with rapid tumor progression, poor prognosis and the limited expression in normal cells and tissue, suggesting high tolerability for a *MYCN*-specific approach, *MYCN* could represent an ideal therapeutic target. Nevertheless, *MYCN* amplification is challenging to inhibit directly. To that end, new strategies have been proposed in the hope of overcoming the failure of the precedent attempt to make *MYCN* a fully available target for HR-NB (109). For instance, bromodomain and extra-terminal domain inhibitors repress *MYCN* transcription, while aurora kinase A inhibitors and phosphatidylinositol 3-kinase/mammalian target of rapamycin (PI3K/mTOR) inhibitors destabilize the MYCN protein (93,109).

2.9.3.2. *ALK* amplification

Apart from *ALK* mutations, amplification of the *ALK* gene is also reported, but only in 1–2% of NB cases. This amplification is leading to increased protein expression and constitutive kinase activity. *ALK* is almost exclusively co-amplified with *MYCN*, as both genes are in close proximity, conferring a poor prognosis (96).

2.9.3.3. *MDM2* amplification

Whereas being mutated in almost 50% of human cancers, the *TP53* tumor suppressor gene is wild type in the vast majority of neuroblastoma tumors. However, upstream p53 pathway inactivation through *MDM2* amplification and suppression of *CDKN2A* (*$p14^{ARF}$* abnormalities) have been reported particularly at relapse (110). These abnormalities converge into the central CDKN2A/MDM2/TP53 axis with increased activity of MDM2, the principal TP53 inhibitor, and subsequent impairment of normal TP53 functioning (111). TP53 is a critical protein for the regulation of apoptosis, cell cycle arrest and DNA damage repair processes in response to DNA damage and cellular stress (109,112). *MDM2* amplification leads to TP53 inhibition by transcription repression or protein ubiquination and degradation, therefore contributing to tumor formation (109,112). MDM2 also exerts TP53-independent oncogenic functions, as MDM2 stabilizes mRNA of vascular endothelial growth factor (*VEGF*), causing increased translation of *VEGF*, stimulating growth of neuroblastoma (109,112). Interestingly, MDM2 may interact with *MYCN* in a similar manner to TP53 in neuroblastoma, resulting in *MYCN* mRNA stabilization and translation increase (109). Clearly, MDM2 is a potential target for anticancer therapy in neuroblastoma.

Idasanutlin is a small-molecule MDM2 inhibitor, preventing the binding of p53 to MDM2. The crystal structure of a peptide derived from p53 and its mode of binding to MDM2 have revealed a deep hydrophobic pocket on the surface of MDM2 (113). The binding between the two proteins is mainly attributed to three critical amino acid residues of p53 (Phe19, Trp23, and Leu26) that project hydrophobic sidechains deep into the cavity of MDM2 (114). These structural characteristics of the p53-MDM2 complex suggest that small-molecule inhibitors capable of blocking the interaction between the two proteins may be identified. Several compounds have been reported to inhibit the binding of p53 and MDM2, including a series of 4,5-dihydroimidazolines, such as nutlin-3a (114). Further optimization efforts to enhance their pharmacological properties for clinical development resulted in the development of idasanutlin, which is currently being evaluated in clinical trials (e.g. ClinicalTrials.gov Identifier for a neuroblastoma-specific trial: NCT04029688 (114)).

2.9.3.4. *CDK4/6* amplification

The cyclin-dependent kinase 4 and 6 (CDK4 and CDK6) cooperate with cyclin D family members to activate the E2F transcription factor through the phosphorylation of RB. E2F transcriptional activity results in the stimulation of cell proliferation by promoting progression through the G1–S cell-cycle checkpoint (115). The CDK4/6 inhibitor ribociclib completed phase 1 single agent testing and demonstrated stable disease as a frequent outcome in neuroblastoma patients (95). It has also been evaluated in combination with topotecan and temozolomide or everolimus in the AcSé-ESMART trial (ClinicalTrials.gov Identifier: NCT02813135) and was found to be well tolerated. A follow-up study of the ribociclib-everolimus combination has been initiated (95,116).

2.9.4. Overexpression

2.9.4.1. BCL-2

In healthy individuals, pro-apoptotic members of the BCL-2 family proteins, such as BAX and PUMA, are in balance with anti-apoptotic members, such as BCL-2 and MCL1 (117). In most neuroblastoma tumors, the prosurvival protein (BCL-2) shows enhanced expression, and MCL1 has been suggested to mimic the BCL-2 function and circumvent the effects of BCL-2 inhibition (111,118). Venetoclax is a specific BCL-2 inhibitor, which is being tested in combinatorial clinical trials (e.g. with idasanutlin, ClinicalTrials.gov Identifier: NCT04029688).

2.9.5. Pathway activation

2.9.5.1. PI3K/Akt/mTOR pathway

The PI3K/Akt/mTOR pathway is constitutively active in neuroblastoma tumors and deregulates cell metabolism via increased expression of multiple growth factor receptors (119). Moreover, this pathway drives oncogenic stabilization of MYCN protein, so inhibition of mTOR functions is a potential strategy for therapeutic targeting of *MYCN*-amplified neuroblastoma tumors (119).

The pathway can be targeted by different strategies, i.e. PI3K inhibition, Akt inhibition and mTOR inhibition (120). Inhibition of mTOR complex 1 (mTORC1) represents the strategy with the most clinical expertise (120). Temsirolimus, a derivative of rapamycin, is a potent and selective inhibitor of mTORC1. The drug was well-tolerated in early phase clinical trials, however, phase II studies demonstrated limited activity of temsirolimus as monotherapy (119,120). Furthermore, resistance to temsirolimus through increased AKT phosphorylation has also been described (120). This prompted to combine temsirolimus with other agents, such as chemotherapeutics, ALK inhibitors and MDM2 inhibitors (119,120).

2.9.6. Combinatorial targeting of pathways to prevent resistance to targeted treatments

Targeted therapeutics are very promising to treat relapse or refractory patients. Moreover, they are being studied in the frontline setting to eradicate the treatment resistant subclones containing specific molecular targets. However, therapeutic resistance is also a concern within molecularly targeted approaches, which could be overcome by identifying well-matched drug combinations (121). Also, by combining targeted treatments, treatment efficacy can increase significantly (96,111).

For instance, a strong synergistic activity is observed when combining the MDM2 inhibitor idasanutlin with the BCL-2 inhibitor venetoclax, irrespective of the basal *BCL-2* and *MCL1* expression levels (111). Idasanutlin can even overcome the resistance to venetoclax in preclinical models, as idasanutlin treatment induces BAX-mediated apoptosis in venetoclax-resistant neuroblastoma cells in the presence of venetoclax (117). This combination is being tested in a clinical trial (ClinicalTrials.gov Identifier: NCT04029688).

A link has been observed between p53 function and *mTOR* expression in neuroblastoma. The tumors maintain two opposing pathways of active p53 that mediates growth arrest and apoptosis, and aberrant mTOR signaling that mediates growth and proliferation (119). In response to stress, p53 transcribes a group of negative regulators of the PI3K/Akt/mTOR pathway, suppressing mTOR signaling and initiating cell-cycle arrest, DNA repair, senescence, or apoptosis (119). In this way, p53 activation via MDM2 inhibition would sensitize neuroblastoma tumors to mTORC1 inhibitors (119). In addition, some studies have highlighted that ALK mutations lead to overactivation of the PI3K/Akt/mTOR pathway, which is why combining ALK inhibitors with mTORC1 inhibitors is also being tested (119,120).

Resistance to ALK inhibitors has been evidenced in pre-clinical studies with ALK-driven NB cell lines and mouse models, by complex relationships between mutation-induced changes in the structure of the ALK tyrosine kinase domain and the differential binding profiles of ALK inhibitors (96). It is anticipated that the long-term use of ALK inhibitors will require combinatorial targeting of pathways downstream of ALK, functionally related bypass mechanisms (e.g. AXL) and concomitant oncogenic pathways (e.g. MDM2), which has shown to increase efficacy of ALK inhibition and overcome *de novo* resistance (96).

2.10. Liquid biopsy biomarkers for neuroblastoma diagnosis and follow-up

The detection of the targets discussed in previous sections can be used in risk stratification of the patient (e.g., *MYCN* amplification). Moreover, early detection of druggable targets can eradicate therapy resistant subclones by a combination of targeted treatments (e.g., detection of *ALK* mutations that can be targeted by ALK inhibitors). Subclonal populations

containing the targets which are driving resistance and relapse are often not captured by tissue biopsies. First of all, only a small part of the tumor is being analyzed at diagnosis, with the chance of missing important targets due to tumor heterogeneity. Furthermore, the molecular profile of the NB tumors can change over time due to selective pressure upon therapy or competition among multiple subclonal populations, resulting in a chemoresistant phenotype. Repetitive tissue sampling is not feasible due to its invasiveness and hampers the longitudinal monitoring of the tumor (8,93,122,123). Current neuroblastoma surveillance strategies rely on cross-sectional anatomic imaging, ^{123}I-MIBG scans and measurement of urinary catecholamine levels. However, these techniques expose young children to radiation and sedation procedures, without the ability to capture chemoresistant subclones (124,125). Liquid biopsies have emerged as a novel, minimally invasive opportunity of detecting and monitoring specific targets in body fluids instead of tumor tissue (8). cfDNA and exRNA biomarkers in liquid biopsies are being evaluated to diagnose and follow-up neuroblastoma tumors.

2.10.1. cfDNA

Several studies have indicated the presence of ctDNA in the plasma from neuroblastoma patients. ctDNA has not only proven useful for the detection of specific targets: also the total cfDNA levels, and therefore ctDNA levels, have value for neuroblastoma surveillance. The cfDNA levels are found to be higher in HR neuroblastoma patients as compared to healthy controls (122). Interestingly, the ctDNA fraction of cfDNA can be predictive of the response to treatment, as an increase has been observed at the time of disease progression, while a decrease has been observed in responsive patients (27). In relation to this, also higher concentrations of cfDNA were obtained from patients with metastatic versus localized disease (i.e. 2,528 versus 175 ng/mL) (126). Some authors also hypothesize that more aggressive cells release more ctDNA (27). The analysis of ctDNA can be performed in a PCR-based approach, requiring prior characterization of the biomarkers of interest, or by a sequencing-based approach where targets are not always specified upfront.

2.10.1.1. PCR-based approach

The majority of research groups have focused on developing assays and analyzing ctDNA through PCR-based approaches, such as digital PCR (dPCR). This requires prior characterization of the biomarkers, such as copy number alterations (CNA, e.g. *MYCN* amplification) and single nucleotide variants (SNV, e.g. *ALK* activating mutations). For instance, Combaret et al. have developed a dPCR-based assay for the detection of *ALK* mutations F1174L and R1275Q in serum or plasma (127). Lodrini et al. optimized a dPCR assay for the *MYCN* and *ALK* copy number status in plasma, accurately discriminating between

MYCN and *ALK* amplification, gain and normal diploid status (128). Peitz et al. optimized dPCR assays that reliably quantify *MYCN* and *ALK* copy numbers and accurately estimate *ALK* F1174L and *ALK* R1275Q mutant allele fractions (MAF) in cfDNA (129).

2.10.1.2. Sequencing-based approach

Apart from the PCR-based approaches, massive parallel sequencing was also successfully applied to cfDNA samples from neuroblastoma patients. For instance, whole exome sequencing (WES) of primary neuroblastoma tissue and matching cfDNA at diagnosis has identified an overlap of only 41% for SNVs, whereas an overlap of 93% was observed for CNAs (27,102). Shallow whole genome sequencing on cfDNA has also proven to be a valid alternative of tissue sampling for copy number profiling (130). Bosse et al. used the FoundationACT assay, a previous version of the FoundationOne Liquid CDx test to profile ctDNA of neuroblastoma patients (125). The Foundation Medicine platform is an NGS-based technology for sensitive detection of variants even at allele frequencies <1% of the total cfDNA, which is more sensitive than WES (125). The FoundationOne Liquid CDx test, however, is focused on cancer driver genes that are more frequently aberrant in adult cancers rather than pediatric cancers. Cimmino et al. developed a targeted NGS gene panel for cfDNA sequencing that is tailored to the genetic landscape of neuroblastoma (102).

2.10.1.3. Lessons learned from ctDNA in neuroblastoma patients

By comparing the detection rate of specific CNAs and SNVs in ctDNA and in primary tumor tissue, spatial and tumoral heterogeneity has proven to be better captured by ctDNA analysis as compared to primary tissue DNA profiling. The detection of SNVs such as *ALK* p.F1174L and *ALK* p.R1275Q is highly different between ctDNA and primary tissue, with in general a higher detection rate (higher MAF) of SNVs in the ctDNA (27,122,125). Even in some cases, the SNV is only detected in the ctDNA. This can be explained by the heterogeneous distribution of SNVs in tumor tissue or a differential shedding of ctDNA from different cells (27). Of note, the heterogeneous distribution of CNAs such as *MYCN* amplification in tumor tissue is less prominent, as the detection rate is often comparable between ctDNA and primary tissue (27,122,125).

Comparison of SNVs present at diagnosis and relapse identifies pathways involved in neuroblastoma progression, such as MAPK pathways and protein kinase A signaling pathways. Moreover, SNVs evolving from diagnostic subclonal to a relapse clonal level preferentially affect pathways of neurogenesis (27). Moreover, the ctDNA MAFs have shown to reflect disease burden and treatment with ALK inhibitors (e.g. lorlatinib) showed reduction or increase in *ALK* mutations according to the response to treatment (27,131).

2.10.2. exRNA

While cfDNA as a blood-based biosource is widely being investigated in neuroblastoma, data on exRNA biomarker potential in neuroblastoma is scarce. Nevertheless, it was recently shown that exRNAs are present in a wide diversity of (blood-based) liquid biopsies and can act as promising precision oncology biomarkers (41). Upon treatment, the transcription of genes can be altered, while the DNA remains more stable. As exRNA is more dynamic than cfDNA, it is better suited to monitor tumor genetics dynamics. Also, it is not only used to identify CNAs or SNVs in genes of interest, but also allows the identification of tumor-specific fusion transcripts and alternative splice events and provides insights into relative expression levels of dedicated genes (38–41).

2.10.2.1. PCR-based approach

So far, most of the plasma or serum exRNA studies have focused on miRNAs. Zeka et al. have identified 9 miRNAs in serum that are correlated to tumor volume in murine xenografts and disease burden in neuroblastoma patients (132). Murray et al. revealed serum miRNAs that are specific for *MYCN*-amplified neurobastoma (133). Ramraj et al. identified serum-circulating miRNAs that can predict the switch from favorable to HR-NB in mouse models (134). These miRNAs have all been identified based on RT-qPCR measurements.

mRNA detection based on RT-qPCR has also proven its utility to predict outcome in HR-NB, however these studies have been performed on peripheral blood. More specifically, high levels of *TH* and *PHOX2B* mRNA in peripheral blood at diagnosis identifies children with relapsed or refractory neuroblastoma at greatest risk of progression or death, who may benefit from novel treatment approaches (135,136).

2.10.2.2. Transcriptome wide approach

So far, to the best of my knowledge, no transcriptome wide studies have been performed on the plasma or serum of neuroblastoma patients. However, the dynamic nature of the transcriptome could enable a real-time monitoring of the tumor response to treatment. This is of great value in the search of biomarkers follow-up a patient's response or resistance to therapy. However, except for focusing on specific tumor aberrations such as mutations or fusion transcripts, it is challenging to distinguish the host response from the tumor response to treatments. Xenografts injected with human tumor cells are excellent models to tackle this issue. The human exRNA in these xenografts is by definition originating from the tumor, while the remaining exRNA is derived from the host (such as mice or rats). My research mainly focused on the optimization of these models to analyze transcriptomic responses of the tumor to treatment.

Research aims

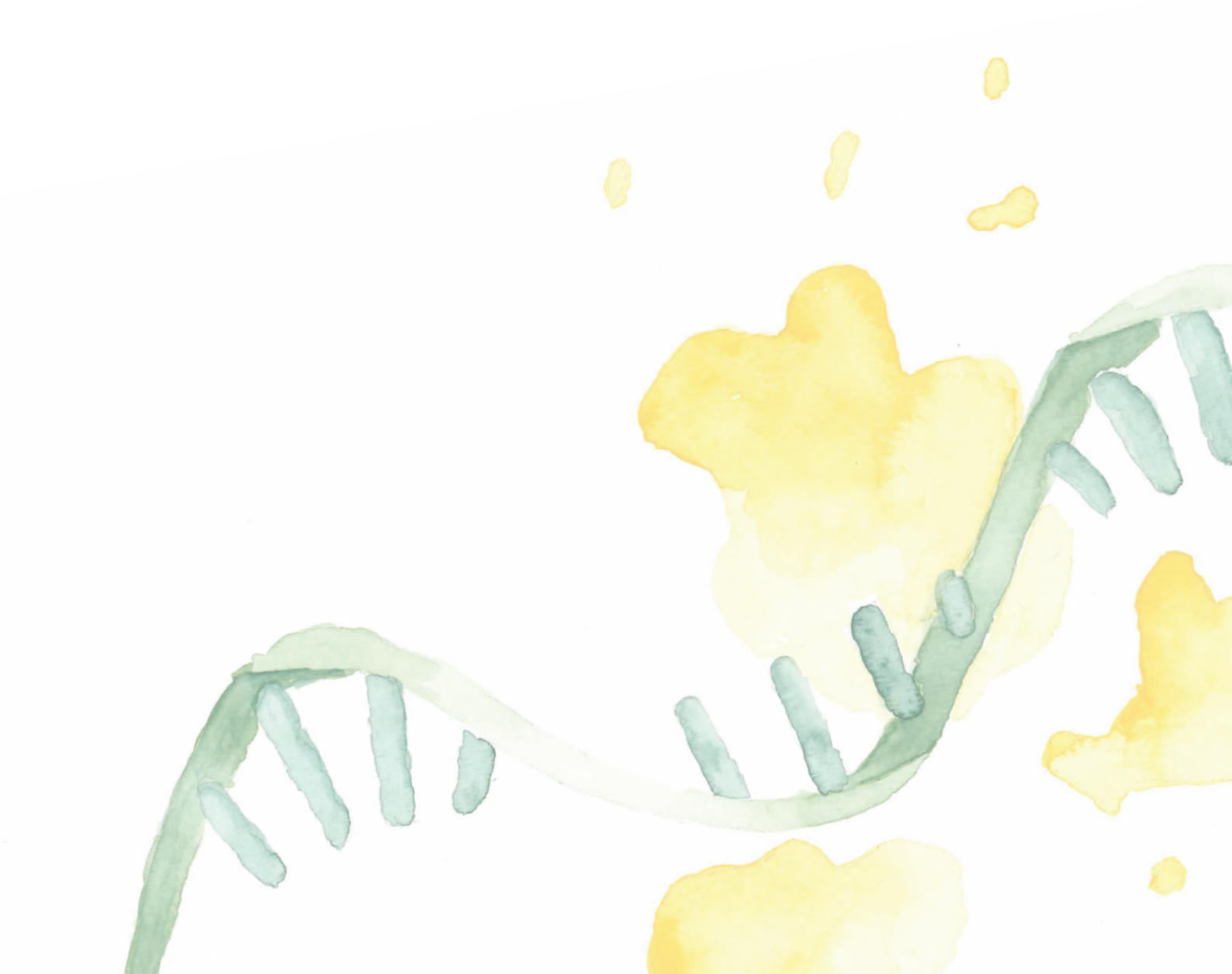

Neuroblastoma patients are assigned to risk classification groups, based on their clinical and genomic features, such as INRG stage, age at diagnosis, tumor histology, *MYCN* status, tumor cell ploidy and 11q aberrations. Patient treatments can vary from watch-and-wait strategy to being treated with intensive multimodal therapies, depending on the risk group they are assigned to. Clearly, correct risk stratification at diagnosis is important to administer the optimal therapy. Furthermore, follow-up of tumor responses to therapy is crucial to timely detect non-response and relapses, as neuroblastoma tumors are typically very heterogeneous and undergo subclonal changes under therapeutic pressure. Tumor tissue biopsies, the current gold standard for diagnosis, do not capture tumor heterogeneity well and do not allow for follow-up by longitudinal sampling, making liquid biopsies promising in the emerging era of precision oncology. cfDNA has already proven its value in neuroblastoma to detect copy number alterations and mutations. Very often, especially in the case of mutations, the detection rate is higher in cfDNA as compared to primary tissue, showing the ability of liquid biopsies to capture tumor heterogeneity. The field of exRNA is still in its infancy and relatively underexplored, although it is better suited to monitor tumor genetics dynamics due to its more dynamic nature than cfDNA. More specifically, treatments can alter the transcription of genes. By conducting longitudinal sampling of liquids and utilizing a whole transcriptomic approach, we can examine the impact of a therapy on cancer cells in greater detail. This enables us to monitor patients' responses or non-responses to treatments, facilitating swift transitions to alternative therapies when appropriate options are available. As it is challenging to distinguish host from tumoral responses in liquid biopsy samples from patients, my research aim was to optimize studies with xenograft models, i.e. mice injected with human tumor cells, to aid in the search for tumoral exRNA treatment response biomarkers. In addition, I wanted to evaluate the added value of a combined cfDNA/exRNA analysis. The aims were pursued by breaking them down into smaller, achievable milestones.

1. Determine the blood fraction with the most prominent tumor signal. Identifying the subcompartment where tumor-derived exRNAs primarily exist in plasma is crucial for studying tumoral exRNA. This knowledge helps minimizing undesirable background signals and enhances the detection sensitivity of tumoral exRNA.
2. Examine how tumor size, engrafted cell line, engraftment site, and tumor vascularity impact the release of tumoral exRNA into the bloodstream. A higher level of tumor-derived exRNA in circulation enhances the ability to detect treatment responses with increased sensitivity.
3. Conduct an evaluation of exRNA/cfDNA co-purification kits. The integration of these kits in the analysis can significantly enhance sensitivity, for instance in detecting targetable mutations.

Results

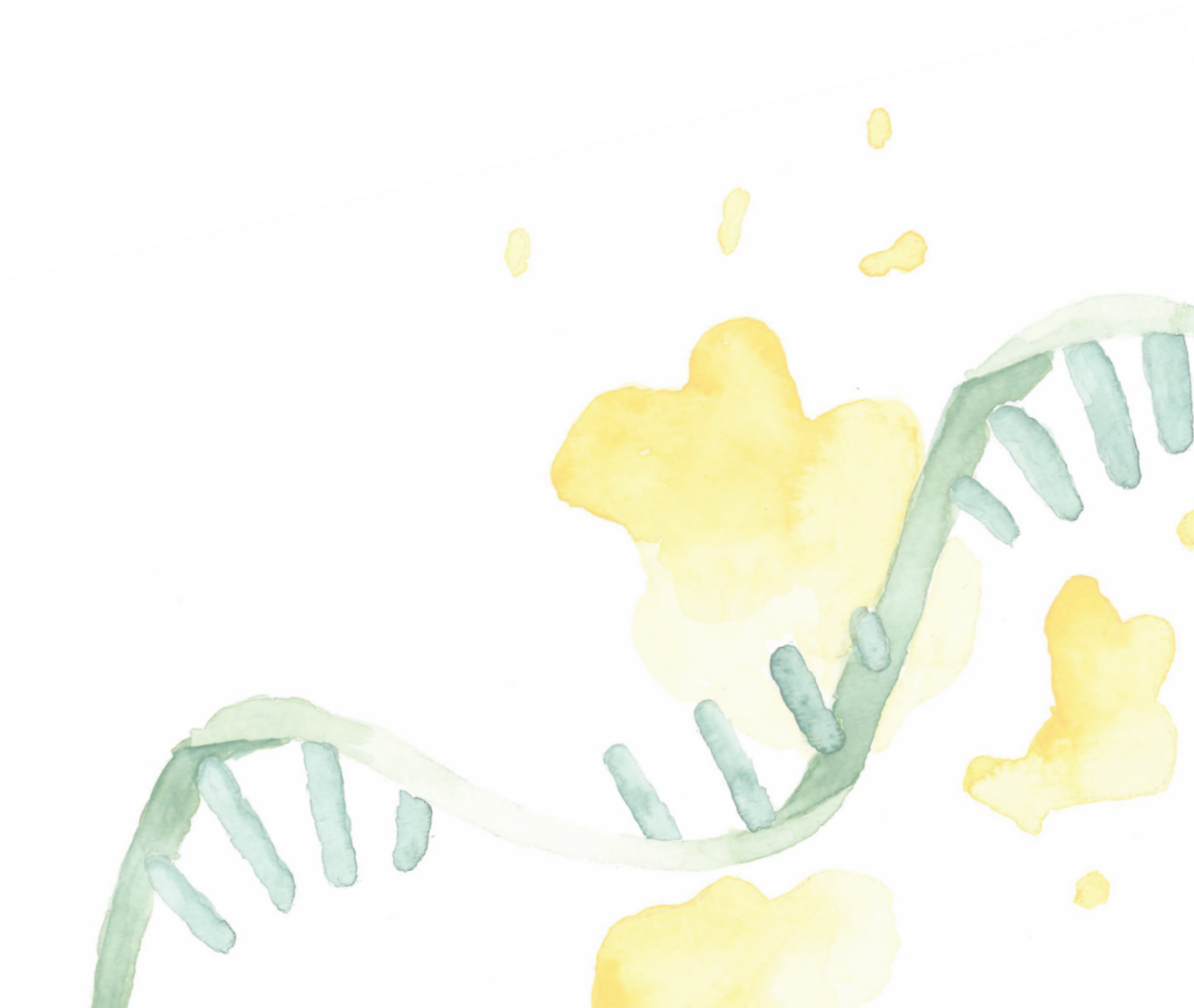

Right before my PhD started, our research group demonstrated the pharmacodynamic biomarker potential of serum miRNAs upon idasanutlin treatment of mouse models xenografted with human neuroblastoma cells (cf. **paper in addendum**, (137)). This key finding was the trigger for the start of my research project (**Figure 5**). I wanted to explore the potential of plasma mRNA to monitor treatment responses by total RNA sequencing. As access to neuroblastoma patients' plasma is restricted, and as it is challenging to distinguish tumoral from host responses in a human context, I decided to explore tumoral responses in a xenograft context first. Growing a human tumor in a mouse model enables the distinction of tumoral (human) from host (murine) responses, by computational deconvolution of human and murine mRNA. First, a host-xenograft deconvolution pipeline applicable to highly fragmented exRNA in liquids was established. Then I applied this pipeline to determine which blood fraction contains the highest tumor-derived signal for future evaluation of tumor-derived treatment responses (**paper 1**, (138)). Then, I treated neuroblastoma xenografts with idasanutlin to evaluate transcriptomic responses. Unfortunately, the abundance of exRNA in plasma was too low to draw biologically meaningful conclusions. However, this experiment resulted in important clues as to what tumor factors might interfere with the measurement of the circulating tumor transcriptome and follow-up experiments looking at tumor sizes, engrafted neuroblastoma cell lines and their vascularity and implantation strategy (orthotopic vs. subcutaneous) were performed (**manuscript under review**). Furthermore, to explore the added value of a combined analysis of cfDNA and cfRNA for treatment response monitoring in the future, I have compared the performance of different cfRNA/cfDNA co-extraction kits resulting in guidelines for their use (**paper 2**, (139)).

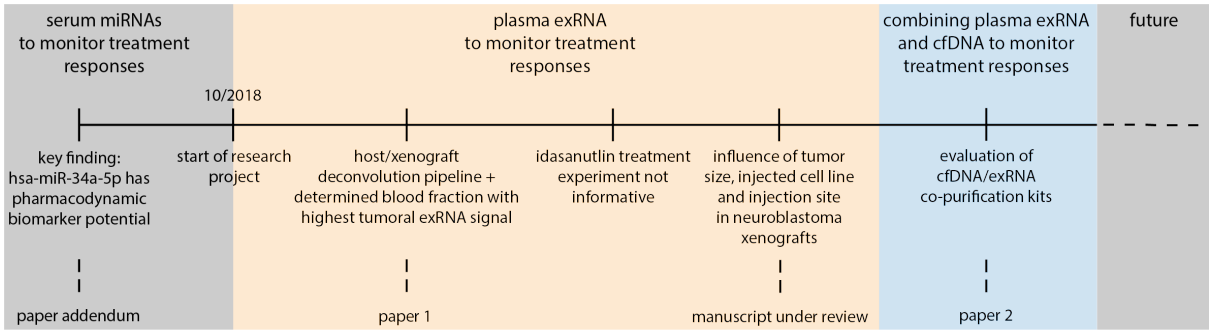

Figure 5. Overview of my PhD trajectory.

1. Whole transcriptome profiling of liquid biopsies from tumour xenografted mouse models enables specific monitoring of tumour-derived extracellular RNA (paper 1)

Vanessa Vermeirssen*, **Jill Deleu***, Annelien Morlion, Celine Everaert, Jilke De Wilde, Jasper Anckaert, Kaat Durinck, Justine Nuytens, Muhammad Rishfi, Franki Speleman, Hanne Van Droogenbroeck, Kimberly Verniers, Maria F. Baietti, Maarten Albersen, Eleonora Leucci, Edward Post, Myron G. Best, Tom Van Maerken, Bram De Wilde, Jo Vandesompele, and Anneleen Decock. (*shared first)

Contribution of JD: In a joint effort, JD secured the plasma samples used in this paper, either obtained via collaborators, or by preparing the plasma by herself. RNA purifications and library preparations were jointly performed by JD, JN and KV. JD took part in the data analysis from the discovery cohort starting from the transcript count tables and performed the GSEA analyses. JD set-up and performed RT-qPCR validation studies and performed the complete analysis of the validation cohort. JD performed the literature search and took part in writing the original draft and generating the figures and graphical abstract.

For this publication, the CrediT contribution system was used to describe the contributions in the manuscript:

conceptualization	AD, BDW, **JD**, JV, TVM, VV	data curation	AD, **JD**, VV
methodology	AD, **JD**, JDW, VV	writing – original draft	AD, **JD**, VV
software	AM, CE, JA, VV	writing- review & editing	AD, AM, BDW, CE, EL, FS, **JD**, JDW, JV, MFB, TVM, VV
validation	**JD**, VV	visualization	AD, **JD**, VV
formal analysis	**JD**, VV, EP, MGB	supervision	JV
investigation	**JD**, JDW, JN, KV, VV	project administration	AD, BDW, **JD**, JV
resources	AD, EL, FS, HVD, **JD**, JDW, JN, KD, KV, MA, MFB, MR, VV	funding acquisition	AD, AM, BDW, FS, JDW, JV, KD, MA, MR, TVM

Published online 28 November 2022

NAR Cancer, 2022, Vol. 4, No. 4 **1**
https://doi.org/10.1093/narcan/zcac037

Whole transcriptome profiling of liquid biopsies from tumour xenografted mouse models enables specific monitoring of tumour-derived extracellular RNA

Vanessa Vermeirssen[1,2,3,4,*,†], Jill Deleu[3,4,†], Annelien Morlion[3,4], Celine Everaert[3,4], Jilke De Wilde[4,5], Jasper Anckaert[3,4], Kaat Durinck[4,6], Justine Nuytens[3,4], Muhammad Rishfi[4,6], Frank Speleman[4,6], Hanne Van Droogenbroeck[3,4], Kimberly Verniers[3,4], Maria Francesca Baietti[7,8], Maarten Albersen[9], Eleonora Leucci[7,8], Edward Post[10,11], Myron G. Best[10,11], Tom Van Maerken[3,4,12], Bram De Wilde[3,4,13], Jo Vandesompele[3,4,‡] and Anneleen Decock[3,4,‡]

[1]Lab for Computational Biology, Integromics and Gene Regulation (CBIGR), Cancer Research Institute Ghent (CRIG), 9000, Ghent, Belgium, [2]Department of Biomedical Molecular Biology, Ghent University, 9000, Ghent, Belgium, [3]OncoRNALab, Cancer Research Institute Ghent (CRIG), 9000, Ghent, Belgium, [4]Department of Biomolecular Medicine, Ghent University, 9000, Ghent, Belgium, [5]Department of Pathology, Ghent University Hospital, 9000, Ghent, Belgium, [6]Pediatric Precision Oncology Lab (PPOL), Cancer Research Institute Ghent (CRIG), 9000, Ghent, Belgium, [7]Laboratory for RNA Cancer Biology, Department of Oncology, KU Leuven, 3000, Leuven, Belgium, [8]TRACE, Leuven Cancer Institute, KU Leuven, 3000, Leuven, Belgium, [9]Department of Development and Regeneration, Laboratory of Experimental Urology, KU Leuven, Department of Urology, University Hospitals Leuven, 3000, Leuven, Belgium, [10]Amsterdam UMC Location Vrije Universiteit Amsterdam, Department of Neurosurgery, Boelelaan 1117, 1081 HV, Amsterdam, the Netherlands, [11]Cancer Center Amsterdam, Brain Tumor Center and Liquid Biopsy Center, 1081 HV, Amsterdam, the Netherlands, [12]Department of Laboratory Medicine, AZ Groeninge, 8500, Kortrijk, Belgium and [13]Department of Paediatric Haematology Oncology and Stem Cell Transplantation, Ghent University Hospital, 9000, Ghent, Belgium

Received January 20, 2022; Revised September 23, 2022; Editorial Decision October 28, 2022; Accepted November 18, 2022

ABSTRACT

While cell-free DNA (cfDNA) is widely being investigated, free circulating RNA (extracellular RNA, exRNA) has the potential to improve cancer therapy response monitoring and detection due to its dynamic nature. However, it remains unclear in which blood subcompartment tumour-derived exRNAs primarily reside. We developed a host-xenograft deconvolution framework, exRNAxeno, with mapping strategies to either a combined human-mouse reference genome or both species genomes in parallel, applicable to exRNA sequencing data from liquid biopsies of human xenograft mouse models. The tool enables to distinguish (human) tumoural RNA from (murine) host RNA, to specifically analyse tumour-derived exRNA. We applied the combined pipeline to total exRNA sequencing data from 95 blood-derived liquid biopsy samples from 30 mice, xenografted with 11 different tumours. Tumoural exRNA concentrations are not determined by plasma platelet levels, while host exRNA concentrations increase with platelet content. Furthermore, a large variability in exRNA abundance and transcript content across individual mice is observed. The tumoural gene detectability in plasma is largely correlated with the RNA expression levels in the tumour tissue or cell line. These findings unravel new aspects of tumour-derived exRNA biology in xenograft models and open new avenues to further investigate the role of exRNA in cancer.

*To whom correspondence should be addressed. Tel: +329 233 39 45; Fax: +329 332 65 49; Email: vanessa.vermeirssen@ugent.be
†The authors wish it to be known that, in their opinion, the first two authors should be regarded as Joint First Authors.
‡The authors wish it to be known that, in their opinion, the last two authors should be regarded as Joint Last Authors.

GRAPHICAL ABSTRACT

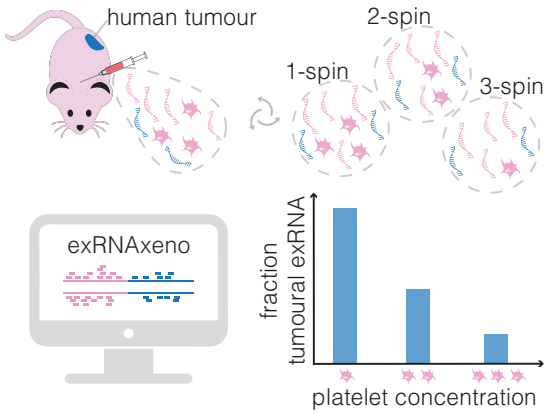

INTRODUCTION

Tumour cells both actively and passively release their content into the blood stream (1). This has opened unprecedented opportunities for accessing tumour-derived molecules without the need to perform an invasive biopsy or surgery aiding in diagnosis and therapy response monitoring. To this end, only a small volume of blood is required. These blood-based liquid biopsies are minimally invasive and therefore more readily executable than tissue biopsies in certain circumstances. They may also provide a more comprehensive picture of the genomic make-up of the entire cancer as liquid biopsies are not restricted to a specific local tumour sampling site. A major advantage is the possibility towards longitudinal sampling, which is in most cases impossible for solid tumours, thus facilitating treatment response monitoring in patients (2). Taken together, these advantages predict an important role for blood-based liquid biopsies in the emerging era of precision oncology (3). Different types of biomolecules within liquid biopsies are being evaluated, including free circulating DNA and RNA. While cell-free DNA (cfDNA) as a blood-based biosource is widely being used and investigated, clinical applications of extracellular RNA (exRNA) are scarce (3,4). Nevertheless, it was recently shown that exRNAs are present in a wide diversity of (blood-based) liquid biopsies and can act as promising precision oncology biomarkers (5–8).

A fundamental open question hampering the set-up of large-scale liquid biopsy collections for tumour exRNA analysis is that it remains unclear in which blood subcompartment tumour-derived exRNAs primarily reside. Blood plasma is amongst the most studied liquid biopsies, but recently also tumour-educated platelets (TEPs) have emerged as a promising liquid biopsy. TEPs arise by exposing blood platelets to tumour cells and to external signals in the tumour microenvironment, leading to the transfer and storage of tumour-associated biomolecules and to the induction of protein translation and specific RNA splicing events in the platelets. Moreover, the RNA content and RNA splicing patterns of these TEPs are claimed to be cancer-specific, therefore serving as cancer biomarkers (9–17). Consequently, differences in plasma preparation procedures, resulting in different amounts of blood platelets being present in samples, may influence the tumour signal that is detected in plasma. It was previously shown that different plasma fractions from cancer patients indeed show distinct exRNA profiles and that particular tumour-specific mutations can only be detected in certain blood-fractions. However, in-depth transcriptome-wide studies specifically focusing on tumour-derived exRNA in different cell-free blood fractions are completely lacking (18,19).

Although tumour-specific structural aberrations, such as fusion genes and single nucleotide or insertion/deletion mutations can be detected in the exRNA of cancer patients, charting the entire tumour-derived extracellular transcriptome is impossible, as tumoural exRNA generally cannot be distinguished from non-tumoural exRNA in the patient's blood (20–23). Therefore, to characterize a tumour's extracellular transcriptome by massively parallel sequencing, human xenograft models are excellent tools, as tumoural and non-tumoural exRNAs originate from a different organism background, enabling to distinguish these exRNA fractions using host-xenograft deconvolution algorithms on RNA sequencing data. Such algorithms are based on mapping of the sequencing reads to a combined host-xenograft reference genome or on parallel mapping to the host and xenograft genomes separately followed by filtering out misaligned reads. So far, several computational pipelines making use of these mapping strategies have been tested on tumour tissue of human xenograft mouse models and have been made available to the xenograft community. For example, Khandelwal *et al*. describe bamcmp for deconvolving host and graft reads in primary tumours and metastases from a melanoma mouse model, based on parallel mapping followed by a filtering approach based on the CIGAR string to discard reads misaligned to the host genome (24). Callari *et al*. use *in silico* combined human-mouse reference genome mapping (ICRG) of patient-derived breast cancer xenograft RNA sequencing data to accurately dissect the transcriptome of human tumour cells and mouse stroma (25). Kluin *et al*. report XenofilteR, which applies a parallel mapping strategy in combination with filtering based on the edit distance between a sequence read and a reference genome, and was evaluated on patient-derived xenograft (PDX) samples for which matched patient tumour samples were available (26). While these different methods have been evaluated on tumour-derived RNA, the performance of host-xenograft deconvolution algorithms on blood-derived exRNA currently remains unknown. This type of RNA is very different because of its extremely low concentration, highly fragmented nature and minority contribution of human tumour RNA relative to host RNA.

In this study, we investigated whether tumour-derived exRNA primarily resides in plasma fractions with higher platelet content, by means of total RNA sequencing of different blood fractions from 11 xenograft models, consisting of a human tumoural xenograft in a murine host; more precisely, 8 patient-derived xenograft (PDX) models and 3 cell line-derived xenograft (CDX) models. These models were analysed in two cohorts, a discovery cohort, which we present in more detail, and a validation cohort, of which

the data are added as Supplementary Data. The discovery cohort consists of a breast cancer PDX model and a neuroblastoma SK-N-BE(2C) CDX model. The validation cohort includes seven PDX models (i.e. two endometrial cancers [EMC], three melanomas [MEL] and two penile cancers [PEN]) and three CDX models (i.e. one lung cancer [A549] and two neuroblastoma cancers (IMR-32 and SK-N-BE(2c)), the latter one being an expansion of the discovery cohort). First, two computational pipelines to reliably differentiate murine host and human tumour sequencing reads from plasma were optimized (exRNAxeno combined and parallel pipelines), demonstrating that read mapping to a combined reference genome is the best strategy for exRNA quantification in xenograft models. Subsequently, we analysed exRNA from platelets and three plasma fractions with different levels of platelets, obtained by applying successive centrifugation steps on murine blood. We show that murine platelets are not enriched for human tumour-derived RNA and that the circulating tumour signal is highly variable across xenograft models and individual mice. Highly abundant tumour transcripts in circulation correspond to high expression levels in tumour tissue, suggesting that circulating exRNA can be used as tumour biomarker in these models.

MATERIALS AND METHODS

Tumour tissue and liquid biopsy collection

The performance of the host-xenograft deconvolution algorithms was evaluated on liquid biopsies from non-tumour bearing control mice (TRACE PDX Platform, KU Leuven, UZ Leuven, Belgium) and human donors (ethical committee approval number EC/2017/1207, Ghent University Hospital, (27)). *In vivo* mice work was performed at the TRACE PDX platform (KU Leuven, approved by the local ethical committee for animal experimentation (P164/2019)). Female immunodeficient nude mice (NMRI-Foxn1^{nu} strain, Taconic Biosciences, Rensselaer, NY, USA, $n = 8$, of which five were used for the performance assessment of the pipelines and three for measuring platelet concentration) were subcutaneously injected with 30 μl of Roswell Park Memorial Institute (RPMI) 1640 medium (Thermo Fisher Scientific, Waltham, MA, USA), suspended in 70 μl Matrigel matrix (Corning, Bedford, MA, UK) at the age of 13 weeks. After 29–35 days, cardiac puncture was performed under anaesthesia to collect blood (volume range between 400 and 1000 μl), followed by cervical dislocation of the mice. The blood, collected in Microvette 500 K3EDTA tubes (Sarstedt, Newton, NC, USA), was processed immediately to complete blood-derived liquid biopsy preparation within 2 h after cardiac puncture. From each animal, three plasma fractions with different platelet content, i.e. single spun (SSP), double spun (DSP), and triple spun plasma (TSP), and platelets were prepared by means of three sequential centrifugation steps (details in Supplementary Figure S1), resulting in approximately 70 μl plasma per fraction. Throughout the manuscript, we make use of the term 'liquid biopsy' to refer to both plasma and platelets (3). Total RNA sequencing data from TSP samples of human donors ($n = 2$, two replicates for each donor) were obtained from Everaert *et al.* ((27); European Genome-Phenome Archive [EGA] sample ID EGAN00002518840-EGAN00002518843 in EGAS00001004428).

The discovery cohort consisted of two different xenograft mouse models, i.e. the BRC0004 patient-derived xenograft (PDX) mouse model (https://www.pdxfinder.org/data/pdx/TRACE/BRC0004) and an SK-N-BE(2C) cell line-derived xenograft (CDX) mouse model (TRACE PDX Platform; https://gbiomed.kuleuven.be/english/research/50488876/54502087/Trace/PDX-repository). To establish SK-N-BE(2C) CDX mice, female NMRI-Foxn1^{nu} mice ($n = 5$) were subcutaneously xenografted in the dorsal flank with 2×10^6 SK-N-BE(2C) cells, in 30 μl RPMI 1640 medium (Thermo Fisher Scientific, Waltham, MA, USA), suspended in 70 μl Matrigel matrix (Corning, Bedford, MA, UK) at the age of 13 weeks. When CDX mice reached specific humane endpoints (i.e. a tumour volume of 2000 mm^3, a weight loss of >20% or clinical signs of significant pain, distress or suffering), cardiac puncture was performed for liquid biopsy collection (as described above; Supplementary Figure S1; blood volume range between 250 and 1000 μl) followed by cervical dislocation. The BRC0004 PDX model was established from a tumour fragment freshly isolated from a triple-negative nodular breast invasive ductal adenocarcinoma patient by interscapular implantation in female NMRI-Foxn1^{nu} mice ($n = 5$). Tumours were propagated in at least three generations of mice and characterized by histology before being biobanked and used for this experiment. SNPs fingerprinting was used to confirm the genealogy before liquid biopsy collection. Liquid biopsies (SSP, DSP and TSP) of saline treated BRC0004 PDX mice were collected 3 weeks after the start of saline administration according to the protocol described in Supplementary Figure S2. From this xenograft model, also tumour tissue biopsies were collected and immediately stored in RNAlater (Thermo Fisher Scientific, Waltham, MA, USA) to be profiled using total RNA sequencing. For the CDX model, publicly available poly-A RNA sequencing data of the SK-N-BE(2C) cell line was used ((28); Gene Expression Omnibus [GEO] sample ID GSM2371256 in GSE89413). The validation cohort consisted of liquid biopsies from 20 additional PDX or CDX mice (neuroblastoma, melanoma, endometrial, penile and lung cancer xenograft models; details in Supplementary material and methods). All patients from whom tumour material was collected, provided informed consent prior to study participation, approved by the Ethical Committee UZ Leuven (S63799, S61605 and S66742).

The degree of haemolysis of all plasma samples was assessed by measuring levels of haemoglobin by spectrophotometric analysis (OD414) using a NanoDrop 1000 Spectrophotometer (Thermo Fisher Scientific, Waltham, MA, USA; Supplementary Tables S1 and 2). To confirm a reduction in platelet concentration upon successive centrifugation steps, platelet counts were measured in pooled SSP, DSP and TSP fractions of three non-tumour bearing female NMRI-Foxn1^{nu} mice, using an XN-1000 Haematology Analyzer (Sysmex, Kobe, Japan; impedance method, Supplemental Table S3).

RNA isolation, spike-in RNA addition and DNase treatment

Extracellular RNA from 60 μl plasma or platelet pellets originating from 70 μl SSP, was isolated using the miRNeasy Serum/Plasma Kit (Qiagen, Hilden, Germany), according to the manufacturer's manual. During RNA extraction, 2 μl of a 10 000-fold dilution of Sequin spike-in controls (Garvan Institute of Medical Research, Darlinghurst, NSW, Australia (29)) was added to the lysate. Upon RNA purification, 2 μl of a 25 000-fold dilution of External RNA Control Consortium (ERCC) RNA Spike-in Mix (Thermo Fisher Scientific, Waltham, MA, USA) was added to 12 μl RNA eluate, followed by gDNA removal (30). To this purpose, 1 μl HL-dsDNase (ArcticZymes Technologies, Tromsø, Norway) and 1.4 μl Heat & Run 10X Reaction Buffer (ArcticZymes Technologies, Tromsø, Norway) were added to the eluates, and RNA samples were incubated for 10 min at 37°C, followed by 5 min at 55°C.

RNA from tumour tissue was isolated using the miRNeasy Micro Kit (Qiagen, Hilden, Germany) in combination with the TissueLyser II system (Qiagen, Hilden, Germany). Upon RNA purification, 12 μl RNA eluate was used for gDNA removal as described above. DNase-treated RNA concentrations were measured by NanoDrop technology (Thermo Fisher Scientific, Waltham, MA, USA), and samples were diluted to 1.25 ng/μl using nuclease-free water (Saint Louis, MO, USA).

RT-qPCR validation

For the validation of 2 Sequin spikes (R2_65 and R2_66) and 4 selected mouse platelet mRNAs (F5, Gng11, Nrgn, Ppbp), assays were carefully designed using the primer3plus tool (https://www.primer3plus.com with default settings, except amplicon size range of 60–100 nucleotides). The performance of the primers was thoroughly evaluated *in silico*. To determine the primer specificity, BiSearch (http://bisearch.enzim.hu with default settings, except for mismatch string, i.e. 1233333333333333) and the UCSC tool (https://genome.ucsc.edu/cgi-bin/hgPcr) were used. Subsequently, the OligoEvaluator tool (http://www.oligoevaluator.com/OligoCalcServlet) was used to check for secondary structure formation and GC content. Primers were ordered with Integrated DNA Technologies (IDT, Leuven, Belgium), purified by standard desalting. Primers were resuspended in TE buffer at 100 μM (10 mM Tris-HCl [pH 8.0], 0.1 mM EDTA) and stored at −20 °C. Primer efficiency and specificity were tested on a dilution series of mouse genomic DNA (Promega, G3091). To ensure that there is no cross-species amplification (i.e. murine primers amplifying human cDNA), we also checked for the absence of amplification on Universal Human Reference RNA (Agilent technologies, 750500), reverse transcribed to cDNA.

About 8 μl of DNase treated plasma RNA was reverse transcribed using the iScript Advanced cDNA Synthesis Kit for RT-qPCR (Bio-Rad, 1725038), according to the manufacturer's manual. Subsequently, the cDNA was diluted 1:4, by adding 60 μl of nuclease free water to 20 μl cDNA and RT-qPCR was performed in a 5 μl reaction in duplicate in a 384-multiwell plate. Briefly, 2.5 μl of SsoAdvanced SYBR Green Supermix (Bio-Rad), 0.25 μl of each primer (5 μM) and 2 μl of diluted cDNA was added to each well, followed by a thermocycling protocol consisting of a preincubation step for 2 min at 95°C, followed by 44 amplification cycles (95°C for 5 s, 60°C for 30 s and 72°C for 1 s), ending with melt curve analysis during 1 s 0.11°C increment steps from 60 to 95°C on a LightCycler 480 system (Roche).

The *C*q values of the platelet genes were normalized by diminishing the mean *C*q of R2_65 and R2_66 spikes of each sample by the *C*q of each platelet gene of the respective sample.

Total RNA library preparation and sequencing

Total RNA libraries were prepared starting from 8 μl DNase-treated RNA using the SMARTer Stranded Total RNA-Seq Kit v2 - Pico Input Mammalian (Takara Bio, CA, USA), according to the manufacturer's manual with minor modifications (27). Briefly, prior to first strand cDNA synthesis, RNA from liquid biopsies and tumour tissue was fragmented for 2 min at 94°C. During final library amplification, 16 PCR cycles were performed on the liquid biopsy samples, while on tumour samples, only 13 cycles were performed. For the liquid biopsy samples, the final clean-up was repeated, since an excessive number of products <200 bp in size was observed on Fragment Analyzer data (data not shown, Agilent Technologies, Santa Clara, CA, USA). Fragment sizes were determined using Fragment Analyzer software for smear analysis in the 200 to 1000 bp range. Library quantification was performed using the KAPA Library quantification Kit (Kapa Biosystems, Wilmington, MA, USA) and libraries were pooled equimolarly. The final pool was quantified using Qubit, and 1.2 pM (for the PDX-derived samples) or 1.3 pM (for the CDX-derived samples) was loaded on a NextSeq 500 instrument (NextSeq 500 HighOutput Kit V2, 150 cycles), with 3% PhiX. Raw sequencing data is available in the European Genome-Phenome archive (EGAS00001005740 and EGAS00001006582).

Preprocessing of RNA sequencing data

Sequencing reads of liquid biopsy and tumour samples were preprocessed by FastQC (v.0.11.8) for quality control and trimmed by Cutadapt (v.1.18) for low quality bases at the 3' end of each read (Q30), for three nucleotides from the 5' end of the second read (due to the template switching adapter) and for the HT-TruSeq adapter sequences. Reads <35 bp were filtered out. Next, duplicated reads were removed with Clumpify (BBMap v.38.26) within clumps based on 60 bp trimmed reads and using default parameters, except for 20 passes. To compare the different samples at similar sequencing depth, we downsampled (Seqtk v.1.3) to the lowest number of reads present within an experiment, i.e. 2223796 for the control and SK-N-BE(2C) CDX mice, and 4999120 for the BRC0004 PDX mice. To have sufficient sequencing depth remaining after downsampling, we removed one sample with very low sequencing depth, i.e. the TSP sample of control mouse CM9 (with only 1472031 reads; Supplementary Table S1). Subsequently, reads were once more analysed by FastQC for quality control. QC analyses resulted in the exclusion of all samples from control mouse CM11, since these samples displayed short read sequences (<70 bp)

and high levels of trimming (34.6–52.8%; Supplementary Table S1) compared to the other control mouse samples.

exRNAxeno computational framework for combined and parallel mapping of RNA sequencing data

Reads were mapped using STAR (v.2.6.0) (specific parameter settings: –outSAMprimaryFlag AllBestScore –outSAMattributes NH HI AS nM NM) to either a combined reference genome of human and mouse (combined mapping) or in parallel to both the human and mouse genome (parallel mapping). The genome index for mapping was built using the Ensembl GRCh38.94 (human) and GRCm38.94 (mouse) DNA primary assembly sequences, containing all chromosomes, the mitochondrial genome and scaffolds, supplemented with ERCC and Sequin spike sequences and the full ribosomal DNA complete repeating unit (U13369.1, BK000964.3). GTF files were downloaded from Ensembl and adapted in a similar way. In the combined reference genome of mouse and human, mouse chromosomes were labelled with a prefix 'm'. For both the combined and parallel mapping, uniquely mapped reads were selected based on the NH:i:1 tag (SAMtools v.1.8, Pysam). In the parallel mapping, read pairs mapping to both human and mouse were assigned to the organism where mapping resulted in the smallest edit distance (i.e. sum of NM tag and CIGAR string soft-clipping from both read pairs in the SAM file; Pysam, Picard v.2.21.1). In both combined and parallel mapping, BAM files were further masked by intersectBed for regions where control murine (n = 15) and human (n = 4) liquid biopsies empirically showed misalignment to the other reference genome (SAMtools v.1.8, BEDtools v.2.27.1, BEDOPS v.2.4.32). Further quality control on the filtered BAM files was done using MultiQC (v.1.7), SAMtools (v.1.8), RseQC (v.2.6.4) and BEDTools (v.2.27.1). Finally, read counts of name-sorted BAM files were generated by HTSeq-count (v.0.11.0) (specific parameter settings: -s reverse –secondary-alignments = ignore –supplementary-alignments = ignore) using appropriate GTF files. Further processing was done with R (v.4.0.3) making use of tidyverse (v.1.3.1). The exRNAxeno combined and exRNAxeno parallel pipeline are available through GitHub (https://github.com/CBIGR/exRNAxeno).

Determination of human and mouse RNA concentration in liquid biopsies using RNA spike-in sequencing data

The mass of endogenous RNA present in 1 ml of plasma was determined based on the known amount of Sequin spike-in controls added during RNA isolation (as described in (30)). First, the mass of all Sequin spike-in controls was calculated, based on the length (in nucleotides) and molar concentration (in attomol/μl) of each Sequin spike-in control (Supplementary Table S4). By multiplying the concentration (in attomol/μl) with the volume of spikes added (2 μl) and the dilution factor (1/10 000), the mass amount (attomol) of each Sequin spike-in control added to the sample was calculated. Second, to convert the amount (attomol) to weight (g), the molecular weight of each Sequin spike-in control was determined, by multiplying its length (nt) with the average molecular weight of a single nucleotide (321.47 g/mol). Next, individual Sequin spike-in control weights were summarized to obtain a total weight of 1.32E-12 g. For the SSP/DSP/TSP samples (with an input volume of 60 μl plasma), this resulted in 21.94 pg Sequin spike-in control added per mL of plasma, while for the platelets (originating from 70 μl SSP), this equaled to 18.81 pg Sequin spike-in controls per platelet lysate. Finally, by multiplying the endogenous RNA over Sequin spike in-control read count ratio with the amount of Sequin spike-in control added per fraction (pg/mL), the endogenous RNA concentration was obtained (pg/mL).

Statistical analysis

To compare the combined and parallel pipelines, we applied a non-parametric two-tailed Wilcoxon rank-sum test using normal approximation on the fraction of misaligned reads. For differential expression analysis between engrafted and non-engrafted mice, RNA sequencing reads were first normalized using the median sum of the Sequin spike-in read counts. Unexpressed genes were excluded from the analyses. Next, ANOVA comparisons were performed using scipy statistics (v.1.1.0) and visualization was performed using seaborn clustermap (v.0.9.0), both in Python. Data were visualized in heatmaps using ward-clustering. *P*-values were calculated using a Fisher's exact test in R (multiple testing correction not performed). To compare the normalized exRNA concentrations and the percentage of tumoral exRNA in the different plasma fractions, the non-parametric Friedman chi-square test for repeated measurements was carried out, followed by the post-hoc Nemenyi all-pairs test with Benjamini–Hochberg multiple hypothesis correction. A two-sample Kolmogorov–Smirnov test investigated if there was a difference in the cumulative abundance of genes detected in the plasma or not, based on their abundance in the tumour tissue.

RESULTS

Read mapping on a combined reference genome is the preferred strategy for the analysis of extracellular RNA from xenograft-derived liquid biopsies

Both combined and parallel mapping approaches are being used for the computational deconvolution of a human tumour xenograft transcriptome in mice. Due to the high homology between human and mouse, these computational approaches result in a limited number of misaligned reads, i.e. false positive RNA signals in either species. Here, we developed and compared two computational pipelines to accurately distinguish between tumour-derived (human origin) and non-tumoural (mouse origin) exRNA in liquid biopsies from human tumour xenograft mouse models: one using a combined mapping approach (exRNAxeno combined) where reads are mapped to a combined reference genome of human and mouse, and one using a parallel mapping strategy (exRNAxeno parallel) where reads are mapped to the human and murine genome separately and subsequently assigned as being either human or murine based on comparison of the edit distances (Figure 1, see

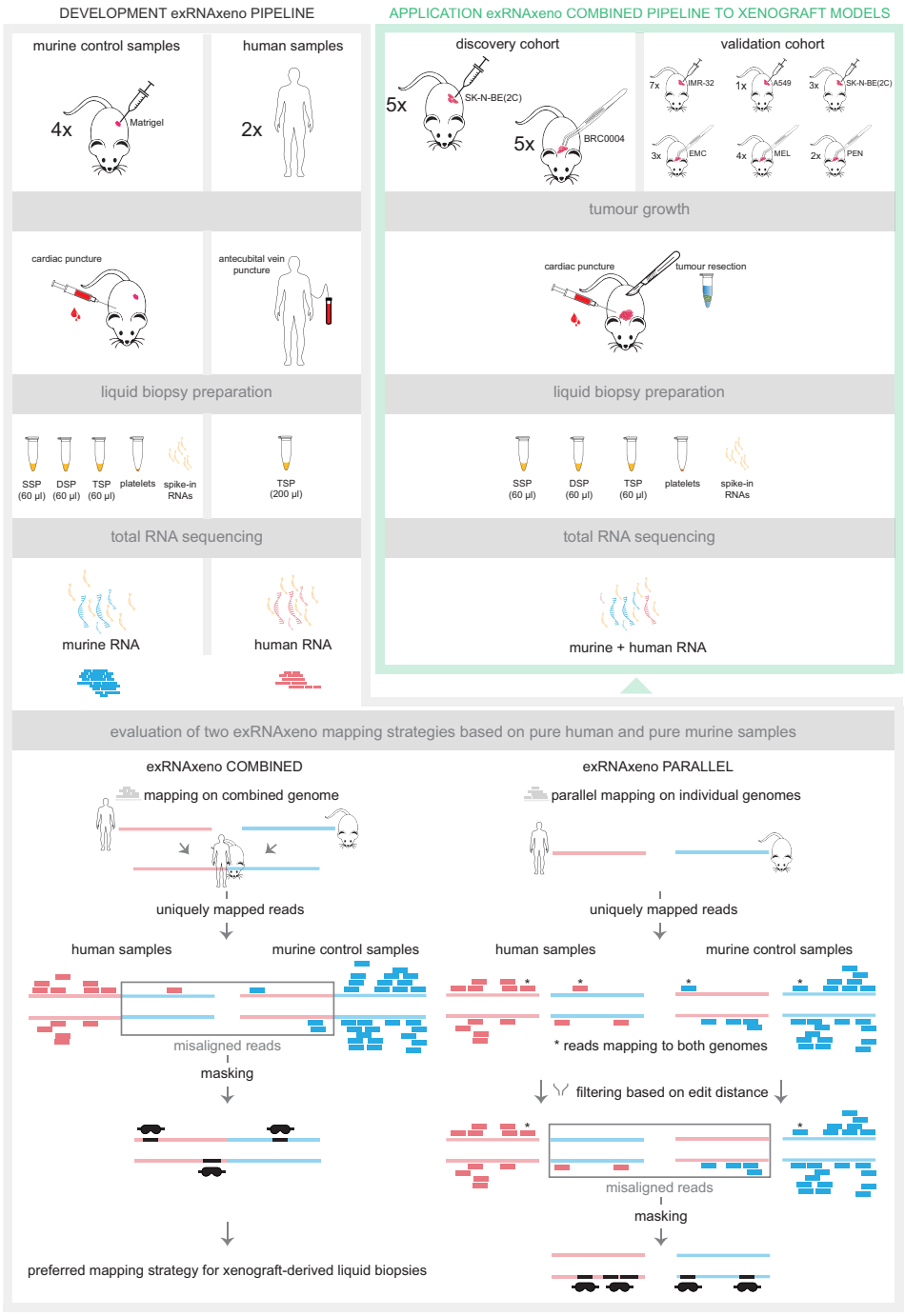

Figure 1. Development and application of a deconvolution pipeline applicable to liquid biopsies from human tumour xenografts. First, both the exRNAxeno combined and parallel mapping analysis pipeline were applied to total RNA sequencing data from pure (non-xenograft) exRNA samples from liquid biopsies (i.e. blood platelets, single spun [SSP], double spun [DSP] and triple spun plasma [TSP]) of mice without tumour xenograft, and from TSP of human donors, in order to characterize and mask genomic regions containing misaligned reads. Subsequently, the optimized exRNAxeno combined mapping pipeline was applied to total RNA sequencing data of exRNA from three different plasma fractions (SSP, DSP and TSP), and platelets from two different xenograft mouse cohorts, a discovery and validation cohort, in order to characterize the human tumoural RNA signal in the murine blood; EMC, endometrial cancer; MEL, melanoma; PEN, penile cancer.

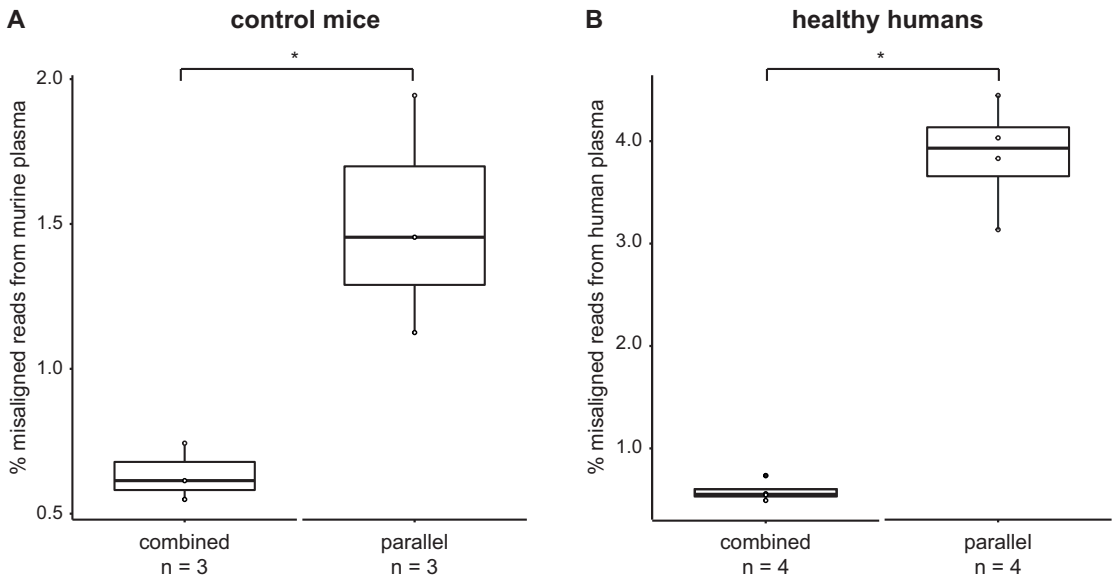

Figure 2. The exRNAxeno combined mapping pipeline results in significantly lower fractions of misaligned reads from both murine and human triple spun plasma. (**A**) Percentage of misaligned reads from murine plasma for both the exRNAxeno combined and parallel mapping pipeline (non-parametric two-tailed Wilcoxon rank-sum test using normal approximation, $P = 0.049$ (*)). (**B**) Percentage of human reads misaligning to the mouse genome for both the exRNAxeno combined and parallel mapping pipeline (non-parametric two-tailed Wilcoxon rank-sum test using normal approximation, $P = 0.021$ (*)). * refers to a significance of $P < 0.05$.

Materials and Methods). The performance of both computational strategies was evaluated by charting the misaligned reads in total RNA sequencing data sourced from pure murine exRNA from blood platelets, single spun (SSP), double spun (DSP) and triple spun plasma (TSP) of control mice, i.e. mice without tumour xenograft of human origin, and of pure human exRNA from TSP from healthy human donors. Both the combined and parallel mapping pipeline detected reads in murine plasma misaligned to the human genome and reads in human plasma misaligned to the murine genome. More precisely, in TSP, 0.5–0.7% and 1.1–1.9% of the murine plasma reads is misaligned to the human genome in the combined mapping and parallel mapping strategy, respectively (Figure 2, non-parametric two-tailed Wilcoxon rank-sum test using normal approximation, $P = 0.049$). Reversely, also mapping of the human plasma reads to the murine genome leads to misaligned reads (0.5–0.7% in the combined mapping and 3.1–4.5% in the parallel mapping, non-parametric two-tailed Wilcoxon rank-sum test using normal approximation, $P = 0.021$). At the gene level, this corresponds to 93 and 314 unique human Ensembl gene IDs that are robustly detected (i.e. $\geq$ 5 read counts) in the murine plasma samples by the combined and parallel mapping pipeline, respectively. In the human plasma samples, we identified 24 and 60 unique murine Ensembl gene IDs, respectively. Most of these misaligned genes correspond to repetitive or highly homologous sequences (https://github.com/CBIGR/exRNAxeno). To further optimize the exRNAxeno framework, we used the misaligned reads in both the human and murine control samples to mask the genome in the analysis of tumour bearing mice samples, as these regions seem to be too homologous to differentiate even with stringent mapping conditions. This resulted in 60 259 720 bp (0.6% of genome sequence) masked from the human genome part and 12 640 841 bp (0.2%) masked from the murine genome part in the combined mapping strategy. In the parallel mapping strategy, 229 383 813 bp (2.3%) of the human genome and 41 627 990 bp (0.7%) of the murine genome are masked. Reprocessing of the human and control murine samples with the masking filter active completely removed the misaligned reads and cross-reference gene IDs (Supplementary Figure S3). In conclusion, as the combined mapping strategy resulted in significantly lower fractions of misaligned reads (Figure 2) and fewer false positive Ensembl gene IDs, and required a smaller masked region, we put forward exRNAxeno combined as the preferred computational pipeline for the analysis of exRNA from xenograft-derived liquid biopsy samples.

The tumoural RNA concentration is not determined by the platelet level in plasma

Next, the optimal computational pipeline, i.e. exRNAxeno combined, was applied to total RNA sequencing data from liquid biopsy exRNA from two human xenograft mouse models, i.e. SSP, DSP, TSP and platelets from a breast cancer patient-derived (BRC0004, PDX) and neuroblastoma cell line-derived (SK-N-BE(2C), CDX) xenograft mouse model (Figure 1 and Supplementary Table S1). Before assessing differences between the different blood fractions, differential abundance analyses were performed between

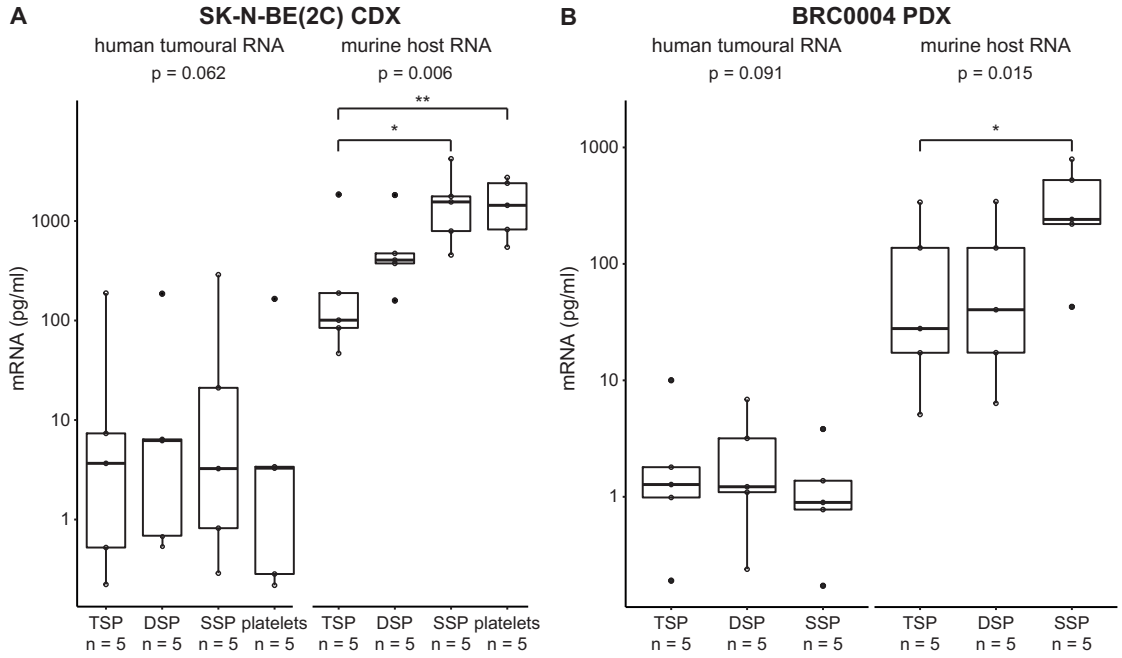

Figure 3. The tumoural exRNA concentration is relatively constant across the different liquid biopsies, in contrast to the host exRNA concentration. (**A**) Tumour and host exRNA concentrations in each plasma fraction and in platelet pellets from the cell line-derived xenograft (CDX) mice (Friedman chi-squared test = 12.6, df = 3, $P = 0.006$; post-hoc test Nemenyi, $P = 0.017$ (*) and $P = 0.008$ (**)). (**B**) Tumour and host exRNA concentrations in each plasma fraction from the patient-derived xenograft (PDX) mice (Friedman chi-squared test = 8.4, df = 2, $P = 0.015$; post-hoc test Nemenyi, $P = 0.012$ (*)). DSP, double spun plasma; SSP, single spun plasma; TSP, triple spun plasma. * refers to a significance of $P < 0.05$; ** refers to a significance of $P < 0.01$.

tumour-bearing and non-tumour-bearing mice, hinting towards differential exRNA abundance profiles between engrafted and non-engrafted mice (Supplemental Figure S4). Next, we investigated the human tumoural and murine host signal in the different blood fractions of the xenografted mice, by quantifying exRNA concentrations using synthetic Sequin spike-in RNAs, added during exRNA purification (see Materials and Methods). RT-qPCR validation of Sequin spikes (R2_65 and R2_66) in the eluates showed that exRNA purification is reproducible among samples and that Sequin spike-in RNA can be used for quantification of exRNA concentrations (Supplementary Figure S5, Pearson's correlation coefficient of 0.6531 and $P < 0.05$ between Cq values of R2_65 and R2_66). Successive centrifugation steps resulted in lower plasma host RNA concentration in both the CDX (Friedman chi-squared test (= 12.6), df = 3, $P = 0.006$) and PDX experiment (Friedman chi-squared test (= 8.4), df = 2, $P = 0.015$) (Figure 3). Gene set enrichment analyses (GSEA) on differentially abundant host genes between SSP, DSP and TSP demonstrated that this host RNA signal is dominated by platelet specific transcripts (Supplementary Table S5), in line with the fact that successive centrifugation resulted in a gradual decrease in plasma platelet concentration. This gradual decrease in platelet concentration was confirmed by platelet counts on pooled SSP, DSP and TSP from three control mice (Supplementary Table S3) and by RT-qPCR validation of platelet mRNA markers (F5, Gng11, Nrgn and Ppbp; Supplementary Figure S6). We were also able to detect tumoural exRNA in all plasma fractions and in platelets from the xenografted mice, but amounts are highly variable across individual animals (Figures 3, 4 and Supplementary Figure S7). More precisely, 0.03–9.27% and 0.10–9.43% of the exRNA is tumour-derived in the CDX and PDX mice, respectively (Figure 4 and Supplementary Figure S7). Remarkably, while we observed a gradual decrease in host RNA concentration with decreasing platelet content, tumoural RNA concentration levels are comparable across the different liquid biopsy types in both experiments (Figure 3). As a result, TSP samples contain the highest fraction of tumour-derived exRNAs, due to the lower background of host exRNAs (Figure 4 and Supplementary Figure S7).These findings have been confirmed in a validation cohort comprising of liquid biopsies from 20 additional CDX and PDX mice (neuroblastoma, melanoma, endometrial, penile and lung cancer xenograft models) using the same workflow technology as used in the discovery cohort (Supplementary Materials and Methods, Supplementary Figure S8).

The circulating tumour transcriptome is highly variable across xenografted mice

Although multiple RNA biotypes are detected in the liquid biopsies, the majority of detected tumour-derived Ensembl gene IDs is protein-coding, i.e. 94.4% in the CDX

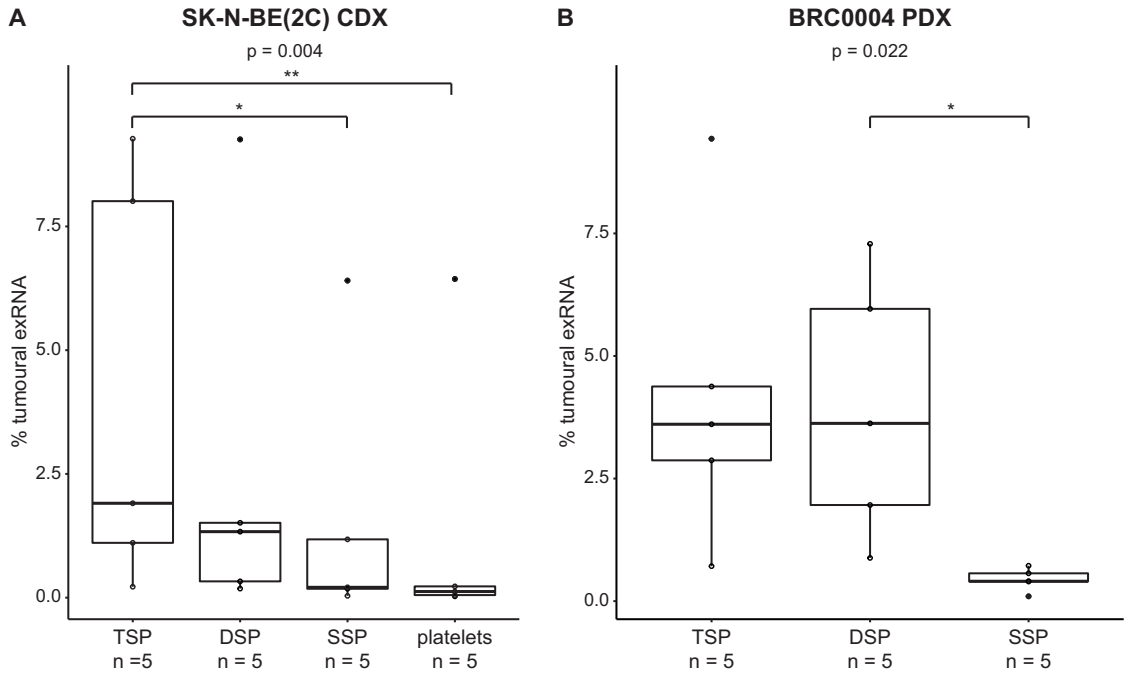

Figure 4. The tumoural exRNA percentage is inversely proportional to the platelet plasma level. Shown are the percentages of tumoural exRNA present in the different liquid biopsies from the CDX (**A**; Friedman chi-squared test = 13.56, df = 3, $P = 0.004$; post-hoc test Nemenyi, $P = 0.036$ (*) and $P = 0.017$ (**)) and PDX (**B**; Friedman chi-squared test = 7.6, df = 2, $P = 0.022$; post-hoc test Nemenyi, $P = 0.031$ (*)) mice. DSP, double spun plasma; SSP, single spun plasma; TSP, triple spun plasma. * refers to a significance of $P < 0.05$; ** refers to a significance of $P < 0.01$.

and 73.2% in the PDX mice samples (Supplementary Figure S9). When focusing on the protein-coding gene fraction, the number of robustly detected host-derived genes in circulation is on average 921 times (ranging from 3 to 5381 times, CDX mice samples) or 326 times (ranging from 15 to 2960 times, PDX mice samples) higher than the number of tumour-derived genes (Figure 5). In general, TSP has the highest number of human tumoural and lowest number of murine host genes, while SSP and platelets show the opposite pattern (Figures 5 and 6). This could also be confirmed in the xenograft models of the validation cohort (Supplemental Figure S10A–F). Although differences between liquid biopsy types can be observed, differences across individual mice are more pronounced (Figures 5 and 6). More specifically we detected 2126 (M7), 244 (M10), 75 (M16), 32 (M14) or 3 (M12) human tumoural protein-coding genes in total, across all liquid biopsy types in the CDX mice, and 612 (M6), 315 (M5), 270 (M3), 91 (M2) or 37 (M1) human tumoural protein-coding genes in the PDX mice. Although sample-specific gene sets largely determine the circulating tumour transcriptomes of the xenograft mice, common gene sets both across different liquid biopsy types and—to a lesser extent—across different mice can be observed (Figure 6, Supplementary Figures S10A–F and 11). The large differences in the number of tumour-derived genes across individual mice cannot be correlated to PDX and CDX tumour volumes, since tumour volumes did not differ across individual PDX (tumour volume range: 1104.1–1286.7 mm^3) and CDX (1962.8–2115.1 mm^3) mice. Next, we investigated the expression levels of tumoural protein-coding genes in total RNA sequencing data of the PDX tumour tissue biopsies and publicly available polyA+ RNA sequencing data of SK-N-BE(2C) cells and linked this to the detectability of these genes in circulation. Given the high variability in the number of tumour-derived genes among the xenografted mice (Figure 6), these analyses were confined to the TSP samples from a few mice with the highest number of protein-coding genes detected, i.e. CDX mice M7 and M10, and PDX mice M3, M5 and M6. As depicted in Figure 7, tumour genes in circulation are significantly higher expressed in the tumour tissue (PDX) or cell line (CDX) than tumour genes not detected in circulation (two-sample Kolmogorov–Smirnov test, $P < 2.2e\text{-}16$).

DISCUSSION

To assess whether blood platelets from cancer patients are preferentially loaded with tumoural RNA, we charted the tumour-derived transcriptome in different types of liquid biopsies from two human xenograft mouse models. Using such models, the circulating human, tumoural transcriptome can be differentiated from the murine, non-tumoural extracellular RNAs using host-xenograft deconvolution algorithms for RNA sequencing read analysis. Although various host-xenograft deconvolution pipelines have been described, either based on a parallel mapping and filtering strategy or a combined mapping strategy (24–26,31–33), they have not been extensively compared and under-

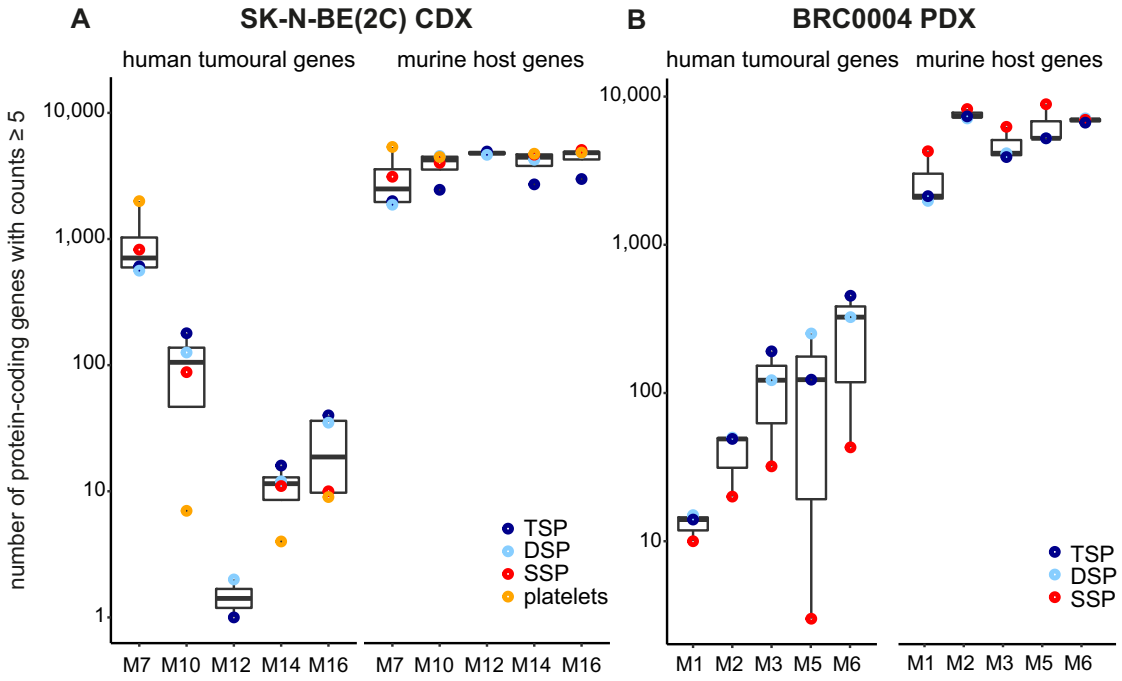

Figure 5. The number of host and tumour protein-coding genes varies across xenografted mice. Shown are the numbers of robustly detected protein-coding genes (i.e. ≥5 counts) in the individual CDX (**A**) or PDX (**B**) mice. The different colours represent the different liquid biopsies; DSP, double spun plasma; SSP, single spun plasma; TSP, triple spun plasma.

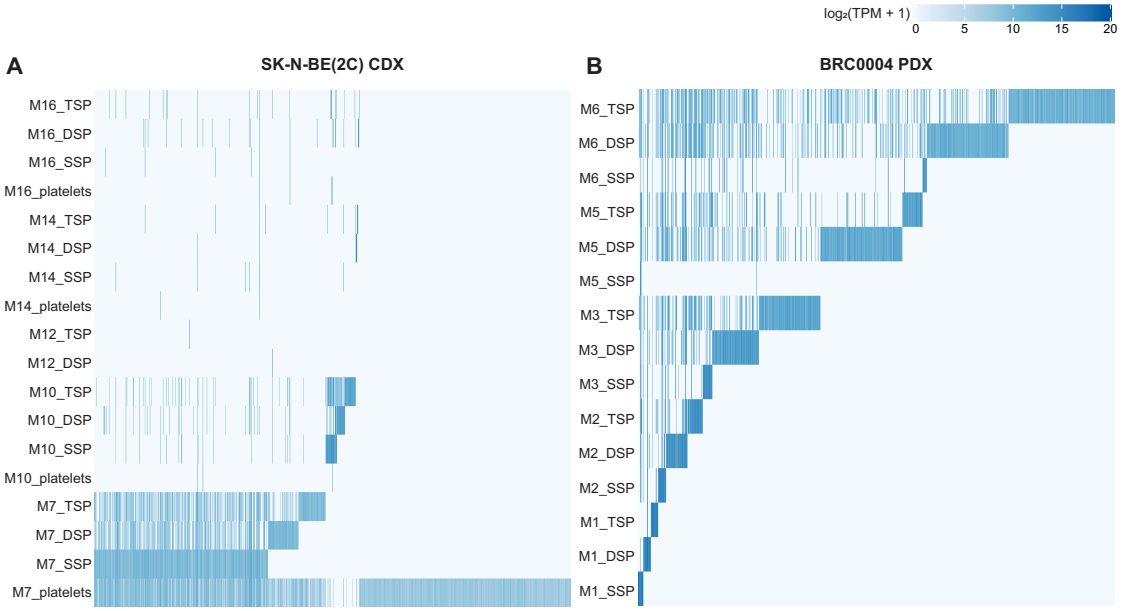

Figure 6. The circulating tumour gene abundance profile is highly variable across individual mice. Log_2(TPM + 1) values of all circulating protein-coding genes robustly detected (i.e. ≥5 counts) in at least one liquid biopsy sample of the CDX (**A**) or PDX (**B**) mice; DSP, double spun plasma; SSP, single spun plasma; TSP, triple spun plasma.

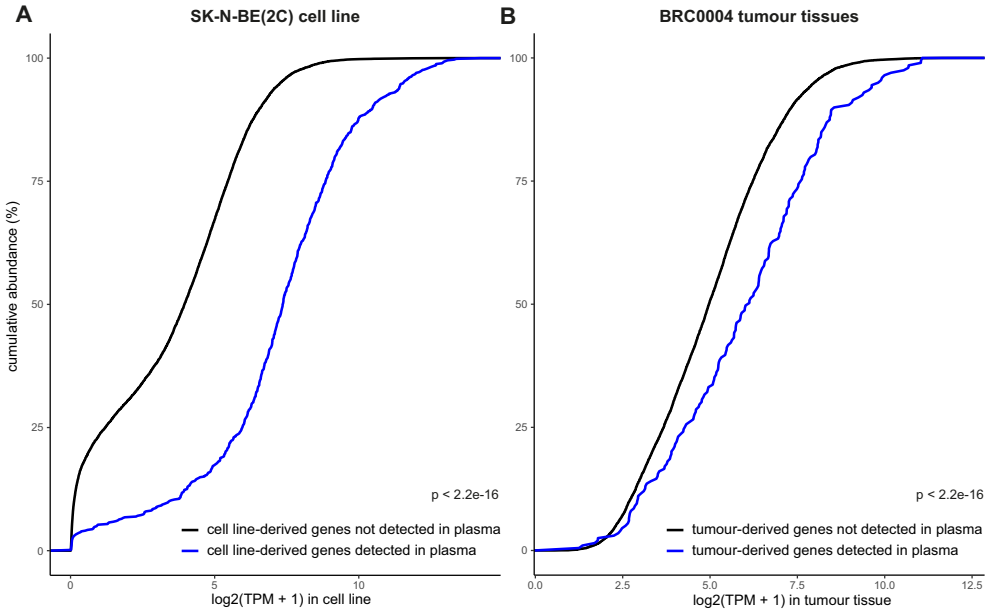

Figure 7. The tumour-derived genes that are circulating in plasma are higher expressed in the originating CDX or PDX cancer cells than the tumour-derived genes that are not circulating in plasma. (**A**) Cumulative abundance of genes only detected in the cell line (black) and genes detected in both the cell line and plasma (blue) of the CDX mice (two-sample Kolmogorov–Smirnov test, $P < 2.2e\text{-}16$). (**B**) Cumulative abundance of genes only detected in the tumour tissue (black) and genes detected in the tumour tissue and plasma (blue) of the PDX mice (two-sample Kolmogorov–Smirnov test, $P < 2.2e\text{-}16$). $Log_2(TPM+1)$ in tumour tissue represents the mean of the $log_2(TPM+1)$ tumour tissue values of mice M3, M5 and M6. A tumour gene is considered to be circulating in plasma if it has ≥ 5 counts in at least one of the triple spun plasma (TSP) samples.

lying bioinformatics pipelines are generally not publicly available. More importantly, these pipelines have not been applied to challenging blood-derived exRNA sequencing data, which is vastly different because of low concentration and fragmented nature. In the first part of this study, we developed and evaluated the performance of two deconvolution pipelines, using a combined (exRNAxeno combined) or parallel (exRNAxeno parallel) mapping strategy, on total exRNA sequencing data of liquid biopsies from non-tumour bearing control mice and healthy human donors. It should be noted that transcriptome profiling was performed using a total library preparation kit that can handle very low input amounts of fragmented RNA from different mammalian organisms and that the performance of the applied RNA sequencing technology has been previously validated (27). Here, exRNA from only 60 μl of plasma was used for sequencing library preparation. Both the exRNAxeno combined and exRNAxeno parallel pipeline demonstrated good performance and were further fine-tuned by masking genomic regions in which misaligned reads were identified in the control samples. By providing the computational pipelines through GitHub (https://github.com/CBIGR/exRNAxeno), we supply the research community with important tools to further explore circulating (tumour) transcriptomes in xenograft models. In addition, all sequencing data have been submitted to the European Genome-phenome Archive (EGA accession ID: EGAS00001005740 and EGAS00001006582). Given that the exRNAxeno combined mapping pipeline resulted in lower fractions of misaligned reads, fewer false positive Ensembl gene IDs and a smaller masked region, this method is preferred for the analysis of liquid biopsies from human xenograft mouse models.

Subsequently, our exRNAxeno combined pipeline was applied to exRNA samples from two xenograft mouse models, i.e. exRNA from platelets and three plasma fractions with decreasing platelet numbers (SSP, DSP and TSP) from SK-N-BE(2C) CDX and BRC0004 PDX mice, enabling to study the impact of plasma platelets levels on the circulating tumoural exRNA concentration and gene content. Finally, results were validated in 10 xenograft models, including neuroblastoma, melanoma, endometrial, penile and lung cancer xenograft models. Although the numbers of animals of the different xenograft models are limited, findings were consistent across the different xenograft models. We observed a gradual decrease in host RNA concentration with decreasing platelet content, while the tumoural RNA concentration remained relatively constant. This points out that murine platelets do contain a significant amount of murine exRNA, but that the tumoural RNA does not primarily reside in platelets. Of note, in contrast to the SK-N-BE(2C) CDX model, host RNA concentration levels in the BRC0004 PDX DSP and TSP samples do not differ (Figures 3 and 4), which may be explained by the different plasma preparation protocol that was used for these two xenograft models. In the PDX model, a longer centrifugation time (15 min versus 10 min in the CDX model) and higher *g*-force (2500 *g* versus 800 *g* in the CDX model) was

used to prepare DSP, resulting in removal of most of the platelets in the PDX DSP sample, and as such comparable platelet levels between the PDX DSP and TSP samples (as confirmed by the GSEA and RT-qPCR results, Supplementary Table S5 and Supplementary Figure S6). This clearly demonstrates that the plasma preparation protocol in exRNA-based tumour xenograft studies has substantial impact on the amount of background host signal that is detected, and thus also the tumoural exRNA proportion (Figure 4 and Supplementary Figure S8). Since platelets or platelet-rich plasma fractions are not enriched for tumour genes (Figure 5) and platelet-deprived plasma fractions display a greater tumour gene diversity (Figure 6 and Supplementary Figure S10A–F), we put forward TSP samples as the preferred biomaterial for tumour extracellular transcriptome profiling using massively parallel sequencing. Moreover, the greater tumour gene diversity from platelet-deprived fractions allows for enhanced detection of tumour aberrations. However, although TSP holds a greater tumour gene diversity, this does not preclude that the abundance of specific tumour genes might be higher in other plasma fractions. Future research should confirm these findings in biofluids from cancer patients (e.g. by focusing on characteristic genetic defects of the tumour, such as somatic mutations), but we expect that platelet depletion is also preferred when working with human plasma, in order to minimize the background signal originating from non-tumoural platelet RNA. We did not study possible enrichment of tumoural RNA in other plasma fractions such as extracellular vesicles (EVs) as this was practically impossible given the low starting volume (i.e. 60 μl) of plasma. Ultrapure purification of EVs cannot be performed on such small volumes and anticipating that EV RNA concentrations will be much lower than total plasma RNA concentrations, we would probably have reached the detection limit of total RNA sequencing (27). Unfortunately, the low number of mice per model and an insufficient sequencing depth did not allow us to analyse differential splicing patterns of platelets between tumour-bearing mice and non-tumour bearing mice, as reported for so-called tumour-educated platelets (15,16,20).

Of note, the number of detected genes and RNA concentration as reported here depend on many factors and should thus primarily be used for comparisons in this study. Apart from the plasma preparation protocol, also other factors influence exRNA profiles, such as the type of blood collection tube and the volume of plasma used for exRNA purification. In mice, the maximum volume of blood that can be collected by cardiac puncture is approximately 1 ml. By focusing on a single plasma fraction in these models, or by making use of xenograft models in larger animals (with higher blood volumes), larger plasma volumes can be obtained, which could result in higher yields of purified exRNA. Other factors that determine exRNA analysis are the RNA purification and sequencing library preparation method, as well as the exRNA eluate fraction used as input for library preparation (34). On top of that, also sequencing depth and specific analysis settings (e.g. the read count cut-off for robust detection) impact results. Clearly, the impact of these pre-analytical and analytical variables on tumour exRNA profiles should be further investigated, with the aim to develop guidelines for tumour exRNA analysis, enabling to compare results from different studies and to implement the use of exRNA-based biomarkers in oncology. Compared to the steps taken to standardize circulating tumour DNA (ctDNA) analysis, the efforts made to setup standard operating procedures for tumour exRNA analysis are still rather limited (35). Nevertheless, exRNAs are promising precision oncology biomarkers that expand the horizons of tumour-derived nucleic acid analysis. For example, it has been previously shown that combined DNA and RNA analyses from plasma result in higher detection rates of EGFR mutant lung cancer (21). This example also underscores the need to further investigate the parallel analysis of tumour exRNA and other blood analytes (such as ctDNA).

Apart from differences across the plasma fractions, individual mice present with even larger differences. Genuine biological variation, rather than technical variation, likely underlies these differences as our data is shown to be of good quality. The quality of the sequencing reads and the preprocessing steps was assured by FastQC and MultiQC analyses; the relatively constant Sequin/ERCC spike-in RNA ratio and the RT-qPCR spike-in RNA measurements (Supplementary Figure S5) all demonstrate that experiments are well executed (Supplementary Tables S1 and 2) (30). In search of tumour features that may explain the observed differences in the number of circulating tumour genes, we assessed the PDX and CDX tumour volumes. Since tumour volumes in PDX and CDX mice do not differ across individual mice, the number of circulating tumour genes is not associated with tumour volume. Also, our results do not point towards preferential shedding of certain tumoural exRNA in circulation, as highly abundant tumour genes in circulation are generally highly expressed in the originating tumour tissue or cell line.

In conclusion, we provide a novel computational framework, exRNAxeno, for the analysis of exRNA in plasma from tumour xenograft models, which enables to distinguish tumoural exRNAs from host background exRNA. Using this workflow, we characterized the entire extracellular tumour transcriptome in different plasma fractions of various human patient tumour-derived and cellular-derived murine xenograft models. As such, we demonstrated that the tumoural RNA concentration is not determined by the blood platelet level in plasma, and that the circulating tumour transcriptome is highly variable across individual xenograft mice. In general, highly abundant tumour-derived transcripts in plasma also display high expression levels in the tumours. These findings open new avenues to further investigate the functional role of circulating exRNAs in cancer models and patients.

DATA AVAILABILITY

The datasets supporting the conclusions of this article are available on the European Genome-Phenome Archive (EGA). Total RNA sequencing data from TSP samples of human donors ($n = 2$, two replicates for each donor) were obtained from Everaert *et al*. (27); European Genome-Phenome Archive (EGA) sample ID EGAN00002518840-EGAN00002518843 in EGAS00001004428). Total RNA sequencing data from the control mice, the BRC0004 PDX

mouse model, the SK-N-BE(2C) CDX mouse model and PDX/CDX validation cohort have been deposited in EGA (EGAS00001005740 and EGAS00001006582). The exRNAxeno combined and parallel pipeline for processing of RNA sequencing data are available in the GitHub repository (https://github.com/CBIGR/exRNAxeno).

SUPPLEMENTARY DATA

Supplementary Data are available at NAR Cancer Online.

ACKNOWLEDGEMENTS

Author contribution: The authors wish it to be known that, in their opinion, J.V. and A.D. should be regarded as joint last authors, and V.V. and J.D. as joint first authors. Author contributions are reported according to the CRediT taxonomy (36). Conceptualization: A.D., B.D.W., J.D., J.V., T.V.M, V.V. Methodology: A.D., J.D., J.D.W., V.V. Software: A.M., C.E., J.A., V.V. Validation: J.D., V.V. Formal analysis: J.D., V.V., E.P., M.G.B. Investigation: J.D., J.D.W., J.N., K.V., V.V. Resources: A.D., E.L., F.S., H.V.D., J.D., J.D.W., J.N., K.D., K.V., M.A., M.F.B., M.R., V.V. Data curation: A.D., J.D., V.V. Writing - original draft: A.D., J.D., V.V. Writing—review and editing: A.D., A.M., B.D.W., C.E., E.L., F.S., J.D., J.D.W., J.V., M.F.B., T.V.M., V.V. Visualization: A.D., J.D., V.V. Supervision: J.V. Project administration: A.D., B.D.W., J.D., J.V. Funding acquisition: A.D., A.M., B.D.W., F.S., J.D.W., J.V., K.D., M.A., M.R., T.V.M.

FUNDING

Belgian Federation for Cancer [2016-054]; Fonds Wetenschappelijk Onderzoek [11C1621N, 11M1422N, 1224021N, 1S90621N, G0B2820N, LIQUIDHOPE TRANSCAN-2 PROJECT]; Bijzonder Onderzoeksfonds [202011/GE/ZAP/018, BOF22/CDV/077]; Fight Kids Cancer [RESTRAIN]; Kom op tegen Kanker [STIVLK2018001401, 12430]; Geconcerteerde Onderzoeksactie (GOA) [BOF22/GOA/009]; Stichting Tegen Kanker [2018-092, 2020-095]. Funding for open access charge: Research Foundation - Flanders.

Conflict of interest statement. J.V. is co-founder of Biogazelle, now a CellCarta company, providing human biofluid exRNA sequencing as a global CRO.

REFERENCES

1. Suraj,S., Dhar,C. and Srivastava,S. (2017) Circulating nucleic acids: an analysis of their occurrence in malignancies (review). *Biomed. Rep.*, **6**, 8–14.
2. Esposito,A., Criscitiello,C., Locatelli,M., Milano,M. and Curigliano,G. (2016) Liquid biopsies for solid tumors: Understanding tumor heterogeneity and real time monitoring of early resistance to targeted therapies. *Pharmacol. Ther.*, **157**, 120–124.
3. Heitzer,E., Roberts,C.E.S. and Speicher,M.R. (2019) Current and future perspectives of liquid biopsies in genomics-driven oncology. *Nat. Rev. Genet.*, **20**, 71–88.
4. Bronkhorst,A.J., Ungerer,V. and Holdenrieder,S. (2019) the emerging role of cell-free DNA as a molecular marker for cancer management. *Biomol. Detect. Quantif.*, **17**, 100087.
5. Hulstaert,E., Morlion,A., Avila Cobos,F., Verniers,K., Nuytens,J., vanden Eynde,E., Yigit,N., Anckaert,J., Geerts,A., Hindryckx,P. *et al.* (2020) Charting Extracellular Transcriptomes in the Human Biofluid RNA Atlas. *Cell Rep.*, **33**, 108552.
6. Zhou,Z., Wu,Q., Yan,Z., Zheng,H., Chen,C.J., Liu,Y., Qi,Z., Calandrelli,R., Chen,Z., Chien,S. *et al.* (2019) Extracellular RNA in a single droplet of human serum reflects physiologic and disease states. *Proc. Natl. Acad. Sci. U.S.A.*, **116**, 19200–19208.
7. Zeka,F., Decock,A., van Goethem,A., Vanderheyden,K., Demuynck,F., Lammens,T., Helsmoortel,H.H., Vermeulen,J., Noguera,R., Berbegall,A.P. *et al.* (2018) Circulating microRNA biomarkers for metastatic disease in neuroblastoma patients. *JCI Insight*, **3**, e97021.
8. Mithraprabhu,S., Morley,R., Khong,T., Kalff,A., Bergin,K., Hocking,J., Savvidou,I., Bowen,K.M., Ramachandran,M., Choi,K. *et al.* (2019) Monitoring tumour burden and therapeutic response through analysis of circulating tumour DNA and extracellular RNA in multiple myeloma patients. *Leukemia*, **33**, 2022–2033.
9. D'Ambrosi,S., Nilsson,R.J. and Wurdinger,T. (2021) Platelets and tumor-associated RNA transfer. *Blood*, **137**, 3181–3191.
10. McAllister,S.S. and Weinberg,R.A. (2014) the tumour-induced systemic environment as a critical regulator of cancer progression and metastasis. *Nat. Cell Biol.*, **16**, 717–727.
11. Calverley,D.C., Phang,T.L., Choudhury,Q.G., Gao,B., Oton,A.B., Weyant,M.J. and Geraci,M.W. (2010) Significant downregulation of platelet gene expression in metastatic lung cancer. *Clin. Transl. Sci.*, **3**, 227–232.
12. Xue,L., Xie,L., Song,X. and Song,X. (2018) Identification of potential tumor-educated platelets RNA biomarkers in non-small-cell lung cancer by integrated bioinformatical analysis. *J. Clin. Lab Anal.*, **32**, e22450.
13. Nilsson,R.J.A., Balaj,L., Hulleman,E., van Rijn,S., Pegtel,D.M., Walraven,M., Widmark,A., Gerritsen,W.R., Verheul,H.M., Vandertop,W.P. *et al.* (2011) Blood platelets contain tumor-derived RNA biomarkers. *Blood*, **118**, 3680–3683.
14. Liu,L., Lin,F., Ma,X., Chen,Z. and Yu,J. (2020) Tumor-educated platelet as liquid biopsy in lung cancer patients. *Crit. Rev. Oncol. Hematol.*, **146**, 102863.
15. Sol,N., in 't Veld,S.G.J.G., Vancura,A., Tjerkstra,M., Leurs,C., Rustenburg,F., Schellen,P., Verschueren,H., Post,E., Zwaan,K. *et al.* (2020) Tumor-educated platelet RNA for the detection and (pseudo)progression monitoring of glioblastoma. *Cell Rep. Med.*, **1**, 100101.
16. Heinhuis,K., in 't Veld,S., Dwarshuis,G., van den Broek,D., Sol,N., Best,M., Koenen,A., Steeghs,N., Coevorden,F., Haas,R. *et al.* (2020) RNA-sequencing of tumor-educated platelets, a novel biomarker for blood based sarcoma diagnostics. *Eur. J. Surg. Oncol.*, **46**, e7.
17. Roweth,H. and Battinelli,E. (2021) Lessons to learn from tumor-educated platelets. *Blood*, **137**, 3174–3180.
18. Jia,J., Yang,S., Huang,J., Zheng,H., He,Y. and Wang,L. (2021) Distinct extracellular RNA Profiles in different plasma components. *Front. Genet.*, **12**, 564780.
19. Brinkman,K., Meyer,L., Bickel,A., Enderle,D., Berking,C., Skog,J. and Noerholm,M. (2020) Extracellular vesicles from plasma have higher tumour RNA fraction than platelets. *J. Extracell Vesicles*, **9**, 1741176.
20. Best,M.G., Sol,N., Kooi,I., Tannous,J., Westerman,B.A., Rustenburg,F., Schellen,P., Verschueren,H., Post,E., Koster,J. *et al.* (2015) RNA-Seq of tumor-educated platelets enables blood-based pan-cancer, multiclass, and molecular pathway cancer diagnostics. *Cancer Cell*, **28**, 666–676.
21. Krug,A.K., Enderle,D., Karlovich,C., Priewasser,T., Bentink,S., Spiel,A., Brinkmann,K., Emenegger,J., Grimm,D.G., Castellanos-Rizaldos,E. *et al.* (2018) Improved EGFR mutation detection using combined exosomal RNA and circulating tumor DNA in NSCLC patient plasma. *Ann. Oncol.*, **29**, 700–706.
22. Vitale,S.R., Helmijr,J.A., Gerritsen,M., Coban,H., van Dessel,L.F., Beije,N., van der Vlugt-Daane,M., Vigneri,P., Sieuwerts,A.M., Dits,N. *et al.* (2021) Detection of tumor-derived extracellular vesicles in plasma from patients with solid cancer. *BMC Cancer*, **21**, 315.
23. Wang,L., Yekula,A., Muralidharan,K., Small,J.L., Rosh,Z.S., Kang,K.M., Carter,B.S. and Balaj,L. (2020) Novel gene fusions in glioblastoma tumor tissue and matched patient plasma. *Cancers (Basel)*, **12**, 1219.
24. Khandelwal,G., Girotti,M.R., Smowton,C., Taylor,S., Wirth,C., Dynowski,M., Frese,K.K., Brady,G., Dive,C., Marais,R. *et al.* (2017) Next-generation sequencing analysis and algorithms for PDX and CDX models. *Mol. Cancer Res.*, **15**, 1012–1016.

25. Callari,M., Batra,A.S., Batra,R.N., Sammut,S.J., Greenwood,W., Clifford,H., Hercus,C., Chin,S.F., Bruna,A., Rueda,O.M. *et al.* (2018) Computational approach to discriminate human and mouse sequences in patient-derived tumour xenografts. *BMC Genomics*, **19**, 19.
26. Kluin,R.J.C., Kemper,K., Kuilman,T., de Ruiter,J.R., Iyer,V., Forment,J.v., Cornelissen-Steijger,P., de Rink,I., ter Brugge,P., Song,J.Y. *et al.* (2018) XenofilteR: Computational deconvolution of mouse and human reads in tumor xenograft sequence data. *BMC Bioinform.*, **19**, 366.
27. Everaert,C., Helsmoortel,H., Decock,A., Hulstaert,E., van Paemel,R., Verniers,K., Nuytens,J., Anckaert,J., Nijs,N., Tulkens,J. *et al.* (2019) Performance assessment of total RNA sequencing of human biofluids and extracellular vesicles. *Sci. Rep.*, **9**, 17574.
28. Harenza,J.L., Diamond,M.A., Adams,R.N., Song,M.M., Davidson,H.L., Hart,L.S., Dent,M.H., Fortina,P., Reynolds,C.P. and Maris,J.M. (2017) Data Descriptor: Transcriptomic profiling of 39 commonly-used neuroblastoma cell lines. *Sci. Data*, **4**, 170033.
29. Deveson,I.W., Chen,W.Y., Wong,T., Hardwick,S.A., Andersen,S.B., Nielsen,L.K., Mattick,J.S. and Mercer,T.R. (2016) Representing genetic variation with synthetic DNA standards. *Nat. Methods*, **13**, 784–791.
30. Hulstaert,E., Decock,A., Morlion,A., Everaert,C., Verniers,K., Nuytens,J., Nijs,N., Schroth,G.P., Kuersten,S., Gross,S.M. *et al.* (2021) Messenger RNA capture sequencing of extracellular RNA from human biofluids using a comprehensive set of spike-in controls. *STAR Protoc.*, **2**, 100475.
31. Ahdesmaki,M.J. (2018) Improved PDX and CDX data processing-letter. *Mol. Cancer Res.*, **16**, 1813.
32. Ahdesmäki,M.J., Gray,S.R., Johnson,J.H. and Lai,Z. (2017) Disambiguate: an open-source application for disambiguating two species in next generation sequencing data from grafted samples. *F1000Res*, **5**, 2741.
33. Jardim-Perassi,B.V., Alexandre,P.A., Sonehara,N.M., de Paula-Junior,R., Reis Júnior,O., Fukumasu,H., Chammas,R., Coutinho,L.L. and Zuccari,D.A.P.deC. (2019) RNA-Seq transcriptome analysis shows anti-tumor actions of melatonin in a breast cancer xenograft model. *Sci. Rep.*, **9**, 966.
34. Anckaert,J., Avila Cobos,F., Decock,A., Deleu,J., de Wever,O., de Wilde,J., Dhondt,B., D'huyvetter,T., Everaert,C., Fierro,C. *et al.* (2021) Performance of RNA purification kits and blood collection tubes in the Extracellular RNA Quality Control (exRNAQC) study. bioRxiv doi: https://doi.org/10.1101/2021.05.11.442610, 11 May 2021, preprint: not peer reviewed..
35. Godsey,J.H., Silvestro,A., Barrett,J.C., Bramlett,K., Chudova,D., Deras,I., Dickey,J., Hicks,J., Johann,D.J., Leary,R. *et al.* (2020) Generic protocols for the analytical validation of next-generation sequencing-based ctDNA Assays: a Joint Consensus Recommendation of the BloodPAC's Analytical Variables Working Group. *Clin. Chem.*, **66**, 1156–1166.
36. Brand,A., Allen,L., Altman,M., Hlava,M. and Scott,J. (2015) Beyond authorship: attribution, contribution, collaboration, and credit. *Learned Publish.*, **28**, 151–155.

SUPPLEMENTAL MATERIAL AND METHODS

For validation purposes, the exRNAxeno pipeline was applied to liquid biopsies from 20 additional PDX or CDX mice. Below we describe the collection, processing and analysis of these samples.

Liquid biopsy collection

In vivo work for the neuroblastoma IMR-32 CDX model (Table 1) was previously described (1). Liquid biopsies were prepared from vehicle-treated animals (n = 7). When mice reached a maximal tumour volume of 2000 mm³ or specific humane endpoints (i.e. a weight gain or loss of more than 20% or clinical signs of significant pain, distress or suffering), mice were sacrificed by cardiac puncture for liquid biopsy collection (blood volume range between 0.8 and 1 ml), followed by cervical dislocation. Liquid biopsies (SSP, DSP and TSP) were collected according to the protocol described in Supplemental Figure 1. The degree of haemolysis of TSP plasma samples was assessed by measuring levels of haemoglobin by spectrophotometric analysis (OD414) using a NanoDrop 1000 Spectrophotometer (Thermo Fisher Scientific, Waltham, MA, USA; Supplemental table 2).

In vivo work for the neuroblastoma (SK-N-BE(2C) (n=3)), melanoma (MEL0002 (n=2), MEL0068 (n=1) and MEL0083 (n=1)), endometrial (EMC0052 (n=2) and EMC0078 (n=1)), penile (PEN0014 (n=1) and PEN0020 (n=1)) and lung (A549 (n=1)) cancer xenograft mice models was done at the TRACE PDX platform (KU Leuven, UZ Leuven, Belgium, approved by the local ethical committee for animal experimentation (P164/2019)). To establish the PDX

models (https://gbiomed.kuleuven.be/english/research/50488876/54502087/Trace/PDX-repository; Table 1), tumour fragments freshly isolated from patients were implanted interscapular or in the flank of female immunodeficient nude mice (NMRI-Foxn1nu strain, Taconic Biosciences, Rensselaer, NY, USA or NSG, Charles River, Wilmington, MA, USA). Tumours were propagated in at least 3 generations of mice and characterized by histology and SNP fingerprinting to confirm genealogy before liquid biopsy collection. All patients of whom tumour material was collected, provided informed consent prior to study participation, approved by the Ethical Committee UZ Leuven (S63799, S61605 and S66742). To establish the SK-N-BE(2C) and A549 CDX models, female NMRI-Foxn1nu mice were subcutaneously xenografted in the dorsal flank with 2 x 106 cells, in 30 µl RPMI 1640 medium (Thermo Fisher Scientific, Waltham, MA, USA), suspended in 70 µl Matrigel matrix (Corning, Bedford, MA, UK) at the age of 13 weeks. When PDX or CDX mice reached at least 1000 mm^3 or specific humane endpoints (i.e. a weight loss of more than 20% or clinical signs of significant pain, distress or suffering), mice were sacrificed by cardiac puncture for liquid biopsy collection (blood volume range between 0.5 and 1.1 ml) followed by cervical dislocation. Liquid biopsies (SSP, DSP and TSP) were collected according to the protocol described in Supplemental Figure 1. The degree of haemolysis of all plasma samples was assessed by measuring levels of haemoglobin by spectrophotometric analysis (OD414) using a NanoDrop 1000 Spectrophotometer (Thermo Fisher Scientific, Waltham, MA, USA; Supplemental table 2).

RNA isolation, spike-in RNA addition and DNase treatment

Extracellular RNA from 60 µl plasma (70 µl plasma for IMR-32 CDX mice), was isolated using the miRNeasy Serum/Plasma Kit (Qiagen, Hilden, Germany), according to the manufacturer's manual. During RNA extraction, 2 µl of a 100,000-fold dilution of Sequin spike-in controls (Garvan Institute of Medical Research, Darlinghurst, NSW, Australia (2)) was added to the lysate. Upon RNA purification, 2 µl of a 70,000-fold dilution of External RNA Control Consortium (ERCC) RNA Spike-in Mix (Thermo Fisher Scientific, Waltham, MA, USA) was added to 12 µl RNA eluate, followed by gDNA removal (3). To this purpose, 1 µl HL-dsDNase (ArcticZymes Technologies, Tromsø, Norway) and 1.4 µl Heat & Run 10X Reaction Buffer (ArcticZymes Technologies, Tromsø, Norway) were added to the eluates, and RNA samples were incubated for 10 min at 37 °C, followed by 5 min at 58 °C.

Total RNA library preparation and sequencing

Total RNA libraries were prepared starting from 8 µl DNase-treated RNA using the SMARTer Stranded Total RNA-Seq Kit v2 - Pico Input Mammalian (Takara Bio, CA, USA), according to the manufacturer's manual with minor modifications (4). Briefly, prior to first strand cDNA synthesis, RNA from liquid biopsies was fragmented for 2 min at 94 °C. During final library

amplification, 16 PCR cycles were performed on the liquid biopsy samples. The final clean-up was repeated, since an excessive number of products < 200 bp in size was observed on Fragment Analyzer data (data not shown, Agilent Technologies, Santa Clara, CA, USA). Fragment sizes were determined using Fragment Analyzer software for smear analysis in the 200 bp to 1000 bp range. Library quantification was performed using the KAPA Library quantification Kit (Kapa Biosystems, Wilmington, MA, USA) and libraries were pooled equimolarly. The final pool was quantified using Qubit, and 0.61 nM was loaded on a Novaseq instrument (Novaseq SP Kit v1.5, 200 cycles), with 2% PhiX. Raw sequencing data is available in the European Genome-Phenome archive (EGAS00001006582).

Preprocessing of RNA sequencing data

Sequencing reads of liquid biopsy and tumour samples were preprocessed by FastQC (v.0.11.8) for quality control and trimmed by Cutadapt (v.1.18) for low quality bases at the 3' end of each read (Q30), for 3 nucleotides from the 5' end of the second read (due to the template switching adapter) and for the HT-TruSeq adapter sequences. Reads shorter than 35 bp were filtered out. Next, duplicated reads were removed with Clumpify (BBMap v.38.26) within clumps based on 60 bp trimmed reads and using default parameters, except for 20 passes. Subsequently, reads were once more analysed by FastQC for quality control.

exRNAxeno computational framework for combined mapping of RNA sequencing data

Reads were mapped using STAR (v.2.6.0) (specific parameter settings: --outSAMprimaryFlag AllBestScore --outSAMattributes NH HI AS nM NM) to a combined reference genome of human and mouse (combined mapping). The genome index for mapping was built using the Ensembl GRCh38.94 (human) and GRCm38.94 (mouse) DNA primary assembly sequences, containing all chromosomes, the mitochondrial genome and scaffolds, supplemented with ERCC and Sequin spike sequences and the full ribosomal DNA complete repeating unit (U13369.1, BK000964.3). GTF files were downloaded from Ensembl and adapted in a similar way. In the combined reference genome of mouse and human, mouse chromosomes were labelled with a prefix 'm'. Uniquely mapped reads were selected based on the NH:i:1 tag (SAMtools v.1.8, Pysam). BAM files were further masked by intersectBed for regions where control murine (n = 15) and human (n = 4) liquid biopsies empirically showed misalignment to the other reference genome (SAMtools v.1.8, BEDtools v.2.27.1, BEDOPS v.2.4.32). Further quality control on the filtered BAM files was done using MultiQC (v.1.7), SAMtools (v.1.8), RseQC (v.2.6.4) and BEDTools (v.2.27.1). Finally, read counts of name-sorted BAM files were generated by HTSeq-count (v.0.11.0) (specific parameter settings: -s reverse –secondary-alignments=ignore –supplementary-alignments=ignore) using appropriate GTF files. Further

processing was done with R (v.4.0.3) making use of tidyverse (v.1.3.1). The exRNAxeno combined is available through GitHub (https://github.com/CBIGR/exRNAxeno).

Table 1. Information on xenograft models.

Xenograft model	Patient diagnosis	Patient age (years)	Patient gender	Primary tumor metastasis	Tumor grade or stage	Tumor characteristics	Host mouse strain	Implantation site	Tumor volume at collection (mm^3)	Passage at collection	Source	Ref
BRC0004 PDX	breast invasive ductal adenocarcinoma	30-35	female	primary tumor	grade 3, pT2N0	triple negative: ER-, PR-, $HER2_{low}$	NMRI-Foxn 1^{nu}	intrascapular	1104-1286	unknown	UZ Leuven, TRACE	(5)
SK-N-BE(2C) CDX	neuroblastoma	0-5	male	metastasis	stage 4	*MYCN* amplification	NMRI-Foxn 1^{nu}	flank	1166 - 2243	unknown	ATCC	CRL-2271, ATCC
IMR-32 CDX	neuroblastoma	0-5	male	primary tumor	unknown	*MYCN* amplification	NU-Foxn 1^{nu}	flank	1949 - 2271	unknown	UGent, PPOL	(1)
MEL0083 PDX	cutaneous melanoma	unknown	male	metastasis	unknown	NRAS Q61R	NMRI-Foxn 1^{nu}	intrascapular	2756	P5	UZ Leuven, TRACE	(6)
MEL0068 PDX	cutaneous melanoma	65-70	female	metastasis	unknown	BRAF mutant	NMRI-Foxn 1^{nu}	intrascapular	2043	P5	UZ Leuven, TRACE	(6-8)
MEL0002	cutaneous melanoma	55-60	male	metastasis	unknown	BRAF mutant	NMRI-	intrascapular	1107-1383	P8	UZ Leuven, TRACE	(6–8)

Xenograft model	Patient diagnosis	Patient age (years)	Patient gender	Primary tumor metastasis	Tumor grade or stage	Tumor characteristics	Host mouse strain	Implantation site	Tumor volume at collection (mm^3)	Passage at collection	Source	Ref
PDX							Foxn 1^{nu}					
EMC0052 PDX	uterine leiomyosarcoma	55-60	female	metastasis	grade 3	Vimentin$_{low}$, Desmin-, Caldesmon-	NSG	flank	1311-2013	P5	UZ Leuven, TRACE	(9)
EMC0078 PDX	uterine leiomyosarcoma	60-65	female	metastasis	grade 3	Vimentin+, Desmin+, Caldesmon+	NSG	flank	2638	P7	UZ Leuven, TRACE	(9)
PEN0014 PDX	penile squamous cell carcinoma	75-80	male	metastasis	grade 2	HPV+	NMRI-Foxn 1^{nu}	interscapular	2105	P2	UZ Leuven, TRACE	(10)
PEN0020 PDX	penile squamous cell carcinoma	65-70	male	metastasis	grade 2	HPV+	NMRI-Foxn 1^{nu}	interscapular	1073	P1	UZ Leuven, TRACE	not published, Albersen, Leucci, *et al.* and (10)
A549 CDX	lung adenocarcinoma	55-60	male	primary tumor	unknown	epithelial-like,	NMRI-	flank	1567	unknown	ATCC	CCL-185, ATCC

Xenograft model	Patient diagnosis	Patient age (years)	Patient gender	Primary tumor metastasis	Tumor grade or stage	Tumor characteristics	Host mouse strain	Implantation site	Tumor volume at collection (mm^3)	Passage at collection	Source	Ref
						KRAS G12S	Foxn 1^{nu}					

REFERENCES

1. Nunes,C., Depestel,L., Mus,L., Keller,K.M., Delhaye,L., Louwagie,A., Rishfi,M., Whale,A., Kara,N., Andrews,S.R., et al. (2022) RRM2 enhances MYCN-driven neuroblastoma formation and acts as a synergistic target with CHK1 inhibition. Sci. Adv., 8, eabn1382.

2.Deveson,I.W., Chen,W.Y., Wong,T., Hardwick,S.A., Andersen,S.B., Nielsen,L.K., Mattick,J.S. and Mercer,T.R. (2016) Representing genetic variation with synthetic DNA standards. Nat. Methods, 13, 784–791.

3. Hulstaert,E., Decock,A., Morlion,A., Everaert,C., Verniers,K., Nuytens,J., Nijs,N., Schroth,G.P., Kuersten,S., Gross,S.M., et al. (2021) Messenger RNA capture sequencing of extracellular RNA from human biofluids using a comprehensive set of spike-in controls. STAR Protoc., 2, 100475.

4. Everaert,C., Helsmoortel,H., Decock,A., Hulstaert,E., Van Paemel,R., Verniers,K., Nuytens,J., Anckaert,J., Nijs,N., Tulkens,J., et al. (2019) Performance assessment of total RNA sequencing of human biofluids and extracellular vesicles. Sci. Rep., 9, 1–16.

5. Moens,S., Zhao,P., Baietti,M.F., Marinelli,O., Van Haver,D., Impens,F., Floris,G., Marangoni,E., Neven,P., Annibali,D., et al. (2021) The mitotic checkpoint is a targetable vulnerability of carboplatin-resistant triple negative breast cancers. Sci. Rep., 11, 1–13.

6. Vendramin,R., Katopodi,V., Cinque,S., Konnova,A., Knezevic,Z., Adnane,S., Verheyden,Y., Karras,P., Demesmaeker,E., Bosisio,F.M., et al. (2021) Activation of the integrated stress response confers vulnerability to mitoribosome-targeting antibiotics in melanoma. J. Exp. Med., 218.

7. Leucci,E., Vendramin,R., Spinazzi,M., Laurette,P., Fiers,M., Wouters,J., Radaelli,E., Eyckerman,S., Leonelli,C., Vanderheyden,K., et al. (2016) Melanoma addiction to the long non-coding RNA SAMMSON. Nature, 531, 518–522.

8. Rambow,F., Rogiers,A., Marin-Bejar,O., Aibar,S., Femel,J., Dewaele,M., Karras,P., Brown,D., Chang,Y.H., Debiec-Rychter,M., et al. (2018) Toward Minimal Residual Disease-Directed Therapy in Melanoma. Cell, 174, 843-855.e19.

9. Cuppens,T., Depreeuw,J., Annibali,D., Thomas,D., Hermans,E., Gommé,E., Trinh,X.B., Debruyne,D., Moerman,P., Lambrechts,D., et al. (2017) Establishment and characterization of uterine sarcoma and carcinosarcoma patient-derived xenograft models. Gynecol. Oncol., 146, 538–545.

10. Elst,L., Van Rompuy,A.S., Roussel,E., Spans,L., Vanden Bempt,I., Necchi,A., Ross,J., Jacob,J.M., Baietti,M.F., Leucci,E., et al. (2022) Establishment and Characterization of Advanced Penile Cancer Patient-derived Tumor Xenografts: Paving the Way for Personalized Treatments. Eur. Urol. Focus, 10.1016/j.euf.2022.04.012.

SUPPLEMENTAL FIGURES

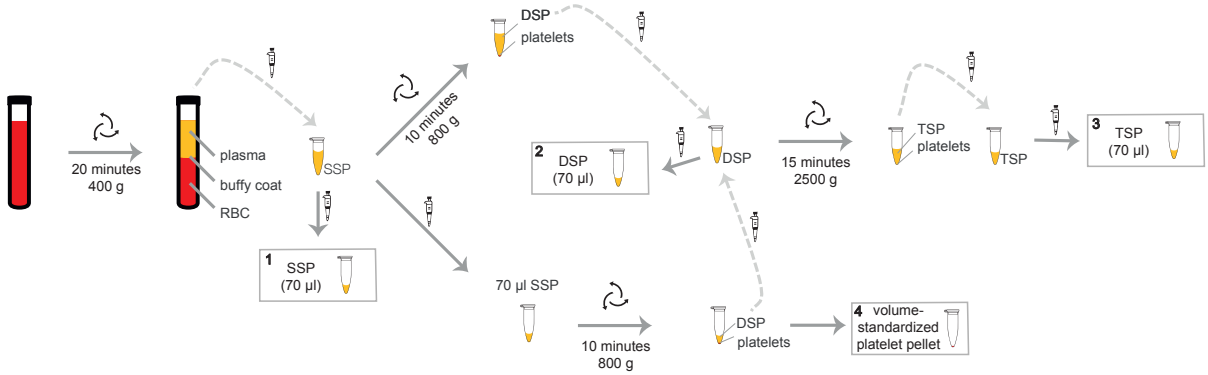

Supplemental figure 1. Liquid biopsy preparation protocol for the non-tumour bearing control mice and SK-N-BE(2C) CDX mice. From each animal, single spun (SSP, box 1), double spun (DSP, box 2), and triple spun (TSP, box 3) plasma, and a volume standardized platelet pellet originating from 70 µl SSP (box 4), were prepared by means of three sequential centrifugation steps. RBC: red blood cells.

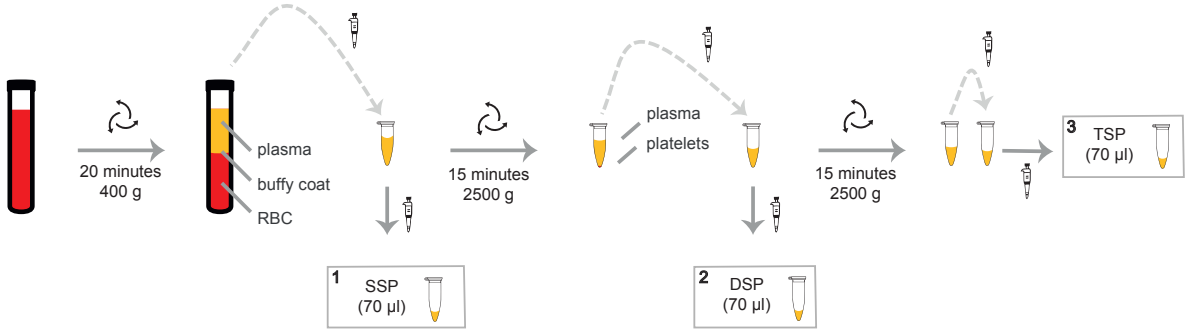

Supplemental figure 2. Liquid biopsy preparation protocol for the BRC0004 PDX mice. From each animal, single spun (SSP, box 1), double spun (DSP, box 2), and triple spun (TSP, box 3) plasma were prepared by means of three sequential centrifugation steps. RBC: red blood cells.

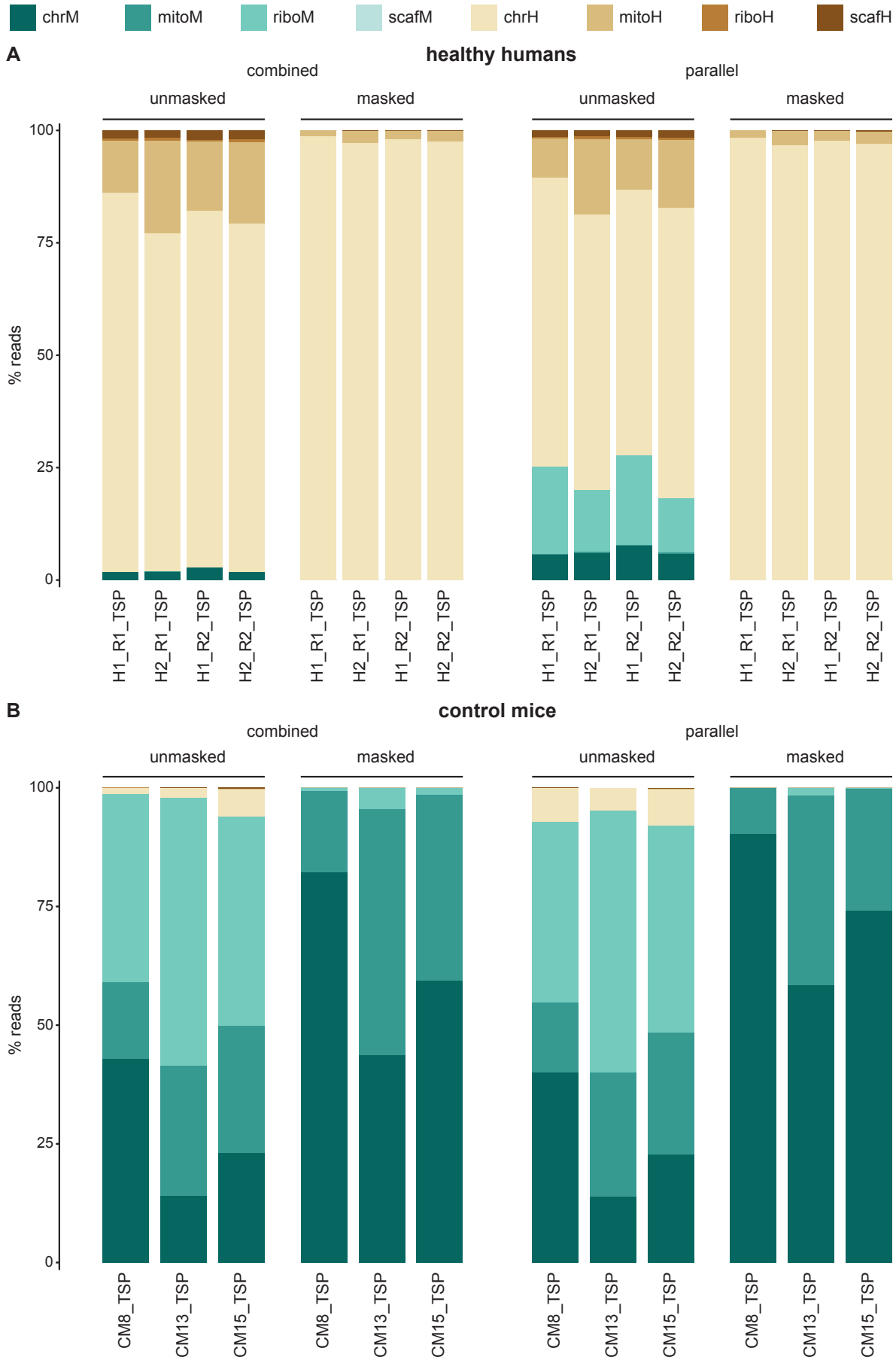
chrM
mitoM
riboM
scafM
chrH
mitoH
riboH
scafH
A
healthy humans
combined
parallel
unmasked
masked
unmasked
masked
100
75
50
25
0
% reads
H1_R1_TSP
H2_R1_TSP
H1_R2_TSP
H2_R2_TSP
B
control mice
combined
parallel
unmasked
masked
unmasked
masked
CM8_TSP
CM13_TSP
CM15_TSP

Supplemental figure 3. In the human and non-tumour bearing control murine plasma samples, the masking step in the processing pipelines removes the initially identified genomic regions consisting of misaligned reads. Shown are the relative percentages of total reads derived from human and murine nuclear RNA (chrH and chrM), mitochrondial RNA (mitoH and mitoM), ribosomal RNA (riboH and riboM) and scaffold RNA (scafH and scafM) for both human (A) and non-tumour bearing control murine (B) plasma samples in the combined and parallel mapping, before and after empirical masking of misaligned reads. CM: control mouse; H: human; R: replicate; TSP: triple spun plasma.

A

SK-N-BE(2C) CDX	murine genes	human genes
platelets	288	28
SSP	225	0
DSP	300	12
TSP	112	0

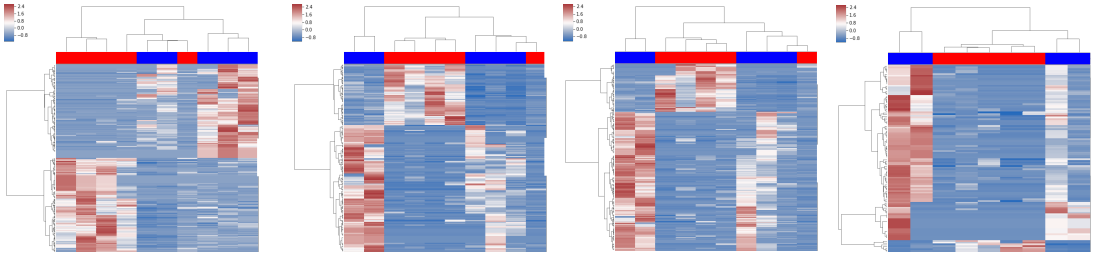

B

BRC0004 PDX	murine genes	human genes
SSP	436	142
DSP	1108	634
TSP	309	156

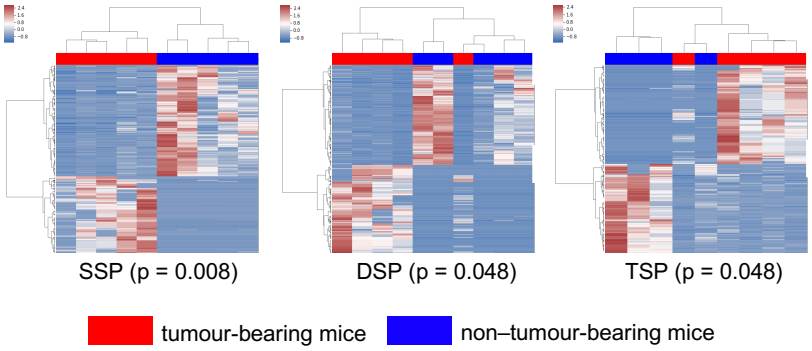

Supplemental figure 4. Tumour-bearing mice contain differential exRNA abundance profiles as compared to non-tumour bearing mice. Number of differential abundant murine and human genes (ANOVA's p-value threshold < 0.05) and heatmaps of unsupervised clustering of platelets, single-spun plasma (SSP), double-spun plasma (DSP) and triple-spun plasma (TSP) from the SK-N-BE(2C) CDX model (A) and BRC0004 PDX model (B). P-values indicate statistical significance of column clustering.

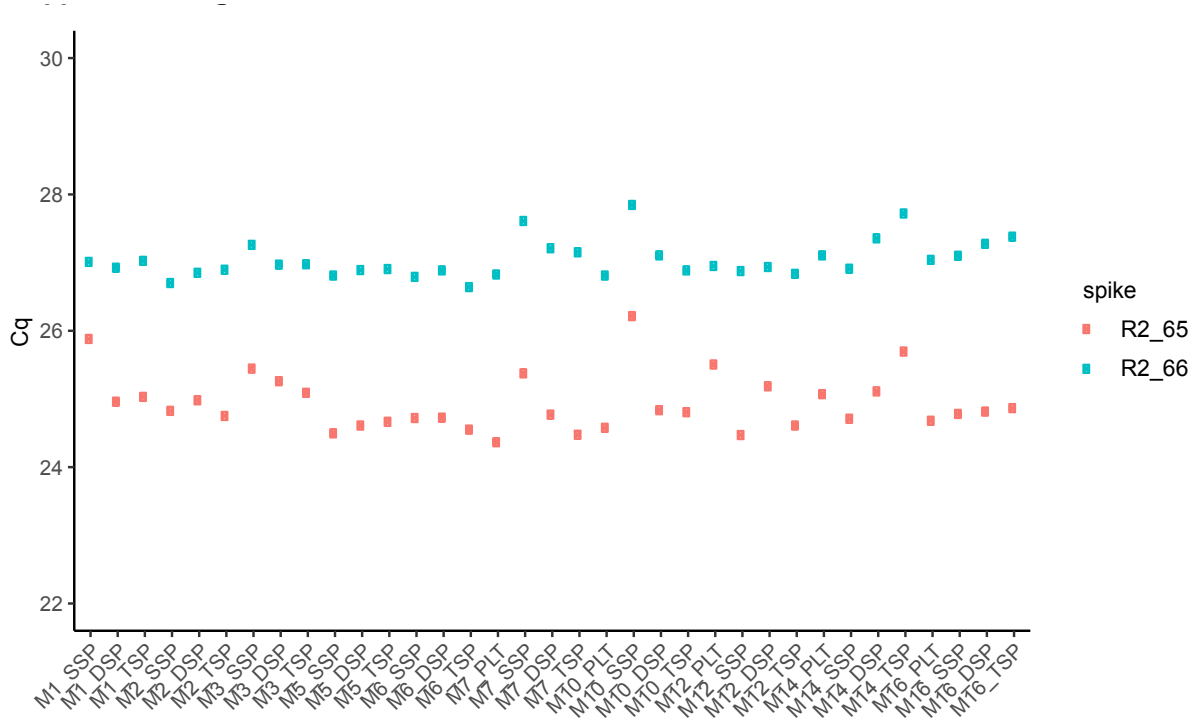

Supplemental figure 5. RT-qPCR analysis for Sequin spikes (R2_65 and R2_66), shows that exRNA purification is reproducible and Sequin spikes can be used for exRNA quantification. The presence of R2_65 and R2_66 Sequin spike-ins in the extracted RNA of all liquid biopsies of the BRC0004 PDX model (M1, M2, M3, M5, M6) and SK-N-BE(2C) CDX model (M7, M10, M12, M14, M16), was confirmed by means of RT-qPCR analysis. DSP: double spun plasma; SSP: single spun plasma; TSP: triple spun plasma.

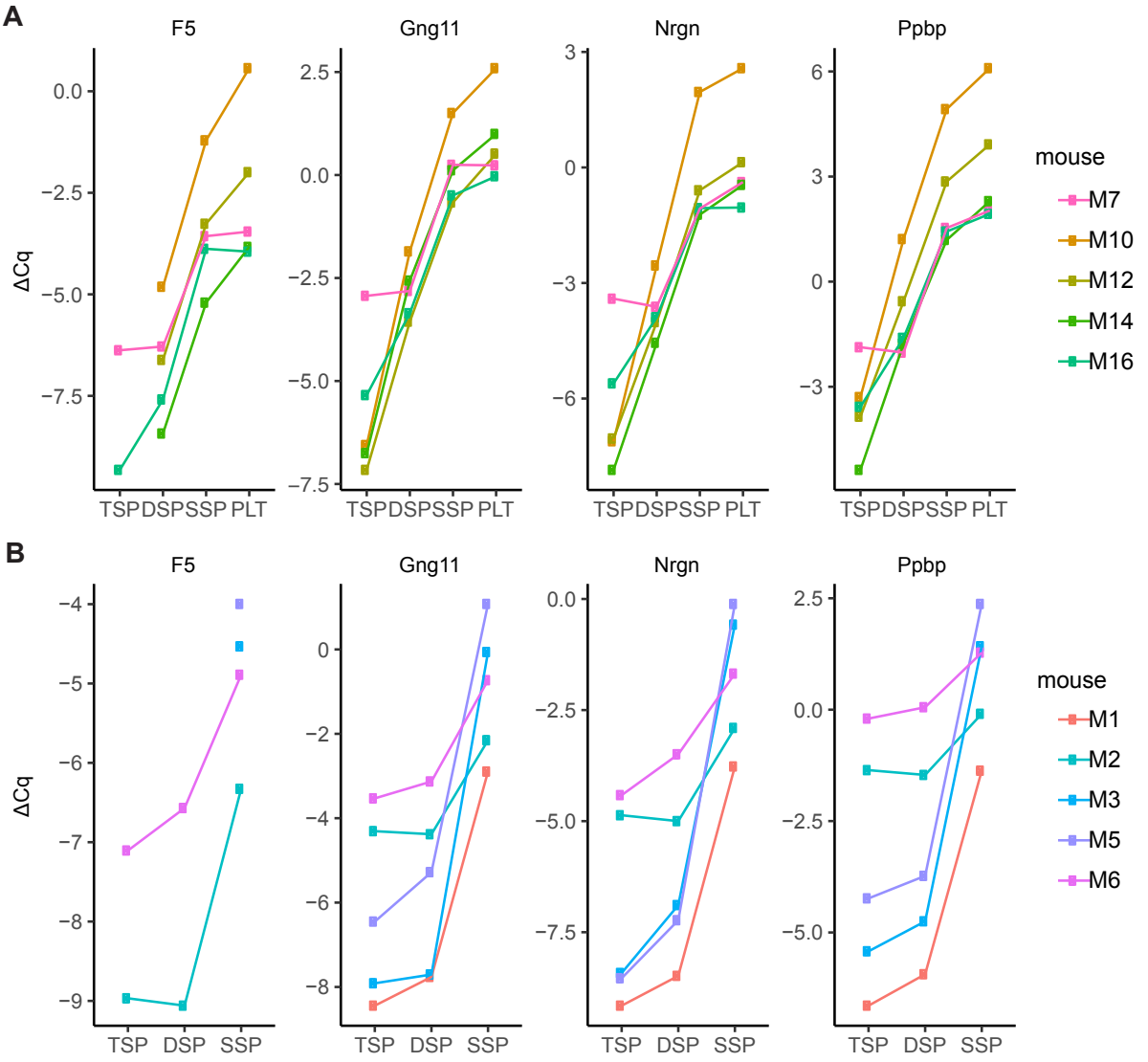

Supplemental figure 6. RT-qPCR analysis for platelet markers confirms a gradual decrease in platelet concentration upon successive centrifugation steps. The ΔCq is obtained by diminishing the mean Cq of R2_65 and R2_66 spikes of each sample by the Cq of each platelet gene of the respective sample. The ΔCq per platelet gene (F5, Gng11, Nrgn and Ppbp) in the different liquid biopsies from the SK-N-BE(2C) CDX model (A) and the BRC0004 PDX model (B) is shown. DSP: double spun plasma; PLT: platelets, SSP: single spun plasma; TSP: triple spun plasma.

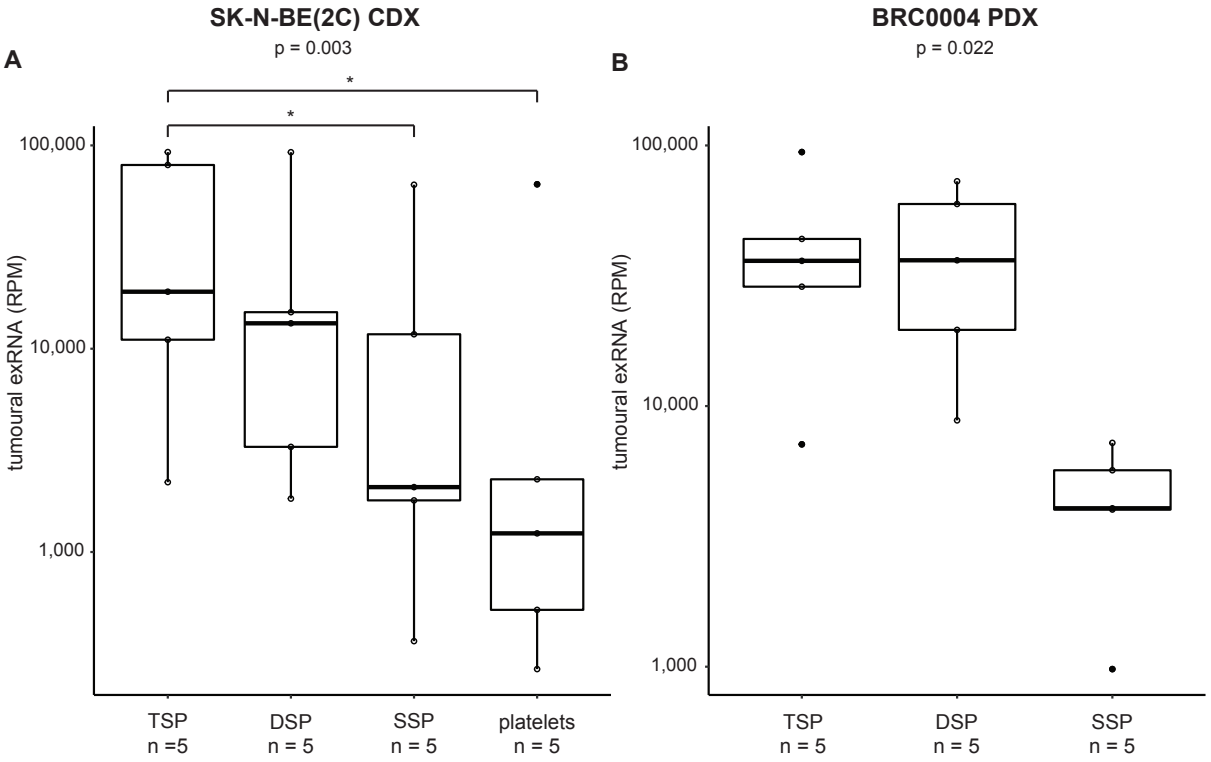

Supplemental figure 7. The relative amount of tumoural exRNA (RPM) is inversely proportional to the platelet plasma level. Shown is the amount of exRNA (RPM, mapped reads per million) present in the different liquid biopsies from the CDX (A; Friedman chi-squared test = 13.56, df = 3, p = 0.003; post-hoc test Nemenyi, p = 0.044 (*)) and PDX (B; Friedman chi-squared test = 7.6, df = 2, p = 0.022) mice. DSP: double spun plasma; SSP: single spun plasma; TSP: triple spun plasma.

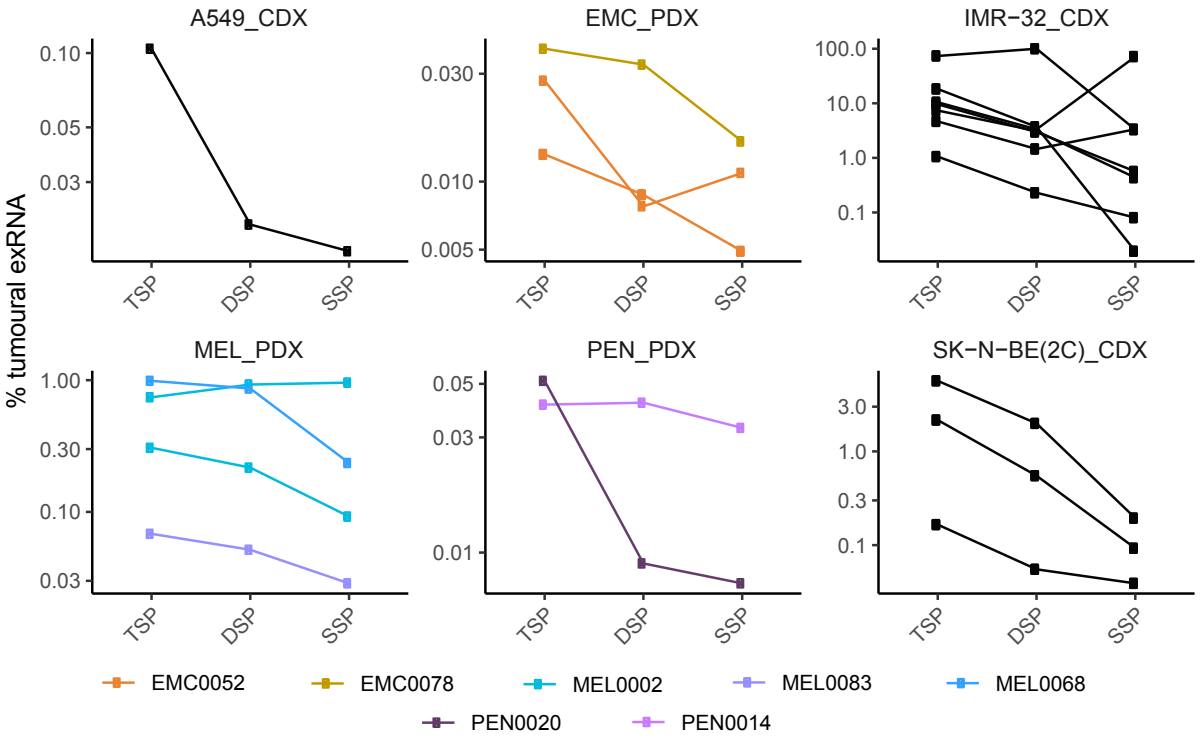

Supplemental figure 8. The tumoural exRNA percentage is inversely proportional to the platelet plasma level for the validation cohort. Shown are the percentages of tumoural exRNA present in the different liquid biopsies from the validation cohort mice, depicted per tumour type (A549: lung cancer, EMC: endometrial cancer, IMR-32: neuroblastoma, MEL: melanoma, PEN: penile cancer and SK-N-BE(2C): neuroblastoma). DSP: double spun plasma; SSP: single spun plasma; TSP: triple spun plasma.

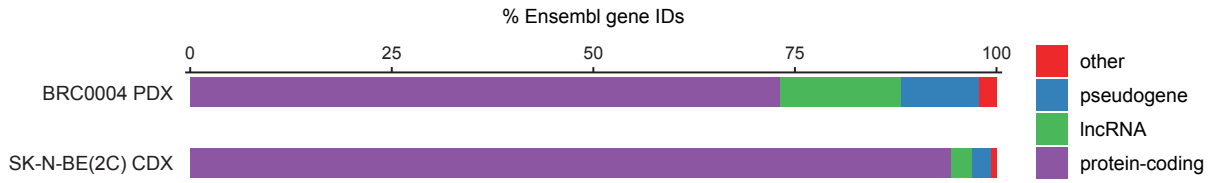

Supplemental figure 9. The majority of the tumour-derived exRNA is protein-coding. For the BRC0004 PDX- and SK-N-BE(2C) CDX-derived liquid biopsies, the percentages of identified human Ensembl IDs annotated as protein-coding, long non-coding RNA (lncRNA), pseudogene or other RNA biotypes are shown.

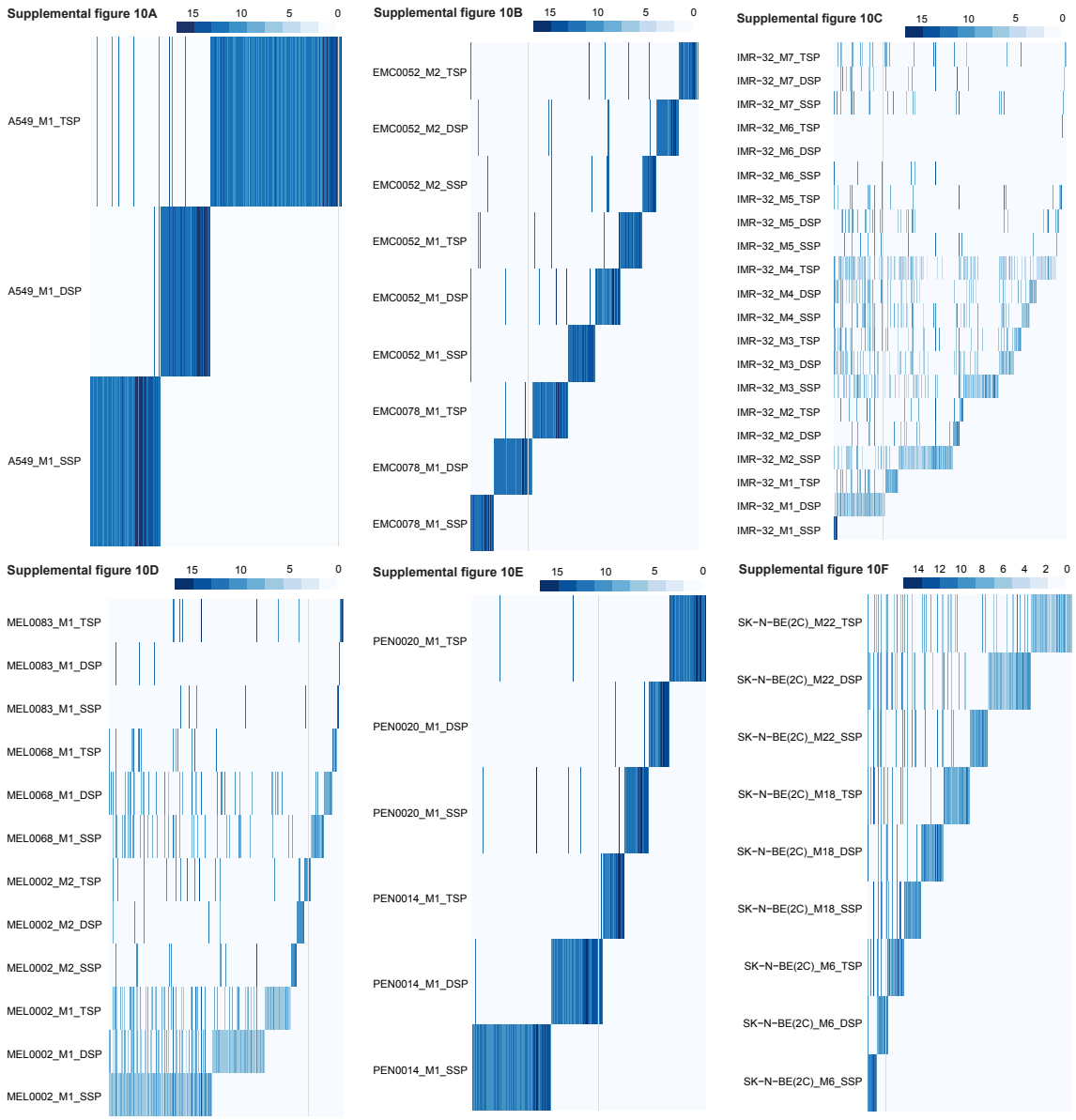

Supplemental figure 10A to F. The circulating tumour gene abundance profile is highly variable across individual mice. Log2(TPM + 1) values of all circulating genes of the validation cohort. DSP: double spun plasma; SSP: single spun plasma; TSP: triple spun plasma.

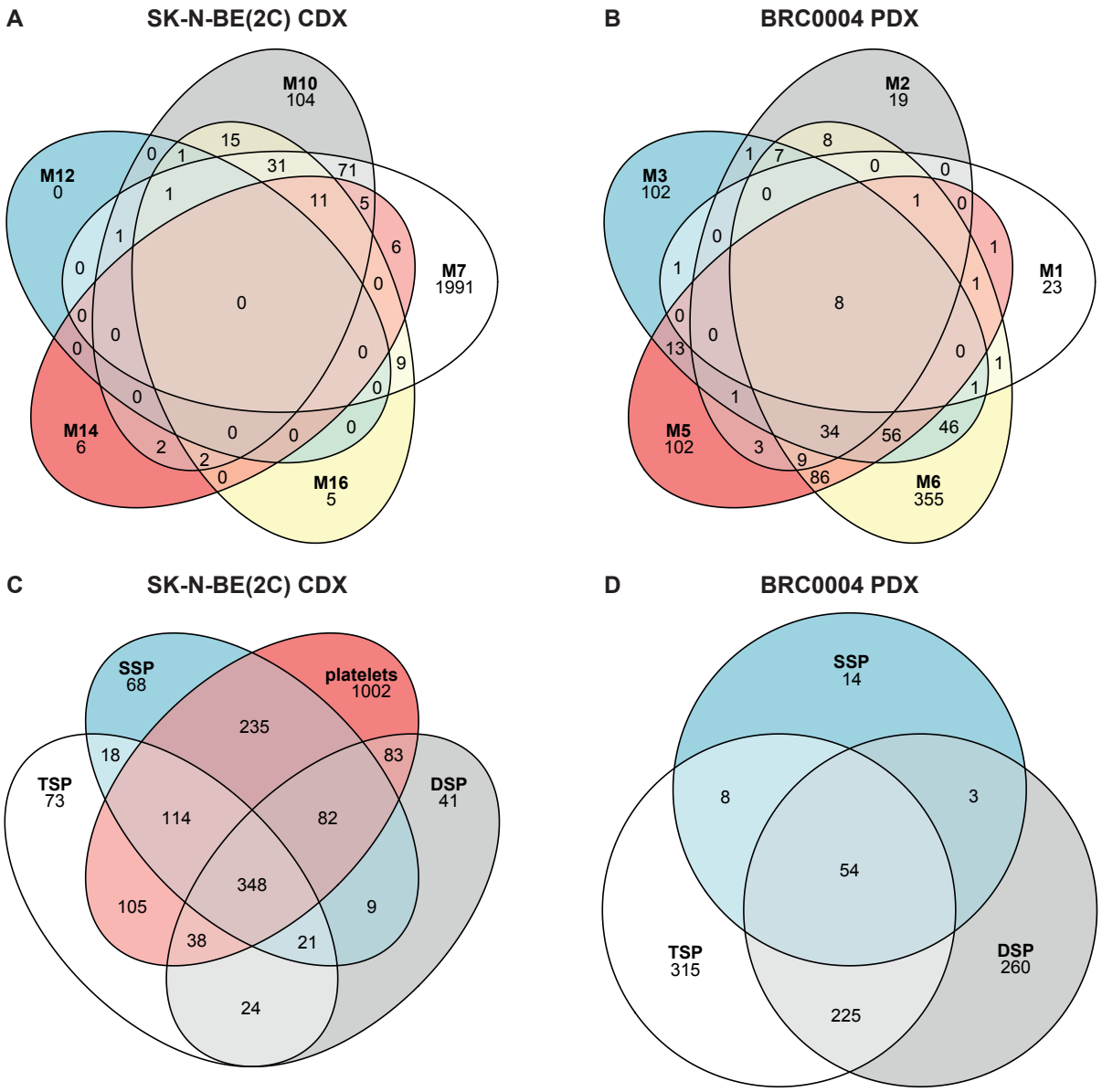

Supplemental figure 11. The circulating tumour gene profiles demonstrate common and distinct gene sets across different mice and across different liquid biopsy types. Overlap of the number of tumour-derived protein-coding genes (i.e. genes with ≥ 5 counts) across the different CDX (A) or PDX (B) mice (using all liquid biopsy types of the discovery cohort), as well as across the different liquid biopsy types for all CDX (C) or PDX (D) mice. DSP: double spun plasma; SSP: single spun plasma; TSP: triple spun plasma.

SUPPLEMENTAL TABLES (cf. NAR Cancer online)

Supplemental table 1. Overall, the SK-N-BE(2C) CDX and BRC0004 PDX sequencing data are of good quality. A. Quality control for the SK-N-BE(2C) CDX mice experiment. B. Quality control for the BRC0004 PDX mice experiment. For each RNA sample (RNA ID), the matching mouse ID, biomaterial ID and sample type is shown, as well as haemolysis levels measured by NanoDrop technology (absorbance of light at 414 nm) and RNA sequencing QC results. Sequencing depth: total read number; % trimmed: percentage total base pairs trimmed; % dups R1 or R2: percentage of downsampled R1 or R2 reads marked as duplicate; % GC R1 or R2: average GC content percentage of downsampled R1 or R2 reads; length R1 or R2: average sequence length (in bp) of downsampled R1 or R2 reads; % aligned to combined, human or mouse genome:percentage of downsampled reads aligned to the combined, human or mouse genome; exonic depth of combined, human or mouse genome: number of downsampled reads mapping to exons in the combined, human or mouse genome. The Sequin/ERCC ratio reflects RNA purification efficiency and should be relatively constant within a single experiment. DSP: double spun plasma; NA: not applicable; SSP: single spun plasma; TSP: triple spun plasma.

Supplemental table 2. The sequencing data of the validation cohort are of good quality. For each RNA sample (RNA ID), the matching mouse ID, biomaterial ID and sample type is shown, as well as haemolysis levels measured by NanoDrop technology (absorbance of light at 414 nm) and RNA sequencing QC results. Sequencing depth: total read number; % trimmed: percentage of total base pairs trimmed; % dups R1 or R2: percentage of downsampled R1 or R2 reads marked as duplicate; % GC R1 or R2: average GC content percentage of downsampled R1 or R2 reads; length R1 or R2: average sequence length (in bp) of downsampled R1 or R2 reads; % aligned to combined, human or mouse genome:percentage of downsampled reads aligned to the combined, human or mouse genome; exonic depth of combined, human or mouse genome: number of downsampled reads mapping to exons in the combined, human or mouse genome. The Sequin/ERCC ratio reflects RNA purification efficiency and should be relatively constant within a single experiment. DSP: double spun plasma; NA: not applicable; SSP: single spun plasma; TSP: triple spun plasma.

Supplemental table 3. Platelet content decreases upon successive centrifugation steps. Shown are the platelet counts per µl of plasma in single-spun (SSP), double-spun (DSP) and triple-spun (TSP) plasma.

Supplemental table 4. Endogenous RNA concentrations are calculated using Sequin spike-in controls. The concentration of Sequin spike-in controls added to each sample, is calculated based on the concentration (in attomol/µl) and length (in nucleotides) of each individual Sequin spike-in control.

Supplemental table 5. Gene set enrichment analyses on differentially abundant host genes between SSP, DSP and TSP demonstrate that murine platelet genes are enriched in SSP. For each xenograft model, the normalized enrichment score (NES), nominal P-value (nom P-value < 0.05), and false discovery rate q-value (FDR q-value <0.05) is indicated.

2. Digital PCR-based evaluation of nucleic acid extraction kit performance for the co-purification of cell-free DNA and RNA (paper 2)

Jill Deleu*, Kathleen Schoofs*, Anneleen Decock, Kimberly Verniers, Sofie Roelandt, Angie Denolf, Joke Verreth, Bram De Wilde, Tom Van Maerken, Katleen De Preter, and Jo Vandesompele. (*shared first)

Contribution of JD: In a joint effort, JD designed the project, optimized digital PCR assays, performed the experiments, conducted data analysis, and wrote and edited the manuscript.

For this publication, the CrediT contribution system was used to describe the contributions in the manuscript:

conceptualization	ADec, **JD**, JVa, KS	data curation	**JD**, KS
methodology	**JD**, JVa, KS	writing – original draft	**JD**, KS
software	**JD**, KS	writing- review & editing	ADec, ADen, BDW, **JD**, JVa, JVe, KDP, KS, KV, SR, TVM
validation	**JD**, KS	visualization	**JD**, KS
formal analysis	**JD**, KS, KV	supervision	JVa
investigation	ADen, **JD**, JVe, KS, KV, SR	project administration	ADec, **JD**, KS
resources	-	funding acquisition	ADec, BDW, **JD**, JVa, KDP, KS, TVM

Deleu *et al. Human Genomics* (2022) 16:73
https://doi.org/10.1186/s40246-022-00446-4

Human Genomics

RESEARCH

Open Access

Digital PCR-based evaluation of nucleic acid extraction kit performance for the co-purification of cell-free DNA and RNA

Jill Deleu[1,2†], Kathleen Schoofs[1,2,3,4†], Anneleen Decock[1,2], Kimberly Verniers[1,2], Sofie Roelandt[2,3,4], Angie Denolf[2,3], Joke Verreth[1,2], Bram De Wilde[1,2,5], Tom Van Maerken[1,2,6], Katleen De Preter[2,3,4] and Jo Vandesompele[1,2*]

Abstract

Background: Blood plasma, one of the most studied liquid biopsies, contains various molecules that have biomarker potential for cancer detection, including cell-free DNA (cfDNA) and cell-free RNA (cfRNA). As the vast majority of cell-free nucleic acids in circulation are non-cancerous, a laboratory workflow with a high detection sensitivity of tumor-derived nucleic acids is a prerequisite for precision oncology. One way to meet this requirement is by the combined analysis of cfDNA and cfRNA from the same liquid biopsy sample. So far, no study has systematically compared the performance of cfDNA and cfRNA co-purification to increase sensitivity.

Results: First, we set up a framework using digital PCR (dPCR) technology to quantify cfDNA and cfRNA from human blood plasma in order to compare cfDNA/cfRNA co-purification kit performance. To that end, we optimized two dPCR duplex assays, designed to quantify both cfDNA and cfRNA with the same assays, by ensuring that primers and probes are located within a highly abundant exon. Next, we applied our optimized workflow to evaluate the co-purification performance of two manual and two semi-automated methods over a range of plasma input volumes (0.06–4 mL). Some kits result in higher nucleic acid concentrations in the eluate, while consuming only half of the plasma volume. The combined nucleic acid quantification systematically results in higher nucleic acid concentrations as compared to a parallel quantification of cfDNA and cfRNA in the eluate.

Conclusions: We provide a framework to evaluate the performance of cfDNA/cfRNA co-purification kits and have tested two manual and two semi-automated co-purification kits in function of the available plasma input amount and the intended use of the nucleic acid eluate. We demonstrate that the combined quantification of cfDNA and cfRNA has a benefit compared to separate quantification. We foresee that the results of this study are instrumental for clinical applications to help increase mutation detection sensitivity, allowing improved disease detection and monitoring.

Keywords: Liquid biopsies, Co-purification, Cell-free RNA, Extracellular RNA, Cell-free DNA, Mutation detection, Digital PCR, Plasma, Cancer

† Jill Deleu and Kathleen Schoofs are joint First Authors

*Correspondence: jo.vandesompele@ugent.be

[1] OncoRNALab, Cancer Research Institute Ghent (CRIG), Ghent, Belgium
Full list of author information is available at the end of the article

Background

For an increasing number of malignancies, the mutation status of particular genes is crucial for diagnosis or treatment decision [1]. Assessing the mutation status of a tumor typically requires a tissue biopsy, which comes with discomfort and risk for the patient. Moreover, a tissue biopsy does not capture genetic heterogeneity well and is not compatible with longitudinal profiling. For these reasons, liquid biopsies are heralded as a promising alternative for both the patient and clinician [2–4].

Blood plasma is one of the most studied liquid biopsies as tumor-derived molecules end up in circulation by either active or passive release from tumor cells [5]. However, also healthy cells release their content into the bloodstream and as such, only a small fraction of circulating molecules is originating from the tumor. Moreover, for patients with small or slow-growing tumors, only a limited amount of nucleic acids may end up in the bloodstream, leading to reduced analytical sensitivity [6]. Consequently, a laboratory workflow for liquid biopsies that comes with high mutation detection sensitivity is a prerequisite for precision oncology. Several strategies exist to enhance the analytical sensitivity, ranging from higher blood plasma input volumes for extraction to advanced error-correcting molecular methods [7]. Recently, the combined analysis of cell-free DNA and RNA has been proposed as another means of increasing mutation detection sensitivity [8–11]. However, most studies have focused on RNA originating only from extracellular vesicles (EVs), thereby ignoring a significant part of the cell-free RNA (cfRNA) repertoire outside vesicles. Although EV concentration is thought to be increased in cancer patients' plasma, purification practices are not standardized among laboratories, are time consuming, and result in loss of material when trying to obtain highly pure and well-characterized EVs [12, 13]. To increase mutation detection sensitivity, it may be advantageous to co-purify cell-free DNA (cfDNA) and cfRNA from the same aliquot of neat plasma. Even if separate downstream analyses for DNA and RNA are desired, co-purification is advantageous, because it is cost and time effective, and allows maximal use of valuable patient samples.

So far, no study has systematically compared the performance of cfDNA and cfRNA co-purification technologies. The purpose of the present study is to provide a framework to compare different purification methods using digital PCR (dPCR) technology. Using healthy donor plasma, we compared two manual and two semi-automated co-purification methods and provide an evaluation in function of the available plasma input amount and the intended use of the nucleic acid eluate (Fig. 1).

Results

A framework for dPCR-based assessment of cfDNA/cfRNA co-purification kit performance

To compare the plasma cfDNA/cfRNA co-purification performance of manual and semi-automated procedures, a dPCR-based method was introduced for accurate and precise determination of the cfDNA and cfRNA concentration using two duplex assays targeting four human genes: CAVIN2 (HEX) / NRGN (FAM) and AIF1 (FAM) / B2M (HEX) (see Methods). Both duplex assays show positive partitions that are well separated from the negative partitions for cfDNA and cfRNA isolated from healthy human donor plasma. A representative example is shown in Fig. 2 for cfDNA/cfRNA co-purified from 0.6 mL of EDTA blood plasma from one donor using the miRNeasy Serum/Plasma Advanced Kit (MIRA0.6).

The framework, as represented in Fig. 1, outlines the steps to compare different co-purification kits on the basis of dPCR quantification. To allow for reliable cfRNA quantification, all DNA should be removed from the sample. Therefore, DNase treatment efficacy was evaluated on the eluates from each kit (Additional file 1: Fig. S1).

In the following sections, we will first discuss the co-purification performance of the evaluated kits, followed by ways to improve detection sensitivity for cfDNA and cfRNA quantification, and a demonstration of the added value of a combined cfDNA/cfRNA quantification instead of a parallel quantification of cfDNA and cfRNA.

Assessment of cfDNA/cfRNA co-purification performance of four commercial kits

The optimized workflow was used to assess the performance of six different commercially available (co-)

(See figure on next page.)

Fig. 1 Experimental design to evaluate (co-)purification kits. Blood from healthy donors, collected in EDTA or citrate tubes, was processed into plasma using a 2-spin protocol. Different plasma volumes were used as input for the different kits: 1 mL and 4 mL for CCF; 2 mL and 4 mL for CAT; 2 mL for MAPss and MAPds; 0.06 mL, 0.2 mL and 0.6 mL for MIRA; 0.06 mL, 0.2 mL and 1 mL for MAX; 0.06 mL and 0.2 mL for MIR. One half of the eluate was DNase treated and reverse transcribed for cfRNA quantification, while the second half remained untouched for cfDNA quantification. Quantification of nucleic acids was performed by digital PCR. *MAP and MAX eluates were concentrated using Vivacon columns and vacuum centrifugation, respectively. Underlined kits (CAT and MAP) are semi-automated procedure systems. *CCF*: QIAamp ccfDNA/RNA Kit, *CAT*: iCatcher Circulating cfDNA/cfRNA 4000 kit, *MAP*: MagNA Pure 24 Total NA Isolation Kit, *MIRA*: miRNeasy Serum/Plasma Advanced Kit, *MAX*: Maxwell ccfDNA LV Plasma Kit, *MIR*: miRNeasy Serum/Plasma Kit

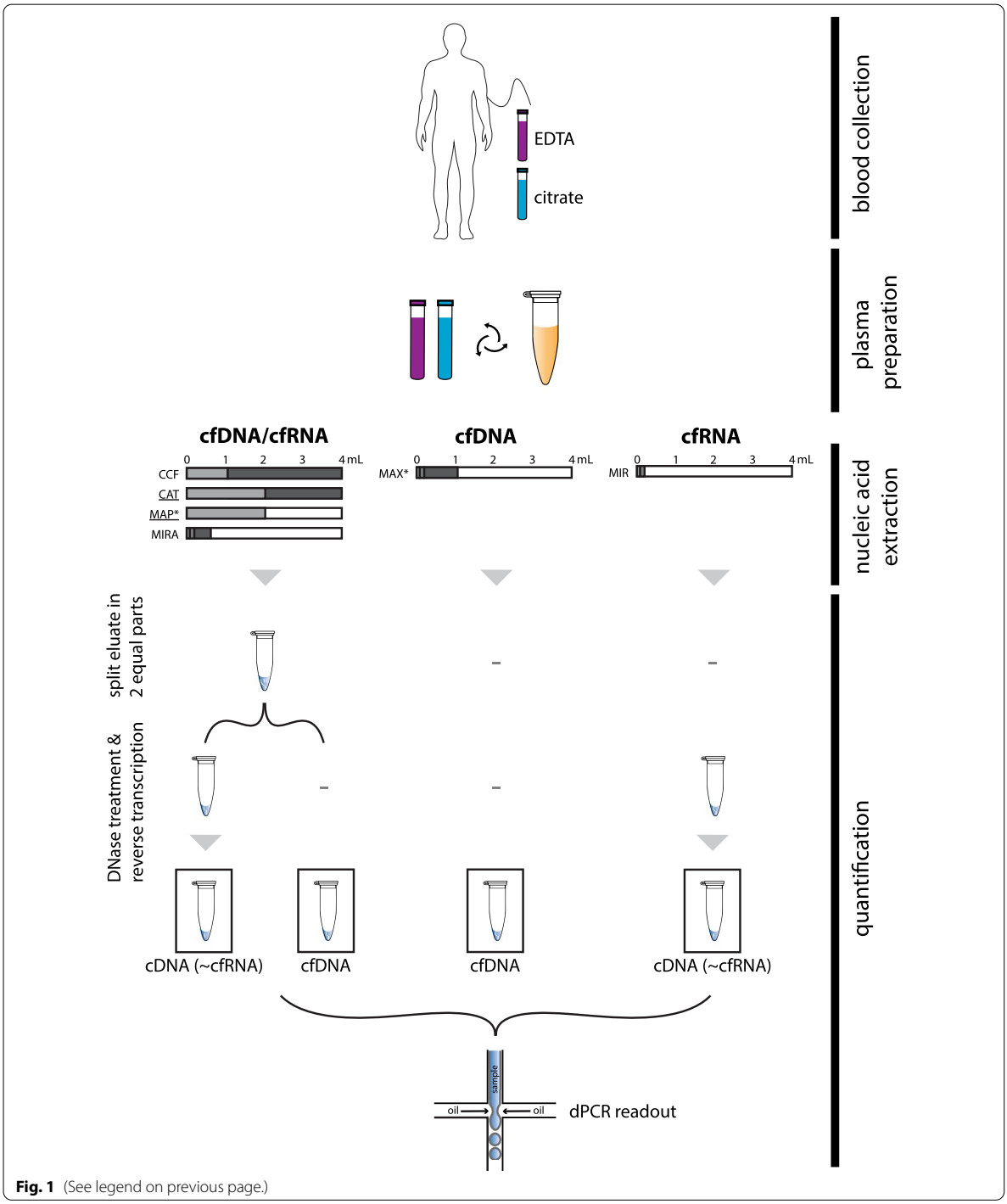

Fig. 1 (See legend on previous page.)

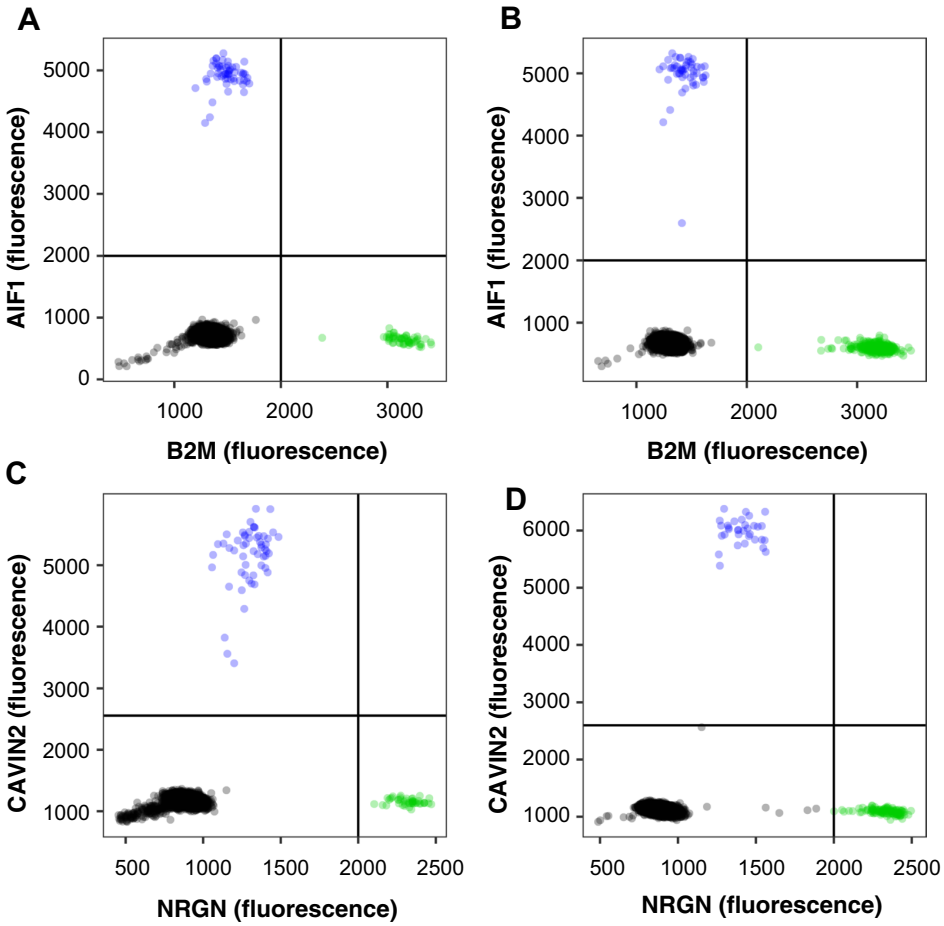

Fig. 2 Representative two-color plots of two dPCR duplex assays for quantification of cfDNA (**A**, **C**) and cfRNA (**B**, **D**) shows a nice distribution of positive and negative partitions. Data from nucleic acids co-purified with MIRA0.6 from healthy donor plasma (blood collected in EDTA tubes). **A**, **B** Duplex assay for AIF1 (FAM, blue) and B2M (HEX, green). **C**, **D** Duplex assay for CAVIN2 (FAM, blue) and NRGN (HEX, green). Green and blue dots represent positive partitions of the two genes, respectively. Black dots represent negative partitions

purification kits: (1) MIRA, (2) QIAamp ccfDNA/RNA Kit (CCF), (3) iCatcher Circulating cfDNA/cfRNA 4000 kit (CAT), (4) MagNA Pure 24 Total NA Isolation Kit with the cfNA ss 2000 and cfNA ds 2000 purification protocols (MAPss and MAPds, respectively), (5) Maxwell ccfDNA LV Plasma Kit (MAX) and (6) miRNeasy Serum/Plasma Kit (MIR). The performance of the four co-purification kits (CAT, MIRA, MAP, CCF) was compared with kits developed to extract only cfDNA (MAX) or cfRNA (MIR). For each kit, a range of plasma input volumes were used to assess kit performance (Fig. 1, Additional file 2: Table S1).

The cfDNA and cfRNA concentration (copies per µl eluate) was determined by dPCR (Fig. 3). In general, results show little variation between donors and blood collection tube types, as can be seen by the small error bars (showing the standard deviation of the geometric mean of all donors and blood collection tubes). As expected, we observe constant cfDNA concentrations as assessed by the four assays, while cfRNA concentrations are widely different among assays, reflecting the dynamic nature of cfRNA. Also, the concentration of extracted nucleic acids in the eluate increases proportionally with

higher input volumes when using the same kit (Fig. 3, Additional file 3: Table S2).

Furthermore, we compared the co-purification performance of the evaluated kits by measuring the cfDNA and cfRNA concentration and determining the cfDNA and cfRNA yield (concentration multiplied by the eluate volume) (Additional file 4: Table S3). All co-purification kits were capable of co-purifying cfDNA and cfRNA. While most of the co-purification kits resulted in reproducible eluate volumes (MIRA, CCF and MAP), eluate volumes after purification with CAT were ranging between 18 and 27 µl. In Additional file 4: Table S3, concentration and yield for each kit and input volume are calculated, followed by rescaling to the maximum concentration or yield (CAT4 in all cases) to obtain relative values (percentages). For cfRNA, the highest concentrations and yields are obtained with CAT4, CAT2 and CCF4 kit. For cfDNA, the highest concentrations and yields are obtained with CAT4, CCF4 and MAPss2 kit. Additional kit characteristics and remarks are provided in Additional file 2: Table S1.

Assessing cfDNA size distribution using microfluid electrophoresis

To ascertain that the measured DNA is cell-free in origin and not high-molecular cellular DNA, fragment size analysis using microfluid electrophoresis (TapeStation) was performed. cfDNA has a typical average fragment length of ~ 170 bp, whereas larger fragments (> 700 bp) originate from lysed cells and are defined as high molecular weight (HMW) DNA. For 30/46 samples with cfDNA concentration above the limit of detection for TapeStation (20 pg/µl), the cfDNA percentage is between 64 and 94%, indicating overall good quality (pure) cfDNA and low fractions of HMW DNA (Additional file 5: Fig. S2). Furthermore, cfDNA concentrations as determined above LOD by TapeStation correlate well with cfDNA concentrations measured by dPCR (Fig. 4).

Increasing detection sensitivity by increasing cfDNA/cfRNA template volume in a digital PCR reaction

Blood plasma is characterized by low cfDNA and cfRNA concentration. To increase the detection sensitivity with dPCR, the template input volume in a 20 µl reaction can be increased. A more concentrated mix of primers and probes can be made and added to the reaction mix as a small volume, enabling the addition of a higher cfDNA/cfRNA eluate volume. However, increasing the eluate input volume may cause inhibition of the dPCR reaction, which may be assay dependent [14]. Therefore, the inhibitory effect of the eluate (cfDNA/cfRNA template molecules with possible carry-over products from sample matrix) in a dPCR reaction was evaluated for the four optimized dPCR assays with input volumes taking up 10–40% of the total reaction volume. The assays used in this study did not show inhibition for cfDNA (Fig. 5A) nor cDNA (~ cfRNA) (Fig. 5B) when increasing eluate input volumes. cfDNA and cfRNA used for this experiment was co-purified using the MIRA kit with 0.6 mL plasma as input volume. As a proof-of-principle, these results show it is possible to confidently maximize input volume up to 40% of total reaction volume using these four assays (for MIRA eluates using the 2 × ddPCR Supermix for Probes and QX100 dPCR instrument). We recommend that users evaluate eluate input inhibition for their own assays and dPCR reaction conditions.

Combined quantification of cfDNA and cfRNA

Until now, we have shown that it is perfectly possible to co-purify cfDNA and cfRNA with all tested co-purification kits by quantifying the nucleic acids separately. However, jointly analyzing both cfDNA and cfRNA at the same time would improve the analytical workflow further: there is no need to split the eluate and do separate enzymatic reactions; instead, downstream analysis (e.g., dPCR quantification) can be done in one reaction, thereby saving materials, reagents and time. As a proof-of-principle, cfDNA and cfRNA was co-purified from plasma from three healthy donors (MIRA kit with 0.6 mL input volume) and quantified both separately and together. Somewhat unexpectedly, results clearly show that the jointly measured nucleic acid concentration is higher than the theoretical concentration defined as the sum of the separately measured cfDNA and cfRNA concentration (Fig. 6).

(See figure on next page.)

Fig. 3 Quantification of cfDNA (**A**) and cfRNA (**B**) extracted from healthy donor plasma with six (co-)purification kits using different input volumes. Per assay the mean concentration of the tube and donors was taken, error bars indicate standard errors. Black horizontal lines indicate geometric means of the four assays. *MIR*: miRNeasy Serum/Plasma kit, *MIRA*: miRNeasy Serum/Plasma Advanced kit, *MAX*: Maxwell ccfDNA plasma kit, *CCF*: QIAamp ccfDNA/RNA Kit, *MAPss*: MagNA Pure 24 Total NA Isolation Kit (Single Strand protocol), *MAPds*: MagNA Pure 24 Total NA Isolation Kit (Double Strand protocol), *CAT*: iCatcher Circulating cfDNA/cfRNA. Numbers after kit abbreviation indicate plasma input volumes in mL

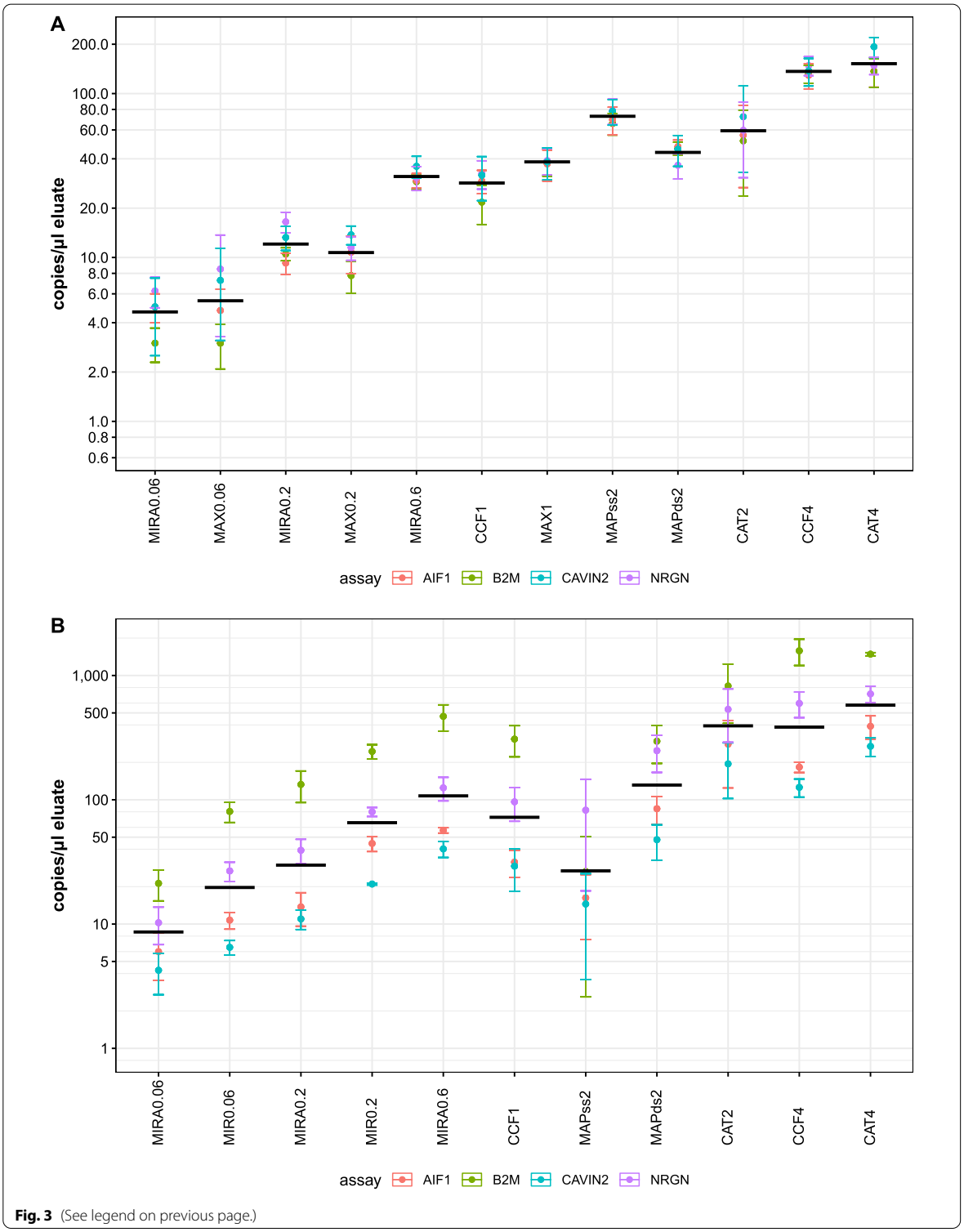

Fig. 3 (See legend on previous page.)

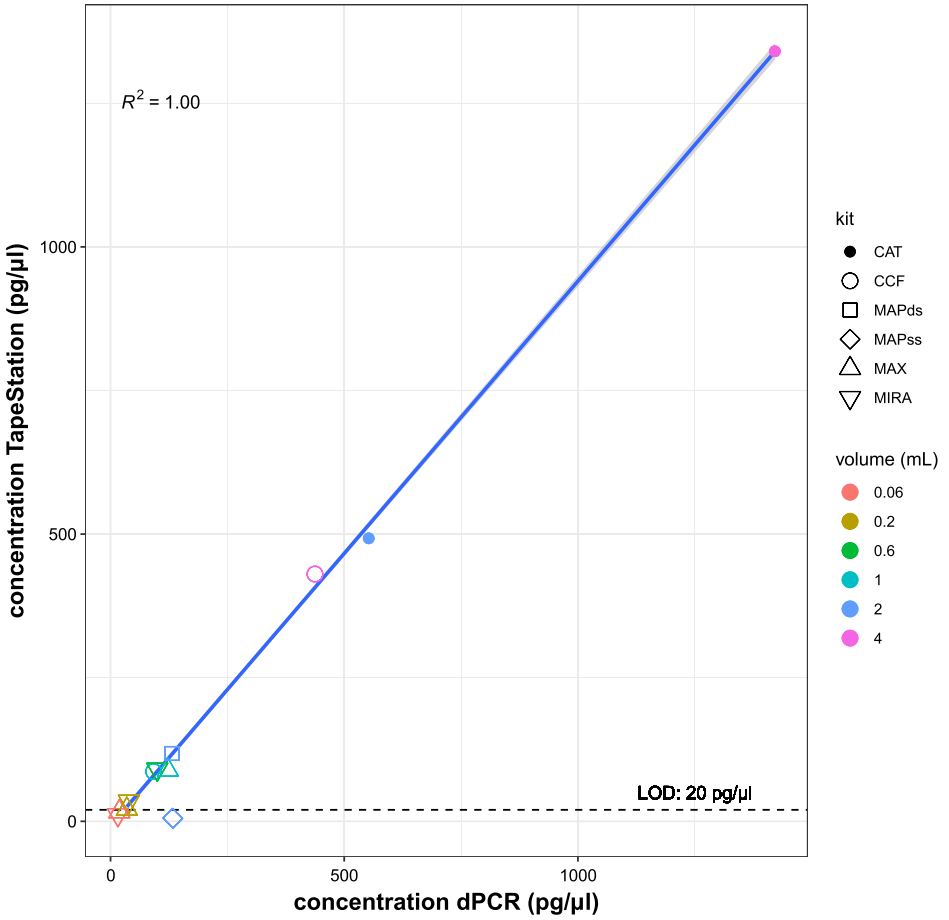

Fig. 4 cfDNA concentration measured with microfluid electrophoresis (*y*-axis) and dPCR (*x*-axis) show a good correlation. Each dot represents the mean of the donors and blood tubes. Concentration dPCR was calculated by taking the mean of the four assays in the input volume used for dPCR. Concentrations from QuantaSoft software (copies/µl) were converted to pg/µl by multiplying by 3.2 pg. Sample means below LOD of TapeStation were excluded for calculating R^2 (3/12)

Discussion

Robust and reproducible workflow

We developed a robust and reproducible workflow to evaluate co-purification kit performance. First of all, DNase treatment was shown to be effective for all but one kit (MAP), despite additional purification (Vivacon columns) prior to DNase treatment to remove inhibitory reagents. Second, there is little variation between donors and collection tube types, with the exception of CAT and MAP, suggesting that co-purifications are less reproducible with these kits. Third, as expected, there is little variability between the cfDNA concentrations measured by the four assays. On the contrary, cfRNA concentrations are highly different between assays, reflecting the wide dynamic range of cfRNA abundance levels. Fourth, increasing the input volume results in a proportionally higher concentration. Fifth, quality of cfDNA was assessed to avoid measurement bias caused by cellular DNA. For 16/46 samples, cfDNA fractions could not reliably be estimated, because concentrations were below the LOD of the TapeStation or showed flat profiles. This includes all samples ($n=8$) with 0.06 mL input volume, indicating that very little cfDNA is co-purified with such low input volume. However, concentrations could be

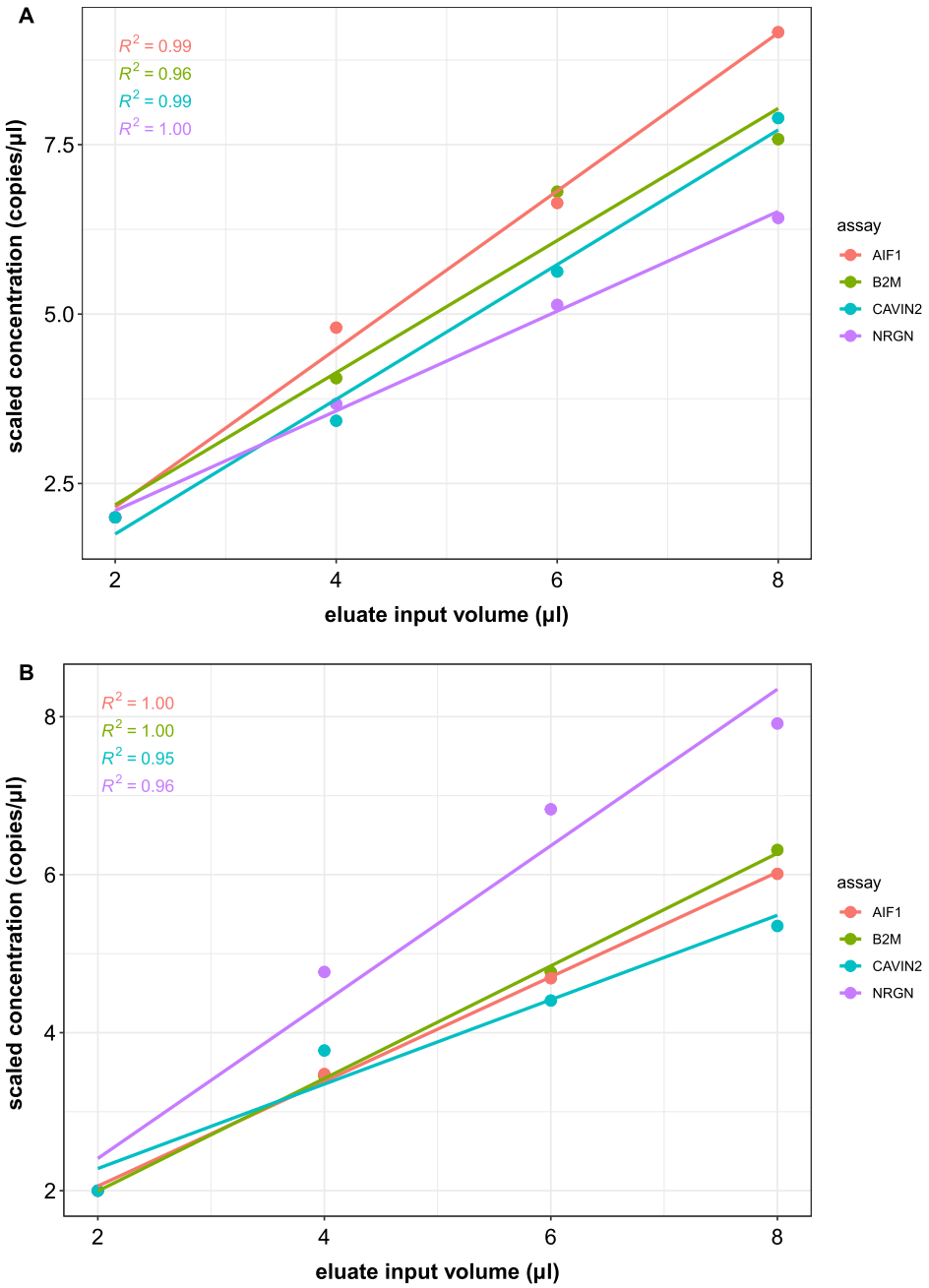

Fig. 5 Increasing the fraction of eluate in the dPCR reaction volume does not inhibit quantification. cfDNA (**A**) and cDNA (**B**) of healthy donor template was added at different percentages of the total reaction volume. For each condition the mean concentration of duplicates is shown

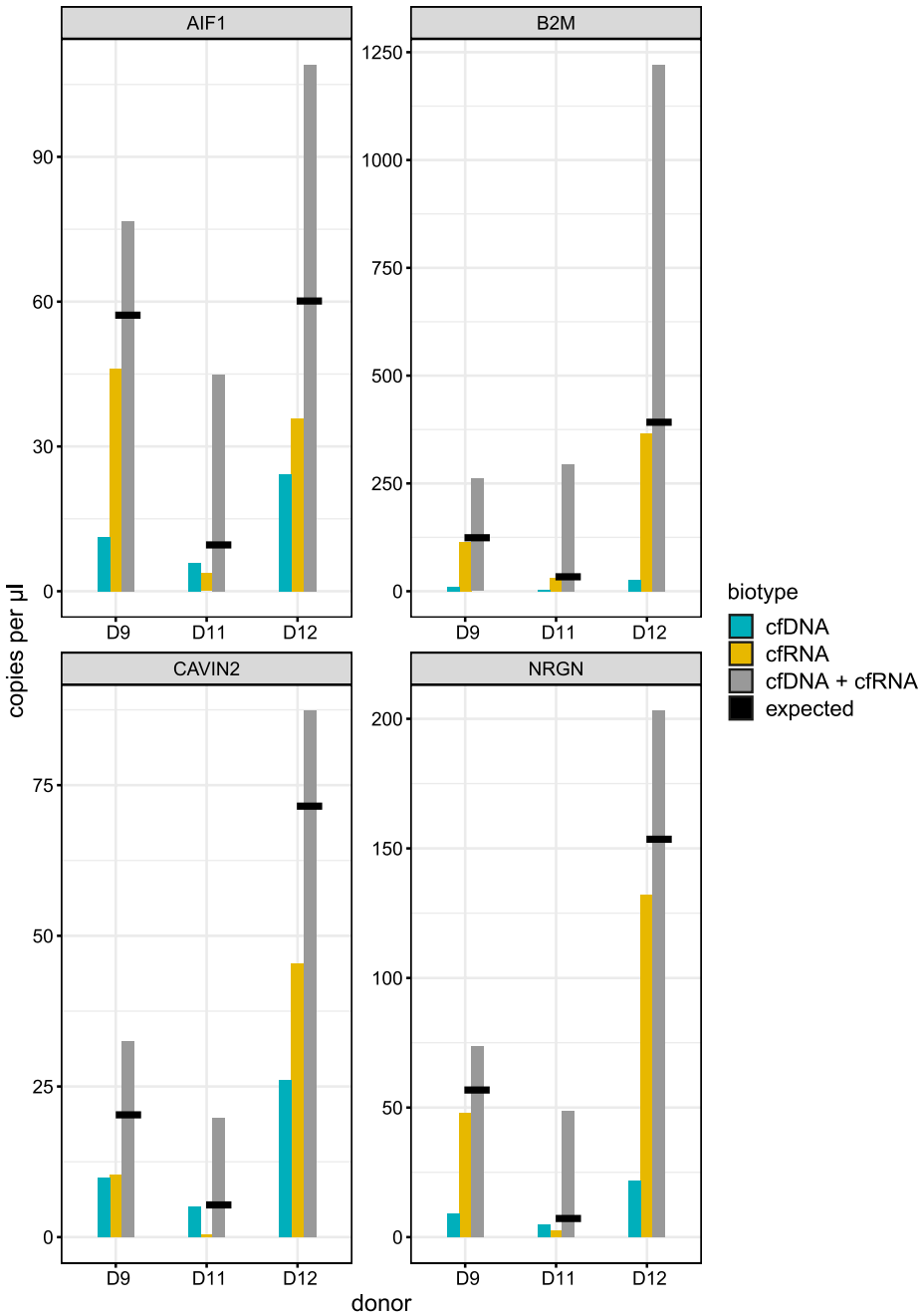

Fig. 6 A combined quantification of nucleic acids results in higher concentrations than the quantification of cfDNA and cfRNA separately in 3 healthy donor plasma samples. Bars show concentrations for cfDNA, cfRNA and jointly measured cfDNA and cfRNA. Horizontal black lines indicate the sum of separately measured cfDNA and cfRNA (theoretical combined concentration)

measured with dPCR assays for both cfDNA and cfRNA, indicating the potential use of extremely low input volumes for the kits tested (MIRA, MAX), e.g., for liquid biopsy analyses in small animal studies. These results should be interpreted with caution, as these low input volumes are below the recommended input volumes by the kit's manufacturer and cfDNA quality cannot be ascertained.

Successful co-purification for all tested kits

By means of our optimized framework, we compared the co-purification efficiency of two manual kits (CCF, MIRA) and two semi-automated kits (MAP, CAT) with different plasma input volumes. For all samples from all kits, a concentration of cfDNA and cfRNA could be measured using the two duplex assays, indicating that all kits successfully co-purified cfDNA and cfRNA. Interestingly, in some cases, a higher eluate concentration for both cfDNA and cfRNA is obtained, by consuming less plasma (e.g., MIRA with 0.6 mL plasma input volume has at least the same eluate concentration for both cfDNA and cfRNA compared to CCF with 1 mL plasma input volume). The different co-purification kits have different eluate volumes that can be adjusted depending on the kit. This should be taken into account depending on the downstream analysis, e.g., highly concentrated eluates may be required. Of note, it is possible to further concentrate the eluate using for instance ultrafiltration columns or nucleic acid precipitation followed by resuspension in a smaller volume. For extractions with the MAPss workflow (2 mL plasma input volume), we encountered problems with the gDNA removal, as our DNase treatment was not compatible with the eluates from the MAP [15]. Extra purification of the eluates with ultrafiltration columns improved the gDNA removal efficiency, but DNA remained present in the samples. Therefore, other gDNA removal protocols should be explored in case MAPss is used for cfRNA-only applications. This example shows the importance to test DNase treatment efficiency to allow for correct quantification of cfRNA.

Increasing detection sensitivity by co-purification

One of the clinically relevant characteristics of cfDNA and cfRNA co-purification is that it allows to increase the detection sensitivity. Detecting mutations in cancer patients' plasma is routinely done using cfDNA, but due to low amounts in blood plasma, existing assays often face sensitivity issues. The analytical sensitivity of mutation detection can be increased by also analyzing cfRNA, at least for genes that are transcribed and for which the mRNA does not undergo non-sense mediated decay [16].

In this study, we have shown that the combined quantification of cfDNA and cfRNA results in a higher signal than their separate quantification. Remarkably, the combined quantification results in a higher concentration compared to the sum of the separate cfDNA/cfRNA concentrations, e.g., the theoretically expected concentration. There are two possible effects in the combined quantification that may in part explain the observed results: (1) no DNase treatment is done on the eluates, omitting any possible negative effects of DNase treatment on cfRNA, and (2) cDNA synthesis may improve cfDNA quantification as well. Nevertheless, these results confirm that quantifying both cfDNA and cfRNA in one single tube leads to an increased sensitivity for the assays included in this study. It is important to note that the added value of combining cfDNA and cfRNA is gene-dependent, meaning that sensitivity will only increase for genes that are sufficiently abundant in the biofluid under investigation.

Conclusions

In this study we provide a framework for dPCR-based quantification of cfDNA and cfRNA that can be used to evaluate the performance of cfDNA/cfRNA co-purification kits. This framework was applied to two manual and two semi-automated co-purification kits. Even more, we demonstrated the added value of the combined co-purification of cfDNA and cfRNA, as combined quantification results in a higher signal compared to separate quantification. Thus, we provide strong evidence that it should be technically feasible to increase mutation detection sensitivity of specific gene targets by co-purification and quantification of cfDNA and cfRNA, which needs to be validated in future studies.

Methods

First, we set up a framework using the dPCR technology to quantify cfDNA and cfRNA from human blood plasma in order to compare cfDNA/cfRNA co-purification kit performance. To that end, we optimized two dPCR duplex assays that are designed to quantify both cfDNA and cfRNA, by ensuring that primers and probes are located within a highly abundant exon. Next, we applied our optimized workflow to evaluate the co-purification performance of two manual and two semi-automated kits using different plasma input volumes (0.06–4 mL).

Donor material and liquid biopsy preparation

Sample collection was approved by the ethics committee of Ghent University Hospital (registration number B670201733701) and written informed consent was obtained from the healthy donors. Venous blood was

collected from healthy donors in 2 different blood collection tubes: BD Vacutainer Plastic K2EDTA tube (EDTA; Becton Dickinson and Company, 367525) and Vacuette Tube 9 mL 9NC Coagulation sodium citrate 3.2% (citrate; Greiner Bio-One, 455322). Immediately after blood draw, blood collection tubes were gently inverted five times and tubes were transported to the laboratory for immediate plasma preparation. Platelet-depleted plasma was prepared within two hours after blood draw, by means of two sequential centrifugation steps (two times 2500*g* for 15 min) on a Centrifuge 5804 (Eppendorf, 5804000013) with Rotor A-4-44 (Eppendorf, 5804709004) and appropriate adapters (Eppendorf, 5804753003). Plasma was snap frozen in liquid nitrogen and stored at − 80 °C immediately after preparation. Hemolysis was assessed by determining the absorbance at 414 nm, i.e., the levels of free heamoglobin, by spectral analysis using a NanoDrop 1000 Spectrophotometer (Thermo Fisher Scientific). Absorbances are ranging from 0.103 to 0.153.

Cell-free nucleic acid extractions

Nucleic acids were extracted with six different commercially available (co-)purification kits by following the manufacturers' manual: (1) miRNeasy Serum/Plasma Advanced Kit (MIRA; Qiagen, 217204), (2) QIAamp ccfDNA/RNA Kit (abbreviated to CCF; Qiagen, 55184), (3) the iCatcher Circulating cfDNA/cfRNA 4000 kit (CatchGene, AC30400) in combination with iCatcher 12 Automated Nucleic Acid Purification System (CAT; CatchGene, IC1200) (4) MagNA Pure 24 Total NA Isolation Kit with the cfNA ss 2000 and cfNA ds 2000 purification protocols (Roche, 07658036001) in combination with the MagNA Pure 24 instrument (MAP; Roche, 07290519001), (5) Maxwell ccfDNA LV Plasma Kit (Promega, AS1480) in combination with the Maxwell RSC Instrument (MAX; Promega, AS4500), and (6) miRNeasy Serum/Plasma Kit (MIR; Qiagen, 217184) (Fig. 1). The MIRA, CCF, MAP and CAT kits were included in the study to examine their capacity to co-purify cfDNA and cfRNA, while MAX and MIR kits served as a reference for cfDNA only and cfRNA only extractions, respectively, as these kits are routinely used in our department for these applications. For each kit, different plasma input volumes, ranging between 0.06 and 4 mL, from two donors (three in case of CAT) were tested with the maximum recommended elution volume (Table 1). Eluates were stored at − 80 °C until further processing.

Eluates of each of the four cfDNA/cfRNA co-purification kits (MIRA, CCF, MAP and CAT) were split in two equal parts, using one part for cfDNA quantification and the other part for cfRNA quantification (Fig. 1). The cfDNA part was immediately used for quantification with digital PCR without any further processing. For the cfRNA part, DNA was removed using HL-dsDNase (ArcticZymes, 70800-202) and Heat & Run 10× Reaction Buffer (ArcticZymes, 66001). Briefly, 1 µl HL-dsDNase and one tenth of the RNA input volume as reaction buffer were added, and incubated for 10 min at 37 °C, followed by 5 min inactivation at 55 °C. Subsequently, reverse transcription was performed using the iScript Advanced cDNA Synthesis Kit for RT-qPCR (Bio-Rad, 1725038) to enable digital PCR-based quantification of the cDNA (~ cfRNA). The full eluate of the MIR kit underwent DNA removal and cDNA synthesis using the same protocol, serving as a cfRNA only control. The volume of the MAX eluate was reduced to 20 µl by means of vacuum centrifugation (Eppendorf, Concentrator Plus, program V-AQ at 30 °C). As previous findings indicated incompatibilities of the MAP elution buffer for downstream DNase treatment [15], and to reduce elution volume, the MAP eluate was further purified and concentrated using Vivacon 500 2000 MWCO Hydrosart ultrafiltration columns (Sartorius, VN01H91) prior to DNA removal [15]. cDNA and cfDNA was stored at − 20 °C until further processing.

Table 1 Overview of plasma input volumes and eluate volumes for each kit and protocol

Kit (purification protocol)	Plasma input volume (mL)	Eluate volume (µl)
MIRA	0.06, 0.2, 0.6	18
CCF	1, 4	18
MAX	0.06, 0.2, 1	20**
MIR	0.06, 0.2	12
MAPss (cfNA ss 2000)	2	24–32***
MAPds (cfNA ds 2000)	2	34–44***
CAT (cfDNA/cfRNA 4000)	2*, 4	17–27

*Diluted to 4 mL with PBS according to instructions of the company (CatchGene), **after vacuum centrifugation, ***after purification with Vivacon columns

Digital PCR assay design

For unbiased quantification of both cfDNA and cfRNA, two digital PCR duplex assays were designed each targeting a single, well covered exon of two highly abundant genes in healthy donor plasma (based on RNA sequencing data from the Extracellular RNA Quality Control study [15]): CAVIN2 (HEX)/NRGN (FAM) and AIF1 (FAM)/B2M (HEX). Designing a primer pair within a single exon allows the usage of the same assay for both cfDNA and cfRNA quantification (Table 2).

Table 2 Primer and probe sequences of the dPCR assays (+N is LNA nucleotide)

Target	Assay component	Sequence (5′ to 3′)	Genomic location amplicon*
NRGN	Forward primer	GTTTCTGATCTCCGTGTGT	chr11:124747135–124747204 (length: 69 bp)
	Reverse primer	CTTGGACATTCCTCTTTATTGTT	
	Probe (HEX)	TGTGACTGTGCTGGGTTGGA	
CAVIN2	Forward primer	GCACAGTTTGTTAATATTGTCTTG	chr2:191834469–191834542 (length: 73 bp)
	Reverse primer	CCTGCCTTTAGTATGAACCA	
	Probe (FAM)	ACT + CTAT + TT + GT + AA + GGTTACTT	
AIF1	Forward primer	AGCGAGAGAAAAGGAAAAGCC	chr6:31616837–31616908 (length: 71 bp)
	Reverse primer	CCTTCAAATCAGGGCAACTCA	
	Probe (FAM)	CCCCCA + GCCAAGAAAG + CTATC	
B2M	Forward primer	GTGGAGCATTCAGACTTGTCT	chr15:44715560–44715658 (length: 98 bp)
	Reverse primer	ACGGCAGGCATACTCATCTT	
	Probe (HEX)	ACA + CTGAATTCACCCCCACTGA	

*Genomic locations based on GRCh38

PCR primers were picked using the Primer3Plus tool (with default settings, except amplicon size range of 60–100 nucleotides [17]). The performance of the primers was thoroughly evaluated in silico. To determine the primer specificity, BiSearch e-PCR (with default settings, except for mismatch string: 1233333333333333 [18]) and the UCSC tool [19] were used. Subsequently, the OligoEvaluator tool [20] was used to check for secondary structure formation and GC content. Lastly, the SBT tool [21] was used to predict the melting temperature (Tm). The hydrolysis probe sequence was picked manually in between forward and reverse primer, aiming for a Tm of at least 3 °C higher than the primers' Tm. Primers and probes were ordered with Integrated DNA Technologies (IDT, Leuven, Belgium). Probes were ordered as double-quenched hydrolysis probes with optional LNA nucleotides to enhance the Tm and purified by HPLC. Primers were purified by standard desalting. All oligonucleotides were resuspended in TE buffer (10 mM Tris–HCl (pH 8.0), 0.1 mM EDTA) to 100 µM (primers) and 10 µM (probes) and stored at − 20 °C. The primer efficiency and specificity was also validated on a dilution series of Quantitative PCR Human Reference Total RNA (Agilent technologies, 750500), reverse transcribed to cDNA.

Quantification of cfDNA and cfRNA using dPCR

Digital PCR was performed using the QX100 Droplet Digital PCR system (Bio-Rad, California, USA), according to the manufacturer's protocol with minor modifications (250 nM primer and 100 nM probe reaction mix concentration). Each 20 µl dPCR reaction contains 10 µl 2 × ddPCR Supermix for Probes (Bio-Rad, 1863010), 2 µl of primer and probe mix (with a total of 4 primers and 2 probes per duplex assay) and 2—8 µl template. After pipetting 20 µl sample mix and 70 µl droplet generation oil (Bio-Rad, 1863005) in the cartridge (Bio-Rad, 1864008), droplets were generated by means of the Bio-Rad QX100 Droplet Generator. Droplets were then transferred from the cartridge to a 96-well plate (Bio-Rad, 12001925) and a thermocycling program was performed on a C1000 Touch Thermal cycler (Bio-Rad): 95 °C for 10 min, followed by 40 cycles of 15 s on 95 °C and 1 min at 56.9 °C (optimized annealing temperature for both duplexes by means of a gradient dPCR). Finally, reactions were heated to 98 °C for 10 min and then cooled down to 12 °C before transferring the plate to the QX100 Droplet Reader (Bio-Rad). Each plate also included a positive control (PC) and negative no template control (NTC). QuantaSoft Analysis Pro Software Version 1.3.2.0 was used to calculate the number of copies per µl in the dPCR reaction by manual thresholding, followed by copies per µl eluate concentration determination (Additional file 6: Fig. S3) to enable comparison among kits.

Combined quantification of cfDNA and cfRNA

To determine the added value of the combined analysis of cfDNA and cfRNA, separate quantification of cfDNA and cfRNA was compared to combined quantification of both. As this is a proof-of-principle experiment, only one kit (MIRA0.06) was used to co-purify nucleic acids from plasma of three healthy donors (platelet-free plasma). Eluates were split into three equal parts to quantify cfDNA, cfRNA and cfDNA/cfRNA using the two dPCR duplex assays (Additional file 7: Fig. S4). For cfDNA/cfRNA combined quantification, only cDNA synthesis was performed on the eluate, as such containing both cfDNA and cDNA, while for cfRNA only quantification,

a DNase treatment was performed prior to cDNA synthesis. For cfDNA quantification, the eluate remained untouched.

Abbreviations
CAT: iCatcher Circulating cfDNA/cfRNA 4000 kit; CCF: QIAamp ccfDNA/RNA Kit; cfDNA: Cell-free DNA; cfRNA: Cell-free RNA; dPCR: Digital PCR; EVs: Extracellular vesicles; HMW: High molecular weight; MAPss: MagNA Pure 24 Total NA Isolation Kit with the cfNA ss 2000; MAPds: MagNA Pure 24 Total NA Isolation Kit with the cfNA ds 2000; MAX: Maxwell ccfDNA LV Plasma Kit; MIR: miRNeasy Serum/Plasma Kit; MIRA: miRNeasy Serum/Plasma Advanced kit.

Supplementary Information

The online version contains supplementary material available at https://doi.org/10.1186/s40246-022-00446-4.

Additional file 1: Figure S1. Efficiency of DNase treatment after cfDNA/cfRNA (co-)purification. Efficiency was assessed with the NRGN assay only. Error bars indicate standard error. Quantifications for CAT2, MAPss2 and MAPds2 are based on one replicate.

Additional file 2: Table S1. Additional kit characteristics and remarks

Additional file 3: Table S2. Comparison of expected and measured cfDNA or cfRNA concentration ratio, based on plasma input volume, within a given nucleic acid extraction kit.

Additional file 4: Table S3. Concentration (geometric mean of four assays) and yield (concentration multiplied by eluate volume) in the eluates from the kits with the different tested input volumes. Relative concentrations and yield were determined by rescaling to the highest value.

Additional file 5: Figure S2. Overview of TapeStation results. Results from TapeStation of all cfDNA samples purified with one of the six (co-)purification kits. There are 13/46 samples that have concentrations below LOD (20 pg/µl), and 2/46 samples without any peaks (flat profiles). For 1/46 samples there was not enough material left for TapeStation.

Additional file 6: Figure S3. Detailed description of laboratory workflow. Workflow used to determine co-purification performance of each kit and subsequent calculations to determine the concentrations in each eluate: (A) MIRA and CCF, (B) MIR, (C) CAT, (D) MAX, and (E) MAP.

Additional file 7: Figure S4. Experimental overview of a combined cfDNA/cfRNA quantification and a parallel quantification of cfDNA and cfRNA.

Author contributions
The authors wish it to be known that, in their opinion, JD and KS should be regarded as joint First Authors. Author contributions are reported according to the CRediT taxonomy [22]. Conceptualization: ADec, JD, JVa, KS. Methodology: JD, JVa, KS. Software: JD, KS. Validation: JD, KS. Formal analysis: JD, KS, KV. Investigation: ADen, JD, JVe, KS, KV, SR. Data curation: JD, KS. Writing—original draft: JD, KS. Writing—review and editing: ADec, ADen, BDW, JD, JVa, JVe, KDP, KS, KV, SR, TVM. Visualization: JD, KS. Supervision: JVa. Project administration: ADec, JD, KS. Funding acquisition: ADec, BDW, JD, JVa, KDP, KS, TVM. All authors read and approved the final manuscript.

Funding
This work was supported by Kom op tegen Kanker [Stand up to Cancer, the Flemish cancer society, Grant to BDW and 2022/13037 to KS]; the Ghent University Special Research Fund [Grant to AD, GOA Gent-Lung, BOF22/CDV/077 to JD and BDW]; Foundation Against Cancer [STK, 2018-092 to BDW and TVM] and the Research Foundation—Flanders [Grant No. G0B2820N to JV, LIQUIDHOPE TRANSCAN-2 project, 1224021N to AD, senior clinical researcher Grant to BDW]. Funding for open access charge: the Research Foundation—Flanders. Funding resources did not influence the study design and results.

Availability of data and materials
The raw data are available on reasonable request from the corresponding author.

Declarations

Ethics approval and consent to participate
Sample collection was approved by the ethics committee of Ghent University Hospital (registration number B670201733701) and written informed consent was obtained from the healthy donors.

Consent for publication
The authors approve the publication of this manuscript.

Competing interests
The authors declare that they have no competing interests.

Author details
[1]OncoRNALab, Cancer Research Institute Ghent (CRIG), Ghent, Belgium. [2]Department of Biomolecular Medicine, Ghent University, Ghent, Belgium. [3]Translational Oncogenomics and Bioinformatics Lab, Cancer Research Institute Ghent (CRIG), Ghent, Belgium. [4]Center for Medical Biotechnology, VIB-UGent, Ghent, Belgium. [5]Department of Paediatric Haematology Oncology and Stem Cell Transplantation, Ghent University Hospital, Ghent, Belgium. [6]Department of Laboratory Medicine, AZ Groeninge, Kortrijk, Belgium.

Received: 6 October 2022 Accepted: 19 December 2022
Published online: 31 December 2022

References

1. Aleksakhina SN, Imyanitov EN. Cancer therapy guided by mutation tests: current status and perspectives. Int J Mol Sci. 2021;22:10931.
2. Martins I, Ribeiro IP, Jorge J, Gonçalves AC, Sarmento-Ribeiro AB, Melo JB, et al. Liquid biopsies: applications for cancer diagnosis and monitoring. Genes. 2021;12:1–20.
3. Bratulic S, Gatto F, Nielsen J. The translational status of cancer liquid biopsies. Regen Eng Transl Med. 2021;7(3):312–52.
4. Marrugo-Ramírez J, Mir M, Samitier J. Blood-based cancer biomarkers in liquid biopsy: a promising non-invasive alternative to tissue biopsy. Int J Mol Sci. 2018;19:2877.
5. Lone SN, Nisar S, Masoodi T, Singh M, Rizwan A, Hashem S, et al. Liquid biopsy: a step closer to transform diagnosis, prognosis and future of cancer treatments. Mol Cancer. 2022;21:1–22.
6. van Paemel R, Vlug R, de Preter K, van Roy N, Speleman F, Willems L, et al. The pitfalls and promise of liquid biopsies for diagnosing and treating solid tumors in children: a review. Eur J Pediatr. 2020;179:191–202.
7. Frank MS, Fuß J, Steiert TA, Streleckiene G, Gehl J, Forster M. Quantifying sequencing error and effective sequencing depth of liquid biopsy NGS with UMI error correction. Biotechniques. 2021;70(4):227–32.
8. Krug AK, Enderle D, Karlovich C, Priewasser T, Bentink S, Spiel A, et al. Improved EGFR mutation detection using combined exosomal RNA and circulating tumor DNA in NSCLC patient plasma. Ann Oncol. 2018;29(3):700–6.
9. Larson MH, Pan W, Kim HJ, Mauntz RE, Stuart SM, Pimentel M, et al. A comprehensive characterization of the cell-free transcriptome reveals tissue- and subtype-specific biomarkers for cancer detection. Nat Commun. 2021;12(1):1–11.
10. Castellanos-Rizaldos E, Grimm DG, Tadigotla V, Hurley J, Healy J, Neal PL, et al. Exosome-based detection of EGFR T790M in plasma from non-small cell lung cancer patients. Clin Cancer Res. 2018;24(12):2944–50.
11. Möhrmann L, Huang HJ, Hong DS, Tsimberidou AM, Fu S, Piha-Paul SA, et al. Liquid biopsies using plasma exosomal nucleic acids and plasma cell-free DNA compared with clinical outcomes of patients with advanced cancers. Clin Cancer Res. 2018;24(1):181–8.
12. van Deun J, Mestdagh P, Sormunen R, Cocquyt V, Vermaelen K, Vandesompele J, et al. The impact of disparate isolation methods for extracellular vesicles on downstream RNA profiling. J Extracell Vesicles. 2014;3(1):24858.
13. König L, Kasimir-Bauer S, Bittner AK, Hoffmann O, Wagner B, Santos Manvailer LF, et al. Elevated levels of extracellular vesicles are associated with therapy failure and disease progression in breast cancer

patients undergoing neoadjuvant chemotherapy. Oncoimmunology. 2018;7(1):e1376153.
14. Sidstedt M, Rådström P, Hedman J. PCR inhibition in qPCR, dPCR and MPS—mechanisms and solutions. Anal Bioanal Chem. 2020;412:2009–23.
15. Anckaert J, Avila Cobos F, Decock A, Deleu J, de Wever O, de Wilde J, et al. Performance of RNA purification kits and blood collection tubes in the Extracellular RNA Quality Control (exRNAQC) study. bioRxiv [Internet]. 2021;2021.05.11.442610. Available from: http://biorxiv.org/content/early/2021/05/11/2021.05.11.442610.abstract
16. Hug N, Longman D, Cáceres JF. Mechanism and regulation of the nonsense-mediated decay pathway. Nucl Acids Res. 2015;44:1483–95.
17. Primer3Plus tool. https://www.primer3plus.com. Accessed 7 October 2020.
18. BiSearch Primer Design and Search Tool. http://bisearch.enzim.hu. Accessed 7 October 2020.
19. UCSC In-Silico PCR. https://genome.ucsc.edu/cgi-bin/hgPcr. Accessed 7 October 2020.
20. OligoEvaluator tool. http://www.oligoevaluator.com/OligoCalcServlet. Accessed 7 October 2020.
21. SBT tool. https://masckareem.shinyapps.io/sbtmodel/. Accessed 7 October 2020.
22. Brand A, Allen L, Altman M, Hlava M, Scott J. Beyond authorship: attribution, contribution, collaboration, and credit. Learned Publishing. 2015;28(2):151–5.

Publisher's Note

SUPPLEMENTAL FIGURES

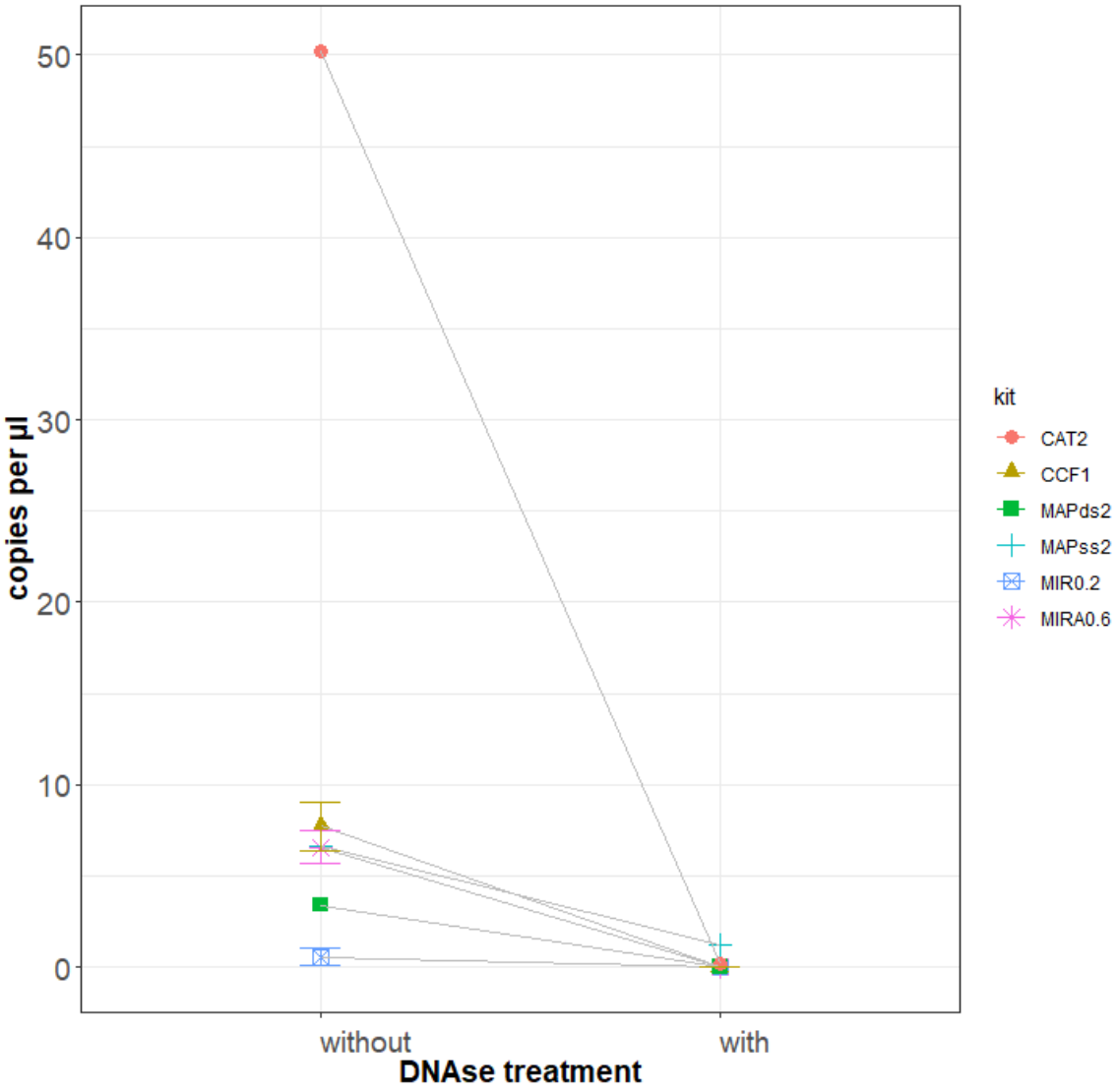

Supplemental Figure 1. Efficiency of DNase treatment after cfDNA/cfRNA (co-)purification. Efficiency was assessed with the NRGN assay only. Error bars indicate standard error. Quantifications for CAT2, MAPss2 and MAPds2 are based on one replicate.

D1_EDTA_CCF_1

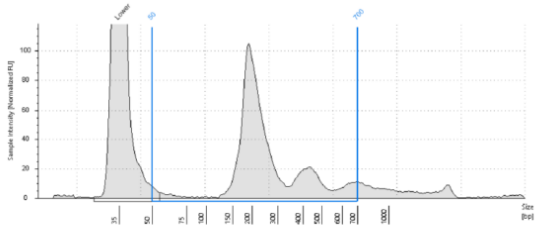

Region Table

From [bp]	To [bp]	Average Size [bp]	Conc. [pg/µl]	Region Molarity [pmol/l]	%of Total	Region Comment	Color
50	700	271	147	1090	85.67	%cfDNA	

D1_EDTA_CCF_4

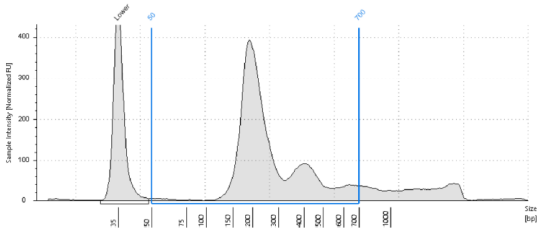

Region Table

From [bp]	To [bp]	Average Size [bp]	Conc. [pg/µl]	Region Molarity [pmol/l]	%of Total	Region Comment	Color
50	700	275	689	4650	82.62	%cfDNA	

D1_EDTA_MIRA_0.06 (<LOD)

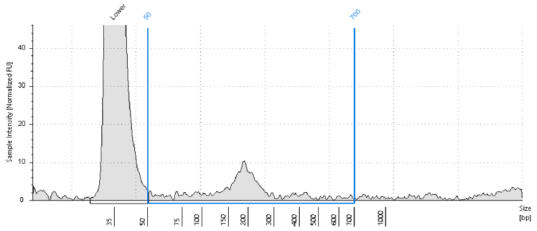

Region Table

From [bp]	To [bp]	Average Size [bp]	Conc. [pg/µl]	Region Molarity [pmol/l]	%of Total	Region Comment	Color
50	700	213	16.4	211	74.00	%cfDNA	

D1_EDTA_MIRA_0.2

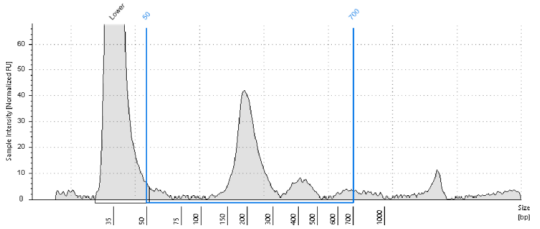

Region Table

From [bp]	To [bp]	Average Size [bp]	Conc. [pg/µl]	Region Molarity [pmol/l]	%of Total	Region Comment	Color
50	700	245	55.1	485	81.13	%cfDNA	

D1_EDTA_MIRA_0.6

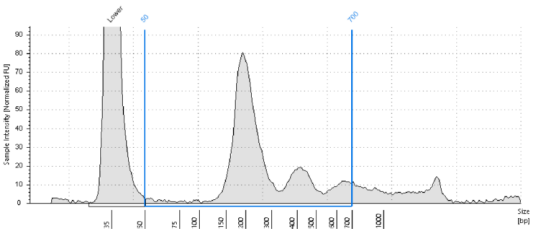

Region Table

From [bp]	To [bp]	Average Size [bp]	Conc. [pg/µl]	Region Molarity [pmol/l]	%of Total	Region Comment	Color
50	700	278	137	971	80.28	%cfDNA	

D1_CITR_CCF_1

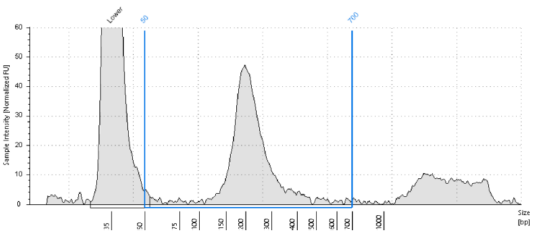

Region Table

From [bp]	To [bp]	Average Size [bp]	Conc. [pg/µl]	Region Molarity [pmol/l]	%of Total	Region Comment	Color
50	700	231	72.3	601	70.30	%cfDNA	

D1_CITR_CCF_4

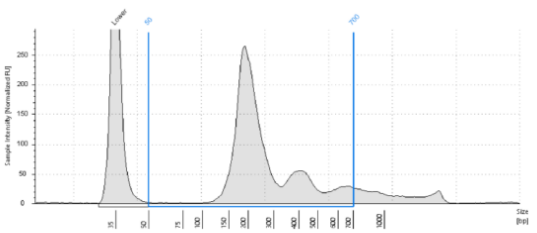

Region Table

From [bp]	To [bp]	Average Size [bp]	Conc. [pg/µl]	Region Molarity [pmol/l]	%of Total	Region Comment	Color
50	700	273	456	3070	86.77	%cfDNA	

D1_CITR_MIRA_0.06 (<LOD)

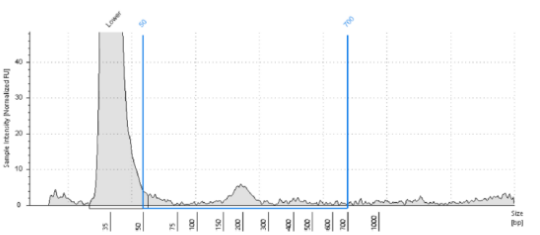

Region Table

From [bp]	To [bp]	Average Size [bp]	Conc. [pg/µl]	Region Molarity [pmol/l]	%of Total	Region Comment	Color
50	700	227	7.80	150	62.04	%cfDNA	

D1_CITR_MIRA_0.2

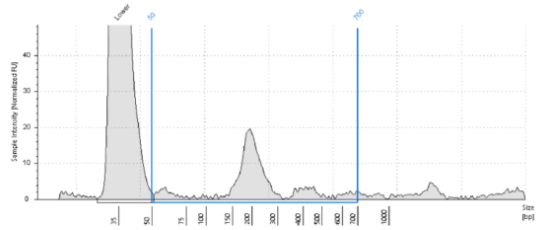

Region Table

From [bp]	To [bp]	Average Size [bp]	Conc. [pg/µl]	Region Molarity [pmol/l]	%of Total	Region Comment	Color
50	700	241	27.0	262	75.63	%cfDNA	

D1_CITR_MIRA_0.6

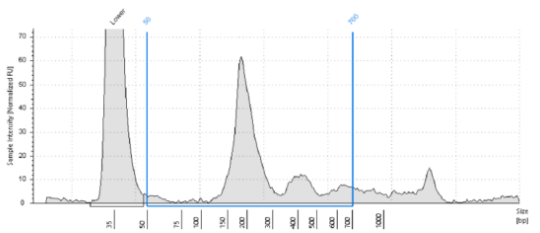

Region Table

From [bp]	To [bp]	Average Size [bp]	Conc. [pg/µl]	Region Molarity [pmol/l]	%of Total	Region Comment	Color
50	700	266	93.0	717	77.85	%cfDNA	

D2_EDTA_CCF_1

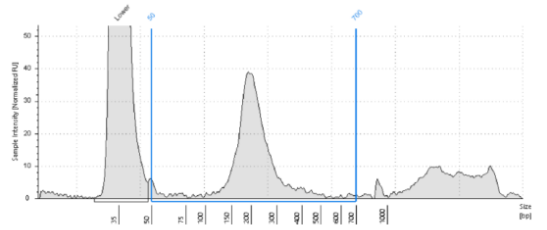

Region Table

From [bp]	To [bp]	Average Size [bp]	Conc. [pg/µl]	Region Molarity [pmol/l]	%of Total	Region Comment	Color
50	700	221	59.0	510	63.74	%cfDNA	

D2_EDTA_CCF_4

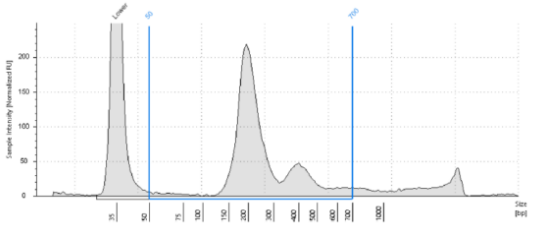

Region Table

From [bp]	To [bp]	Average Size [bp]	Conc. [pg/µl]	Region Molarity [pmol/l]	%of Total	Region Comment	Color
50	700	260	323	2320	84.36	%cfDNA	

D2_EDTA_MIRA_0.06 (<LOD)

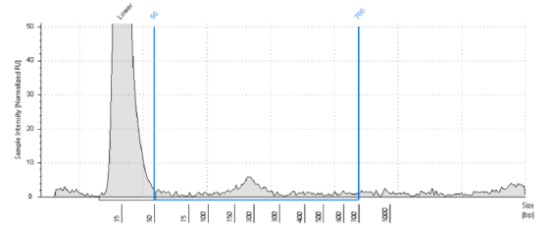

Region Table

From [bp]	To [bp]	Average Size [bp]	Conc. [pg/µl]	Region Molarity [pmol/l]	%of Total	Region Comment	Color
50	700	242	10.8	141	55.79	%cfDNA	

D2_EDTA_MIRA_0.2 (<LOD)

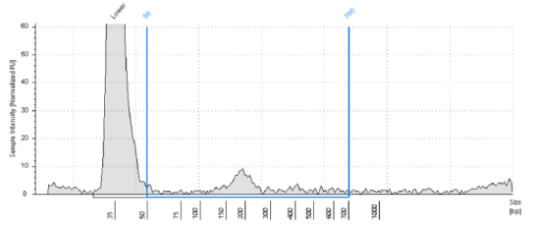

Region Table

From [bp]	To [bp]	Average Size [bp]	Conc. [pg/µl]	Region Molarity [pmol/l]	%of Total	Region Comment	Color
50	700	253	15.7	181	62.57	%cfDNA	

D2_EDTA_MIRA_0.6

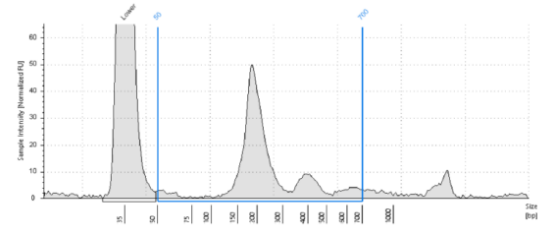

Region Table

From [bp]	To [bp]	Average Size [bp]	Conc. [pg/µl]	Region Molarity [pmol/l]	%of Total	Region Comment	Color
50	700	250	67.4	555	84.25	%cfDNA	

D2_CITR_CCF_1

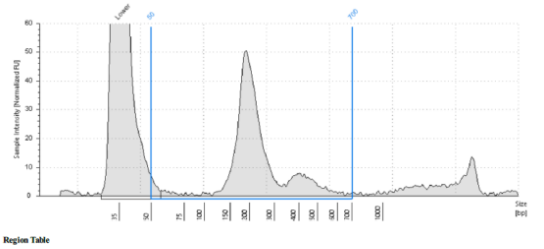

Region Table

From [bp]	To [bp]	Average Size [bp]	Conc. [pg/µl]	Region Molarity [pmol/l]	%of Total	Region Comment	Color
50	700	243	68.3	576	78.86	%cfDNA	

D2_CITR_CCF_4

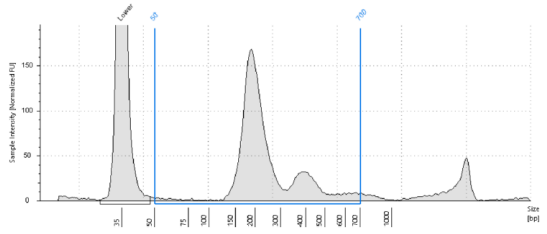

Region Table

From [bp]	To [bp]	Average Size [bp]	Conc. [pg/µl]	Region Molarity [pmol/l]	%of Total	Region Comment	Color
50	700	252	254	1850	83.49	%cfDNA	

D2_CITR_MIRA_0.06 (<LOD)

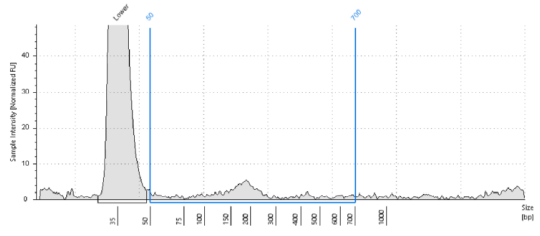

Region Table

From [bp]	To [bp]	Average Size [bp]	Conc. [pg/µl]	Region Molarity [pmol/l]	%of Total	Region Comment	Color
50	700	231	11.4	148	60.08	%cfDNA	

D2_CITR_MIRA_0.2

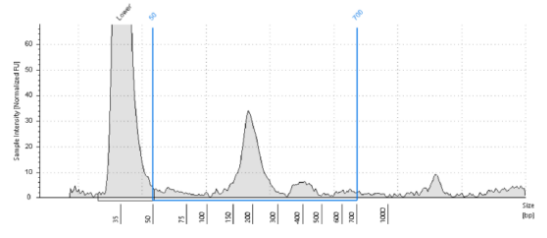

Region Table

From [bp]	To [bp]	Average Size [bp]	Conc. [pg/µl]	Region Molarity [pmol/l]	%of Total	Region Comment	Color
50	700	234	41.8	428	79.41	%cfDNA	

D2_CITR_MIRA_0.6

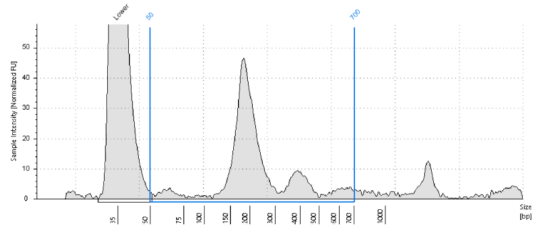

Region Table

From [bp]	To [bp]	Average Size [bp]	Conc. [pg/µl]	Region Molarity [pmol/l]	%of Total	Region Comment	Color
50	700	243	65.3	563	80.19	%cfDNA	

D1_EDTA_MAX_0.06 (<LOD)

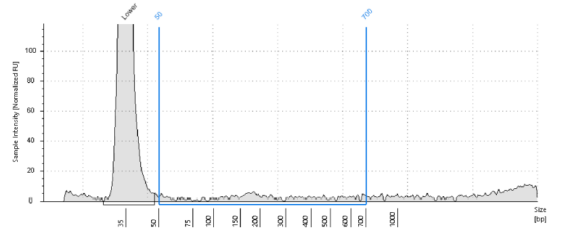

Region Table

From [bp]	To [bp]	Average Size [bp]	Conc. [pg/µl]	Region Molarity [pmol/l]	%of Total	Region Comment	Color
50	700	280	15.0	212	34.80	%cfDNA	

D1_EDTA_MAX_0.2

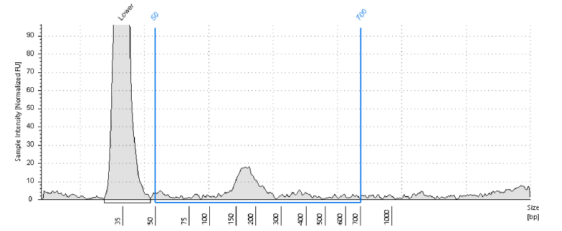

Region Table

From [bp]	To [bp]	Average Size [bp]	Conc. [pg/µl]	Region Molarity [pmol/l]	%of Total	Region Comment	Color
50	700	221	29.7	374	65.29	%cfDNA	

D1_EDTA_MAX_1

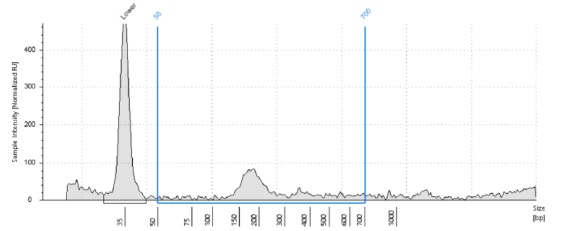

Region Table

From [bp]	To [bp]	Average Size [bp]	Conc. [pg/µl]	Region Molarity [pmol/l]	%of Total	Region Comment	Color
50	700	261	138	1510	64.82	%cfDNA	

D1_CITR_MAX_0.06 (<LOD)

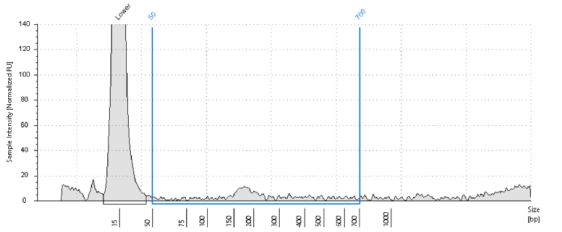

Region Table

From [bp]	To [bp]	Average Size [bp]	Conc. [pg/µl]	Region Molarity [pmol/l]	%of Total	Region Comment	Color
50	700	261	18.8	278	42.69	%cfDNA	

D1_CITR_MAX_0.2

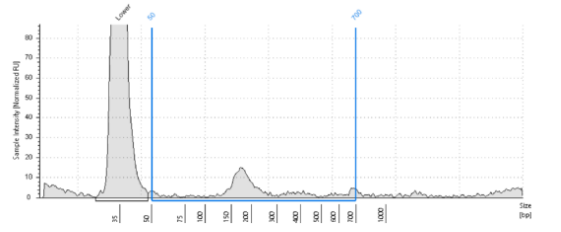

Region Table

From [bp]	To [bp]	Average Size [bp]	Conc. [pg/µl]	Region Molarity [pmol/l]	%of Total	Region Comment	Color
50	700	255	22.5	236	69.20	%cfDNA	

D1_CITR_MAX_1

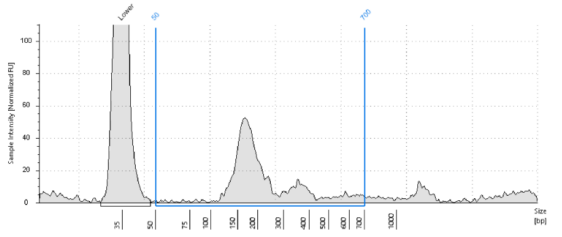

Region Table

From [bp]	To [bp]	Average Size [bp]	Conc. [pg/µl]	Region Molarity [pmol/l]	%of Total	Region Comment	Color
50	700	241	88.1	761	76.99	%cfDNA	

D2_EDTA_MAX_0.06 (flat profile)

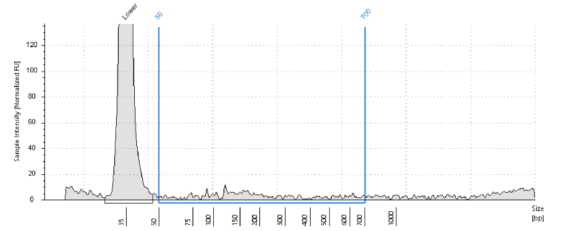

Region Table

From [bp]	To [bp]	Average Size [bp]	Conc. [pg/µl]	Region Molarity [pmol/l]	%of Total	Region Comment	Color
50	700	242	21.3	307	47.51	%cfDNA	

D2_EDTA_MAX_0.2 (flat profile)

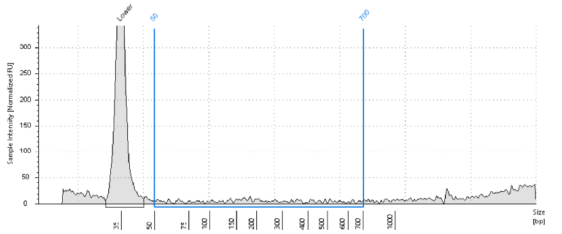

Region Table

From [bp]	To [bp]	Average Size [bp]	Conc. [pg/µl]	Region Molarity [pmol/l]	%of Total	Region Comment	Color
50	700	260	28.0	530	21.42	%cfDNA	

D2_EDTA_MAX_1

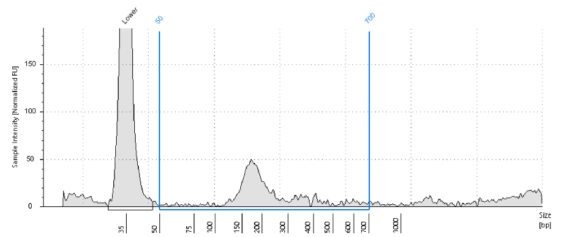

Region Table

From [bp]	To [bp]	Average Size [bp]	Conc. [pg/µl]	Region Molarity [pmol/l]	%of Total	Region Comment	Color
50	700	243	73.1	723	66.62	%cfDNA	

D2_CITR_MAX_0.06 (<LOD)

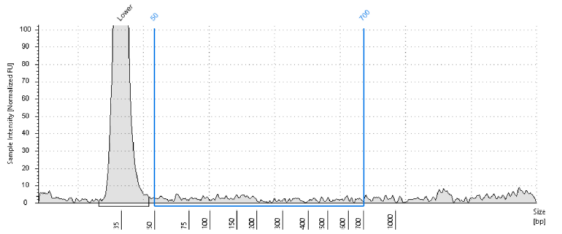

Region Table

From [bp]	To [bp]	Average Size [bp]	Conc. [pg/µl]	Region Molarity [pmol/l]	%of Total	Region Comment	Color
50	700	239	11.9	272	37.58	%cfDNA	

D2_CITR_MAX_0.2 (<LOD)

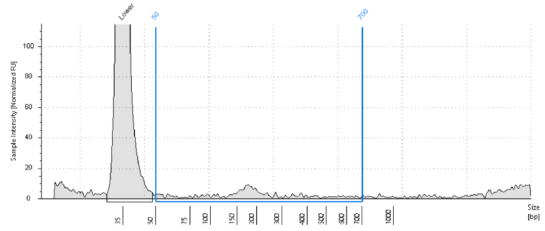

Region Table

From [bp]	To [bp]	Average Size [bp]	Conc. [pg/µl]	Region Molarity [pmol/l]	%of Total	Region Comment	Color
50	700	231	4.71	235	37.78	%cfDNA	

D2_CITR_MAX_1

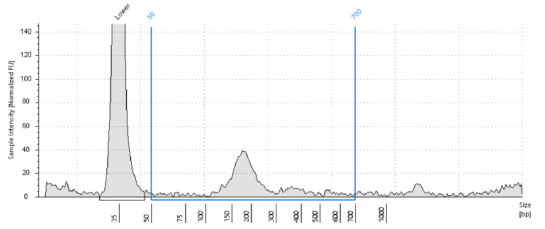

Region Table

From [bp]	To [bp]	Average Size [bp]	Conc. [pg/µl]	Region Molarity [pmol/l]	%of Total	Region Comment	Color
50	700	232	57.9	662	73.79	%cfDNA	

D1_CITR_MAPss_2 (<LOD)

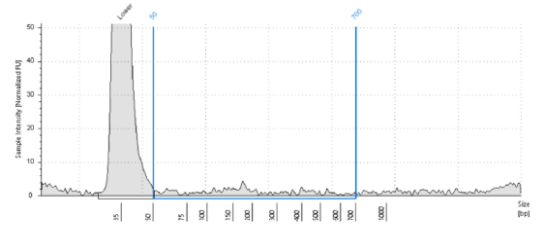

Region Table

From [bp]	To [bp]	Average Size [bp]	Conc. [pg/µl]	Region Molarity [pmol/l]	%of Total	Region Comment	Color
50	700	234	4.00	124	44.60	%cfDNA	

D2_CITR_MAPss_2 (<LOD)

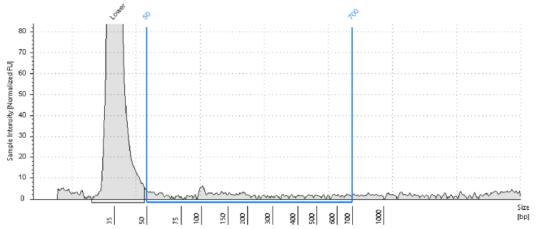

Region Table

From [bp]	To [bp]	Average Size [bp]	Conc. [pg/µl]	Region Molarity [pmol/l]	%of Total	Region Comment	Color
50	700	233	3.46	186	48.45	%cfDNA	

D1_EDTA_MAPss_2 (<LOD)

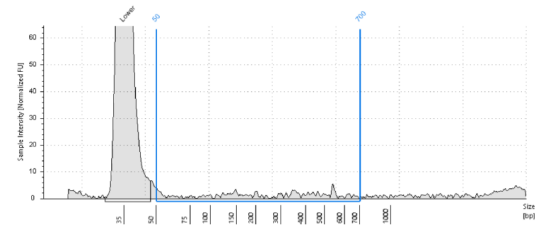

Region Table

From [bp]	To [bp]	Average Size [bp]	Conc. [pg/µl]	Region Molarity [pmol/l]	%of Total	Region Comment	Color
50	700	290	5.35	116	43.69	%cfDNA	

D2_EDTA_MAPss_2 (<LOD)

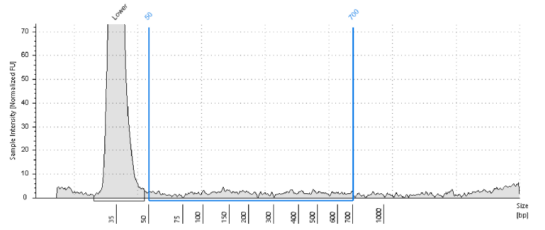

Region Table

From [bp]	To [bp]	Average Size [bp]	Conc. [pg/µl]	Region Molarity [pmol/l]	%of Total	Region Comment	Color
50	700	275	8.80	192	51.36	%cfDNA	

D1_CITR_MAPds_2

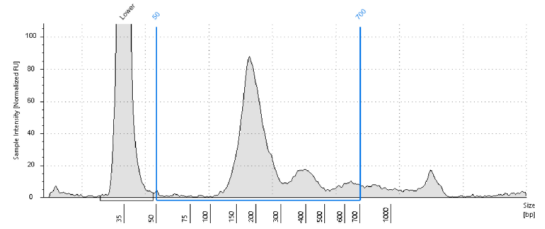

Region Table

From [bp]	To [bp]	Average Size [bp]	Conc. [pg/µl]	Region Molarity [pmol/l]	%of Total	Region Comment	Color
50	700	258	150	1170	85.51	%cfDNA	

D2_CITR_MAPds_2

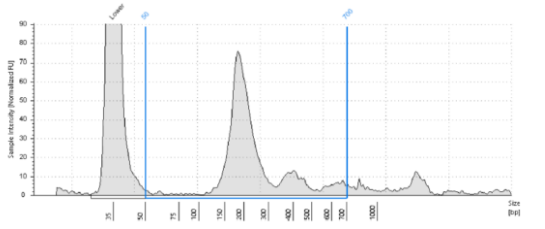

Region Table

From [bp]	To [bp]	Average Size [bp]	Conc. [pg/µl]	Region Molarity [pmol/l]	%of Total	Region Comment	Color
50	700	253	109	865	86.37	%cfDNA	

D1_EDTA_MAPds_2

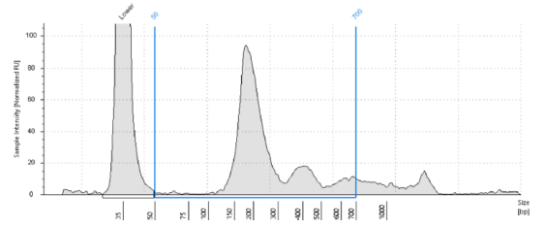

Region Table

From [bp]	To [bp]	Average Size [bp]	Conc. [pg/µl]	Region Molarity [pmol/l]	%of Total	Region Comment	Color
50	700	263	155	1160	85.61	%cfDNA	

D2_EDTA_MAPds_2

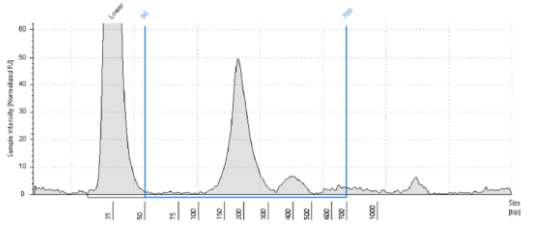

Region Table

From [bp]	To [bp]	Average Size [bp]	Conc. [pg/µl]	Region Molarity [pmol/l]	%of Total	Region Comment	Color
50	700	235	58.4	491	89.46	%cfDNA	

D1(PLA016740)_EDTA_CAT_4

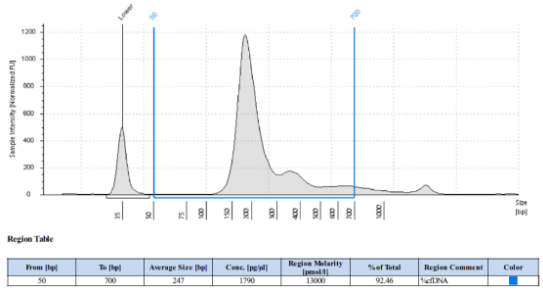

Region Table

From [bp]	To [bp]	Average Size [bp]	Conc. [pg/µl]	Region Molarity [pmol/l]	%of Total	Region Comment	Color
50	700	247	1790	13000	92.46	%cfDNA	

D2(PLA016741)_EDTA_CAT_4

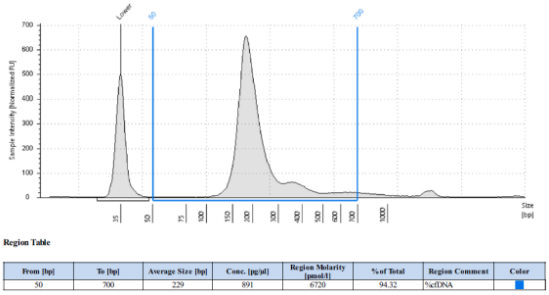

Region Table

From [bp]	To [bp]	Average Size [bp]	Conc. [pg/µl]	Region Molarity [pmol/l]	%of Total	Region Comment	Color
50	700	229	891	6720	94.32	%cfDNA	

D3(PLA016768)_EDTA_CAT_4

Not enough material left for TapeStation

D1(PLA016740)_EDTA_CAT_2

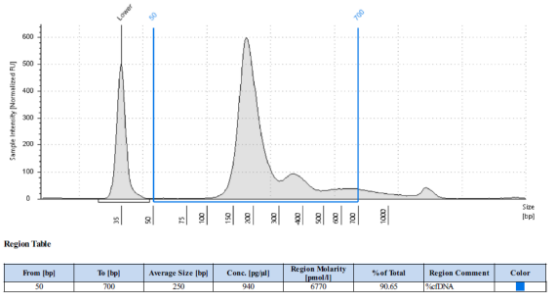

Region Table

From [bp]	To [bp]	Average Size [bp]	Conc. [pg/µl]	Region Molarity [pmol/l]	%of Total	Region Comment	Color
50	700	250	940	6770	90.65	%cfDNA	

D2(PLA016741)_EDTA_CAT_2

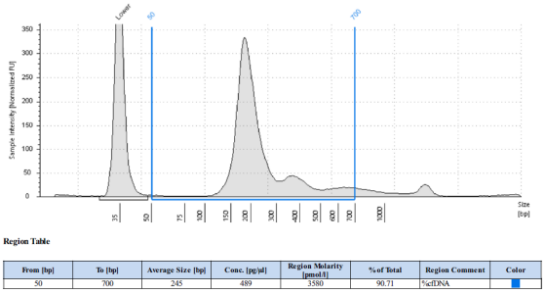

Region Table

From [bp]	To [bp]	Average Size [bp]	Conc. [pg/µl]	Region Molarity [pmol/l]	%of Total	Region Comment	Color
50	700	245	489	3580	90.71	%cfDNA	

D3(PLA016768)_EDTA_CAT_2

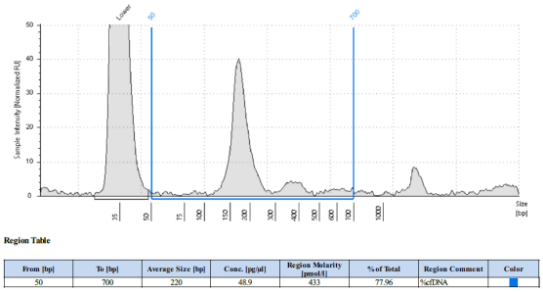

Region Table

From [bp]	To [bp]	Average Size [bp]	Conc. [pg/µl]	Region Molarity [pmol/l]	%of Total	Region Comment	Color
50	700	220	48.9	433	77.96	%cfDNA	

Supplemental Figure 2. Overview of TapeStation results. Results from TapeStation of all cfDNA samples purified with one of the six (co-)purification kits. There are 13/46 samples that have concentrations below LOD (20 pg/µl), and 2/46 samples without any peaks (flat profiles). For 1/46 samples there was not enough material left for TapeStation.

A

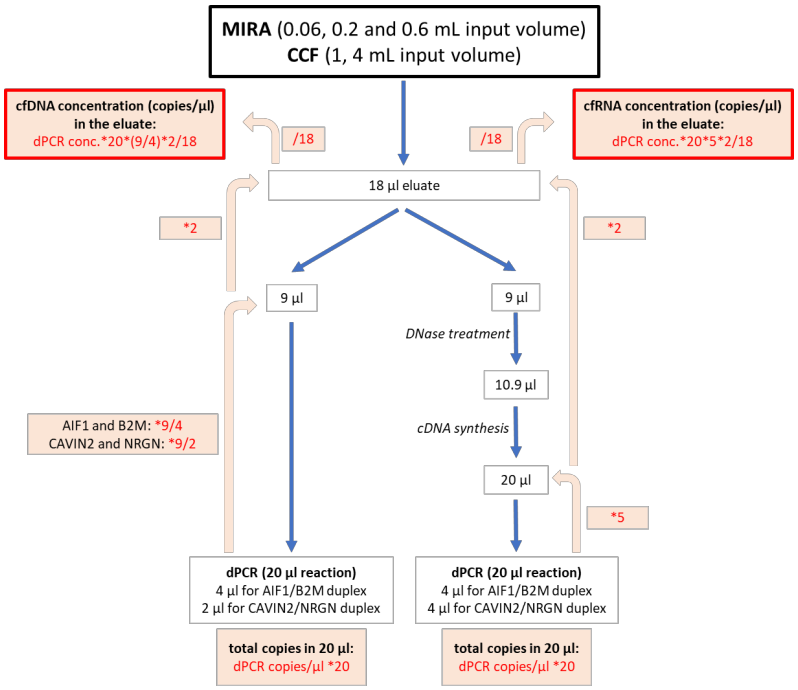
MIRA (0.06, 0.2 and 0.6 mL input volume)
CCF (1, 4 mL input volume)
cfDNA concentration (copies/µl) in the eluate: dPCR conc.*20*(9/4)*2/18
/18
/18
cfRNA concentration (copies/µl) in the eluate: dPCR conc.*20*5*2/18
18 µl eluate
*2
*2
9 µl
9 µl
DNase treatment
10.9 µl
cDNA synthesis
20 µl
*5
AIF1 and B2M: *9/4
CAVIN2 and NRGN: *9/2
dPCR (20 µl reaction)
4 µl for AIF1/B2M duplex
2 µl for CAVIN2/NRGN duplex
total copies in 20 µl: dPCR copies/µl *20
dPCR (20 µl reaction)
4 µl for AIF1/B2M duplex
4 µl for CAVIN2/NRGN duplex
total copies in 20 µl: dPCR copies/µl *20

B

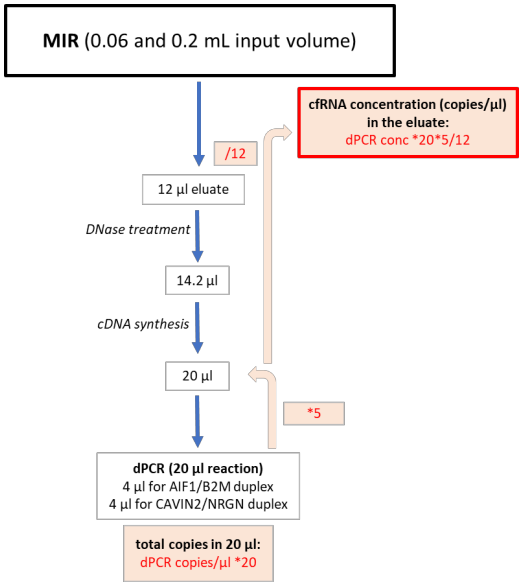
MIR (0.06 and 0.2 mL input volume)
cfRNA concentration (copies/µl) in the eluate: dPCR conc *20*5/12
/12
12 µl eluate
DNase treatment
14.2 µl
cDNA synthesis
20 µl
*5
dPCR (20 µl reaction)
4 µl for AIF1/B2M duplex
4 µl for CAVIN2/NRGN duplex
total copies in 20 µl: dPCR copies/µl *20

C

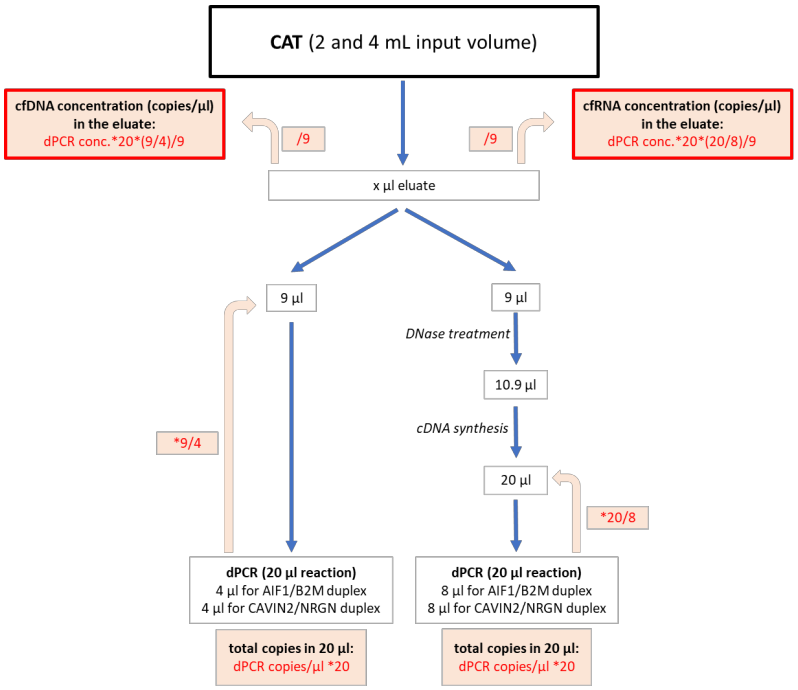

CAT2	
sample	**x**
D1 (EDTA)	19 µl
D2 (EDTA)	19 µl
D3 (EDTA)	27 µl

CAT4	
sample	**x**
D1 (EDTA)	21 µl
D2 (EDTA)	23 µl
D3 (EDTA)	18 µl

D

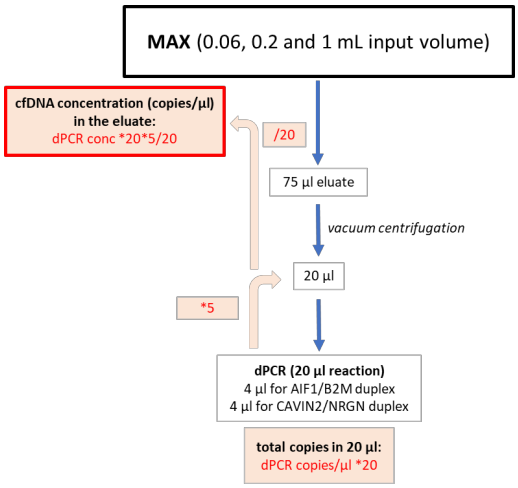

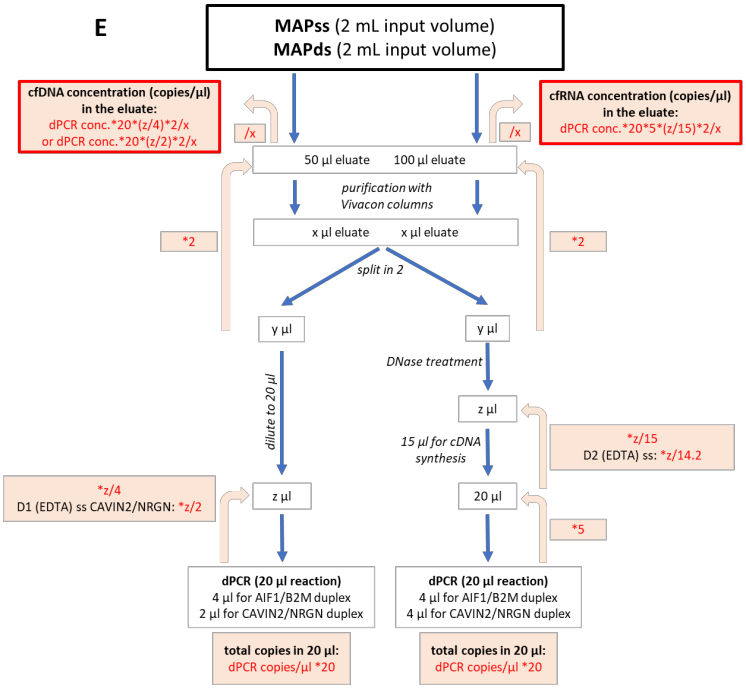

MAPss		MAPds	
sample	x	sample	x
D1 (citrate)	32 µl	D1 (citrate)	34 µl
D2 (citrate)	32 µl	D2 (citrate)	36 µl
D1 (EDTA)	30 µl	D1 (EDTA)	42 µl
D2 (EDTA)	24 µl	D2 (EDTA)	44 µl

cfDNA		cfRNA	
sample	y	sample	y
D1 (citrate) ss	16 µl	D1 (citrate) ss	16 µl
D2 (citrate) ss	16 µl	D2 (citrate) ss	16 µl
D1 (EDTA) ss	15 µl	D1 (EDTA) ss	15 µl
D2 (EDTA) ss	12 µl	D2 (EDTA) ss	12 µl
D1 (citrate) ds	17 µl	D1 (citrate) ds	17 µl
D2 (citrate) ds	18 µl	D2 (citrate) ds	18 µl
D1 (EDTA) ds	21 µl	D1 (EDTA) ds	21 µl
D2 (EDTA) ds	22 µl	D2 (EDTA) ds	22 µl

cfDNA		cfRNA	
sample	z	sample	z
D1 (citrate) ss	20 µl	D1 (citrate) ss	18.6 µl
D2 (citrate) ss	20 µl	D2 (citrate) ss	18.6 µl
D1 (EDTA) ss	20 µl	D1 (EDTA) ss	17.5 µl
D2 (EDTA) ss	20 µl	D2 (EDTA) ss	14.2 µl
D1 (citrate) ds	20 µl	D1 (citrate) ds	19.7 µl
D2 (citrate) ds	20 µl	D2 (citrate) ds	21.8 µl
D1 (EDTA) ds	21 µl	D1 (EDTA) ds	25.1 µl
D2 (EDTA) ds	22 µl	D2 (EDTA) ds	26.2 µl

Supplemental Figure 3. Detailed description of laboratory workflow. Workflow used to determine co-purification performance of each kit and subsequent calculations to determine the concentrations in each eluate: (A) MIRA and CCF, (B) MIR, (C) CAT, (D) MAX, and (E) MAP.

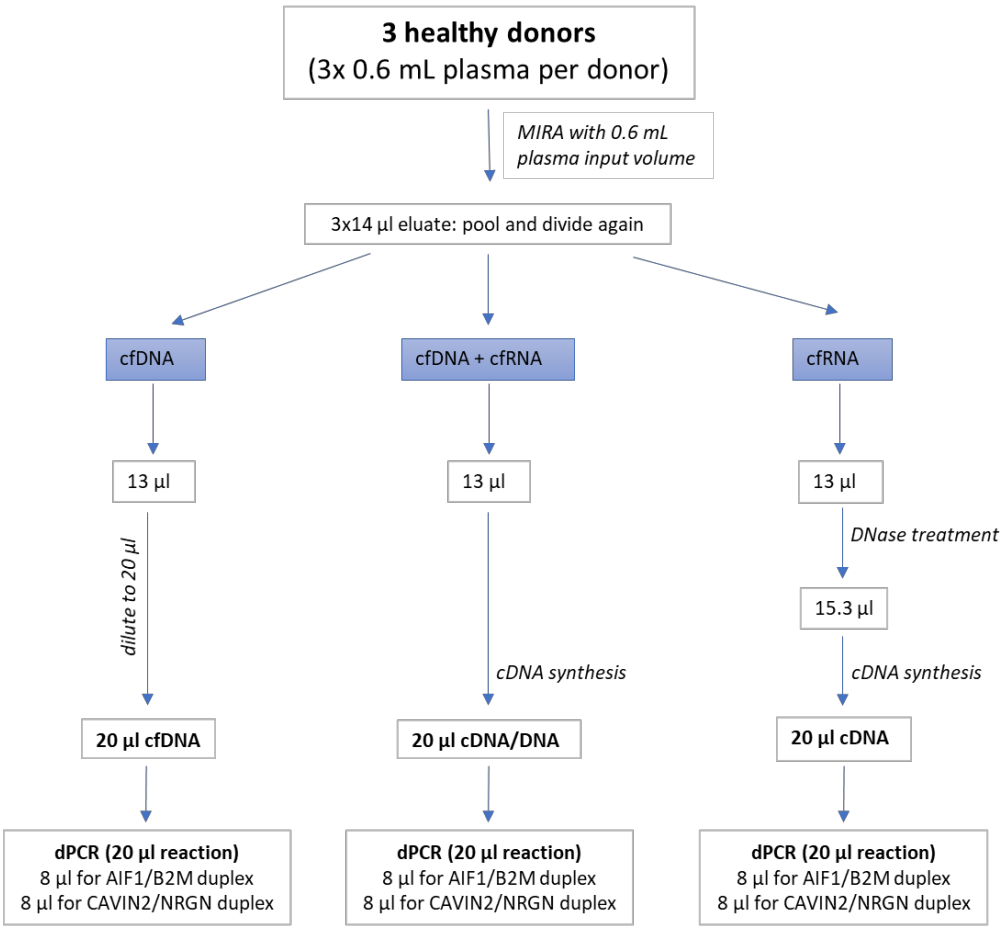

Supplemental Figure 4. Experimental overview of a combined cfDNA/cfRNA quantification and a parallel quantification of cfDNA and cfRNA.

SUPPLEMENTAL TABLES

Supplemental Table 1. Additional kit characteristics and remarks.

kit (protocol)	plasma input volumes tested (mL)	hands-on time (min)	time on instrument (min)	Number of samples	total turn-around time (min)	eluate volumes (µl)	manual/semi-automated	remarks
MIRA	0.06, 0.2, 0.6	60	*NA*	12**	60	18	manual	
CCF	1, 4	120	*NA*	12**	120	18	manual	
MAX	0.06, 0.2, 1	45	70*	16	115	20***	semi-automated	
MIR	0.06, 0.2	90	*NA*	12**	90	12	manual	
MAP (ss and ds)	2	45	70	24	115	24-32 (ss) and 34-44 (ds)****	semi-automated	beads in some eluates, difficulties generating droplets for dPCR
CAT (cfDNA/cfRNA 4000)	2, 4	55	205	12	260	18-27	semi-automated	varying eluate volumes

*including 40 min incubation of beads, **depending on centrifuge capacity, ***after vacuum centrifugation, ****after purification with Vivacon columns

Supplemental Table 2. Comparison of expected and measured cfDNA or cfRNA concentration ratio, based on plasma input volume, within a given nucleic acid extraction kit.

plasma volumes (mL)		0.2/0.06	0.6/0.2	0.6/0.06	4/1	1/0.06	1/0.2	4/2
expected ratio		3.3	3	10	4	16.7	5	2
measured ratio (cfDNA)	MIRA	2.6	2.5	6.5	*NA*	*NA*	*NA*	*NA*
	CCF	*NA*	*NA*	*NA*	4.7	*NA*	*NA*	*NA*
	MAX	1.9	*NA*	*NA*	*NA*	6.5	3.5	
	CAT	*NA*	*NA*	*NA*	*NA*	*NA*	*NA*	1.5
measured ratio (cfRNA)	MIR	3.1	*NA*	*NA*	*NA*	*NA*	*NA*	*NA*
	MIRA	4.7	3.5	16.6	*NA*	*NA*	*NA*	*NA*
	CCF	*NA*	*NA*	*NA*	5.3	*NA*	*NA*	*NA*
	CAT	*NA*	*NA*	*NA*	*NA*	*NA*	*NA*	2.6

Supplemental Table 3. Concentration (geometric mean of four assays) and yield (concentration multiplied by eluate volume) in the eluates from the kits with the different tested input volumes. Relative concentrations and yield were determined by rescaling to the highest value.

		cfRNA				cfDNA			
kit	eluate (µl)	(concentrated) eluate concentration (copies/µl)	(concentrated) eluate yield (copies)	relative concentration	relative yield	(concentrated) eluate concentration (copies/µl)	(concentrated) eluate yield (copies)	relative concentration	relative yield
CAT4	**20.7***	**577.3**	**11950.3**	**100**	**100**	**152.2**	**3150.5**	**100**	**100**
CAT2	21.7*	393.5	8539.1	68.2	71.5	59.3	1287	39	40.9
CCF1	18	72.3	1301.3	12.5	10.9	28.5	512.4	18.7	16.3
CCF4	18	384.2	6916.2	66.6	57.9	136.6	2458.1	89.7	78
MAPds2	39**	131.4	5122.7	22.8	42.9	43.8	1706.8	28.8	54.2
MAPss2	29.5**	26.8	790.3	4.6	6.6	72.7	2144.7	47.8	68.1
MIRA0.06	18	8.6	155.4	1.5	1.3	4.7	83.8	3.1	2.7
MIRA0.2	18	29.8	536.3	5.2	4.5	12.1	217.3	7.9	6.9
MIRA0.6	18	107.5	1935.6	18.6	16.2	31.2	561.5	20.5	17.8
MIR0.06	12	19.7	236.3	3.4	2	*NA*	*NA*	*NA*	*NA*
MIR0.2	12	65.4	785	11.3	6.6	*NA*	*NA*	*NA*	*NA*
MAX0.06	20***	*NA*	*NA*	*NA*	*NA*	5.4	108.9	3.6	3.5
MAX0.2	20***	*NA*	*NA*	*NA*	*NA*	10.7	214.3	7	6.8
MAX1	20***	*NA*	*NA*	*NA*	*NA*	38.3	766.1	25.2	24.3

*average of three extractions, **average of samples after purification with Vivacon columns, ***average of samples, after vacuum centrifugation

3. Exploration of neuroblastoma xenograft models for tumor extracellular RNA profiling in murine blood plasma (manuscript under review)

Jill Deleu*, Hanne Van Droogenbroeck*, Jasper Anckaert, Anneleen Decock, Jilke De Wilde, Kaat Durinck, Liselot Mus, Justine Nuytens, Muhammad Rishfi, Kathleen Schoofs, Frank Speleman, Maaike Van Trimpont, Kimberly Verniers, Nurten Yigit, Jo Vandesompele, Bram De Wilde, and Tom Van Maerken. (*shared first)

Contribution of JD: In a joint effort, JD set-up the experiments, secured plasma samples, performed the experiments, analyzed the data, conducted the literature search, and wrote the manuscript.

Exploration of neuroblastoma xenograft models for tumor extracellular RNA profiling in murine blood plasma

Jill Deleu[1,2†], Hanne Van Droogenbroeck[1,2†], Jasper Anckaert[1,2], Anneleen Decock[1,2], Jilke De Wilde[2,3], Kaat Durinck[2,4], Liselot M. Mus[2,4,5], Justine Nuytens[1,2], Muhammad Rishfi[2,4], Kathleen Schoofs[1,2,6], Frank Speleman[2,4], Maaike Van Trimpont[2,7,8], Kimberly Verniers[1,2], Nurten Yigit[1,2], Jo Vandesompele[1,2*], Bram De Wilde[1,2,4,5‡], Tom Van Maerken[1,2,9‡]

[1]OncoRNALab, Cancer Research Institute Ghent (CRIG), Ghent, Belgium

[2]Department of Biomolecular Medicine, Ghent University, Ghent, Belgium

[3]Department of Pathology, Ghent University Hospital, Ghent, Belgium

[4]Pediatric Precision Oncology Lab (PPOL), Cancer Research Institute Ghent (CRIG), Ghent, Belgium

[5]Department of Paediatric Haematology Oncology and Stem Cell Transplantation, Ghent University Hospital, Ghent, Belgium

[6]TOBI lab, VIB – Ghent University, Zwijnaarde, Belgium

[7]Department of Diagnostic Sciences, Ghent University, Ghent, Belgium

[8]Lab Normal and Malignant Hematopoiesis, Cancer Research Institute Ghent (CRIG), Ghent, Belgium

[9]Department of Laboratory Medicine, AZ Groeninge, Kortrijk, Belgium

[†]are joint first authors and contributed equally to this work

[‡]are joint last authors and contributed equally to this work

*corresponding author (jo.vandesompele@ugent.be, Tel +32 9 332 6979)

Abstract

Background: Minimally invasive liquid biopsies are becoming increasingly important in the diagnosis and treatment follow-up of cancer patients, including children with neuroblastoma. Such biopsies contain various biomarker analytes, including extracellular RNA (exRNA) with the potential to reflect dynamic changes in the tumor. However, it is challenging to distinguish tumor-derived exRNA from normal RNA. To overcome this limitation, xenograft models serve as a practical tool. In a mouse engrafted with human tumor cells, human exRNA is by definition originating from the tumor, whereas murine exRNA is host-derived. To study treatment response by monitoring tumor-derived exRNA, xenograft models with a high release of tumor exRNA into the circulation are desirable.

Methods: The aim of this study was to evaluate whether and to what extent the cell line, its engraftment site, or the tumor size influence the amount of tumoral exRNA detected in blood plasma. To that end, four different neuroblastoma cell lines were engrafted in nude mice, either subcutaneously in the flank or orthotopically in the adrenal gland. Tumor sizes were monitored by caliper measurements (subcutaneous grafts) or MRI scans (orthotopic grafts) and blood was collected via terminal cardiac puncture to evaluate the tumoral exRNA fraction.

Results: We demonstrate that the tumoral exRNA levels are correlated with the size of the subcutaneous tumor grafts. These levels are also highly dependent on the engrafted cell line. Furthermore, orthotopic engraftment potentially results in superior levels of tumoral exRNA, likely because of higher vascularity of the tumor tissue.

Conclusion: Factors as cell line, tumor size and injections site should carefully be considered when performing experiments to study circulating RNA biomarkers.

In vivo mice studies were performed in agreement with the local ethical committee approvals P164/2019 (Trace, KU Leuven), ECD 18-58 (UGent), ECD 18-74 (UGent), ECD 20-55 (UGent) and ECD 20-63 (UGent). Raw sequencing data is available in the European Genome-Phenome archive (EGAS00001007295).

Keywords

liquid biopsies, extracellular RNA, cell-free RNA, murine xenografts, neuroblastoma

Key findings:

- We demonstrate for the first time that tumor size, cell line, engraftment site, and tumor vascularity have a crucial influence on tumoral extracellular RNA levels in blood plasma from murine cellular xenograft models.

What is known and what is new?

- While cell-free DNA is widely being investigated as a liquid biopsy analyte in cancer including neuroblastoma, its application is primarily limited to patients with high-stage disease. Due to its responsive nature and wide dynamic range, extracellular RNA has shown promise in the biomarker field for cancer diagnosis and treatment monitoring.
- We set out to evaluate tumoral extracellular RNA levels in preclinical model systems by scrutinizing the factors that influence the release of tumoral extracellular RNA.

What is the implication, and what should change now?

- By careful optimization of the preclinical model system, extracellular RNA can be exploited to predict and follow-up a patient's response to therapy.

Introduction

Neuroblastoma is the most frequent extracranial childhood tumor, accounting for up to 15% of pediatric oncology deaths (1). It presents with a broad clinical behavior ranging from an asymptomatic benign malignancy with spontaneous regression to very aggressively proliferative tumors that are widely disseminated and often fatal (2). High-risk neuroblastoma (HR-NB) patients are treated with intensive multimodal therapies, consisting of induction chemotherapy, surgery to remove the primary tumor, consolidation with high-dose chemotherapy followed by autologous stem cell transplantation, radiotherapy to the site of the primary tumor and maintenance therapy consisting of anti-GD2 immunotherapy and 13-cis-retinoic acid (3,4). Despite these intensive multimodal therapies, half of HR-NB patients still show relapsed or refractory disease, due to treatment-resistant minimal residual disease (MRD) (3). Additionally, small tissue biopsies may not represent the entire tumor, because of intratumor heterogeneity (5). Furthermore, such spatial heterogeneity may lead to acquired resistance to therapy (6). Performing sequential tissue biopsies to follow-up on therapeutic tumor responses is not feasible due to its invasiveness, the need for sedation, and tumors often not being accessible (7). Detecting (chemo)resistant MRD at the earliest possible stage is key to improving the outcome of HR-NB patients by initiating targeted treatments early on (8). Hence, liquid biopsies such as blood plasma, have emerged as a novel, minimally invasive opportunity of detecting and monitoring neuroblastoma in biofluids instead of tumor tissue (5).

Several studies have indicated the presence of circulating tumor DNA (ctDNA) in the blood plasma of neuroblastoma patients. Targetable single nucleotide variants (SNVs, e.g. ALK mutations) and copy number alterations (CNAs, e.g. MYCN amplification and ALK

amplification) are detectable in ctDNA by digital PCR and (shallow) whole genome sequencing (7,9–15). Moreover, some SNVs are only detected in the ctDNA and not in the tissue biopsy, reflecting the spatial heterogeneity of neuroblastoma tumors. In contrast, CNAs are similar between ctDNA and primary tissue, suggesting that the spatial heterogeneity is minimal for CNAs (7,8,15). Furthermore, it has been demonstrated that the (tumor-derived) cell-free DNA (cfDNA) levels are higher in HR-NB patients compared to healthy controls, and in metastatic versus localized disease (8,14,16). Therefore, capturing CNAs and SNVs was only successful in a minority of low stage localized tumors (8,10,14,16). ExRNA may be able to overcome this challenge due to its wide dynamic range. In addition, while DNA is the static blueprint for cellular processes, RNA is produced on demand when specific processes are needed and is therefore – in principle - more suited to evaluate treatment responses. exRNA includes a variety of RNA types, e.g., microRNA, long non-coding RNA, messenger RNA, circular RNA, piwi-interacting RNA, and transfer RNA (fragments), all of which have been identified in various biofluids (17,18). To protect exRNA from degradation, they are encapsulated in extracellular vesicles or lipid nanoparticles, or they bind to proteins (19). Except for microRNAs, all types of RNA are present in our dataset (because of the specific library prep method), with the majority being messenger RNA (20). To explore the value of exRNA, we have developed neuroblastoma cell line derived xenograft models, i.e., mouse models engrafted with human tumor cells. In our previous work, we developed a computational pipeline to distinguish human (tumor) from murine (host) sequencing reads in fragmented and low abundant exRNA present in murine plasma (20). In addition, we put forward platelet-depleted plasma to study therapeutic responses as host background exRNA levels increased with increasing platelet levels and showed that the detectability of tumor transcripts in plasma exRNA is associated with the abundance levels in the tissue of neuroblastoma and

breast cancer xenograft models (20). Here, we evaluate the influence of the engrafted cell line, the engraftment site, and the tumor size on the tumoral exRNA levels in murine blood plasma. To exclude biases caused by tumor heterogeneity, we opted to use cell line derived xenograft models, as patient-derived xenograft models have shown to be associated with a higher degree of tumor heterogeneity (21).

We present the following article in accordance with the ARRIVE checklist.

Methods

Tumor tissue and plasma collection

In vivo mice studies were performed in agreement with the local ethical committee approvals P164/2019 (Trace, KU Leuven), ECD 18-58 (UGent), ECD 18-74 (UGent), ECD 20-55 (UGent) and ECD 20-63 (UGent). Two mouse cohorts were investigated: a first cohort to evaluate the influence of tumor size and the engrafted cell line on the exRNA amount (referred to as cell line cohort (n = 45, Table 1) and a second cohort to evaluate the influence of the engraftment site on the exRNA amount (referred to as engraftment site cohort (n = 37, Table 1). Mice were engrafted with four different neuroblastoma cell lines: IMR-32, NGP, SK-N-AS and SK-N-BE(2C). Plasma from mice in the cell line cohort was obtained as residual material from other studies, meaning that the selection of these cell lines was opportunistic. Of note, IMR-32, NGP, SK-N-AS and, SK-N-BE(2C) are commonly used neuroblastoma cell lines in the field of neuroblastoma research (22). In addition, our laboratory has a track record of using these cell lines and has demonstrated the ability to successfully establish murine xenografts, which is not possible with all neuroblastoma cell lines (23,24). Supplemental Table 1 shows the characteristics and genetic profile of each of the cell lines used. STR genotyping has been performed before engraftment to confirm cell identity.

Sample sizes were determined according to the sample size guidelines for mice experiments of Donna Neuberg (25). A single animal is considered as the experimental unit in both cohorts. Female nude immunodeficient mice were used as it is easier to perform surgery (no shaving required), they are less aggressive, and have a larger adrenal gland compared to male mice (26,27). A non-engrafted control group was not included as we only investigated the differences in exRNA levels between the models. The pipeline used to distinguish human (tumoral) and murine (host) reads was previously optimized using non-engrafted mice as a control (20). Since the mice included in the cell line cohort were obtained as residual material from other experiments, different immunodeficient strains were included in this cohort: NMRI-Foxn1nu strain (IMSR_TAC:NMRINU; Taconic Biosciences, Rensselaer, NY, US), crl:nu-foxn1nu (RRID:IMSR_CRL:088; Charles River laboratories, Les Oncins, France) and BALB/c nude J no. 633 (RRID:IMSR_JAX:001026 Charles River Laboratories). Part of our analyses was performed on publicly available sequencing data that was previously generated (i.e. 3-spin plasma from IMR-32 grafts and SK-N-BE(2C) grafts in the cell line cohort, Table 1) (20). Of note, only mice that were administered with a vehicle control or did not receive any treatment, were included in this study. Four to five mice were housed per cage, and nesting material was provided for enrichment. Before any intervention, mice acclimatized for one week.

To establish subcutaneous, heterotopic models, a predefined number of cancer cells in 30 µl RPMI 1640 medium (Thermo Fisher Scientific, Waltham, MA, USA), suspended in 70 µl Matrigel matrix (Corning, Bedford, MA, UK), were engrafted in the dorsal flank (Table 1). Follow-up of tumor volume was performed two to three times per week by caliper measurements ($V=0.5*a*b*b$, with a the longest side of the tumor and b the shortest side of the tumor). To establish orthotopic models, mice were anesthetized with isoflurane 4% and

anesthesia was maintained with 2.6-2.7% isoflurane and 270 mL/min O_2, while keeping the mice on a heating plate to maintain body temperature. Buprenorphine (100 µl of an 11.4 µg/mL solution) was administered subcutaneously prior to the start of the surgery. After disinfection of the skin with chlorhexidine, an incision was made in the left flank at the level of the spleen. Subsequently, the neuroblastoma cell suspension (Table 1) was engrafted into the adrenal gland directed towards the kidney, as the adrenal gland became visible by carefully moving the spleen aside. The cell suspension was prepared upfront by suspending a predefined number of cells in 9 µl medium and 21 µl of Matrigel. The syringes, containing 30 µl of the suspension, were kept on 4 °C until engraftment, preventing the Matrigel to polymerize. Successful engraftment was confirmed by a visible swelling of the adrenal gland. After engraftment, the muscle layer was sutured with a coated vicryl suture 5-0 (polyglactin 910, C3 13mm 3/8c) and the skin was glued with Vetbond (3M). After surgery, mice were closely monitored for clinical signs of pain or distress. MRI scans were performed to follow up on the tumor size in the IMR-32 orthotopic mouse model. All mice were also weighed two to three times per week. After a predefined timeframe, or when mice reached specific humane endpoints (i.e., a weight loss of more than 20% or clinical signs of significant pain, distress, or suffering), cardiac puncture was performed under isoflurane anesthesia, to collect blood, followed by cervical dislocation of the mice. The blood, collected in Microvette 500 K3EDTA tubes (Sarstedt, Newton, NC, USA), was processed immediately to prepare platelet-depleted plasma within two hours after cardiac puncture. The platelet-depleted plasma was prepared either by a 2-spin protocol (2 times 1900 g for 10 minutes) or a 3-spin protocol (400 g for 20 minutes, 800 g for 10 minutes and 2500 g for 15 minutes). In the engraftment site cohort, a part of the tumor was snap frozen and subjected to formalin-fixed paraffin embedding (FFPE) for histological analysis. The degree of hemolysis of plasma samples was assessed by

measuring levels of hemoglobin by spectrophotometric analysis (OD414) using a NanoDrop 1000 spectrophotometer (Thermo Fisher Scientific; Supplemental Table 2). Engraftment, follow-up and euthanasia were performed by the same unblinded investigators to minimize experimental bias.

Hematoxylin and eosin staining of tumor tissue

Tissues were fixed in 10% neutral-buffered formalin and after 24 hours embedded in paraffin. Hematoxylin and eosin (H&E) staining was performed on 2-4 µm sections for morphological analysis. The mitotic count was obtained by counting the number of mitotic figures per 10 high-power fields (1 HPF = 0.26 mm^2). The tumor sections were ranked based on the average microvascular density (with 0 = no vessels and 5 = highest density) by a blinded pathologist.

RNA isolation, spike-in RNA addition and gDNA removal

exRNA from 60-200 µl platelet-depleted plasma was isolated using the miRNeasy Serum/Plasma Kit (Qiagen, Hilden, Germany), according to the manufacturer's manual. During RNA extraction, 2 µl per 200 µl of plasma of a 3,000-fold or 30,000-fold dilution of Sequin spike-in controls (Garvan Institute of Medical Research, Darlinghurst, NSW, Australia (28)) was added to the lysate. Upon RNA purification, 2 µl of a 25,000-fold, 50,000-fold or 70,000-fold dilution of External RNA Control Consortium (ERCC) RNA Spike-in Mix (Thermo Fisher Scientific) was added to 12 µl RNA eluate, followed by gDNA removal (29). To remove residual DNA, 1 µl HL-dsDNase (ArcticZymes Technologies, Tromsø, Norway) and 1.4 µl Heat & Run 10X Reaction Buffer (ArcticZymes Technologies) were added to the eluates, and RNA samples were incubated for 10 min at 37 °C, followed by 5 min at 58 °C. An overview of the plasma input volumes and the amount of Sequin and ERCC spike-in controls added is shown in Supplemental Table 2.

Total RNA library preparation and sequencing

Total RNA libraries were prepared starting from 8 µl DNase-treated RNA using the SMARTer Stranded Total RNA-Seq Kit v2 - Pico Input Mammalian (Takara Bio, CA, USA), according to the manufacturer's manual with minor modifications (30). Briefly, prior to first strand cDNA synthesis, RNA was fragmented for 2 min at 94 °C. During final library amplification, 16 PCR cycles were performed on the liquid biopsy samples. Final clean-up was repeated if an excessive number of products < 200 bp in size was observed on FragmentAnalyzer data (data not shown, Agilent Technologies, Santa Clara, CA, USA). Fragment sizes were determined using FragmentAnalyzer software for smear analysis in the 200 bp to 1,000 bp range. Library quantification was performed using the KAPA Library quantification Kit (Kapa Biosystems, Wilmington, MA, USA) and libraries were pooled equimolarly. The final pool was quantified using Qubit, and either 1.3 pM was loaded on a NextSeq 500 instrument (NextSeq 500 HighOutput Kit V2, 150 cycles, Illumina, San Diego, California, United States), with 1-3% PhiX (Illumina), or 0.61-0.65 nM was loaded on a NovaSeq instrument (NovaSeq S1 Reagent kit v1.5, 200 cycles, Illumina) with 1-2% PhiX (Supplemental Table 2). Raw sequencing data is available in the European Genome-Phenome archive (EGAS00001007295).

Preprocessing and combined mapping of RNA sequencing data

The 'exRNAxeno combined' pipeline was used to preprocess and map the RNA sequencing data (https://github.com/CBIGR/exRNAxeno) (20). By a combined mapping strategy to the murine and human transcriptome, total RNA sequencing reads are assigned to the right species, either Homo sapiens or Mus musculus. The quality of the data was assessed, and no data points were excluded (Supplemental Table 2). The output of this pipeline is a count table, on which subsequent analyses were performed with RStudio (PBC, version 2022.07.2 Build 576). The MYCN transcription factor target genes used for our analyses are originating from

from the Ma'ayan laboratory of computational systems biology (https://maayanlab.cloud/Harmonizome/gene_set/MYCN/CHEA+Transcription+Factor+Targets). The list of neuroblastoma-associated associated mRNAs is derived from a paper of Uemura et al. (https://www.ncbi.nlm.nih.gov/pmc/articles/PMC6558004/)(31). The percentage of tumoral exRNA is calculated by dividing the number of human reads by the sum of human and murine reads.

Statistical analysis

Statistical tests were performed by an unblinded researcher with RStudio (PBC, version 2022.07.2 Build 576). The Wilcoxon test, also known as the Wilcoxon rank sum test, was applied to compare group means. This non-parametric test was used as it does not rely on the assumption of a normal distribution, making it suitable for analyzing data with non-normally distributed values. In addition, it is robust to outliers, which is particularly important given the presence of potential extreme values in our dataset. Furthermore, the Wilcoxon test performs well, even with small sample sizes, which is advantageous for our study given the limited number of observations in each group. To explore correlations between random variables, we calculated the Spearman rank correlation coefficient. This test is well-suited for our analysis as it does not assume a linear relationship between variables. In addition, the Spearman rank correlation coefficient is robust to outliers, which is beneficial given the variability observed in our cohorts. Finally, we used the log-rank test to assess differences in survival between groups. This statistical test is commonly used in survival analysis, such as the evaluation of Kaplan-Meier plots. The log-rank test allowed us to determine if there were significant differences in survival outcomes between the groups studied. The pairwise Jaccard similarity coeffient was calculated by counting the number of genes where both samples have

transcripts per million (TPM) values greater than 0 and dividing it by the number of genes where at least one sample has a TPM value greater than 0.

Results

The amount of exRNA in blood plasma is driven by tumor size

Mice were subcutaneously engrafted with four different neuroblastoma cell lines: IMR-32, NGP, SK-N-AS and SK-N-BE(2C). A significant correlation between tumor size and exRNA release into the circulation is observed (Spearman correlation = 0.415, $P = 5x10^{-3}$, Figure 1). However, the minimal tumor size for sufficient release of tumoral exRNA (e.g., 1% tumoral exRNA in plasma) depends on the cell line. For instance, IMR-32 reaches more than 1% as soon as tumor size is ~ 700 mm^3, while other mice need to be sacrificed at higher tumor sizes to be able to reach 1% tumoral exRNA. Furthermore, SK-N-AS tumors are slightly deviating from the observed positive correlation. If the SK-N-AS model is excluded from our analysis, the positive correlation between tumor size and percentage of tumoral exRNA is stronger and more significant (Spearman correlation = 0.554, $P = 7x10^{-4}$, data not shown). Moreover, when considering each cell line separately, a significant trend is not observed, which could be explained by a smaller sample size (reduced power) and by the limited tumor size range (SK-N-AS: Spearman correlation = 0.515, $P = 0.14$; SK-N-BE(2C): Spearman correlation = -0.452, $P = 0.27$; NGP: Spearman correlation = 0.750, $P = 0.07$; IMR-32: Spearman correlation = 0.442, $P = 0.05$).

The amount of exRNA in blood plasma is cell line dependent

We demonstrate a high variability in the fraction of tumoral exRNA across different cell lines, with IMR-32 cell line-derived xenografts displaying the highest fraction (Figure 2). Also, a high variability is observed in the number and identity of genes that are detected in mice engrafted

with the same cells, even when selecting mice with a tumor size above 1,000 mm^3 (Supplemental Figure 1). Also, no commonly detected genes are observed in mice engrafted with different neuroblastoma cell lines (data not shown). Of note, the mouse strain is not associated with the fraction of tumoral exRNA (Supplemental Figure 2).

Orthotopic engraftment further increases exRNA levels in IMR-32 model

In a second cohort (i.e., the engraftment site cohort), we studied the potential benefits of orthotopic (intra-adrenal) engraftment compared to heterotopic (subcutaneous) engraftment by selecting the two cell lines with the highest RNA release in the cell line cohort: IMR-32 and SK-N-BE(2C). Subcutaneous engraftment was successful in all mice (IMR-32: n = 10/10, SK-N-BE(2C): n = 10/10). However, three mice dropped out from the orthotopically engrafted group, either during the surgical procedure (IMR-32 engraftment); during follow-up due to an unexpectedly fast deterioration (SK-N-BE(2C) engrafted mouse), or as a consequence of sedation during MRI imaging of an IMR-32 engrafted mouse (IMR-32: n = 8/10, SK-N-BE(2C): n = 9/10). The growth rate of SK-N-BE(2C) tumors is significantly higher than that of IMR-32 tumors, both upon subcutaneous as well as orthotopic engraftment (Supplemental Figure 3).

First, we compared the release between orthotopic and subcutaneous conditions. We found that IMR-32, having a high capacity of releasing tumoral RNA into the circulation from subcutaneous engraftment, releases significantly more exRNA in an orthotopic setting (Figure 3). In some cases, the fraction of human reads reached up to 70%. In contrast, orthotopic SK-N-BE(2C) xenografts do not display higher exRNA levels compared to subcutaneous xenografts (Figure 3).

To investigate whether the increased fraction of tumoral circulating RNA leads to improved detectability of relevant genes, we investigated the detectability of a MYCN transcriptional

target gene signature (2671 genes) in blood plasma from mice in the engraftment site cohort, which only includes MYCN amplified cell lines. We demonstrate that orthotopic engraftment of IMR-32 significantly increases the percentage of MYCN-associated genes in circulation detected with at least one read, compared to subcutaneous engraftment ($P < 0.001$). More specifically, 48.41 - 80.04 % (median: 65.99 %) of MYCN-associated genes are detected orthotopically and 28.75 - 53.69 % (median: 47.83%) are detected subcutaneously (Figure 4A). No significant difference is observed between orthotopic and subcutaneous engraftment of SK-N-BE(2C) cells ($P = 0.55$), i.e., 1.35 – 16.10 % (median: 10.33%) orthotopically versus 0.15 – 39.57 % (median: 11.76%) subcutaneously (Figure 4B). In addition to a MYCN transcriptional target gene signature, we also evaluated the detectability of other neuroblastoma-associated genes, and we observed similar patterns (Supplemental Figure 4, (31)).

Orthotopic engraftment reduces inter-mice variability in tumoral exRNA levels in IMR-32 model

Using the engraftment site cohort, we further evaluate the variability in exRNA transcripts detected across individual mice from a single xenograft model (Supplemental Figure 5). The Jaccard similarity coefficient of detected genes through pairwise comparison of mice in a given model is generally low for each of the xenograft models, confirming a high inter-mice variability (Figure 5). Of note, both IMR-32 xenograft models are less variable compared to the SK-N-BE(2C) models (Wilcoxon $P < 0.001$). Moreover, orthotopic engraftment of IMR-32 cells significantly reduces the variability in tumoral exRNA transcripts detected across individual mice compared to subcutaneous engraftment of the cells (Wilcoxon $P < 0.001$, Figure 5). The variability in murine exRNA transcripts shows the opposite trend in IMR-32

engrafted mice (Supplemental Figure 6). Overall, inter-sample variability is expectedly lower for murine transcripts as compared to human transcripts (Figure 5, Supplemental Figure 6).

In the engraftment site cohort, we further measured tumor growth rate and vascularization to assess potential associations with tumor exRNA amount. Overall, the amount of circulating tumoral RNA is significantly positively correlated with the degree of vascularization (Spearman correlation = 0.84 and $P < 0.001$, Figure 6), while this is not observed for the mitotic count (Spearman correlation = 0.058 and $P = 0.74$, Figure 6). Of note, the overall correlation between exRNA and vascularization was not found when each mouse model was considered separately (SK-N-BE(2C) orthotopic: Spearman correlation = 0.55 and $P = 0.16$, and subcutaneous: Spearman correlation = 0.45 and $P = 0.23$; IMR-32 orthotopic: Spearman correlation = 0 and $P = 1$, and subcutaneous: Spearman correlation = -0.10 and $P = 0.78$). We extended this analysis by performing a histological assessment of the vascularity of subcutaneous SK-N-AS and NGP tumors The significant positive correlation between tumor size and percentage of exRNA remains (Spearman rank correlation = 0.634 and $P < 0.01$, Supplemental Figure 7), but is somewhat less pronounced.

Based on H&E staining, IMR-32 tumors are significantly more vascularized than SK-N-BE(2C) tumors (Figure 7), which is in line with our macroscopic observation that IMR-32 tumors appear as solid masses, while SK-N-BE(2C) tumors are more fluid and disintegrated (data not shown).

Discussion

Accurate assessment of the response to treatment in neuroblastoma patients is highly desired, as half of HR-NB patients experience relapse or refractory disease. Due to its dynamic nature, exRNA is a good analyte to evaluate treatment responses. So far, several studies have

been set up, demonstrating the potential of exRNA for detecting and monitoring cancer (32–34). Due to the limited availability of blood plasma samples from patients participating in clinical trials, and the difficulty in differentiating between normal body and tumor cell-free RNA responses (except for tumor-specific aberrations), we have embarked upon exploring neuroblastoma xenograft models to identify conditions with maximal release of tumoral exRNA into the blood plasma which might be helpful to identify biomarkers. Computational deconvolution of the human and murine sequencing reads from the plasma transcriptome allows the identification of tumor-specific signals.

Mice were engrafted with four different neuroblastoma cell lines: IMR-32, NGP, SK-N-AS and SK-N-BE(2C). A first examination showed a significant correlation between the tumor size and the extent of tumor RNA release into the circulation. The correlation between tumor load and concentration of tumoral cell-free nucleic acids has previously been demonstrated for microRNAs. Zeka et al. found 9 miRNAs of which abundance in serum is associated with disease burden and treatment response in children with metastatic neuroblastoma (35). Further, Van Goethem et al. showed that the serum levels of 57 tumoral miRNAs increase with the tumor size of mice, orthotopically engrafted with a SH-SY5Y neuroblastoma cell line (36). Now, for the first time, we show similar results for long RNAs such as messenger RNA and long non-coding RNA, jointly called exRNA. Given the assumed higher stability of miRNAs in circulation, this is an important and encouraging finding for future biomarker studies focusing on longer RNA biotypes.

Furthermore, we show that the exRNA levels are dependent on the type of engrafted cells, with IMR-32 being the neuroblastoma cell line with the highest RNA release into the blood circulation in both study cohorts. The observed differences among models is consistent with our previous finding that the fraction of tumoral exRNA varies widely among engrafted tumor

entities (both pediatric and adult cancers, i.e., melanoma, penile, endometrial, breast and lung cancer) (20). When examined at the macroscopic level, tumors display a varied composition across different cell lines. Some tumors consist of solid masses (e.g. IMR-32), while others are more hemorrhagic and disintegrate during the process of tumor resection (e.g. SK-N-BE(2C)). Through microscopic analysis of H&E stained tumor tissue, IMR-32 engrafted tumors are more vascularized than SK-N-BE(2C) tumors. This may underly the observation of higher levels of tumoral exRNA in the plasma of IMR-32 engrafted mice. This hypothesis is further supported by a significant positive correlation between vascularity and the fraction of tumoral exRNA in the plasma.

The SK-N-AS engrafted mice are slightly deviating from the observed correlation. More specifically, for a given tumor size or vascularity score, the percentage of exRNA is variable. This suggests that also other characteristics of the engrafted cells not studied here, such as metastatic potential, genetic profile, origin of neuroblastoma cell lines (abdominal, bone etc.), or release potential of extracellular vesicles may contribute to the observed exRNA differences. Unfortunately, in our study, the extent of metastatic disease was not assessed since follow-up of the orthotopic xenografts was done using MRI, focusing only on the left adrenal gland, and no organs were collected. Moreover, the amount of cell lines included was too sparse to define a correlation with the genetic background or origin of neuroblastoma cell lines. Furthermore, it remains to be determined whether treatment would alter the quantities of tumoral exRNA.

When looking deeper into the differences between orthotopic and subcutaneous engraftment, we observe that orthotopic IMR-32 grafts have significantly higher levels of vascularization, possibly contributing to higher levels of tumor exRNA in the plasma. Intriguingly, for SK-N-BE(2C), orthotopic engraftment is associated with reduced vascularity

and less tumoral exRNA in the plasma. This might be caused by the aggressive nature of SK-N-BE(2C), which is a very rapidly growing cell line *in vivo*. The short duration of SK-N-BE(2C) tumor growth might be insufficient for the development of blood vessels and the entry of tumoral RNA into circulation. Orthotopic engraftment of the SK-N-BE(2C) cells further enhanced the tumor growth rate as compared to subcutaneous engraftment of SK-N-BE(2C), which may also explain why the fraction of tumoral exRNA and the amount of blood vessels are further reduced in this orthotopic setting. Neo-angiogenesis in adrenal tumors has previously been shown to occur at day 15, while the orthotopic SK-N-BE(2C) mice in our study were sacrificed between 10 and 17 days after engraftment (37). Of note, other tumor characteristics, such as necrosis have been studied as well, for instance demonstrating that the extent of necrosis of lung adenocarcinoma positively correlates with the amount of tumoral extracellular DNA that can be detected in blood plasma (38). Clearly, tumor characteristics may play a role, even in the absence of immunosurveillance.

Another important finding is the high variability in number of detectable tumor transcripts among mice engrafted with different cells, but also within one model. This is remarkable since mice from the same model are being engrafted with cells originating from the same homogeneous cell suspension. This high variability in detected tumor transcripts makes biomarker discovery challenging. To address this, we evaluated whether orthotopic engraftment of two different cell lines reduces the inter-mice variability within a single model. We demonstrate that this is indeed the case for IMR-32 when considering tumoral exRNA. The murine exRNA shows the opposite trend in IMR-32 engrafted cells, likely because of the compositional nature of sequencing data as a finite number of reads are generated during a sequencing run. If the proportion of human-derived reads increases, fewer reads will represent murine exRNA. The exRNA transcript variability within the IMR-32 engrafted mice

is in general significantly lower than the variability detected in the SK-N-BE(2C) model. Furthermore, orthotopic engraftment instead of subcutaneous engraftment of IMR-32 cells, causes the fraction of human reads to increase significantly. The reduced variability in the (orthotopic) IMR-32 model might be attributed to the higher tumoral exRNA fraction that is observed in all mice of this model.

In future studies, it might be valuable to study the effect of metastatic disease on exRNA levels. For ctDNA, it has been reported that metastatic lesions are associated with a higher ctDNA fraction in the circulation of patients with neuroblastoma or adult cancers, such as breast cancer (8,14,16,39). Also, evaluating another animal model, such as a xenografted rat, may provide additional insights into the biomarker potential of liquid biopsies of xenografts. A rat contains about 10 times more blood than a mouse, enabling an investigator to collect weekly volumes of ~1.4 ml, allowing to study how the tumoral exRNA quantity and dynamics change during disease progression or treatment.

Conclusions

In conclusion, the type of cell line, its site of engraftment and tumor size are factors that contribute to the amount of circulating tumoral RNA and should therefore carefully be considered when performing experiments studying and exploiting circulating RNA biomarkers.

Acknowledgements

We thank Benedicte Descamps and Christian Vanhove from the INFINITY imaging core at Ghent University for their assistance in performing the MRI scans on the mice and for their help in interpreting the obtained images. We would also like to acknowledge that part of the

results of this research was presented as a poster entitled ‘Exploration of neuroblastoma xenograft models for the analysis of tumoral cell-free RNA in murine blood plasma’ at the ANR (Advances in Neuroblastoma Research association) meeting held in Amsterdam in May 2023.

Funding: This work was supported by Kom op tegen Kanker [Stand up to Cancer, the Flemish cancer society, granted to BDW, 2022/13037 to KS]; the Ghent University Special Research Fund [BOF22/CDV/077 to JD and BDW, 202011/GE/ZAP/018 to KD]; the Research Foundation – Flanders [G0B2820N to JV, LIQUIDHOPE TRANSCAN-2 project, 1224021N to AD, senior clinical researcher grant to BDW, 1S90621N to JDW, 11M1422N to MR] and the “Geconcerteerde onderzoeksactie” (GOA), Ghent University: Replication fork protector dependency factors as novel targets for combination treatment and immunomodulation in neuroblastoma (BOF22/GOA/009 to FS, BDW and JV).

Footnote

Reporting Checklist

The authors have completed the ARRIVE reporting checklist.

Data sharing statement

Raw sequencing data is available in the European Genome-Phenome archive (EGAS00001007295).

Conflict of Interest

All authors have completed the ICMJE uniform disclosure form. The authors have no conflicts of interest to declare.

Ethical Statement

The authors are accountable for all aspects of the work in ensuring that questions related to the accuracy or integrity of any part of the work are appropriately investigated and resolved. Experiments were performed under a project license (NO.: P164/2019, ECD 18-58, ECD 18-74, ECD 20-55 and ECD 20-63) granted by institutional ethics committees of KU Leuven and UGent in compliance with the universities' (KU Leuven and UGent) national or institutional guidelines for the care and use of animals.

References

1. Johnsen JI, Dyberg C, Wickström M. Neuroblastoma—A neural crest derived embryonal malignancy. Front Mol Neurosci. 2019 Feb 12;12.
2. Gomez RL, Ibragimova S, Ramachandran R, Philpott A, Ali FR. Tumoral heterogeneity in neuroblastoma. Biochim Biophys Acta Rev Cancer. 2022 Nov 1;1877(6).
3. DuBois SG, Macy, ME, Henderson TO. High-Risk and Relapsed Neuroblastoma: Toward More Cures and Better Outcomes. American Society of Clinical Oncology Educational Book. 2022 Jul;(42):768–80.
4. Pasqualini C, Valteau-Couanet D, Ladenstein R. High-risk neuroblastoma standard clinical practice recommendations [Internet]. [cited 2023 Feb 14]. Available from: https://www.srohp.ro/wp-content/uploads/2022/01/escp-high-risk-neuroblastoma-standard-clinical-practice-recommendations.pdf
5. Pinzani P, D'Argenio V, Re M Del, Pellegrini C, Cucchiara F, Salvianti F, et al. Updates on liquid biopsy: Current trends and future perspectives for clinical application in solid tumors. Vol. 59, Clinical Chemistry and Laboratory Medicine. De Gruyter Open Ltd; 2021. p. 1181–200.

6. Schmelz K, Toedling J, Huska M, Cwikla MC, Kruetzfeldt LM, Proba J, et al. Spatial and temporal intratumour heterogeneity has potential consequences for single biopsy-based neuroblastoma treatment decisions. Nat Commun. 2021 Nov 23;12(1):6804.

7. Chicard M, Colmet-Daage L, Clement N, Danzon A, Bohec M, Bernard V, et al. Whole-exome sequencing of cell-free DNA reveals temporo-spatial heterogeneity and identifies treatment-resistant clones in neuroblastoma. Clinical Cancer Research. 2018 Feb 15;24(4):939–49.

8. Lodrini M, Graef J, Thole-Kliesch TM, Astrahantseff K, Sprussel A, Grimaldi M, et al. Targeted Analysis of Cell-free Circulating Tumor DNA is Suitable for Early Relapse and Actionable Target Detection in Patients with Neuroblastoma. Clinical Cancer Research. 2022 May 1;28(9):1809–20.

9. Cimmino F, Lasorsa VA, Vetrella S, Iolascon A, Capasso M. A Targeted Gene Panel for Circulating Tumor DNA Sequencing in Neuroblastoma. Front Oncol. 2020 Dec 14;10.

10. Combaret V, Iacono I, Bellini A, Bréjon S, Bernard V, Marabelle A, et al. Detection of tumor ALK status in neuroblastoma patients using peripheral blood. Cancer Med. 2015 Apr 1;4(4):540–50.

11. Lodrini M, Sprüssel A, Astrahantseff K, Tiburtius D, Konschak R, Lode HN, et al. Using droplet digital PCR to analyze MYCN and ALK copy number in plasma from patients with neuroblastoma. Oncotarget [Internet]. 2017;8(49):85234–51. Available from: www.impactjournals.com/oncotarget/

12. Peitz C, Sprüssel A, Linke RB, Astrahantseff K, Grimaldi M, Schmelz K, et al. Multiplexed Quantification of Four Neuroblastoma DNA Targets in a Single Droplet Digital PCR Reaction. Journal of Molecular Diagnostics. 2020 Nov 1;22(11):1309–23.

13. Kahana-Edwin S, Cain LE, McCowage G, Darmanian A, Wright D, Mullins A, et al. Neuroblastoma molecular risk-stratification of dna copy number and alk genotyping via cell-free circulating tumor dna profiling. Cancers (Basel). 2021 Jul 1;13(13).

14. Van Roy N, Van Der Linden M, Menten B, Dheedene A, Vandeputte C, Van Dorpe J, et al. Shallow whole genome sequencing on circulating cell-free DNA allows reliable noninvasive copy-number profiling in neuroblastoma patients. Clinical Cancer Research. 2017 Oct 15;23(20):6305–15.

15. Bosse KR, Anna ;, Giudice M, Lane M V, Mcintyre B, Patrick ;, et al. Serial profiling of circulating tumor DNA identifies dynamic evolution of clinically actionable genomic alterations in high-risk neuroblastoma. Available from: http://aacrjournals.org/cancerdiscovery/article-pdf/doi/10.1158/2159-8290.CD-22-0287/3207490/cd-22-0287.pdf

16. Chicard M, Boyault S, Daage LC, Richer W, Gentien D, Pierron G, et al. Genomic copy number profiling using circulating free tumor DNA highlights heterogeneity in neuroblastoma. Clinical Cancer Research. 2016 Nov 15;22(22):5564–73.

17. Cao M. The extracellular RNA and drug resistance in cancer: a narrative review. ExRNA. 2023 Jan;5:1–1.

18. Ni Y, Zhang W, Mu G, Gu Y, Wang H, Wei K, et al. Extracellular RNA profiles in non-small cell lung cancer plasma. J Thorac Dis. 2023 May;15(5):2742–53.

19. Li Z, Gao Y, Cao Y, He F, Jiang R, Liu H, et al. Extracellular RNA in melanoma: Advances, challenges, and opportunities. Front Cell Dev Biol. 2023 May 4;11.

20. Vermeirssen V, Deleu J, Morlion A, Everaert C, De Wilde J, Anckaert J, et al. Whole transcriptome profiling of liquid biopsies from tumour xenografted mouse models

enables specific monitoring of tumour-derived extracellular RNA. NAR Cancer. 2022 Dec;4(4):zcac037.

21. Wang Y, Cui J, Wang L. Patient-derived xenografts: a valuable platform for clinical and preclinical research in pancreatic cancer. Chin Clin Oncol. 2019 Apr;8(2):17–17.

22. Harenza JL, Diamond MA, Adams RN, Song MM, Davidson HL, Hart LS, et al. Transcriptomic profiling of 39 commonly-used neuroblastoma cell lines. Sci Data. 2017 Mar 28;4(1):170033.

23. Van Goethem A, Yigit N, Moreno-Smith M, Vasudevan SA, Barbieri E, Speleman F, et al. Dual targeting of MDM2 and BCL2 as a therapeutic strategy in neuroblastoma. Oncotarget. 2017;8(34):57047–57.

24. Rihani A, Van Goethem A, Ongenaert M, De Brouwer S, Volders PJ, Agarwal S, et al. Genome wide expression profiling of p53 regulated miRNAs in neuroblastoma. Sci Rep. 2015 Mar 12;5(1):9027.

25. Neuberg D. How many mice? Design considerations for murine studies. Blood Adv. 2017 Aug 8;1(18):1466–1466.

26. Takahashi A. Toward Understanding the Sex Differences in the Biological Mechanism of Social Stress in Mouse Models. Front Psychiatry. 2021 Feb 16;12.

27. Bielohuby M, Herbach N, Wanke R, Maser-Gluth C, Beuschlein F, Wolf E, et al. Growth analysis of the mouse adrenal gland from weaning to adulthood: time- and gender-dependent alterations of cell size and number in the cortical compartment. American Journal of Physiology-Endocrinology and Metabolism. 2007 Jul;293(1):E139–46.

28. Deveson IW, Chen WY, Wong T, Hardwick SA, Andersen SB, Nielsen LK, et al. Representing genetic variation with synthetic DNA standards. Nat Methods. 2016 Sep 8;13(9):784–91.

29. Hulstaert E, Decock A, Morlion A, Everaert C, Verniers K, Nuytens J, et al. Messenger RNA capture sequencing of extracellular RNA from human biofluids using a comprehensive set of spike-in controls. STAR Protoc. 2021 Jun;2(2):100475.

30. Everaert C, Helsmoortel H, Decock A, Hulstaert E, Van Paemel R, Verniers K, et al. Performance assessment of total RNA sequencing of human biofluids and extracellular vesicles. Sci Rep. 2019 Nov 26;9(1):17574.

31. Uemura S, Ishida T, Thwin KKM, Yamamoto N, Tamura A, Kishimoto K, et al. Dynamics of Minimal Residual Disease in Neuroblastoma Patients. Front Oncol. 2019 Jun 4;9.

32. Krug AK, Enderle D, Karlovich C, Priewasser T, Bentink S, Spiel A, et al. Improved EGFR mutation detection using combined exosomal RNA and circulating tumor DNA in NSCLC patient plasma. Annals of Oncology. 2018 Mar 1;29(3):700–6.

33. Larson MH, Pan W, Kim HJ, Mauntz RE, Stuart SM, Pimentel M, et al. A comprehensive characterization of the cell-free transcriptome reveals tissue- and subtype-specific biomarkers for cancer detection. Nat Commun. 2021 Dec 1;12(1).

34. Happel C, Ganguly A, Tagle DA. Extracellular RNAs as potential biomarkers for cancer. J Cancer Metastasis Treat. 2020 Sep 17;2020.

35. Zeka F, Van Goethem A, Vanderheyden K, Demuynck F, Lammens T, Decock A, et al. Circulating microRNA biomarkers for metastatic disease in neuroblastoma patients. bioRxiv. 2018.

36. Van Goethem A, Deleu J, Yigit N, Everaert C, Moreno-Smith M, Vasudevan SA, et al. Longitudinal evaluation of serum microRNAs as biomarkers for neuroblastoma burden and therapeutic p53 reactivation. NAR Cancer. 2023 Jan 11;5(1).

37. Daudigeos-Dubus E, LE Dret L, Rouffiac V, Bawa O, Leguerney I, Opolon P, et al. Establishment and characterization of new orthotopic and metastatic neuroblastoma models. In Vivo. 2014;28(4):425–34.

38. Karasaki T, Moore DA, Veeriah S, Naceur-Lombardelli C, Toncheva A, Magno N, et al. Evolutionary characterization of lung adenocarcinoma morphology in TRACERx. Nat Med. 2023 Apr;29(4):833–45.

39. BERA A, RUSS E, KARAIAN J, LANDA A, RADHAKRISHNAN S, SUBRAMANIAN M, et al. Circulating Cell-free DNA in Serum as a Marker for the Early Detection of Tumor Recurrence in Breast Cancer Patients. Cancer Diagnosis & Prognosis. 2022 May 3;2(3):285–92.

Tables

Table 1 Overview of mouse xenograft cohorts

number of mice	cell line (number of cells)	engraftment site (age)	treatment	tumor size at sacrifice (mm^3) (range and median)	plasma preparation protocol	mouse strain	housing
cell line cohort (female, n = 45)							
10	SK-N-AS (2.00 x 10^6)	subcutaneous (5 weeks)	vehicle	779-2871 (2262)	2-spin	crl:nu-foxn1^{nu}	Ghent University
13	IMR-32 (2.00 x 10^6)	subcutaneous (5-6 weeks)	vehicle	1949-2617 (2149)	2-spin (n=6) 3-spin (n=7)	crl:nu-foxn1^{nu}	Ghent University
7	IMR-32 (2.41 x 10^6)	subcutaneous (6 weeks)	vehicle	0-3323 (1949)	2-spin	BALB/c nude J no. 633	Ghent University
7	NGP (2.30 x 10^6)	subcutaneous (6 weeks)	vehicle	34-2564 (786)	2-spin	BALB/c nude J no. 633	Ghent University
8	SK-N-BE(2C) (2.00 x 10^6)	subcutaneous (13 weeks)	-	1166-2243 (2096)	3-spin	NMRI-foxn1^{nu}	KU Leuven
engraftment site cohort (female, n = 37)							
9	SK-N-BE(2C) (1.00 x 10^6)	orthotopic (5-6 weeks)	-	no data	2-spin	BALB/c nude J no. 633	Ghent University
10	SK-N-BE(2C) (2.20 x 10^6)	subcutaneous (5-6 weeks)	-	807-3352 (2126)	2-spin		
8	IMR-32 (1.00 x 10^6)	orthotopic (5-6 weeks)	-	175-3215 (1698)	2-spin		
10	IMR-32 (3.00 x 10^6)	subcutaneous (5-6 weeks)	-	1879-2789 (2071)	2-spin		
82 in total							

Figures

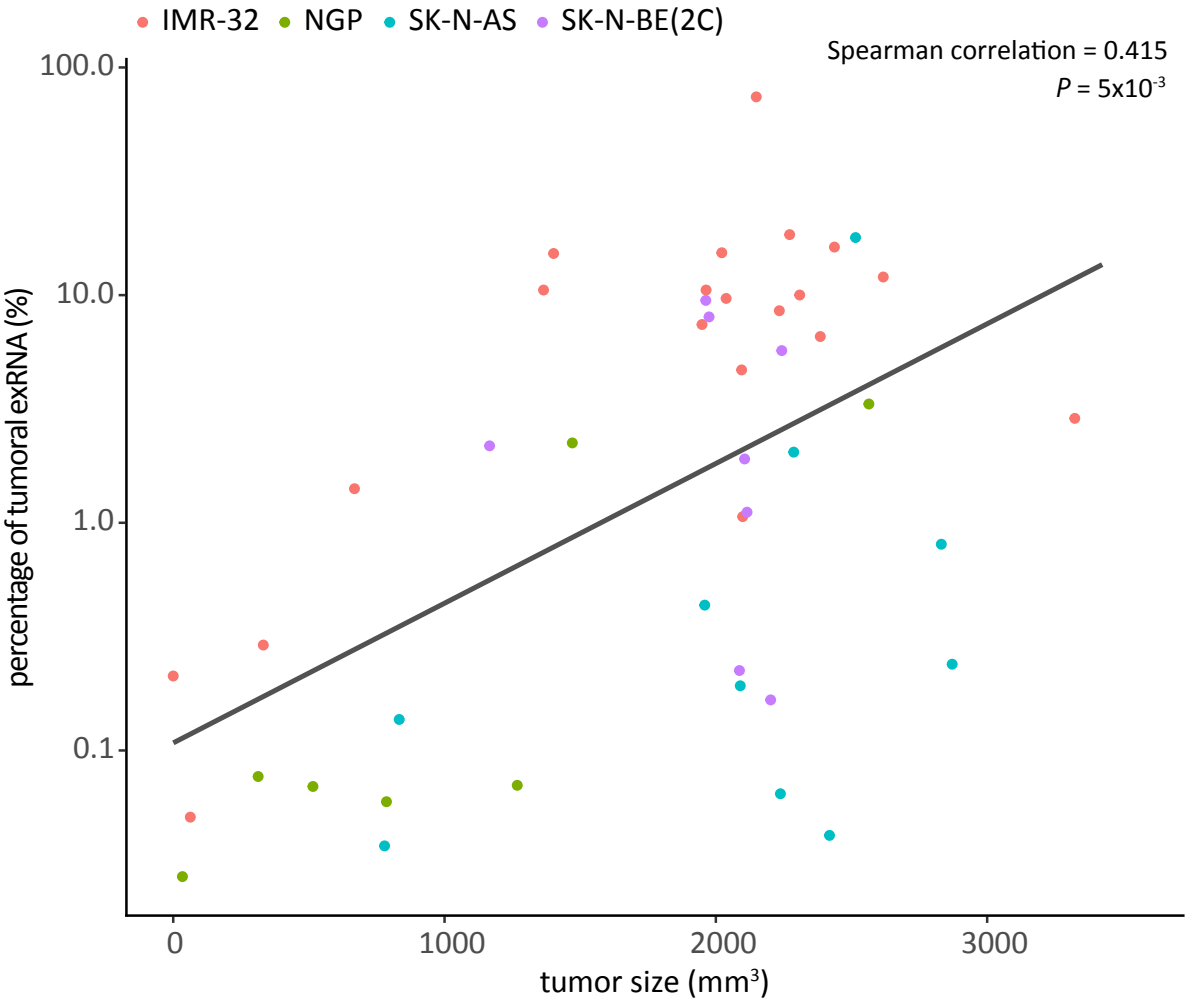

Figure 1. Percentage of tumoral exRNA in function of tumor size in the cell line cohort (n = 45). The different colors represent the different cell-lines. The gray line represents the linear regression line.

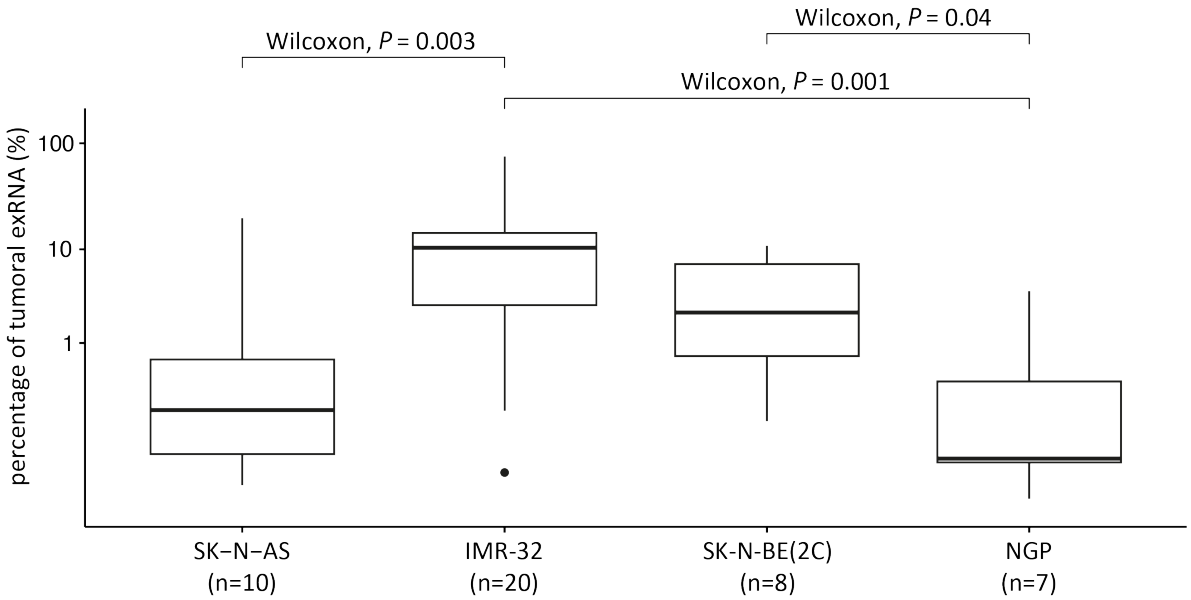

Figure 2. The percentage of tumoral exRNA, grouped per cell line xenograft model. Significant differences between cell lines are indicated with their corresponding Wilcoxon *P* value.

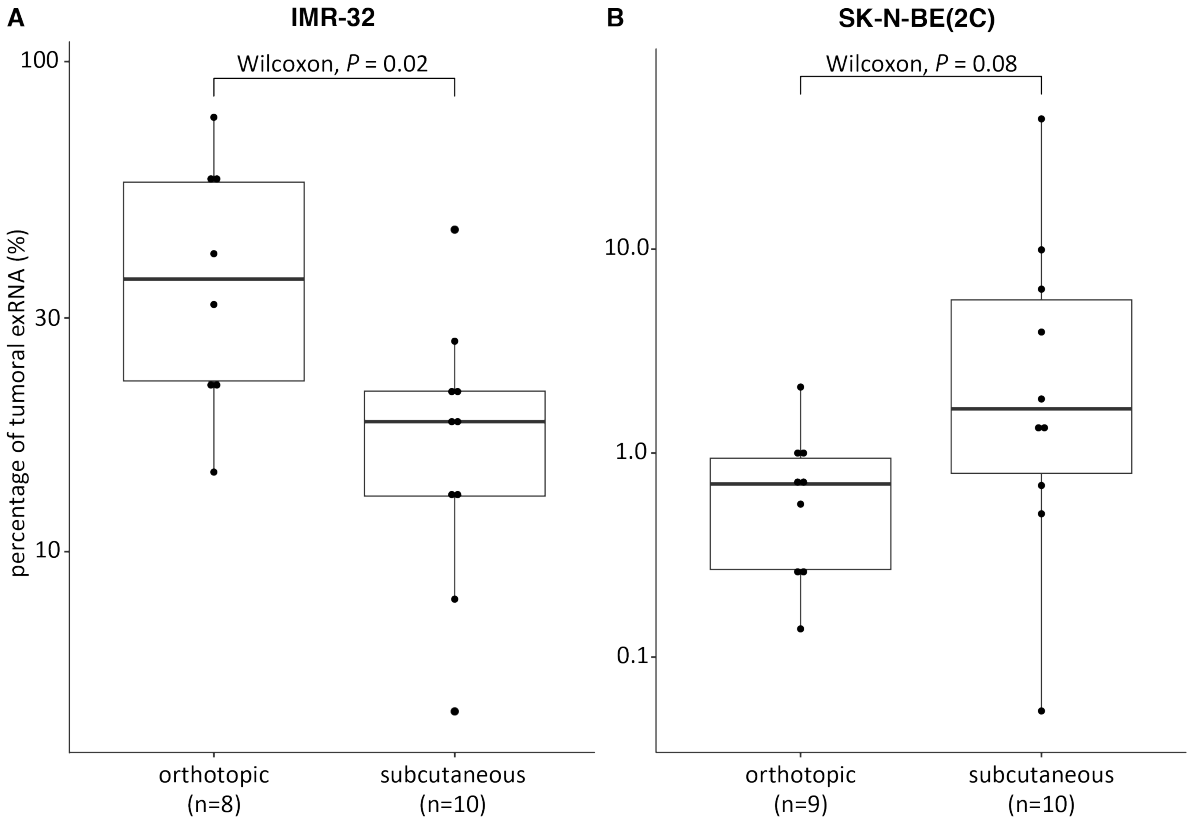

Figure 3. The percentage of tumoral exRNA in mice engrafted orthotopically versus subcutaneously with IMR-32 (A) or SK-N-BE(2C) (B) cells.

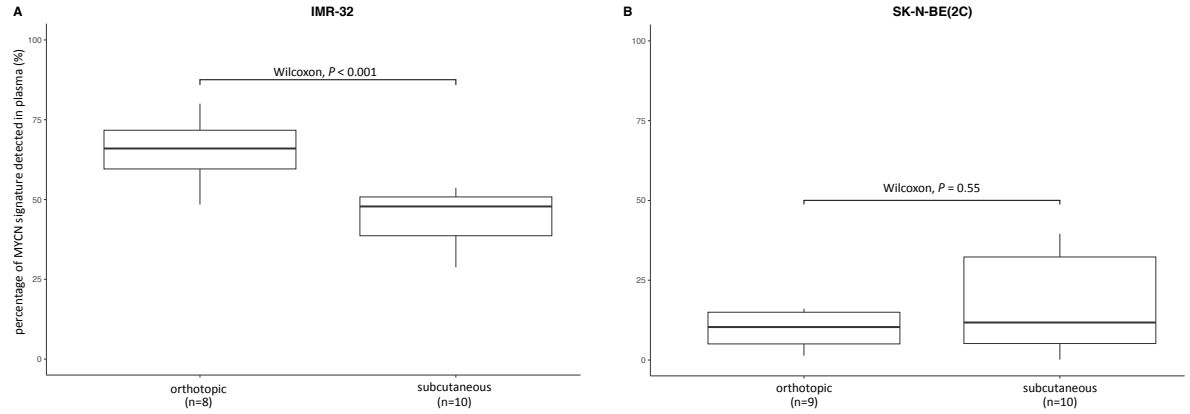

Figure 4. Percentage of MYCN transcriptional target genes, detected in the blood plasma of orthotopically and subcutaneously engrafted mice with IMR-32 (A) or SK-N-BE(2C) (B) cells.

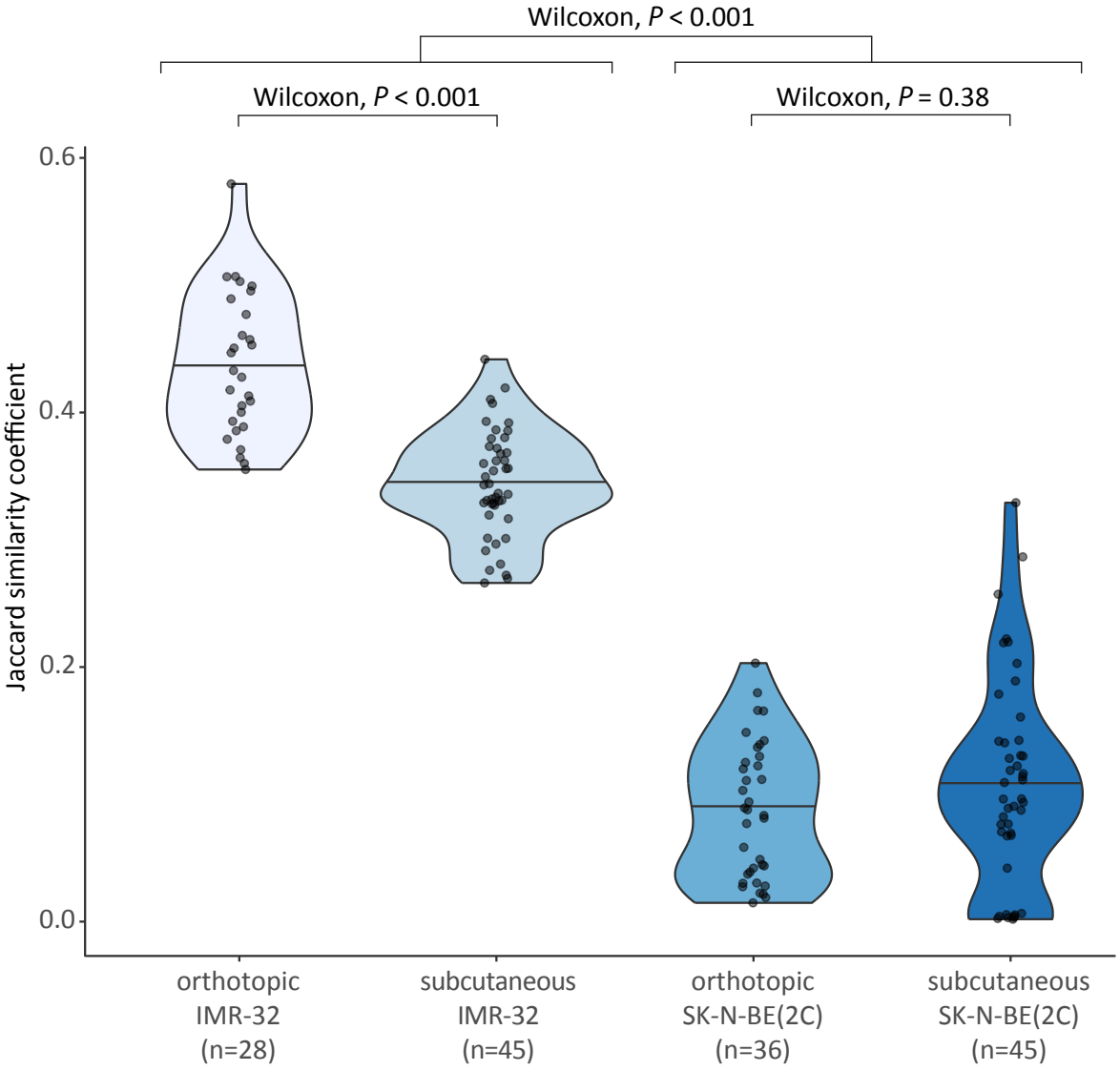

Figure 5. Jaccard similarity coefficient of detected human genes through pairwise comparison of the mice within each model (orthotopic IMR-32, subcutaneous IMR-32, orthotopic SK-N-BE(2C) and subcutaneous SK-N-BE(2C)). The horizontal black line in each model represents the median. IMR-32 and SK-N-BE(2C) tumors display different growth rate and vascularization.

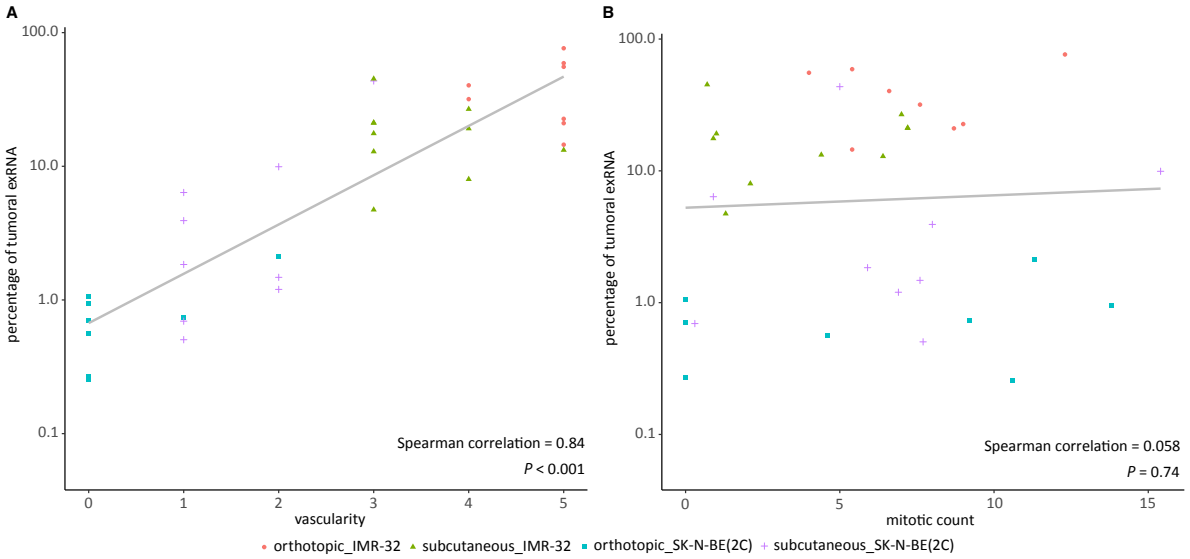

Figure 6. Correlation analysis of the percentage of tumoral exRNA in function of vascularity (A) and mitotic count (B). The gray line represents the linear regression line. All animals from the engraftment site cohort are included (n = 37).

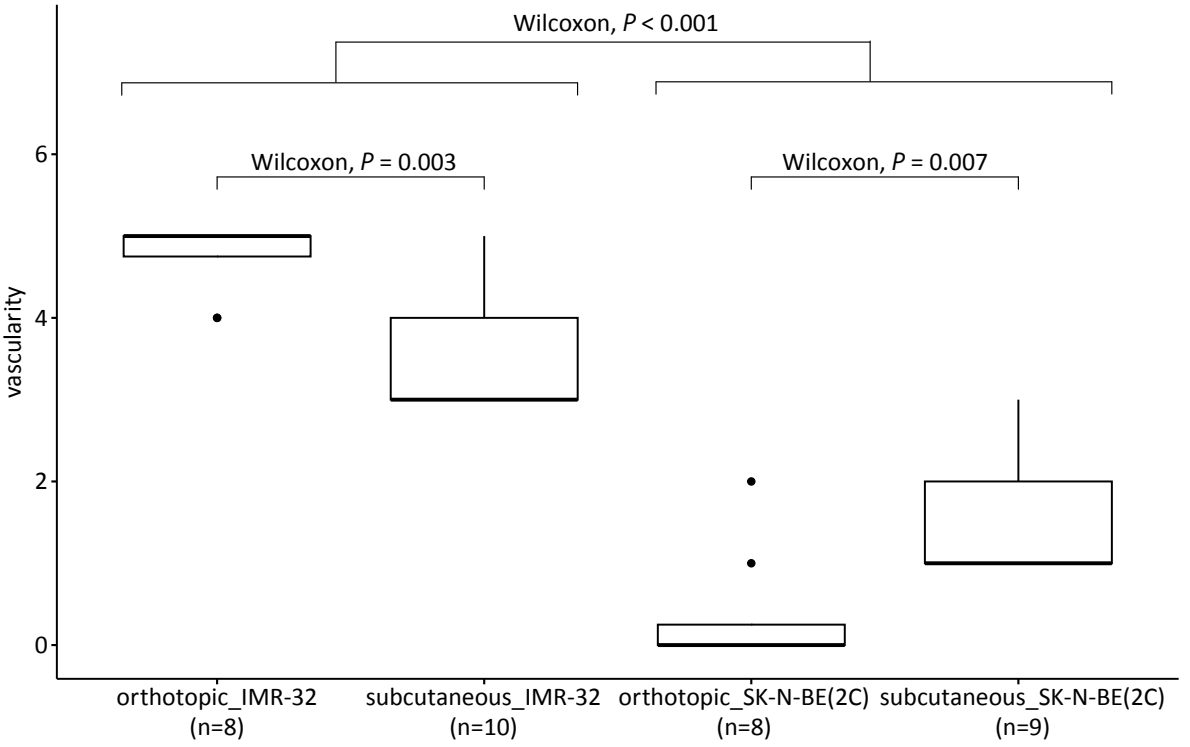

Figure 7. Vascularity levels upon H&E staining of the tumors in the four different models.

Supplementary appendix

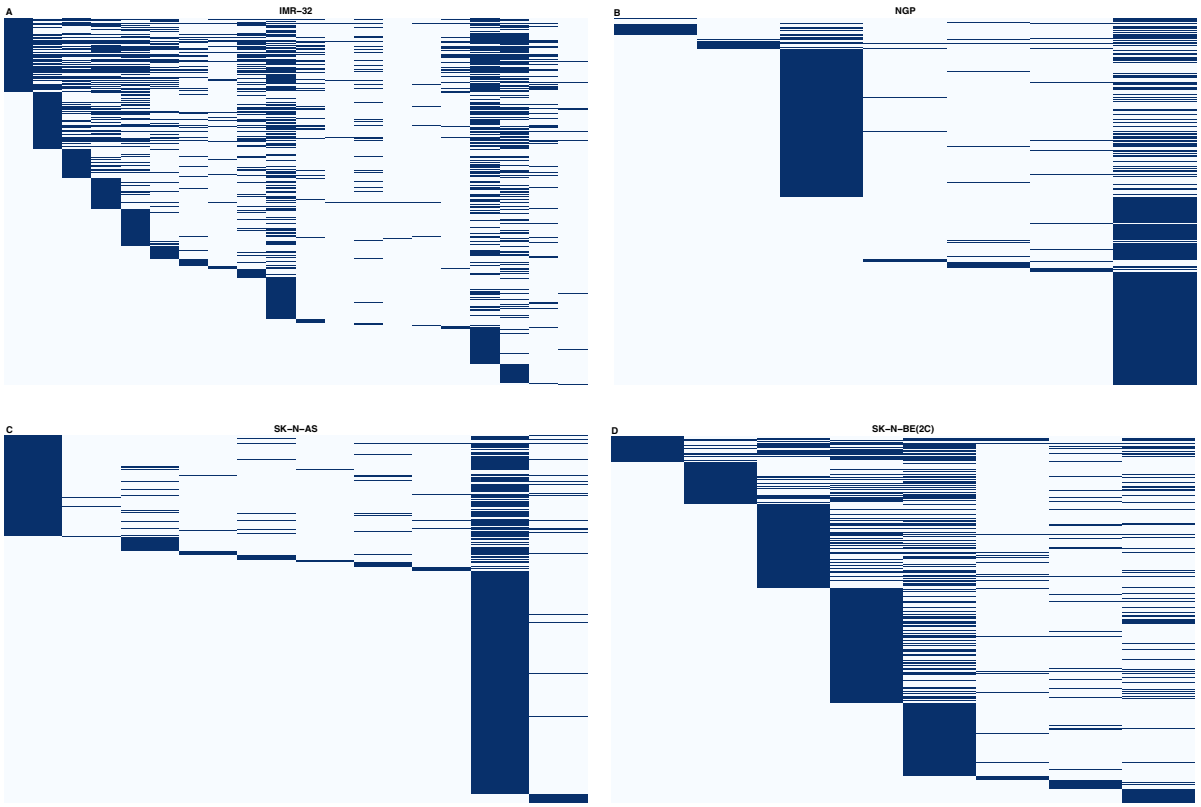

Supplemental Figure 1. The overlap of genes between the mice engrafted with IMR-32 (A; n = 16), NGP (B; n = 3), SK-N-AS (C; n = 8) or SK-N-BE(2C) (D; n = 8). Based on a binary count table, heatmaps were created. In the heatmap, different columns represent different samples while the rows represent the genes detected in one of the samples. A blue line represents a gene that is detected in the plasma of a sample.

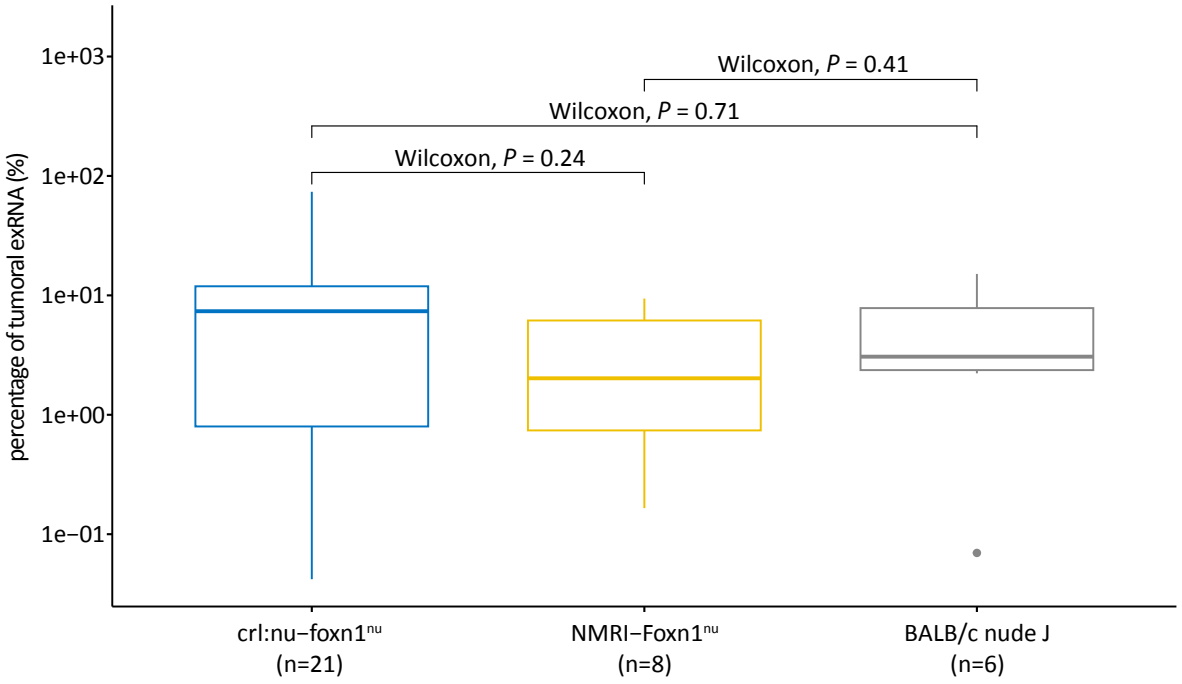

Supplemental Figure 2. Percentage of tumoral exRNA in the different engrafted mouse strains.

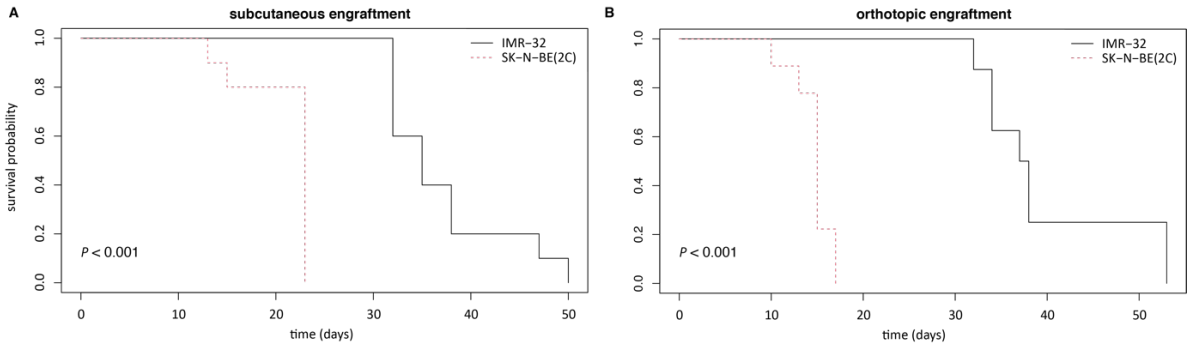

Supplemental Figure 3. Kaplan-Meier curve depicting the probability of survival in function of the lifespan (days) for four different mouse cohorts: subcutaneously engrafted mice with either IMR-32 or SK-N-BE(2C) cells (A) and orthotopically engrafted mice with either IMR-32 or SK-N-BE(2C) cells (B). *P* values of log rank tests are indicated. The lifespan of the mice is defined by the tumor size, as animals were sacrificed at maximally allowed tumor sizes. All animals from the engraftment site cohort are included (n = 37).

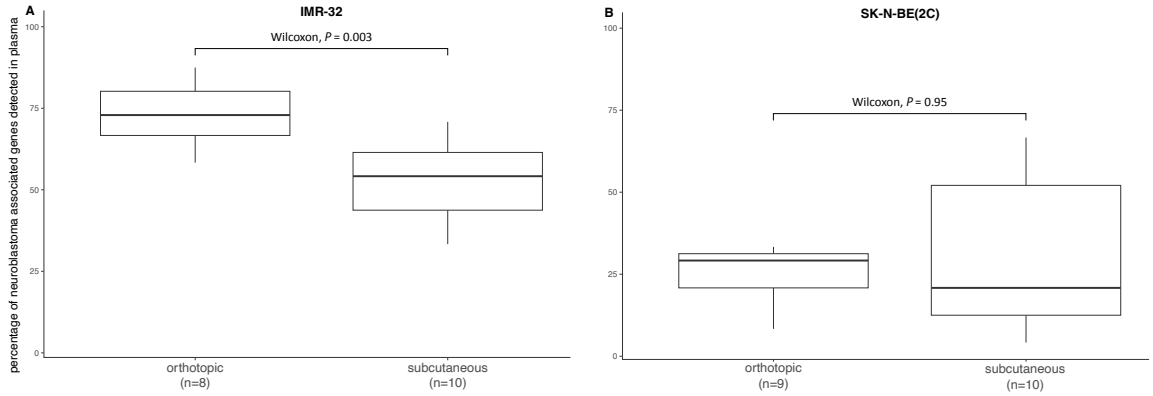

Supplemental Figure 4. Percentage of neuroblastoma associated genes, detected in the blood plasma of orthotopically and subcutaneously engrafted mice with IMR-32 (A) or SK-N-BE(2C) (B) cells.

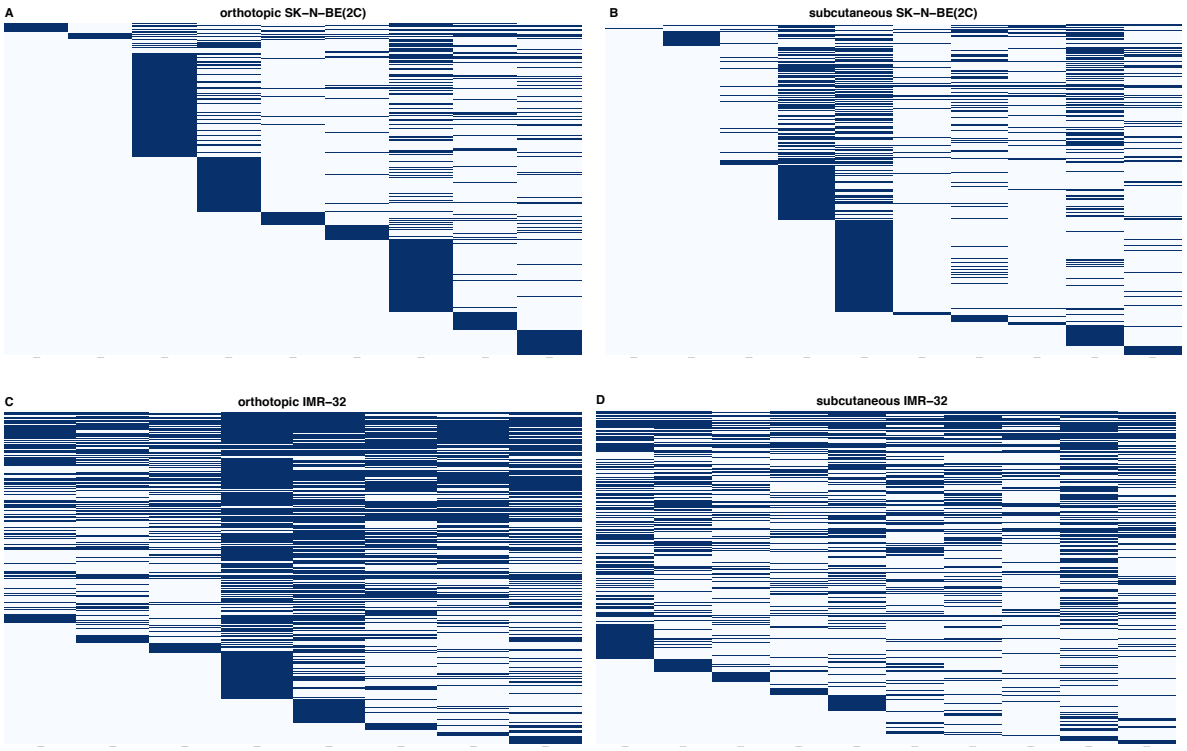

Supplemental Figure 5. Gene overlap in orthotopically (A; n = 9) and subcutaneously (B; n = 10) engrafted SK-N-BE(2C) xenografts, and orthotopically (C; n = 8) and subcutaneously (D; n = 10) engrafted IMR-32 xenografts. Based on a binary count table, heatmaps were created. In the heatmap, different columns represent different samples while the rows represent the genes detected in one of the samples. A blue line represents a gene that is detected in the plasma of a sample.

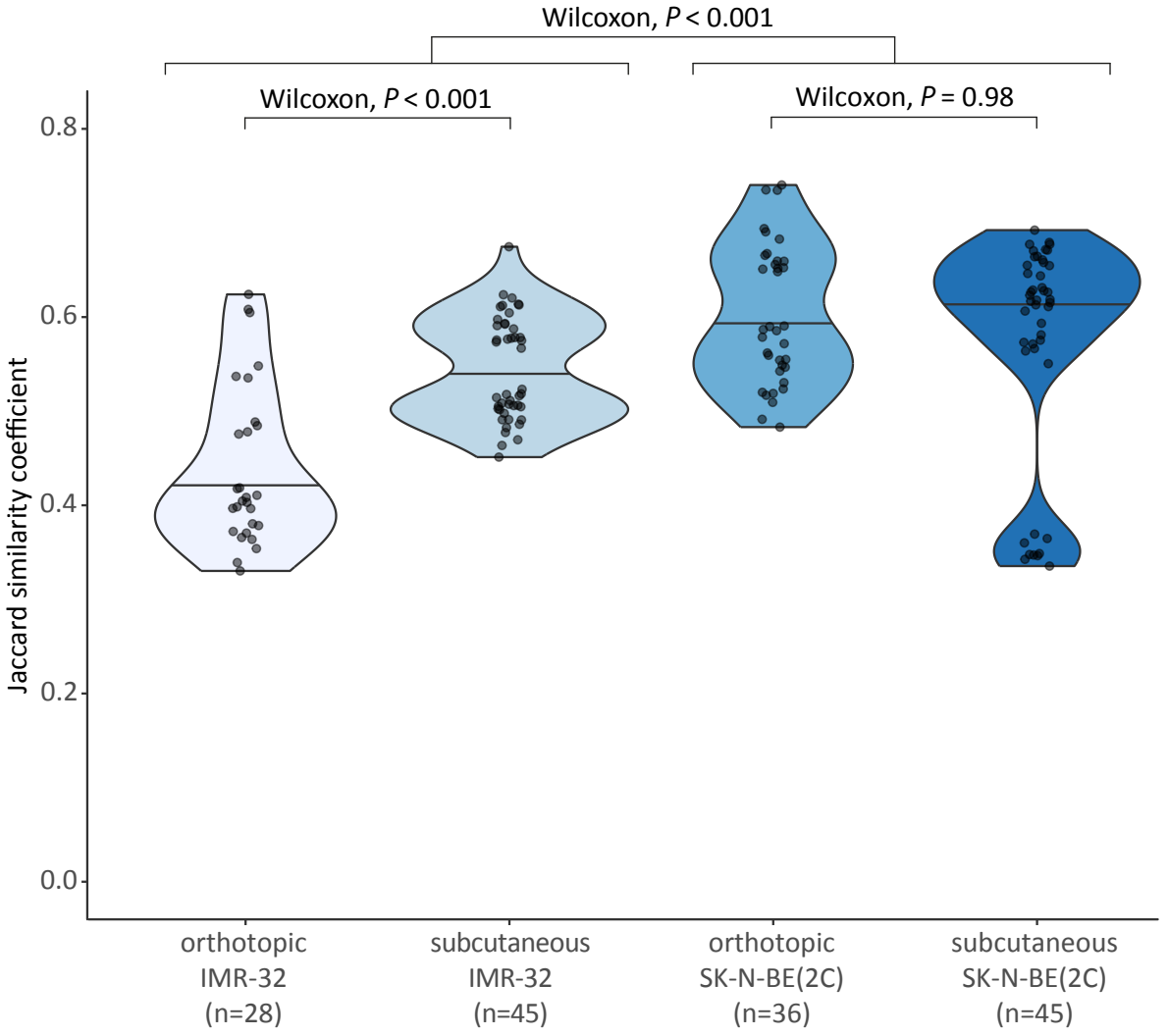

Supplemental Figure 6. Jaccard similarity coefficient obtained by pairwise comparison of murine gene counts (transcripts per million) of the samples within each model (orthotopic IMR-32, subcutaneous IMR-32, orthotopic SK-N-BE(2C) and subcutaneous SK-N-BE(2C)). The horizontal black line in each model represents the median.

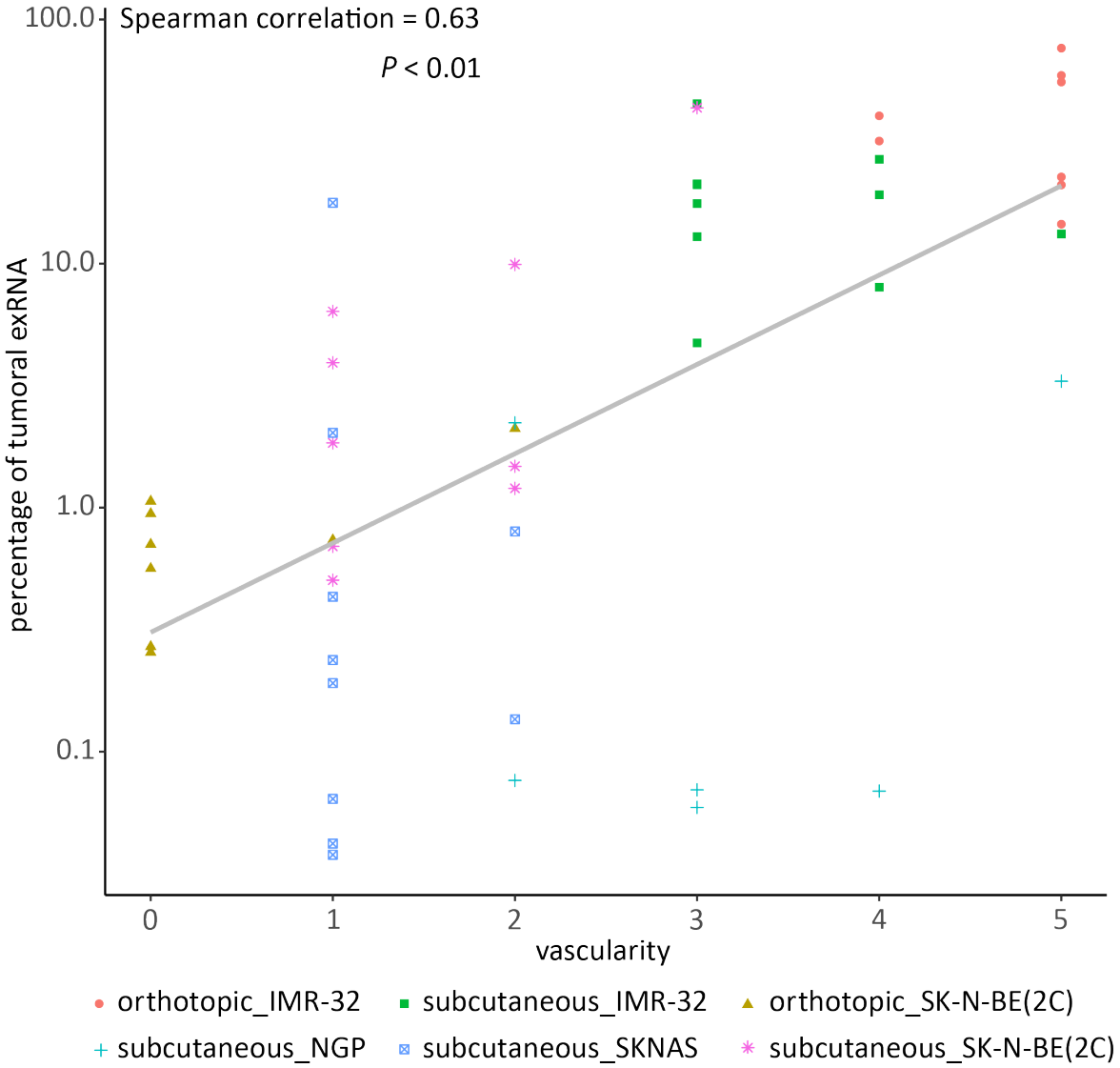

Supplemental Figure 7. Correlation analysis of the percentage of tumoral exRNA in function of vascularity. The gray line represents the linear regression line. All animals from the engraftment site cohort are included, and NGP and SK-N-AS engrafted mice from the cell line cohort (n = 53).

Supplemental Table 1. Characteristics and genetic background of the cell lines that were engrafted in the mice included in our study (1–3)**.** Empty cells are either wild type or no reported aberration.

	NGP	**IMR-32**	**SK-N-AS**	**SK-N-BE(2C)**
location of biopsy	lung	abdomen	bone marrow	bone marrow
cell type	neurite bearing	neurite bearing	substrate adherent	intermediate
MYCN	amplification	amplification		amplification
ALK				
TP53	mutation		mutation	mutation
MDM2	amplification			
CDK4	amplification			
TERT				
ATRX				mutation
NRAS			mutation	
PTPN11				
ATM		mutation		
CDKN2A				
KRAS				
PIK3CA	mutation			
11q loss	yes	yes	yes	
17q gain	yes	yes	yes	yes

1p loss	yes	yes	yes

Supplemental Table 2. Overall, the sequencing data is of good quality. For each RNA sample (RNA ID), the matching mouse ID, biomaterial ID, sample type, mouse cohort, tumor size, plasma input volume and added spike concentrations are shown, as well as haemolysis levels measured by NanoDrop technology (absorbance of light at 414 nm) and RNA sequencing QC results. Sequencing depth: total read number; % trimmed: percentage total base pairs trimmed; % dups R1 or R2: percentage of R1 or R2 reads marked as duplicate; % GC R1 or R2: average GC content percentage of R1 or R2 reads; length R1 or R2: average sequence length (in bp) of R1 or R2 reads; % aligned to combined, human or mouse genome:percentage of reads aligned to the combined, human or mouse genome; exonic depth of combined, human or mouse genome: number of reads mapping to exons in the combined, human or mouse genome. The Sequin/ERCC ratio reflects RNA purification efficiency and should be relatively constant within a single experiment. (cf. excel file https://www.dropbox.com/scl/fo/bop5iddwhbo5m4od6pv26/h?rlkey=hcli8t4j4cexpgy8wj8bc60at&dl=0)

1. Linder S, Bachmann HS, Odersky A, Schaefers S, Klein-hitpass L, Hero B, et al. Absence of telomerase reverse transcriptase promoter mutations in neuroblastoma. Biomed Rep. 2015 Jul;3(4):443–6.
2. Chen L, Rousseau RF, Middleton SA, Nichols GL, Newell DR, Lunec J, et al. Pre-clinical evaluation of the MDM2-p53 antagonist RG7388 alone and in combination with chemotherapy in neuroblastoma. Oncotarget. 2015 Apr 30;6(12):10207–21.
3. Thiele CJ. Neuroblastoma Cell Lines. J Human Cell Culture. 1998;1:21–53.

Discussion and future perspectives

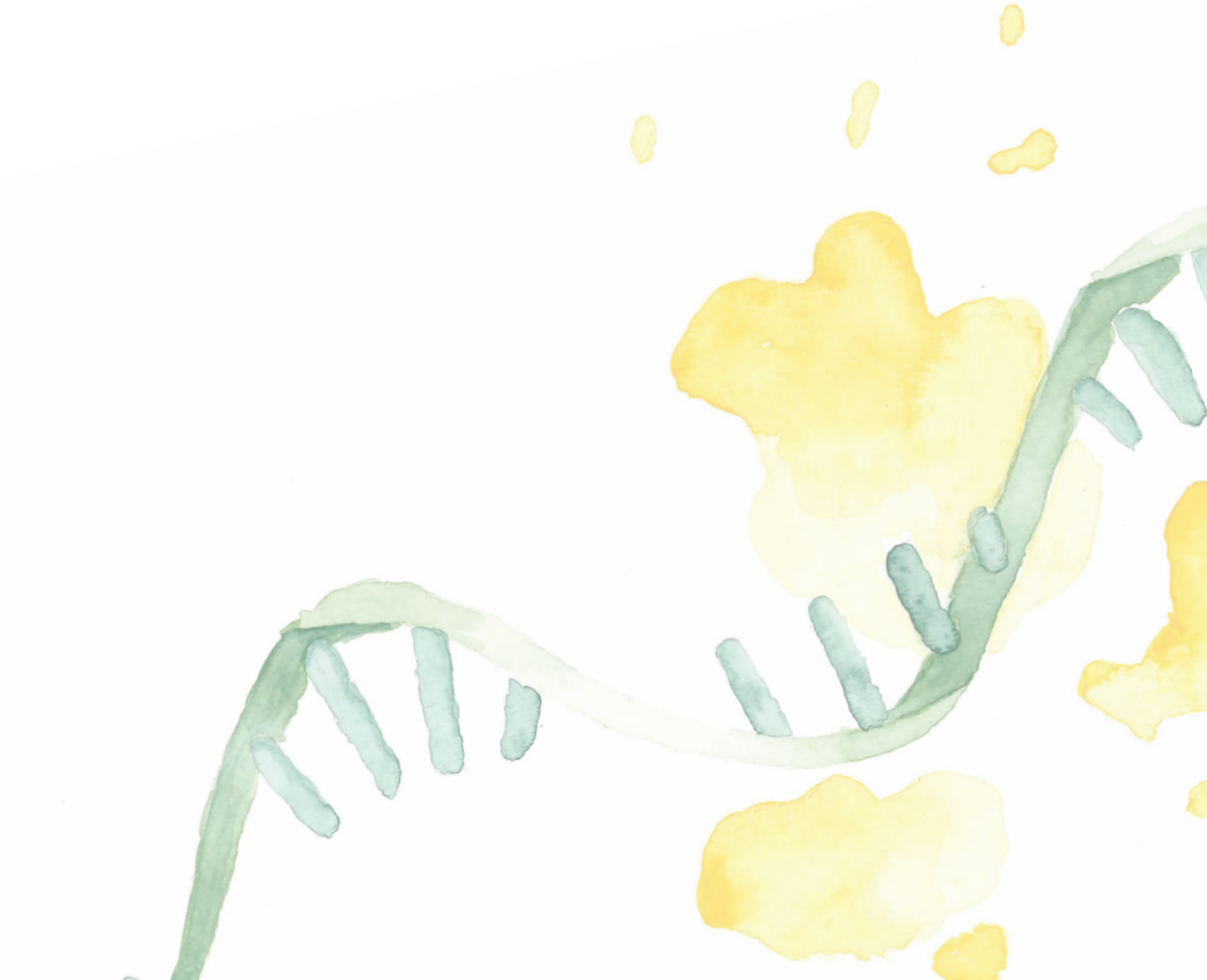

In my thesis, I aimed to explore the value of extracellular RNA (exRNA) in liquid biopsies to monitor treatment response in neuroblastoma. However, given the rarity of the disease, obtaining (sufficient) liquid biopsy samples from neuroblastoma patients is a major challenge. Furthermore, distinguishing tumor from host-derived responses is nearly impossible, except when considering specific tumor aberrations (140). To overcome these limitations, I set out to investigate and optimize animal models to gain insights in tumoral exRNA treatment response signatures. The hybrid context of xenograft models, i.e. mice engrafted with human tumor cells, enables the separation of tumoral (human) from non-tumoral (murine/host) exRNA. Before performing actual treatment response evaluations using xenograft model exRNA, many unresolved questions needed to be addressed. I extensively tackled the question in which blood compartment tumor-derived exRNA resides. Furthermore, it was unclear what impact experimental conditions, such as tumor size, tumor type, and injection site, may have on the tumoral exRNA levels in the blood plasma. I tried to chart the factors impacting the exRNA levels in neuroblastoma xenograft models and highlighted important findings on the route to an optimal modelling tool for further use in research.

1. Blood compartment with the highest tumoral exRNA content

Extracellular RNA can either be freely floating in circulation, or associated with ribonucleoprotein complexes, lipoprotein complexes or extracellular vesicles (EVs) (8,42). Furthermore, the concept of tumor educated platelets (TEPs) has also emerged recently. The biomarker potential of TEPs is mainly demonstrated through the alternative splicing patterns of platelet RNA, which were shown to be cancer specific. However, TEPs also sequester tumor-derived molecules, such as exRNA (e.g. EML4-ALK fusion transcript in (56)). In-depth transcriptome-wide studies specifically focusing on tumor-derived exRNA in different cell-free blood fractions were completely lacking. By charting the tumoral transcriptome in platelets and three plasma fractions with variable levels of platelets obtained by three sequential centrifugation steps, I demonstrated that tumoral exRNA does not primarily reside in platelets, while host exRNA levels are -expectedly- highest in platelets and platelet-rich plasma fractions (**paper 1**, (138)). I was able to generalize these findings across 11 different mouse models from 6 cancer types (i.e., neuroblastoma, melanoma, breast, endometrial, penile, and lung cancer). Consequently, I put forward that platelet depleted plasma is the preferred fraction to study tumoral exRNA. This represents crucial knowledge to initiate large-scale sample collections for future exRNA studies. Locally, I have helped to define the liquid biopsy collection protocol recently set up by HIRUZ and the Cancer Center of Ghent University Hospital to sample cancer patients. In addition, this knowledge also defined the plasma collection procedures that are being used in pediatric clinical trials, and I was able to secure

access to (part of) these patient samples for exRNA analyses. Of note, I did not study possible enrichment of tumoral exRNA in other plasma fractions such as EVs as this was practically impossible given the low starting volume (i.e., 60 µl) of plasma. Ultrapure purification of EVs cannot be performed on such small volumes and anticipating that EV exRNA concentrations will be much lower than neat plasma exRNA concentrations, we would probably have reached the analytical sensitivity limits of total RNA sequencing. Interestingly, Brinkman et al. have shown that BRAF V600E mutations, as confirmed on tumor tissue of patients, are detectable in EVs from blood, while they are not detected in the platelets, which is in line with our findings (140). Apart from the differences in tumoral exRNA content between blood fractions, a large variability in exRNA abundance and transcript content was observed across cancer types and across individual mice with the same tumor entity (**paper 1**, (138)). This variability might be attributed to different factors, such as tumor size, vascularity, and metastasis pattern, which is further discussed in more detail.

2. Treatment response evaluation in murine xenograft models

After putting forward platelet depleted plasma as the preferred biotype for tumoral exRNA analyses, I set out to evaluate treatment responses in xenograft models. In a first xenograft experiment initiated before the start of the thesis, the biomarker potential of serum miRNAs to monitor neuroblastoma tumor burden and treatment responses was demonstrated (**paper in addendum,** (137)). 57 miRNAs corresponding to neuroblastoma tumor burden were identified and hsa-miR-34a-5p was put forward as a potential pharmacodynamic biomarker of p53 activation in serum upon idasanutlin treatment (137). Based on this evidence, I was triggered to evaluate the biomarker potential of the total exRNA (a bit of a misnomer as miRNAs are not included in the library prep) for the monitoring of treatment responses of neuroblastoma tumors. Although assumed less stable and less explored than miRNAs, the biomarker potential of other exRNAs has been demonstrated in cancer patients, but also in other diseases, such as liver disease, neurodegeneration, and obstetrics (41,47–50). In a first attempt to monitor tumoral exRNA responses to idasanutlin, mice engrafted with *in vitro* responsive cell lines, were treated with idasanutlin and total RNA sequencing was performed on their plasma. While clear treatment responses were observed in the tumor tissue, the plasma exRNA did not reveal biologically meaningful alterations upon treatment. In fact, the tumoral exRNA levels were simply too low in most mice. This finding, in combination with the large variability that was observed previously between mice engrafted with the same tumor entity (paper 1, (138)), made me take a step back and investigate factors responsible for the tumoral exRNA levels in blood plasma (**manuscript under review**).

3. Determinants of the tumoral exRNA levels in murine plasma

3.1. Tumor size

I demonstrated a correlation between tumor size and tumoral exRNA levels (**manuscript under review**). With a subcutaneous tumor size of ~1000 mm^3 (dimensions of ± 12.6 x 12.6 mm), a decent fraction of tumoral exRNA is detectable (0.0420% to 73.6%, median 4.65%) in the blood plasma for treatment response experiments. This tumor size is still ethically allowed in mice, however, when translating this to the human situation, we end up with tumor sizes that are surreal. A tumor with a volume of 1000 mm^3 weighs on average 1 g, which corresponds to 5 % of the body weight of a 20 g weighing mouse. By translating this to the human situation, this would be a tumor of 3.5 kg in a person weighing 70 kg, or a 3500 cm^3 tumor (± 15.2 cm x 15.2 cm dimensions) in a 70,000 cm^3 human being (1 g/cm^3). These dimensions are very rare, if not impossible, for human tumors. Furthermore, exRNA biomarkers for diagnosis or detection of early relapse (that is not detectable on imaging yet) need to have utility for tumor sizes that are much smaller. Also, a surgical resection of big tumors might precede administration of adjuvant treatments. Hence, monitoring the tumoral exRNA response to treatment will be performed at smaller, postsurgical tumor sizes. Of note, this tumor size dependency has only been shown in heterotopic, subcutaneous models. Orthotopic injection might result in higher exRNA levels at lower, more realistic, tumor sizes. This can be assessed in future experiments by longitudinal sampling of mice at different tumor sizes.

3.2. Tumor entity

The tumoral exRNA levels also depend on the cancer type (such as neuroblastoma, melanoma, breast, penile, lung and endometrial cancer) and cancer subtype (i.e., neuroblastoma cell lines), as described in the **manuscript under review and paper 1** (138)). The tumor entity cannot be controlled in a human situation. However, this can be considered when performing preclinical studies. For instance, when comparing exRNA alterations upon treatment in responders and non-responders, the cell lines can be carefully selected based on their predetermined exRNA levels in the circulation.

Related to tumor entity, patient-derived xenografts might be better suited than cell line-derived xenografts to monitor treatment responses. Cells cultured *in vitro* can undergo selection, developing aberrant and irreversible genetic, transcriptional, and phenotypic changes, which are not consistent with the properties of the original patient tumor (141–143). The study from Braekeveldt et al. demonstrated that gene signatures, correlating with neuroblastoma-associated processes and with clinical characteristics including patient

prognosis, remain stable over a period of more than 2 years of *in vivo* serial passaging of patient-derived xenografts in mice (144). However, when multiple patient-derived orthotopic xenografts were generated from a single high-risk patient tumor, diverse transcriptional profiles were observed, indicating significant intra-tumor heterogeneity (144). This highlights the importance of considering spatial intra-tumor heterogeneity as a component of high-risk neuroblastoma, which complicates the interpretation of patient-derived xenograft liquid biopsy studies for biomarker discovery and treatment guidance in personalized oncology. Furthermore, the orthotopic tumor engraftment rate using patient-derived material is only around 50% in mice, which is even lower in subcutaneous models (141).

3.3. Engraftment site

I demonstrated that the engraftment site can have an influence on the amount of circulating tumoral exRNA. For, instance, in case of neuroblastoma, orthotopic, intra-adrenal engraftment may increase the tumoral exRNA levels in circulation as compared to subcutaneous engraftment. In my experiments, this was the case for one of the two tested cell lines, i.e., IMR-32 (**manuscript under review**). Intriguingly, for the other cell line, SK-N-BE(2C), I observed the opposite trend, i.e. lower levels of tumoral exRNA in orthotopically engrafted mice. These observations were positively correlated to the vascularity of the tumor. The vascularity score was determined based on visual inspection of hematoxylin and eosin (H&E) stained FFPE samples. Although this ranking was assigned by an independent pathologist without prior knowledge of the sample, better ways for objective scoring of vascularity were exploited. For instance, we attempted platelet endothelial cell adhesion molecule-1 (PECAM) immunostaining, but the tumor tissue morphology was not conserved well after snap freezing in liquid nitrogen. In future experiments, tumors should be formalin-fixed paraffin-embedded immediately after tumor resection, to enable immunohistochemistry.

Apart from a distinct vascularity, higher tumoral exRNA levels may also be the result from metastatic lesions. Orthotopic engraftment has been shown to be associated with a higher metastatic capacity than subcutaneous engraftment in neuroblastoma and other tumor types (145,146). Orthotopically injected IMR-32 cells metastasize mainly to the lung, liver, and bone (147). In neuroblastoma, higher ctDNA levels are found in metastatic patients as compared to localized tumors, and I anticipate that this could be the case for tumoral exRNA as well (126). In this way, the higher levels of tumoral exRNA in the orthotopic IMR-32 model could be explained by potentially metastasizing tumor cells that are not present in subcutaneous models. Furthermore, neo-angiogenesis with large vessels, essential for tumor cell proliferation, invasion and metastasis, has been detected by Doppler ultrasonography in

adrenal tumors, which was increasing over time (147,148). As mice engrafted with orthotopic SK-N-BE(2C) tumors were sacrificed on average after 2 weeks, I hypothesize that this timeframe was too short for neo-angiogenesis and that tumors are therefore less vascularized than their subcutaneously engrafted counterparts and IMR-32 tumors. The extent of metastasis was unfortunately not evaluated but should be assessed in further research. Also, this was a small study on only two neuroblastoma cell lines, so these findings cannot be generalized to all neuroblastoma tumors or other tumor types and should be evaluated more in depth in future studies. Of note, the establishment of orthotopic neuroblastoma tumors is technically challenging, time consuming and requires *in vivo* imaging methods such as magnetic resonance imaging or bioluminescence imaging (141,144).

4. Questioning the studied biofluid, species and biomarker

4.1. Biofluid

I was able to detect tumoral exRNA using only 60 µL blood plasma as input in the RNA extraction procedure. While this is a very small volume, it is still a relatively high fraction of the total blood volume of a mouse. A mouse weighing 20 g contains a theoretical blood volume of 1.6 mL (80 µL/g). By cardiac puncture, up to 1 mL of blood is collected, resulting in approximately 500 µL of plasma after centrifugation. I used 60-200 µL of plasma input in my analyses, which corresponds to 120-400 µL of blood, being 7.5-25 % of the mouse blood volume. Assuming a blood volume of 5 L in a human being, a blood draw of 375 – 1250 mL should be performed. This is not feasible in clinical practice. And even if collecting 375 mL would be feasible, this plasma should be concentrated to lower volumes, as current techniques do not allow to extract exRNA from 375 mL of plasma. Of note, our lab routinely uses 200 µL of human plasma for all its liquid biopsy exRNA studies. Nevertheless, it might be of interest to analyze liquids that are more closely related to the tumor site (3). For instance, neuroblastoma tumors are often implanted in the kidney, or when engrafted in the adrenal gland, tumor infiltration to the kidney is not unusual (141,149,150). Injection in the adrenal gland is technically challenging as it is typically the size of a pinhead. Accommodating large volumes is not feasible, making it hard to standardize the number of injected cells between mice. In addition, the kidney is an excellent vascular medium that allows for the successful growth of tumor models (149). As production of urine occurs in the kidneys, urine might pose a suitable biofluid to study exRNA biomarkers after intrarenal tumor growth in xenograft models. However, translatability to the clinical situation is questionable, as primary, and metastatic renal neuroblastoma is rare (151,152). Of note, urinary catecholamine metabolite levels are routinely assessed at diagnosis of neuroblastoma and are elevated in 90-95% of

patients (153). Apart from accumulation of catecholamine metabolites, nucleic acids might also be accumulated in the urine of neuroblastoma patients.

4.2. Preclinical species

4.2.1. Mouse strain

The mouse strain might impact the amount of tumoral exRNA. A controlled experiment to test this, has not been performed yet. I did use different mouse strains in my experiments so far, but different cell lines were injected in these mice, and they were all sacrificed at different tumor sizes. Moreover, these were all nude mice with no thymus or an abnormal thymus, resulting in a suppressed immune system due to a decreased number of T-cells. Perhaps, the bias would be more pronounced when comparing nude mice with SCID, NOD-SCID and NSG mice (with a relative increase in degree of immunodeficiency). For instance, the neuroblastoma tumor growth rate in NSG mice has shown to be approximately twice as rapid when compared to nude mice (154). In addition, NSG mice injected intravenously with neuroblastoma cells showed a profile of distant metastasis that was not observed in nude mice (154). These factors can have an influence on the number and type of exRNAs.

4.2.2. Other preclinical species

Given the low blood volumes of mice, repetitive sampling longitudinally to follow-up treatment responses is challenging. According to the Institutional Animal Care and Use Committee guidelines, a maximum of 7.5% of the blood volume can be collected weekly in rats and mice. This corresponds to 145-150 µL of blood in a 25 g mouse, and 1.2 to 1.6 mL in a 300 g rat. When multiple sampling timepoints are desired, switching to a rat xenograft model could be considered. In addition, our lab is developing a transgenic *MYCN* rat model, driven by the Dbh promoter. These tumors are of murine origin, increasing the complexity to distinguish tumor from normal responses, but they have an intact immune system, which makes it a more physiologically relevant model.

4.2.3. Preclinical to clinical translation

It remains unclear whether the exRNA in mice models will be similar compared to those in humans. So far, no one else has performed transcriptome-wide studies, focusing on tumor-derived exRNA in mouse models. By consequence, comparison to the human exRNA has not been performed yet. For a fair comparison of the circulating tumoral RNA in xenograft models and humans, we need to compare exRNA from mice engrafted with the same tumor as its human counterpart. But even then, finding an overlap might be tricky, as even mice engrafted with the same cells, do show a high inter-mice variability in the detected transcripts in circulation. The first step would be to understand what is causing this variability to take these

factors into account when establishing a model. Moreover, the feasibility of detecting pharmacodynamic biomarkers and the translatability of our findings will also depend largely on tumor characteristics such as the vascularity, aggressiveness, growth rate and metastatic potential. These factors have been evaluated, on a small scale, in the manuscript which is currently under review.

Although we are not sure how our findings can be extrapolated to the human situation, I still think xenograft models might provide a valuable source of information as to how the tumor reacts transcriptionally to the treatment. When analyzing the circulating RNA in humans, we cannot easily distinguish the responses of the tumor from the normal responses, while this is straightforward in the xenograft models by distinguishing human (tumor) RNA from murine (host) RNA. Moreover, mice are widely used model systems and they do have a lot of similarities with humans. If we can reveal pharmacodynamic biomarkers in the plasma of mice, of course, we need to evaluate their potential to monitor treatment responses in humans in future research.

When specifically considering miRNAs, we did compare the tumoral miRNAs in serum from mice carrying orthotopic neuroblastoma xenografts (cell line-derived xenograft), with the serum from high-risk neuroblastoma patients. We found that 21 out of 57 tumoral miRNAs in mouse serum were also upregulated in serum of high-risk NB patients as compared to healthy serum (paper in addendum (137)).

4.2.4. In vitro alternatives

In vitro models can be used to evaluate the transcriptomic effects of a treatment on tumor cells and the conditioned medium can serve as an *in vitro* alternative for liquid biopsies. However, this conditioned medium is highly artificial and lacks physiological relevance to humans (e.g. absence of vasculature, also in 3D spheroids or organoids). Nevertheless, it is useful to first evaluate transcriptomic activity of the drug by treating and profiling the tumor cells. If no transcriptomic activity is observed *in vitro*, we expect no transcriptomic changes in the plasma of mice.

4.3. Biomarker

Focusing only on exRNA as a biomarker for monitoring treatment responses might not be the best strategy. The field of exRNA is underexplored as compared to cfDNA, since exRNA is assumed to be more prone to degradation and is more sensitive to pre-analytical variables. Therefore, a standardized sample processing procedure is an important prerequisite for exRNA to be applied as a biomarker in a clinical setting. Consortia were founded with the aim to standardize some of these pre-analytical variables, including the NIH's Extracellular RNA

Communication Consortium (ERCC), Blood Profiling Atlas in Cancer (BloodPAC) Consortium (www.bloodpac.org), SPIDIA/SPIDIA4P and CANCER-ID. However, most studies investigating the impact of pre-analytical variables to date have either been focusing on microRNAs or were restricted to mRNA from a limited number of genes. Also, interactions between pre-analytical variables have generally not been investigated to date. The exRNAQC consortium, of which I am part of, has evaluated the impact of blood collection tubes, RNA purification kits, and time to processing, as well as their interactions, by massively parallel sequencing of healthy donor plasma. Even though it is generally known in the field that pre-analytical variables do have a high impact on downstream analysis, pre-analytical variables are typically not or poorly reported in literature, making it challenging to reproduce or compare results.

The advantage of exRNA is its more dynamic character, enabling the real-time monitoring of treatment responses and the detection of genes that are highly expressed, even for tumors that have low shedding rates of DNA to the circulation. It is more dynamic in that sense that treatments will influence the transcription of genes, while the DNA will remain largely unchanged. For a combined analysis of cfDNA and exRNA in the limited amounts of murine plasma (but also for small volumes of blood obtained from infants), co-purification of both nucleic acids from the same plasma sample is highly desired. I have compared the performance of different exRNA/cfDNA co-purification kits resulting in guidelines for their use (**paper 2**, (139)). Furthermore, as we already demonstrated, the potential of miRNAs as pharmacodynamic biomarkers for TP53 reactivation (**paper in addendum**), miRNAs should also be further evaluated in future research.

5. The future to identify predictive biomarkers for a patient's treatment response

In the ideal world, each patient has his or her own "avatar" in the lab. When a patient enters the clinic, all possible biofluids should be collected and stored in an internationally standardized way for a further combined, multi-analyte analysis of all types of circulating biomarkers. Furthermore, a tissue biopsy should be collected at diagnosis for further analysis and for implantation in one or more laboratory animals, representing the patient's avatar. Those avatars could then be used to guide treatment decisions, by revealing the responsiveness of a tumor to specific treatments. By longitudinal collection of biofluids from the patients and their avatars, we can evaluate the potential of analytes in circulation, such as exRNA, to monitor treatment responses. In this way, we might be able to identify biomarkers for a patient's treatment response.

So, to come back to the million-dollar question: "Extracellular RNA in liquid biopsies: entering a new era for cancer treatment monitoring?" I tried to enter the gate to the new era, but I'm still trying to find the key to open the gate. I put a lot of effort in optimizing a xenograft model

to monitor treatment responses of a tumor, but multiple remaining questions are hampering a concrete implementation. Furthermore, exRNA biomarkers in liquid biopsies alone will not offer a comprehensive picture of the treatment response. The new era of treatment response monitoring will rather be based on a multi-analyte approach, integrating the different fields such as transcriptomics, (epi)genomics and proteomics.

References

References

1. Roy AL, Conroy RS. Toward mapping the human body at a cellular resolution. Mol Biol Cell. 2018 Aug 1;29(15):1779–85.

2. Tosar JP, Witwer K, Cayota A. Revisiting Extracellular RNA Release, Processing, and Function. Vol. 46, Trends in Biochemical Sciences. Elsevier Ltd; 2021. p. 438–45.

3. Hulstaert E, Morlion A, Avila Cobos F, Verniers K, Nuytens J, Vanden Eynde E, et al. Charting Extracellular Transcriptomes in The Human Biofluid RNA Atlas. Cell Rep. 2020 Dec 29;33(13):108552.

4. Esposito A, Criscitiello C, Locatelli M, Milano M, Curigliano G. Liquid biopsies for solid tumors: Understanding tumor heterogeneity and real time monitoring of early resistance to targeted therapies. Pharmacol Ther. 2016;157:120–4.

5. Zhang B, Ao B, Lu X, Yang S, Bao P, Wang H, et al. Global research trends on precision oncology: A systematic review, bibliometrics, and visualized study. Medicine (United States). 2022 Oct 28;101(43):E31380.

6. Schwartzberg L, Kim ES, Liu D, Schrag D. Precision Oncology: Who, How, What, When, and When Not? Am Soc Clin Oncol Educ Book. 2017;37:160–9.

7. Heitzer E, Roberts CES, Speicher MR. Current and future perspectives of liquid biopsies in genomics-driven oncology. Nat Rev Genet. 2019;20(February).

8. Pinzani P, D'Argenio V, Re M Del, Pellegrini C, Cucchiara F, Salvianti F, et al. Updates on liquid biopsy: Current trends and future perspectives for clinical application in solid tumors. Vol. 59, Clinical Chemistry and Laboratory Medicine. De Gruyter Open Ltd; 2021. p. 1181–200.

9. Fernández-Lázaro D, Hernández JLG, García AC, Martínez AC, Mielgo-Ayuso J, Cruz-Hernández JJ. Liquid biopsy as novel tool in precision medicine: Origins, properties, identification and clinical perspective of cancer's biomarkers. Diagnostics. 2020 Apr 1;10(4):215.

10. Füzéry AK, Levin J, Chan MM, Chan DW. Translation of proteomic biomarkers into FDA approved cancer diagnostics: Issues and challenges. Clin Proteomics. 2013;10(1).

11. Goetze S, Schüffler P, Athanasiou A, Koetemann A, Poyet C, Fankhauser CD, et al. Use of MS-GUIDE for identification of protein biomarkers for risk stratification of patients with prostate cancer. Clin Proteomics. 2022 Dec 1;19(1).

12. Yang W, Luo Y, Hu S, Li Y, Liu Q. Value of combined detection of serum carcino-embryonic antigen, carbohydrate antigen 19-9 and cyclooxygenase-2 in the diagnosis of colorectal cancer. Oncol Lett. 2018 Aug 1;16(2):1551–6.

13. Pin-Vieito N, Iglesias MJ, Remedios D, Álvarez-Sánchez V, Fernández-Bañares F, Boadas J, et al. Predictive value of carcinoembryonic antigen in symptomatic patients without colorectal cancer: A post-hoc analysis within the colonpredict cohort. Diagnostics. 2020 Dec 1;10(12).

14. Mukama T, Fortner RT, Katzke V, Hynes LC, Petrera A, Hauck SM, et al. Prospective evaluation of 92 serum protein biomarkers for early detection of ovarian cancer. Br J Cancer. 2022 May 18;126(9):1301–9.

15. Cohen JG. In 2014, can we do better than CA125 in the early detection of ovarian cancer? World J Biol Chem. 2014;5(3):286.

16. Cramer DW, Bast RC, Berg CD, Diamandis EP, Godwin AK, Hartge P, et al. Ovarian cancer biomarker performance in prostate, lung, colorectal, and ovarian cancer screening trial specimens. Cancer Prevention Research. 2011 Mar;4(3):365–74.

17. Merriel SWD, Pocock L, Gilbert E, Creavin S, Walter FM, Spencer A, et al. Systematic review and meta-analysis of the diagnostic accuracy of prostate-specific antigen (PSA) for the detection of prostate cancer in symptomatic patients. BMC Med. 2022 Dec 1;20(1).

18. Abcam. ab264604 Human CEA SimpleStep ELISA® Kit [Internet]. 2021 [cited 2023 Jul 28]. Available from: https://www.abcam.com/ps/products/264/ab264604/documents/Human-CEA-ELISA-Kit-protocol-book-v2-ab264604%20(website).pdf

19. Hasin Y, Seldin M, Lusis A. Multi-omics approaches to disease. Genome Biol. 2017 May 5;18(1).

20. Millner LM, Linder MW, Valdes R. Circulating Tumor Cells: A Review of Present Methods and the Need to Identify Heterogeneous Phenotypes. Ann Clin Lab Sci. 2013;43(3):295–304.

21. Ju S, Chen C, Zhang J, Xu L, Zhang X, Li Z, et al. Detection of circulating tumor cells: opportunities and challenges. Biomark Res. 2022 Dec 1;10(1).

22. Lin D, Shen L, Luo M, Zhang K, Li J, Yang Q, et al. Circulating tumor cells: biology and clinical significance. Vol. 6, Signal Transduction and Targeted Therapy. Springer Nature; 2021.

23. Tibbe AGJ, Miller MC, Terstappen LWMM. Statistical considerations for enumeration of circulating tumor cells. Cytometry Part A. 2007 Mar 1;71(3):154–62.

24. Akpe V, Kim TH, Brown CL, Cock IE. Circulating tumour cells: a broad perspective. J R Soc Interface. 2020 Jul 1;17(168).

25. Edd JF, Mishra A, Dubash TD, Herrera S, Mohammad R, Williams EK, et al. Microfluidic concentration and separation of circulating tumor cell clusters from large blood volumes. Lab Chip. 2020;20(3):558–67.

26. Stejskal P, Goodarzi H, Srovnal J, Hajdúch M, van ’t Veer LJ, Magbanua MJM. Circulating tumor nucleic acids: biology, release mechanisms, and clinical relevance. Mol Cancer. 2023 Jan 21;22(1):15.

27. Chicard M, Colmet-Daage L, Clement N, Danzon A, Bohec M, Bernard V, et al. Whole-exome sequencing of cell-free DNA reveals temporo-spatial heterogeneity and identifies treatment-resistant clones in neuroblastoma. Clinical Cancer Research. 2018 Feb 15;24(4):939–49.

28. Alcaide M, Cheung M, Hillman J, Rassekh SR, Deyell RJ, Batist G, et al. Evaluating the quantity, quality and size distribution of cell-free DNA by multiplex droplet digital PCR. Sci Rep. 2020 Dec 1;10(1).

29. List of Cleared or Approved Companion Diagnostic Devices (In Vitro and Imaging Tools) [Internet]. [cited 2023 Mar 2]. Available from: https://www.fda.gov/medical-devices/in-vitro-diagnostics/list-cleared-or-approved-companion-diagnostic-devices-in-vitro-and-imaging-tools

30. FDA. cobas EGFR Mutation Test v2 [Internet]. [cited 2023 Mar 2]. Available from: https://www.fda.gov/drugs/resources-information-approved-drugs/cobas-egfr-mutation-test-v2

31. Krug AK, Enderle D, Karlovich C, Priewasser T, Bentink S, Spiel A, et al. Improved EGFR mutation detection using combined exosomal RNA and circulating tumor DNA in NSCLC patient plasma. Annals of Oncology. 2018 Mar 1;29(3):700–6.

32. Ding SC, Lo YMD. Cell-Free DNA Fragmentomics in Liquid Biopsy. Diagnostics (Basel). 2022 Apr 13;12(4).

33. Esfahani MS, Hamilton EG, Mehrmohamadi M, Nabet BY, Alig SK, King DA, et al. Inferring gene expression from cell-free DNA fragmentation profiles. Nat Biotechnol. 2022 Apr;40(4):585–97.

34. Zeng H, He B, Yi C, Peng J. Liquid biopsies: DNA methylation analyses in circulating cell-free DNA. Journal of Genetics and Genomics. 2018 Apr;45(4):185–92.

35. Smith ZD, Meissner A. DNA methylation: roles in mammalian development. Nat Rev Genet. 2013 Mar 12;14(3):204–20.

36. Baylin SB, Jones PA. A decade of exploring the cancer epigenome — biological and translational implications. Nat Rev Cancer. 2011 Oct 23;11(10):726–34.

37. Baylin SB. Aberrant patterns of DNA methylation, chromatin formation and gene expression in cancer. Hum Mol Genet. 2001 Apr 1;10(7):687–92.

38. Decock A, Creytens D, Lefever S, van der Meulen J, Anckaert J, de Ganck A, et al. mRNA Capture Sequencing and RT-qPCR for the Detection of Pathognomonic, Novel, and Secondary Fusion Transcripts in FFPE Tissue: A Sarcoma Showcase. Int J Mol Sci. 2022 Oct 1;23(19).

39. Wei R, Gao F, Zeng Z, Gui Z, Shang Y, Shen N, et al. Molecular profiling of gene fusions in soft tissue sarcomas by Ion AmpliSeqTM: a study of 35 cases. Transl Cancer Res. 2022 Mar 1;11(3):488–99.

40. Han P, Zhu J, Feng G, Wang Z, Ding Y. Characterization of alternative splicing events and prognostic signatures in breast cancer. BMC Cancer. 2021 Dec 1;21(1).

41. Larson MH, Pan W, Kim HJ, Mauntz RE, Stuart SM, Pimentel M, et al. A comprehensive characterization of the cell-free transcriptome reveals tissue- and subtype-specific biomarkers for cancer detection. Nat Commun. 2021 Dec 1;12(1).

42. Happel C, Ganguly A, Tagle DA. Extracellular RNAs as potential biomarkers for cancer. J Cancer Metastasis Treat. 2020 Sep 17;2020.

43. Anckaert J, Avila Cobos F, Decock A, Deleu J, de Wever O, de Wilde J, et al. Performance of RNA purification kits and blood collection tubes in the Extracellular RNA Quality Control (exRNAQC) study. bioRxiv [Internet]. 2021;2021.05.11.442610. Available from: http://biorxiv.org/content/early/2021/05/11/2021.05.11.442610.abstract

44. O'Brien J, Hayder H, Zayed Y, Peng C. Overview of microRNA biogenesis, mechanisms of actions, and circulation. Vol. 9, Frontiers in Endocrinology. Frontiers Media S.A.; 2018.

45. Raghavendra P, Pullaiah T. RNA-Based Applications in Diagnostic and Therapeutics for Cancer. In: Advances in Cell and Molecular Diagnostics. Elsevier; 2018. p. 33–55.

46. Tutrone R, Donovan MJ, Torkler P, Tadigotla V, McLain T, Noerholm M, et al. Clinical utility of the exosome based ExoDx Prostate(IntelliScore) EPI test in men presenting for initial Biopsy with a PSA 2–10 ng/mL. Prostate Cancer Prostatic Dis. 2020 Dec 7;23(4):607–14.

47. Vorperian SK, Moufarrej MN, Quake SR. Cell types of origin of the cell-free transcriptome. Nat Biotechnol. 2022 Jun 1;40(6):855–61.

48. Chalasani N, Toden S, Sninsky JJ, Rava RP, Braun J V, Zhuang J, et al. Noninvasive stratification of nonalcoholic fatty liver disease by whole transcriptome cell-free mRNA characterization. Am J Physiol Gastrointest Liver Physiol. 2021;320(4):G439–49.

49. Moufarrej MN, Vorperian SK, Wong RJ, Campos AA, Quaintance CC, Sit R v., et al. Early prediction of preeclampsia in pregnancy with cell-free RNA. Nature. 2022 Feb 24;602(7898):689–94.

50. Toden S, Zhuang J, Acosta AD, Karns AP, Salathia NS, Brewer JB, et al. Noninvasive characterization of Alzheimer's disease by circulating, cell-free messenger RNA next-generation sequencing. Sci Adv. 2020;6(50):1654.

51. Pathan M, Fonseka P, Chitti S V., Kang T, Sanwlani R, Van Deun J, et al. Vesiclepedia 2019: A compendium of RNA, proteins, lipids and metabolites in extracellular vesicles. Nucleic Acids Res. 2019 Jan 8;47(D1):D516–9.

52. Geeurickx E, Lippens L, Rappu P, De Geest BG, De Wever O, Hendrix A. Recombinant extracellular vesicles as biological reference material for method development, data normalization and assessment of (pre-)analytical variables. Nat Protoc. 2021 Feb 15;16(2):603–33.

53. Bettin B, Gasecka A, Li B, Dhondt B, Hendrix A, Nieuwland R, et al. Removal of platelets from blood plasma to improve the quality of extracellular vesicle research. Journal of Thrombosis and Haemostasis. 2022 Nov 1;20(11):2679–85.

54. Nguyen PHD, Le AH, Pek JSQ, Pham TT, Jayasinghe MK, Do DV, et al. Extracellular vesicles and lipoproteins – Smart messengers of blood cells in the circulation. Journal of Extracellular Biology. 2022 Jul 5;1(7).

55. Varkey J, Nicolaides T. Tumor-Educated Platelets: A Review of Current and Potential Applications in Solid Tumors. Cureus. 2021 Nov 1;13(11):e19189.

56. Jonas R, Nilsson A, Karachaliou N, Berenguer J, Gimenez-Capitan A, Schellen P, et al. Rearranged EML4-ALK fusion transcripts sequester in circulating blood platelets and enable blood-based crizotinib response monitoring in non-small-cell lung cancer. Oncotarget. 2015;7(1):1066–75.

57. Best MG, Sol N, Kooi I, Tannous J, Westerman BA, Rustenburg F, et al. RNA-Seq of Tumor-Educated Platelets Enables Blood-Based Pan-Cancer, Multiclass, and Molecular Pathway Cancer Diagnostics. Cancer Cell. 2015 Nov 9;28(5):666–76.

58. Best MG, In ’t Veld SGJG, Sol N, Wurdinger T. RNA sequencing and swarm intelligence–enhanced classification algorithm development for blood-based disease diagnostics using spliced blood platelet RNA. Nat Protoc. 2019 Apr 1;14(4):1206–34.

59. Best MG, Sol N, In ‘t Veld SGJG, Vancura A, Muller M, Niemeijer ALN, et al. Swarm Intelligence-Enhanced Detection of Non-Small-Cell Lung Cancer Using Tumor-Educated Platelets. Cancer Cell. 2017 Aug 14;32(2):238-252.e9.

60. Heinhuis K, in ’t Veld S, Dwarshuis G, van den Broek D, Sol N, Best M, et al. RNA-Sequencing of Tumor-Educated Platelets, A Novel Biomarker for Blood Based Sarcoma Diagnostics. European Journal of Surgical Oncology. 2020;46(2):e7.

61. Liefaard MC, Moore KS, Mulder L, van den Broek D, Wesseling J, Sonke GS, et al. Tumour-educated platelets for breast cancer detection: biological and technical insights. Br J Cancer. 2023 Feb 10;128(8):1572–81.

62. Chen G, Zhang J, Fu Q, Taly V, Tan F. Integrative analysis of multi-omics data for liquid biopsy. Br J Cancer. 2023 Feb 16;128(4):505–18.

63. Paoletti C, Schiavon G, Dolce EM, Darga EP, Carr TH, Geradts J, et al. Circulating Biomarkers and Resistance to Endocrine Therapy in Metastatic Breast Cancers: Correlative Results from AZD9496 Oral SERD Phase I Trial. Clinical Cancer Research. 2018 Dec 1;24(23):5860–72.

64. Putcha G, Liu TY, Ariazi E, Bertin M, Drake A, Dzamba M, et al. Blood-based detection of early-stage colorectal cancer using multiomics and machine learning. Journal of Clinical Oncology. 2020 Feb 1;38(4_suppl):66–66.

65. Cohen JD, Javed AA, Thoburn C, Wong F, Tie J, Gibbs P, et al. Combined circulating tumor DNA and protein biomarker-based liquid biopsy for the earlier detection of pancreatic cancers. Proc Natl Acad Sci U S A. 2017 Sep 19;114(38):10202–7.

66. Killock D. CancerSEEK and destroy — a blood test for early cancer detection. Nat Rev Clin Oncol. 2018 Mar 6;15(3):133–133.

67. Cohen JD, Li L, Wang Y, Thoburn C, Afsari B, Danilova L, et al. Detection and localization of surgically resectable cancers with a multi-analyte blood test. Science (1979). 2018 Feb 23;359(6378):926–30.

68. Johnsen JI, Dyberg C, Wickström M. Neuroblastoma—A neural crest derived embryonal malignancy. Front Mol Neurosci. 2019 Feb 12;12.

69. Gomez RL, Ibragimova S, Ramachandran R, Philpott A, Ali FR. Tumoral heterogeneity in neuroblastoma. Biochim Biophys Acta Rev Cancer. 2022 Nov 1;1877(6).

70. Schoenwolf GC, Bleyl SB, Brauer PR, Fracis-West PH, Larsen WJ. Larsen's human embryology. Fourth Edition. Churchill Livingstone; 2009.

71. Lumb R, Schwarz Q. Sympathoadrenal neural crest cells: The known, unknown and forgotten? Vol. 57, Development Growth and Differentiation. 2015. p. 146–57.

72. Rothstein M, Bhattacharya D, Simoes-Costa M. The molecular basis of neural crest axial identity. Vol. 444, Developmental Biology. Elsevier Inc.; 2018. p. S170–80.

73. Takita J. Molecular Basis and Clinical Features of Neuroblastoma. JMA J. 2021 Oct 7;4(4).

74. Lissauer T, Carroll W. Illustrated Textbook of Paediatrics. Fifth Edition. Elsevier; 2018.

75. Ponzoni M, Bachetti T, Corrias MV, Brignole C, Pastorino F, Calarco E, et al. Recent advances in the developmental origin of neuroblastoma: an overview. Vol. 41, Journal of Experimental and Clinical Cancer Research. BioMed Central Ltd; 2022.

76. Irwin MS, Naranjo A, Zhang FF, Cohn SL, London WB, Gastier-Foster JM, et al. Revised Neuroblastoma Risk Classification System: A Report From the Children's Oncology Group. J Clin Oncol. 2021;39:3229–41.

77. Sokol E, Desai A V. The evolution of risk classification for neuroblastoma. Children. 2019 Feb 1;6(2).

78. University of Chicago. INRG Data Commons [Internet]. [cited 2023 Mar 15]. Available from: https://commons.cri.uchicago.edu/inrg/

79. Morgenstern DA, Pötschger U, Moreno L, Papadakis V, Owens C, Ash S, et al. Risk stratification of high-risk metastatic neuroblastoma: A report from the HR-NBL-1/SIOPEN study. Pediatr Blood Cancer. 2018 Nov 1;65(11).

80. Liang WH, Federico SM, London WB, Naranjo A, Irwin MS, Volchenboum SL, et al. Tailoring Therapy for Children With Neuroblastoma on the Basis of Risk Group Classification: Past, Present, and Future. JCO Clin Cancer Inform. 2020 Nov;(4):895–905.

81. Paolini L, Hussain S, Galardy PJ. Chromosome instability in neuroblastoma: A pathway to aggressive disease. Front Oncol. 2022 Oct 20;12.

82. Schleiermacher G, Mosseri V, London WB, Maris JM, Brodeur GM, Attiyeh E, et al. Segmental chromosomal alterations have prognostic impact in neuroblastoma: a report from the INRG project. Br J Cancer. 2012 Oct 13;107(8):1418–22.

83. SIOPEN R-NET [Internet]. [cited 2023 Feb 14]. Available from: https://www.siopen.net

84. Meany HJ. Non-high-risk neuroblastoma: Classification and achievements in therapy. Children. 2019 Jan 1;6(1).

85. Pearson ADJ, Pinkerton R, Lewis IJ, Imeson J, Ellershaw C, Machin D. High-dose rapid and standard induction chemotherapy for patients aged over 1 year with stage 4 neuroblastoma: a randomised trial. The Lancet Oncology. 2008;9(3):247–56.

86. Garaventa A, Poetschger U, Valteau-Couanet D, Luksch R, Castel V, Elliott M, et al. Randomized Trial of Two Induction Therapy Regimens for High-Risk Neuroblastoma: HR-NBL1.5 International Society of Pediatric Oncology European Neuroblastoma Group Study. Journal of Clinical Oncology. 2021 Aug 10;39(23):2552–63.

87. Amoroso L, Erminio G, Makin G, Pearson ADJ, Brock P, Valteau-Couanet D, et al. Topotecan-vincristine-doxorubicin in stage 4 high-risk neuroblastoma patients failing to achieve a complete metastatic response to rapid COJEC: A SIOPEN study. Cancer Res Treat. 2018 Jan 1;50(1):148–55.

88. Ladenstein R, Pötschger U, Pearson ADJ, Brock P, Luksch R, Castel V, et al. Busulfan and melphalan versus carboplatin, etoposide, and melphalan as high-dose chemotherapy for high-risk neuroblastoma (HR-NBL1/SIOPEN): an international, randomised, multi-arm, open-label, phase 3 trial. Lancet Oncol. 2017 Apr 1;18(4):500–14.

89. Pasqualini C, Valteau-Couanet D, Ladenstein R. High-risk neuroblastoma standard clinical practice recommendations [Internet]. [cited 2023 Feb 14]. Available from: https://www.srohp.ro/wp-content/uploads/2022/01/escp-high-risk-neuroblastoma-standard-clinical-practice-recommendations.pdf

90. Pasqualini C. high-risk neuroblastoma: standard clinical practice recommendations [Internet]. 2022 [cited 2023 Feb 15]. Available from: https://siope.eu/media/documents/escp-webinar-22sept-slides.pdf

91. Corallo D, Frabetti S, Candini O, Gregianin E, Dominici M, Fischer H, et al. Emerging Neuroblastoma 3D In Vitro Models for Pre-Clinical Assessments. Front Immunol. 2020 Nov 26;11.

92. Jazmati D, Butzer S, Hero B, Ahmad Khalil D, Merta J, Bäumer C, et al. Proton Beam Therapy for Children With Neuroblastoma: Experiences From the Prospective KiProReg Registry. Front Oncol. 2021 Jan 20;10.

93. DuBois SG, Macy, ME, Henderson TO. High-Risk and Relapsed Neuroblastoma: Toward More Cures and Better Outcomes. American Society of Clinical Oncology Educational Book. 2022 Jul;(42):768–80.

94. Alba Rubio. Prioritization trial strategy in relapsed neuroblastoma [Internet]. [cited 2023 Feb 15]. Available from: https://www.siopen.net/scripts/files/637e2e7c16fd34.74865346/prioritization-trial-strategy-in-relapsed-neuroblastoma-siopen.pdf

95. Moreno L, Barone G, DuBois SG, Molenaar J, Fischer M, Schulte J, et al. Accelerating drug development for neuroblastoma: Summary of the Second Neuroblastoma Drug Development Strategy forum from Innovative Therapies for Children with Cancer and International Society of Paediatric Oncology Europe Neuroblastoma. Vol. 136, European Journal of Cancer. Elsevier Ltd; 2020. p. 52–68.

96. Trigg RM, Turner SD. ALK in neuroblastoma: Biological and therapeutic implications. Cancers (Basel). 2018 Apr 1;10(4).

97. O'donohue T, Gulati N, Mauguen A, Kushner BH, Shukla N, Rodriguez-Sanchez M, et al. Differential Impact of ALK Mutations in Neuroblastoma. JCO Precis Oncol. 2021;5(PO.20.00181).

98. Berry T, Luther W, Bhatnagar N, Jamin Y, Poon E, Sanda T, et al. The ALKF1174L Mutation Potentiates the Oncogenic Activity of MYCN in Neuroblastoma. Cancer Cell. 2012 Jul 10;22(1):117–30.

99. Goldsmith KC, Mosse YP, Kayser K, Chi YY, Chioda M, Thurm HC, et al. Phase I trial of lorlatinib in combination with topotecan/cyclophosphamide in children with ALK-driven refractory or relapsed neuroblastoma: A new approaches to neuroblastoma therapy consortium study. In: Phase I trial of lorlatinib in combination with topotecan/cyclophosphamide in children with ALK-driven refractory or relapsed neuroblastoma: A new approaches to neuroblastoma therapy consortium study. Journal of Clinical Oncology 40; 2022. p. 10041–10041.

100. Goldsmith KC, Park JR, Kayser K, Malvar J, Chi YY, Groshen SG, et al. Lorlatinib with or without chemotherapy in ALK-driven refractory/relapsed neuroblastoma: phase 1 trial results. Nat Med. 2023 May;29(5):1092–102.

101. Cimmino F, Montella A, Tirelli M, Avitabile M, Lasorsa VA, Visconte F, et al. FGFR1 is a potential therapeutic target in neuroblastoma. Cancer Cell Int. 2022 Dec 1;22(1).

102. Cimmino F, Lasorsa VA, Vetrella S, Iolascon A, Capasso M. A Targeted Gene Panel for Circulating Tumor DNA Sequencing in Neuroblastoma. Front Oncol. 2020 Dec 14;10.

103. Brown LM, Ekert PG, Fleuren EDG. Biological and clinical implications of FGFR aberrations in paediatric and young adult cancers. Oncogene. 2023 Jun 6;42(23):1875–88.

104. Ackermann S, Cartolano M, Hero B, Welte A, Kahlert Y, Roderwieser A, et al. A mechanistic classification of clinical phenotypes in neuroblastoma. Science (1979). 2018;(6419):1165–70.

105. Mlakar V, Morel E, Mlakar SJ, Ansari M, Gumy-Pause F. A review of the biological and clinical implications of RAS-MAPK pathway alterations in neuroblastoma. Journal of Experimental and Clinical Cancer Research. 2021 Dec 1;40(1).

106. Eleveld TF, Oldridge DA, Bernard V, Koster J, Daage LC, Diskin SJ, et al. Relapsed neuroblastomas show frequent RAS-MAPK pathway mutations. Nat Genet. 2015 Aug 30;47(8):864–71.

107. Padovan-Merhar OM, Raman P, Ostrovnaya I, Kalletla K, Rubnitz KR, Sanford EM, et al. Enrichment of Targetable Mutations in the Relapsed Neuroblastoma Genome. PLoS Genet. 2016 Dec 1;12(12).

108. Koneru B, Farooqi A, Nguyen TH, Chen WH, Hindle A, Eslinger C, et al. ALT neuroblastoma chemoresistance due to telomere dysfunction-induced ATM activation is reversible with ATM inhibitor AZD0156. Sci Transl Med. 2021 Aug 18;13(607).

109. Bartolucci D, Montemurro L, Raieli S, Lampis S, Pession A, Hrelia P, et al. MYCN Impact on High-Risk Neuroblastoma: From Diagnosis and Prognosis to Targeted Treatment. Vol. 14, Cancers. MDPI; 2022.

110. Chen L, Pastorino F, Berry P, Bonner J, Kirk C, Wood KM, et al. Preclinical evaluation of the first intravenous small molecule MDM2 antagonist alone and in combination with temozolomide in neuroblastoma. Int J Cancer. 2019 Jun 15;144(12):3146–59.

111. Van Goethem A, Yigit N, Moreno-Smith M, Vasudevan SA, Barbieri E, Speleman F, et al. Dual targeting of MDM2 and BCL2 as a therapeutic strategy in neuroblastoma. Oncotarget. 2017;8(34):57047–57.

112. Wang W, Wang X, Rajaei M, Youn JY, Zafar A, Deokar H, et al. Targeting MDM2 for neuroblastoma therapy: In vitro and in vivo anticancer activity and mechanism of action. Cancers (Basel). 2020 Dec 1;12(12):1–16.

113. Vassilev LT, Vu BT, Graves B, Carvajal D, Podlaski F, Filipovic Z, et al. In Vivo Activation of the p53 Pathway by Small-Molecule Antagonists of MDM2. Science (1979). 2004 Feb 6;303(5659):844–8.

114. Vu B, Wovkulich P, Pizzolato G, Lovey A, Ding Q, Jiang N, et al. Discovery of RG7112: A Small-Molecule MDM2 Inhibitor in Clinical Development. ACS Med Chem Lett. 2013 May 9;4(5):466–9.

115. Hart LS, Rader JA, Raman P, Batra V, Russell MR, Tsang M, et al. Preclinical therapeutic synergy of MEK1/2 and CDK4/6 inhibition in neuroblastoma. Clinical Cancer Research. 2017 Apr 1;23(7):1785–96.

116. Bautista F, Paoletti ; Xavier, Rubino J, Brard C, Keyvan Rezai ;, Nebchi S, et al. Phase I or II Study of Ribociclib in Combination With Topotecan-Temozolomide or Everolimus in Children With Advanced Malignancies: Arms A and B of the AcSé-ESMART Trial. J Clin Oncol. 2021;39:3546–60.

117. Vernooij L, Bate-Eya LT, Alles LK, Lee JY, Koopmans B, Jonus HC, et al. High-throughput screening identifies idasanutlin as a resensitizing drug for venetoclax-resistant neuroblastoma cells. Mol Cancer Ther. 2021 Jun 1;20(6):1161–72.

118. Lamers F, Schild L, den Hartog IJM, Ebus ME, Westerhout EM, Ora I, et al. Targeted BCL2 inhibition effectively inhibits neuroblastoma tumour growth. Eur J Cancer. 2012 Nov;48(16):3093–103.

119. Moreno-Smith M, Lakoma A, Chen Z, Tao L, Scorsone KA, Schild L, et al. p53 Nongenotoxic Activation and mTORC1 Inhibition Lead to Effective Combination for Neuroblastoma Therapy. Clinical Cancer Research. 2017 Nov 1;23(21):6629–39.

120. King D, Yeomanson D, Bryant HE. PI3King the Lock. J Pediatr Hematol Oncol. 2015 May;37(4):245–51.

121. Plana D, Palmer AC, Sorger PK. Independent Drug Action in Combination Therapy: Implications for Precision Oncology. Cancer Discov. 2022 Mar 1;12(3):606–24.

122. Lodrini M, Graef J, Thole-Kliesch TM, Astrahantseff K, Sprussel A, Grimaldi M, et al. Targeted Analysis of Cell-free Circulating Tumor DNA is Suitable for Early Relapse and Actionable Target Detection in Patients with Neuroblastoma. Clinical Cancer Research. 2022 May 1;28(9):1809–20.

123. Thwin KKM, Ishida T, Uemura S, Yamamoto N, Lin KS, Tamura A, et al. Level of Seven Neuroblastoma-Associated mRNAs Detected by Droplet Digital PCR Is Associated with Tumor Relapse/Regrowth of High-Risk Neuroblastoma Patients. Journal of Molecular Diagnostics. 2020 Feb 1;22(2):236–46.

124. Zhuo Z, Lin L, Miao L, Li M, He J. Advances in liquid biopsy in neuroblastoma. Fundamental Research. 2022 Nov 1;2(6):903–17.

125. Bosse KR, Giudice AM, Lane M v., McIntyre B, Schürch PM, Pascual-Pasto G, et al. Serial Profiling of Circulating Tumor DNA Identifies Dynamic Evolution of Clinically Actionable Genomic Alterations in High-Risk Neuroblastoma. Cancer Discov. 2022 Dec 1;12(12):2800–19.

126. Chicard M, Boyault S, Daage LC, Richer W, Gentien D, Pierron G, et al. Genomic copy number profiling using circulating free tumor DNA highlights heterogeneity in neuroblastoma. Clinical Cancer Research. 2016 Nov 15;22(22):5564–73.

127. Combaret V, Iacono I, Bellini A, Bréjon S, Bernard V, Marabelle A, et al. Detection of tumor ALK status in neuroblastoma patients using peripheral blood. Cancer Med. 2015 Apr 1;4(4):540–50.

128. Lodrini M, Sprüssel A, Astrahantseff K, Tiburtius D, Konschak R, Lode HN, et al. Using droplet digital PCR to analyze MYCN and ALK copy number in plasma from patients with neuroblastoma. Oncotarget. 2017;8(49):85234–51.

129. Peitz C, Sprüssel A, Linke RB, Astrahantseff K, Grimaldi M, Schmelz K, et al. Multiplexed Quantification of Four Neuroblastoma DNA Targets in a Single Droplet Digital PCR Reaction. Journal of Molecular Diagnostics. 2020 Nov 1;22(11):1309–23.

130. Van Roy N, Van Der Linden M, Menten B, Dheedene A, Vandeputte C, Van Dorpe J, et al. Shallow whole genome sequencing on circulating cell-free DNA allows reliable noninvasive copy-number profiling in neuroblastoma patients. Clinical Cancer Research. 2017 Oct 15;23(20):6305–15.

131. Kahana-Edwin S, Cain LE, McCowage G, Darmanian A, Wright D, Mullins A, et al. Neuroblastoma molecular risk-stratification of dna copy number and alk genotyping via cell-free circulating tumor dna profiling. Cancers (Basel). 2021 Jul 1;13(13).

132. Zeka F, Decock A, Van Goethem A, Vanderheyden K, Demuynck F, Lammens T, et al. Circulating microRNA biomarkers for metastatic disease in neuroblastoma patients. JCI Insight. 2018 Dec 6;3(23).

133. Murray MJ, Raby KL, Saini HK, Bailey S, Wool S V., Tunnacliffe JM, et al. Solid tumors of childhood display specific serum microRNA profiles. Cancer Epidemiology Biomarkers and Prevention. 2015 Feb 1;24(2):350–60.

134. Ramraj SK, Aravindan S, Somasundaram DB, Herman TS, Natarajan M, Aravindan N. Serum-circulating miRNAs predict neuroblastoma progression in mouse model of high-risk metastatic disease. Oncotarget. 2016 Apr 5;7(14):18605–19.

135. Viprey VF, Gregory WM, Corrias M V., Tchirkov A, Swerts K, Vicha A, et al. Neuroblastoma mRNAs predict outcome in children with stage 4 neuroblastoma: A European HR-NBL1/SIOPEN study. Journal of Clinical Oncology. 2014 Apr 1;32(10):1074–83.

136. Moreno L, Weston R, Viprey V, Tchirkov A, Corrias M, Lammens T, et al. Predicting outcomes with circulating adrenergic neuroblastoma mRNAs in children with relapsed and refractory neuroblastoma: A BEACON-Neuroblastoma biomarker study. Journal of Clinical Oncology. 2022 Jun 1;40(16_suppl):10039–10039.

137. Van Goethem A, Deleu J, Yigit N, Everaert C, Moreno-Smith M, Vasudevan SA, et al. Longitudinal evaluation of serum microRNAs as biomarkers for neuroblastoma burden and therapeutic p53 reactivation. NAR Cancer. 2023 Jan 11;5(1).

138. Vermeirssen V, Deleu J, Morlion A, Everaert C, De Wilde J, Anckaert J, et al. Whole transcriptome profiling of liquid biopsies from tumour xenografted mouse models enables specific monitoring of tumour-derived extracellular RNA. NAR Cancer. 2022 Dec;4(4):zcac037.

139. Deleu J, Schoofs K, Decock A, Verniers K, Roelandt S, Denolf A, et al. Digital PCR-based evaluation of nucleic acid extraction kit performance for the co-purification of cell-free DNA and RNA. Hum Genomics. 2022 Dec 1;16(1).

140. Brinkman K, Meyer L, Bickel A, Enderle D, Berking C, Skog J, et al. Extracellular vesicles from plasma have higher tumour RNA fraction than platelets. J Extracell Vesicles. 2020 Jan 1;9(1).

141. Braekeveldt N, Wigerup C, Gisselsson D, Mohlin S, Merselius M, Beckman S, et al. Neuroblastoma patient-derived orthotopic xenografts retain metastatic patterns and geno- and phenotypes of patient tumours. Int J Cancer. 2015 Mar 1;136(5):E252–61.

142. Stewart E, Shelat A, Bradley C, Chen X, Federico S, Thiagarajan S, et al. Development and characterization of a human orthotopic neuroblastoma xenograft. Vol. 407, Developmental Biology. Academic Press Inc.; 2015. p. 344–55.

143. Sausen M, Leary RJ, Jones S, Wu J, Reynolds CP, Liu X, et al. Integrated genomic analyses identify ARID1A and ARID1B alterations in the childhood cancer neuroblastoma. Nat Genet. 2013 Jan;45(1):12–7.

144. Braekeveldt N, Von Stedingk K, Fransson S, Martinez-Monleon A, Lindgren D, Axelson H, et al. Patient-derived xenograft models reveal intratumor heterogeneity and temporal stability in neuroblastoma. Cancer Res. 2018 Oct 15;78(20):5958–69.

145. Hoffman RM. Patient-derived orthotopic xenografts: Better mimic of metastasis than subcutaneous xenografts. Nat Rev Cancer. 2015 Aug 27;15(8):451–2.

146. Khanna C, Jaboin JJ, Drakos E, Tsokos M, Thiele CJ. Biologically relevant orthotopic neuroblastoma xenograft models: primary adrenal tumor growth and spontaneous distant metastasis. In Vivo. 2002;16(2):77–85.

147. Daudigeos-Dubus E, LE Dret L, Rouffiac V, Bawa O, Leguerney I, Opolon P, et al. Establishment and characterization of new orthotopic and metastatic neuroblastoma models. In Vivo. 2014;28(4):425–34.

148. Han R, Zhao W, Gu X, Gao X, Yang YG, Zhang X. Different tumorigenicity and distinct metastasis and gene signature between orthotopic and subcutaneous neuroblastoma xenografted mice. Aging. 2022 Feb 23;14(4):1932–40.

149. Kim ES, Soffer SZ, Huang J, McCrudden KW, Yokoi A, Manley CA, et al. Distinct response of experimental neuroblastoma to combination antiangiogenic strategies. J Pediatr Surg. 2002;37(3):518–22.

150. Patterson DM, Shohet JM, Kim ES. Preclinical Models of Pediatric Solid Tumors (Neuroblastoma) and Their Use in Drug Discovery. Curr Protoc Pharmacol. 2011 Mar;52(1).

151. Fan R. Primary renal neuroblastoma--a clinical pathologic study of 8 cases. Am J Surg Pathol. 2012 Jan;36(1):94–100.

152. Yoshikawa T, Tanizawa A, Suzuki K, Ikeda K, Nomura E, Maeda Y, et al. High-Risk Neuroblastoma with Metastases to Bilateral Kidneys at Diagnosis. Case Rep Pediatr. 2017;2017:1–5.

153. Harding M, Deyell RJ, Blydt-Hansen T. Catecholamines in neuroblastoma: Driver of hypertension, or solely a marker of disease? Cancer Rep. 2022 Aug 6;5(8).

154. Sartelet H, Durrieu L, Fontaine F, Nyalendo C, Haddad É. Description of a New Xenograft Model of Metastatic Neuroblastoma Using NOD/SCID/Il2rg Null (NSG) Mice. In Vivo (Brooklyn) [Internet]. 2012 Jan 1;26(1):19. Available from: http://iv.iiarjournals.org/content/26/1/19.abstract

Curriculum vitae

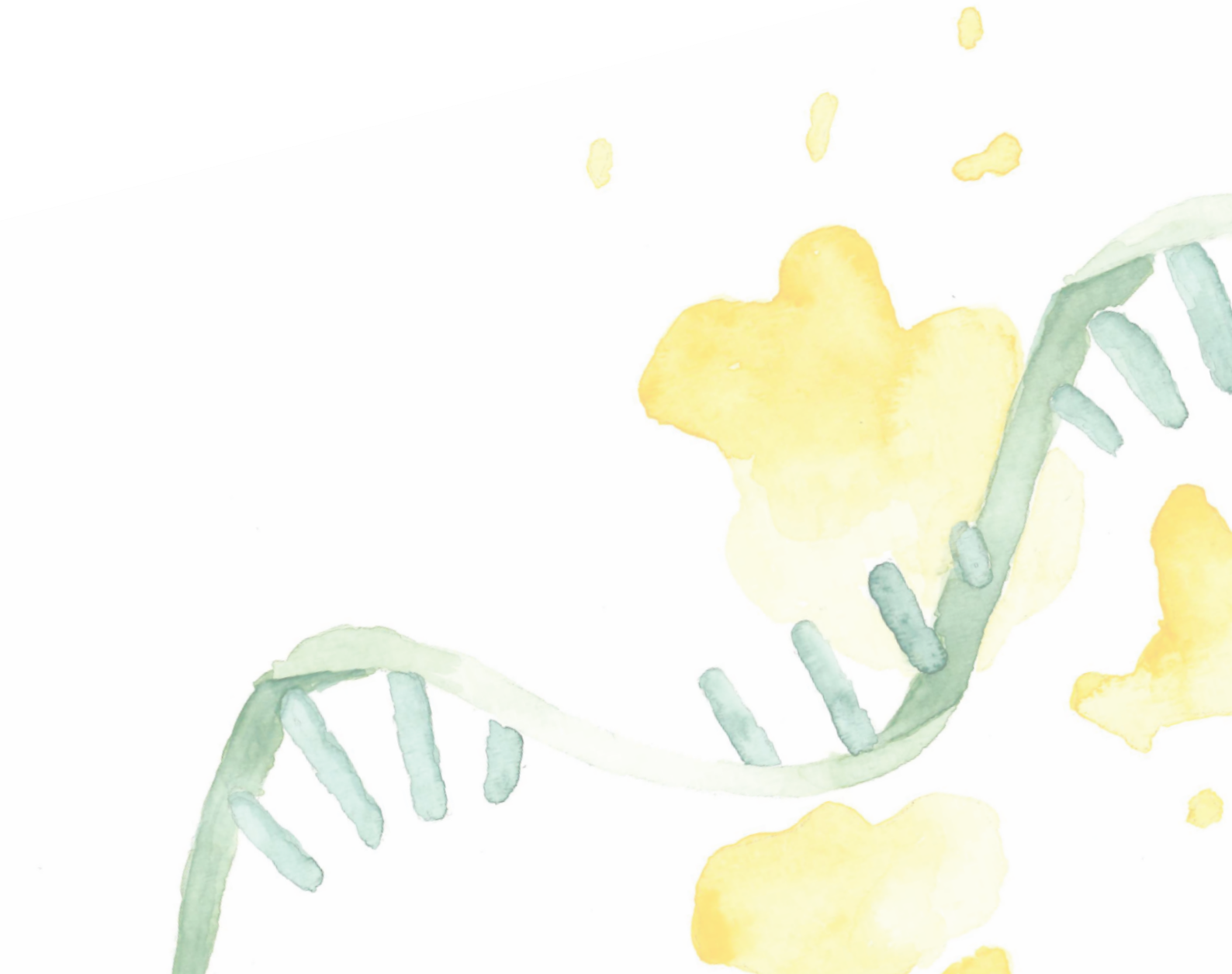

Curriculum vitae

PERSONAL DETAILS

name	Jill Deleu
address	Meersstraat 90, 9070 Heusden, Belgium
telephone	+32 472 34 79 66
e-mail	jill.deleu@ugent.be
born	on November 8, 1995 in Ieper
nationality	Belgian

EXPERIENCE AND EDUCATION

2018-2023 **PhD fellowship**
"Extracellular RNA in liquid biopsies: entering a new era for cancer treatment monitoring?"
Ghent University, Department of biomolecular medicine, OncoRNALab

2016-2018 **Master of Science in Drug Development**
Ghent university, Belgium
Master thesis
"Stabilization of drug nanocrystals with Janus dendrimers"
University of Helsinki, Finland

2013-2016 **Bachelor of Science in Pharmaceutical Sciences**
Ghent University

2007-2013 **Highschool, Latin-Mathematics**
Sint-Vincentiuscollege, Ieper

SKILLS

wet lab plasma preparation, cell culturing, cell transductions, RNA and DNA isolations, qPCR, digital PCR, library preparation, flow cytometry, laboratory mouse experiments (injections, blood draws, MRI scans, subcutaneous and orthotopic xenografting), UV spectrophotometry
Ghent University, Department of biomolecular medicine, OncoRNALab

UV spectrophotometry, dynamic light scattering technique, differential scanning calorimetry
University of Helsinki, Finland

microbiological techniques: inoculation culture plates (manually and by means of a WASP), operating GeneXpert, gram stainings, analysis rapid tests, spa-typing and extended antibiogram
Jan Yperman Hospital, clinical lab, microbiology department, Ieper, Belgium &
University of Groningen, Groningen, Netherlands &
McBride, microbiology department, Ieper, Belgium

bioinformatics next generation sequencing data-analysis, dPCR and qPCR data processing, statistics and data visualization (R), capture probe design, primer design
Ghent University, Department of biomolecular medicine, OncoRNALab

other skills leadership, guidance of people
adobe illustrator

languages Dutch – native language
French – professional working proficiency
English – professional working proficiency

COURSES AND CERTIFICATES

2021 Advanced academic English: Effective slides (online)

2019 CRIG specialist course on 'Cancer' (Ghent)

Laboratory animal science I and II by Prof. Hermans. The course has been recognized by the Belgian Federal Public service of Public Health, Food Chain Safety and Environment as being in compliance with Annex VIII (education of persons responsible for directing animal experiments) of the Royal Decree of the 14th of November 1993 covering the protection of experimental animals (Ghent University)

qPCR course, 2 day training by Biogazelle (Ghent)

Next generation sequencing introduction training by Janick Mathys (Leuven)

Bulk RNA sequencing course by Janick Mathys (Leuven)

Specialist course on digital PCR (Ghent)

Introduction to HPC @UGent (Ghent)

Creative thinking by Jamie McDonald (Ghent)

2018 ICES course in Data Analysis 2018-2019, Module 1 'Introduction to R' (Ghent University)

2017 Summerschool on antimicrobial resistance (University of Groningen)

AWARDS AND GRANTS

Runner-up 'Pieter Van Vlierberghe best paper in oncology award' 2023
Whole transcriptome profiling of liquid biopsies from tumor xenografted mouse models enables specific monitoring of tumor-derived RNA, NAR Cancer, 2022

Paper published as the editor's choice in NAR Cancer
Whole transcriptome profiling of liquid biopsies from tumor xenografted mouse models enables specific monitoring of tumor-derived RNA, NAR Cancer, 2022

Best poster presentation of RNA2022
Whole transcriptome profiling of liquid biopsies from tumor xenografted mouse models enables specific monitoring of tumor-derived RNA, June, 2022, Boulder, Colorado

BOF mobility fund
Grant to attend RNA2022 congress

Best 2' pitch presentation of OncoDot.3, 2021
Whole transcriptome profiling of liquid biopsies from tumor xenografted mouse models enables specific monitoring of tumor-derived RNA, April 28, 2021, online

MENTORSHIP OF BACHELOR AND MASTER STUDENTS

Hanne Van Droogenbroeck – master biomedical sciences (2021-2022)
The RNA signature of model systems treated with the small kinase inhibitor repotrectinib.
Thesis submitted to obtain the degree of master of Biomedical Sciences (Ghent University, Faculty of Medicine and Health Sciences).
Promotor: Bram De Wilde, co-promotor: Tom Van Maerken, mentor: Jill Deleu

Joke Verreth – bachelor farmaceutical and biological laboratory techniques (FBT, 2021)
Optimalization of a PCR-based workflow for the validation of fusion transcripts in plasma.
Thesis submitted to obtain the degree of FBT (Erasmus Hogeschool, Brussels).

Büsra Kutlu – master biomedical sciences (2020-2021)
Validation of circulating biomarkers for early detection of esophageal adenocarcinoma.
Thesis submitted to obtain the degree of master of Biomedical Sciences (Ghent University, Faculty of Medicine and Health Sciences)
Promotor: Katleen De Preter, mentors: Jill Deleu and Kathleen Schoofs

Angie Denolf – bachelor agrotechnology and biotechnology (2020-2021)
Analysis of cfDNA originating from a liquid biopsy for tumor detection. Traineeship to obtain the degree of bachelor in agrotechnology and biotechnology.
Promotor: Katleen De Preter, mentors: Jill Deleu and Kathleen Schoofs.

PUBLICATIONS AND PREPRINTS

Exploration of neuroblastoma xenograft models for tumor extracellular RNA profiling in murine blood plasma. **Jill Deleu***, Hanne Van Droogenbroeck*, Jasper Anckaert, Anneleen Decock, Jilke De Wilde, Kaat Durinck, Liselot Mus, Justine Nuytens, Muhammad Rishfi, Kathleen Schoofs, Frank Speleman, Maaike Van Trimpont, Kimberly Verniers, Nurten Yigit, Jo Vandesompele, Bram De Wilde*, and Tom Van Maerken*. (*shared contribution) ExRNA, 2023 (under review)

Longitudinal evaluation of serum microRNAs as biomarkers for neuroblastoma burden and therapeutic p53 reactivation. Alan Van Goethem, **Jill Deleu,** Nurten Yigit, Celine Everaert, Myrthala Moreno-Smith, Sanjeev A Vasudevan, Fjoralba Zeka, Fleur Demuynck, Eveline Barbieri, Frank Speleman, Pieter Mestdagh, Jason Shohet, Jo Vandesompele* and Tom Van Maerken*. (*shared contribution) NAR Cancer, 2023.

Digital PCR-based evaluation of nucleic acid extraction kit performance for the co-purification of cell-free DNA and RNA. **Jill Deleu***, Kathleen Schoofs*, Anneleen Decock, Kimberly Verniers, Sofie Roelandt, Angie Denolf, Joke Verreth, Bram De Wilde, Tom Van Maerken, Katleen De Preter and Jo Vandesompele. (*shared contribution) Human Genomics, 2022.

Whole transcriptome profiling of liquid biopsies from tumor xenografted mouse models enables specific monitoring of tumor-derived RNA. **Jill Deleu***, Vanessa Vermeirssen*, Annelien Morlion, Celine Everaert, Jilke De Wilde, Jasper Anckaert, Kaat Durinck, Justine Nuytens, Muhammad Rishfi, Franki Speleman, Hanne Van Droogenbroeck, Kimberly Verniers, Maria Francesca Baietti, Maarten Albersen, Eleonora Leucci, Edward Post, Myron G. Best, Tom Van Maerken, Bram De Wilde, Jo Vandesompele*, and Anneleen Decock*. (*shared contribution) NAR Cancer, 2022. **Editor's choice + Runner-up 'Pieter Van Vlierberghe best paper in oncology award' 2023**

mRNA capture sequencing and RT-qPCR for the detection of pathognomonic, novel, and secondary fusion transcripts in FFPE tissue : a sarcoma showcase. Anneleen Decock* , David Creytens*, Steve Lefever, Joni Van der Meulen, Jasper Anckaert, Ariane De Ganck, **Jill Deleu**, Bram De Wilde, Carolina Fierro, Scott Kuersten, Manuel Luypaert, Isabelle Rottiers, Gary P. Schroth, Sandra Steyaert, Katrien Vanderheyden, Eveline Vanden Eynde, Kimberly Verniers, Joke Verreth, Jo Van Dorpe* and Jo Vandesompele*. (*shared contributions) Int. J. Mol. Sci., 2022.

Performance of RNA purification kits and blood collection tubes in the Extracellular RNA Quality Control (exRNAQC) study exRNAQC Consortium. (in alphabetical order) Jasper Anckaert, Francisco Avila Cobos, Anneleen Decock, **Jill Deleu**, Olivier De Wever, Jilke De Wilde, Bert Dhondt, Thibaut D'huyvetter, Celine Everaert, Carolina Fierro, Hetty Hilde Helsmoortel, An Hendrix, Eva Hulstaert, Scott Kuersten, Pieter Mestdagh, Annelien Morlion, Nele Nijs, Justine Nuytens, Annouck Philippron, Thomas Piofczyk, Kathleen Schoofs, Gary P. Schroth, Eveline Vanden Eynde, Jo Vandesompele, Tom Van Maerken, Ruben Van Paemel, Kimberly Verniers, Nurten Yigit. bioRxiv 2021.05.11.442610; doi: https://doi.org/10.1101/2021.05.11.442610

High-Generation Amphiphilic Janus-Dendrimers as Stabilizing Agents for Drug Suspensions. Markus Selin*, Sami Nummelin*, **Jill Deleu**, Jarmo Ropponen, Tapani Viitala, Manu Lahtinen, Jari Koivisto, Jouni Hirvonen, Leena Peltonen, Mauri A. Kostiainen, and Luis M. Bimbo. (*shared contribution) Biomacromolecules, 2018.

ORAL AND POSTER PRESENTATIONS

ANR2023, May, 2023, Amsterdam

Whole transcriptome profiling of liquid biopsies from tumor xenografted mouse models enables specific monitoring of tumor-derived RNA.

Jill Deleu*, Vanessa Vermeirssen*, Annelien Morlion, Celine Everaert, Jilke De Wilde, Jasper Anckaert, Kaat Durinck, Justine Nuytens, Muhammad Rishfi, Franki Speleman, Hanne Van Droogenbroeck, Kimberly Verniers, Maria F. Baietti, Maarten Albersen, Eleonora Leucci, Edward Post, Myron G. Best, Tom Van Maerken, Bram De Wilde, Jo Vandesompele, and Anneleen Decock. (*shared contribution)

ANR2023, May, 2023, Amsterdam

Longitudinal evaluation of serum microRNAs as biomarkers for neuroblastoma burden and therapeutic p53 reactivation.

Jill Deleu, Alan Van Goethem, Nurten Yigit, Celine Everaert, Myrthala Moreno-Smith, Sanjeev A. Vasudevan, Fjoralba Zeka, Fleur Demuynck, Eveline Barbieri, Franki Speleman, Pieter Mestdagh, Jason Shohet, Jo Vandesompele, and Tom Van Maerken.

GOA REINFORCE, January, 2023, Ghent

Transcriptome profiling of liquid biopsies from tumor xenografted mouse models enables specific monitoring of tumor-derived RNA.

LiquidHope annual meeting, September, 2022

Murine xenograft models to differentiate host from tumor response in liquid biopsies.

RNA2022, June, 2022, Boulder

Whole transcriptome profiling of liquid biopsies from tumor xenografted mouse models enables specific monitoring of tumor-derived RNA.

Deleu Jill*, Vermeirssen Vanessa*, Everaert Celine, Morlion Annelien, Verniers Kimberly, Anckaert Jasper, Vandesompele Jo, Van Maerken Tom, Decock Anneleen, De Wilde Bram. (*shared contribution)

GOA REINFORCE, May, 2022, Ghent

Murine xenograft models to differentiate host from tumor response in liquid biopsy.

Research Day, March, 2022, Ghent

Whole transcriptome profiling of liquid biopsies from tumor xenografted mouse models enables specific monitoring of tumor-derived RNA."

Deleu Jill*, Vermeirssen Vanessa*, Everaert Celine, Morlion Annelien, Verniers Kimberly, Anckaert Jasper, Vandesompele Jo, Van Maerken Tom, Decock Anneleen, De Wilde Bram. (*shared contribution)

Meet the PhD Jury, meeting with Manfred Gessler, September, 2021, Ghent

Therapy response monitoring with exRNA

OncoDot.3, April, 2021

Whole transcriptome profiling of liquid biopsies from tumor xenografted mouse models enables specific monitoring of tumor-derived RNA.

Deleu Jill*, Vermeirssen Vanessa*, Everaert Celine, Morlion Annelien, Verniers Kimberly, Anckaert Jasper, Vandesompele Jo, Van Maerken Tom, Decock Anneleen, De Wilde Bram. (*shared contribution)

SIOPEN Biology and Liquid biopsy meeting, April, 2021, online

Validation of 9-miR metastatic load signature in neuroblastoma patients + Tumoral RNA signature in xenograft models

SIOP2020, October, 2020

Whole transcriptome profiling of liquid biopsies from tumor xenografted mouse models enables specific monitoring of tumor-derived RNA.
Deleu Jill*, Vermeirssen Vanessa*, Everaert Celine, Morlion Annelien, Verniers Kimberly, Anckaert Jasper, Vandesompele Jo, Van Maerken Tom, Decock Anneleen, De Wilde Bram. (*shared contribution)

CONGRESSES, WORKSHOPS AND MEETINGS

miniANR 2022
May, 2022, Antwerpen

EU H2020 LiquidHope annual meeting
February, 2021, online

ANR 2021
January, 2021, online

Invited speaker seminar by Prof. Esther Nolte-'t Hoen
Beyond miRNAs: non-coding RNAs in EVs as biomarkers for disease"
February 17, 2020, UZ Ghent

Invited speaker seminar by dr. Stephen Roberts
Innoviation in clinical trial design for pediatric cancer: the MSKCC approach"
February 3, 2020, UZ Ghent

LiquidHope kick-off meeting
January 29, 2020, Charité, Berlin

Precision steering committee meeting
October 15, 2019, Kankercentrum Sciensano Brussel

Knowledge 2 connect and workshop, Grant proposal writing
September 13, 2019, UZ Gent

Symposium "From neuroblast to neuroblastoma"
June 12, 2019, Het Pand, Ghent

2nd KiTZ-Symposium
January 24 & 25, 2019, German Cancer Research Center, Heidelberg

Childhood Cancer Predisposition Symposium
January 23, 2019, German Cancer Research Center, Heidelberg

8th Scientific Progress Meeting Villa Joep
Princess Maxima centrum voor pediatrische oncologie, December 13, 2018, Utrecht

CRIG's Single Cell mini-symposium
December 5, 2018, VIB Ghent

Knowledge 2 connect, 'Give your research a real life. Introduction to TechTransfer'
November 23, 2018, UZ Gent

Addenda

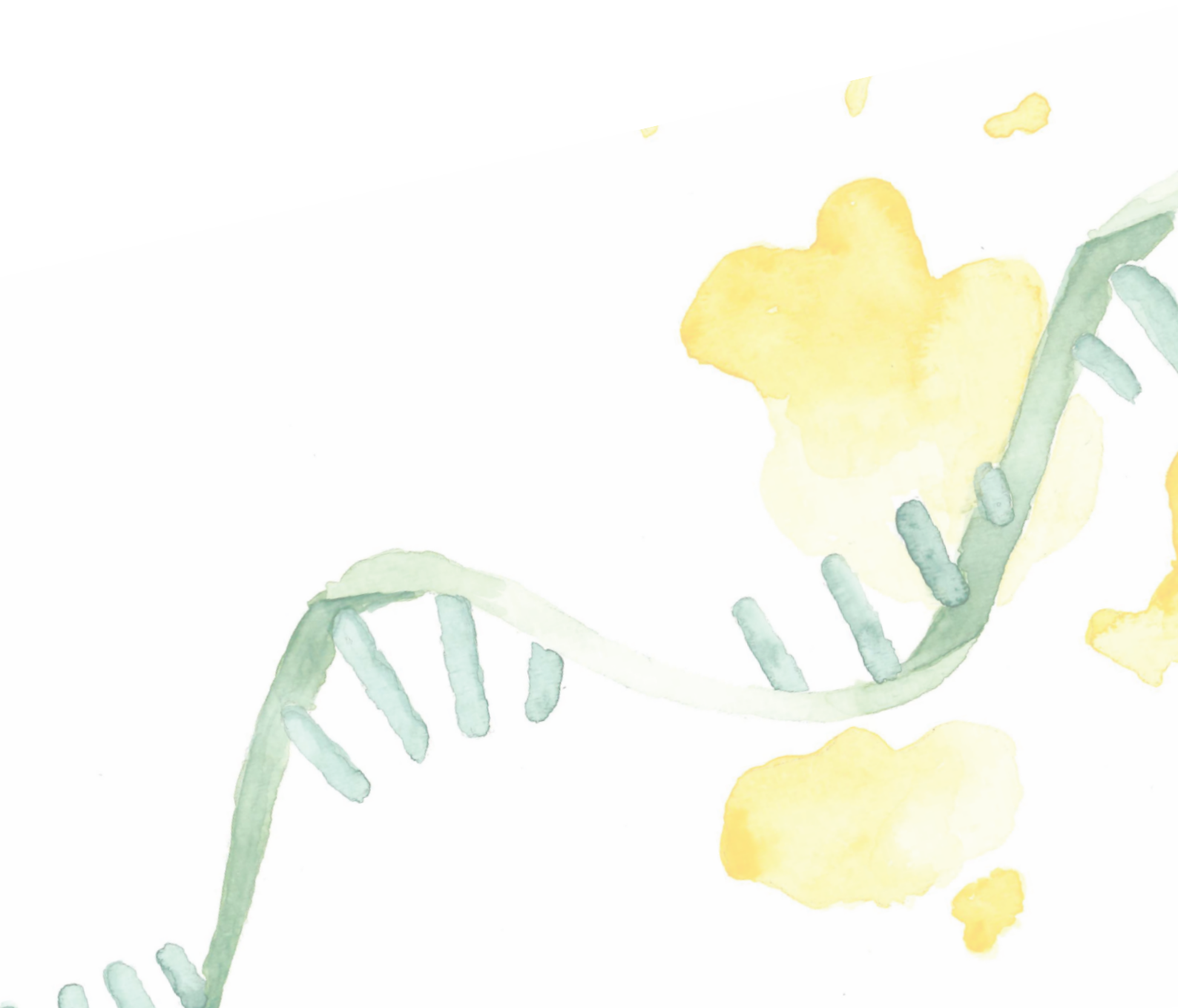

1. Longitudinal evaluation of serum microRNAs as biomarkers for neuroblastoma burden and therapeutic p53 reactivation (addendum paper)

Alan Van Goethem, **Jill Deleu**, Nurten Yigit, Celine Everaert, Myrthala Moreno-Smith, Sanjeev A. Vasudevan, Fjoralba Zeka, Fleur Demuynck, Eveline Barbieri, Franki Speleman, Pieter Mestdagh, Jason Shohet, Jo Vandesompele, and Tom Van Maerken.

Contribution of JD: AVG performed the experiments and wrote a draft manuscript, which was completed by JD by updating literature, finalizing text and figures, submitting the raw sequencing data to the European Genomics Archive, submitting the paper and taking the lead for the rebuttal.

Published online 18 January 2023

NAR Cancer, 2023, Vol. 5, No. 1 **1**
https://doi.org/10.1093/narcan/zcad002

Longitudinal evaluation of serum microRNAs as biomarkers for neuroblastoma burden and therapeutic p53 reactivation

Alan Van Goethem[1,2], Jill Deleu[1,2], Nurten Yigit[1,2], Celine Everaert[1,2], Myrthala Moreno-Smith[3], Sanjeev A. Vasudevan[3], Fjoralba Zeka[1,2], Fleur Demuynck[1,2], Eveline Barbieri[3], Frank Speleman[2,4], Pieter Mestdagh[1,2], Jason Shohet[5], Jo Vandesompele[1,2,†] and Tom Van Maerken[1,2,6,*,†]

[1]OncoRNALab, Cancer Research Institute Ghent (CRIG), Ghent, Belgium, [2]Department of Biomolecular Medicine, Ghent University, Ghent, Belgium, [3]Department of Pediatrics, Section of Hematology-Oncology, Texas Children's Cancer Center, Baylor College of Medicine, Houston, TX, USA, [4]PPOL, Cancer Research Institute Ghent (CRIG), Ghent, Belgium, [5]Department of Pediatrics, Division of Pediatric Hematology-Oncology, University of Massachusetts Chan Medical School, Worcester, MA, USA and [6]Department of Laboratory Medicine, AZ Groeninge, Kortrijk, Belgium

Received October 14, 2022; Revised November 30, 2022; Editorial Decision January 04, 2023; Accepted January 06, 2023

ABSTRACT

Accurate assessment of treatment response and residual disease is indispensable for the evaluation of cancer treatment efficacy. However, performing tissue biopsies for longitudinal follow-up poses a major challenge in the management of solid tumours like neuroblastoma. In the present study, we evaluated whether circulating miRNAs are suitable to monitor neuroblastoma tumour burden and whether treatment-induced changes of miRNA abundance in the tumour are detectable in serum. We performed small RNA sequencing on longitudinally collected serum samples from mice carrying orthotopic neuroblastoma xenografts that were exposed to treatment with idasanutlin or temsirolimus. We identified 57 serum miRNAs to be differentially expressed upon xenograft tumour manifestation, out of which 21 were also found specifically expressed in the serum of human high-risk neuroblastoma patients. The murine serum levels of these 57 miRNAs correlated with tumour tissue expression and tumour volume, suggesting potential utility for monitoring tumour burden. In addition, we describe serum miRNAs that dynamically respond to p53 activation following treatment of engrafted mice with idasanutlin. We identified idasanutlin-induced serum miRNA expression changes upon one day and 11 days of treatment. By limiting to miRNAs with a tumour-related induction, we put forward hsa-miR-34a-5p as a potential pharmacodynamic biomarker of p53 activation in serum.

GRAPHICAL ABSTRACT

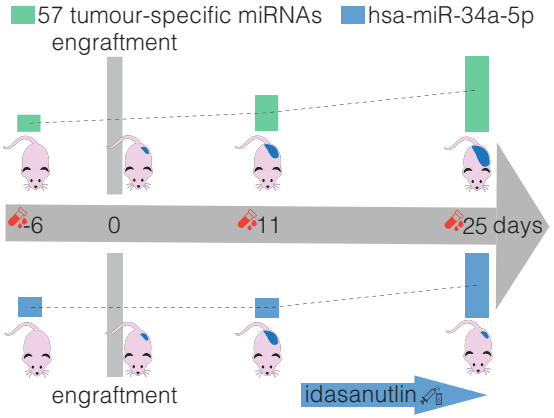

INTRODUCTION

The ongoing improvements in the field of genomic profiling have enabled to study tumour biology in unprecedented detail and to unveil the molecular composition of tumours.

*To whom correspondence should be addressed. Tel: +32 56634200; Email: tom.vanmaerken@ugent.be
†The authors wish it to be known that, in their opinion, the last two authors should be regarded as Joint Last Authors.

However, a hurdle to translate potentially relevant findings into the clinical management of cancer patients is the need for tissue biopsies. This holds especially true for the monitoring of disease activity and the response to treatment over time, as longitudinal invasive sampling is difficult to justify. Novel, non-invasive biomarkers for assessing tumour burden and treatment response are highly desirable for patients with solid tumours like neuroblastoma, a pediatric malignant neoplasm originating from the developing sympathetic nervous system (1). Several non-invasive methodological strategies are under investigation to achieve this goal. Measurement of cell-free DNA for instance, using either a genome-wide approach or quantification restricted to neuroblastoma-associated genes or chromosomal regions, has proven to faithfully recapitulate neuroblastoma tumour biology (2–12).

MicroRNAs, a class of small, non-coding RNAs often found deregulated in numerous cancer types including neuroblastoma (13–16), have recently emerged as promising circulating biomarkers (17–22). In neuroblastoma, reports on miRNAs in circulation are rather scarce. Murray *et al.* found five miRNAs to be higher expressed in the serum of high-risk neuroblastoma patients, the expression levels of which could be used to distinguish MYCN-amplified neuroblastoma from other neuroblastoma tumours (23). Ramraj *et al.* performed miRNome profiling by RT-qPCR on serum collected from mouse models of favorable and unfavorable neuroblastoma to identify miRNAs that can distinguish favorable from high-risk neuroblastoma (24). Zeka *et al.* found nine miRNAs in serum samples strongly associated with tumour volume of murine xenografts and neuroblastoma disease burden and treatment response in metastatic neuroblastoma patients (25). In the present study, we evaluated whether miRNAs are suitable to monitor neuroblastoma tumour burden and whether treatment-induced changes of miRNA abundance in the tumour can be detected in the serum. In order to do so, we performed small RNA sequencing on longitudinally collected serum samples obtained from mice carrying orthotopic neuroblastoma xenografts that were exposed to treatment with idasanutlin (RG7388) or temsirolimus. The low frequency of TP53 mutations counterbalanced by an augmented MDM2 activity renders neuroblastoma highly sensitive to MDM2 antagonists such as idasanutlin (26–32). The rapamycin-derived mTOR-inhibitor temsirolimus has proven therapeutic efficacy in neuroblastoma and is currently under clinical investigation (33,34).

We identified 57 serum miRNAs to be differentially abundant upon xenograft tumour manifestation, out of which 21 were also found specifically expressed in the serum of human high-risk neuroblastoma patients. The murine serum levels of these 57 miRNAs correlated with both tumour tissue expression and tumour volume, suggesting potential utility for monitoring of tumour burden. In addition, we identified idasanutlin-induced serum miRNA expression changes both one day after the start of treatment and upon 11 days of treatment. By limiting to miRNAs with a tumour-related induction, we put forward hsa-miR-34a-5p as a potential pharmacodynamic biomarker of p53 activation in serum.

MATERIALS AND METHODS

Orthotopic xenograft model

Orthotopic neuroblastoma xenografts were generated in four to six week old female athymic immunodeficient NCr nude mice as previously described (35). Briefly, 1×10^6 human luciferase-SH-SY5Y neuroblastoma cells were surgically implanted beneath the renal capsule, towards the superior pole of the kidney. The detailed workflow has been described previously (36). This model closely resembles the growth characteristics of primary adrenal neuroblastoma tumours in humans. Tumour size was determined by luciferase imaging. Mice were peritoneally injected with luciferin and were sedated 15 min later using vaporized isoflurane in an induction chamber and luciferase signal intensity was measured. All animal work was approved by the Baylor College of Medicine Institutional Animal Care and Use Committee (IACUC) protocols (AN-3705 and AN-4810) and carried out in accordance with the relevant guidelines and regulations.

Treatment of mice

Mice were treated with 30 mg/kg idasanutlin (dissolved in hydroxypropylcellulose/Tween-80) or 9 mg/kg temsirolimus (dissolved in PBS/PEG/Tween-20) by oral gavage on a daily basis, five times a week, for a total of 12 days. Idasanutlin was kindly provided by Roche. Temsirolimus was purchased from Sigma Aldrich (PZ0020). After 12 days of treatment, mice were sacrificed and tumours were collected, weighed and snap frozen in liquid nitrogen.

Blood collection and serum preparation

At five different time points—6 days before engraftment, 2 days after engraftment, 11 days after engraftment, 15 days after engraftment and 25 days after engraftment (treatment of the mice was started 14 days after engraftment)—100 μl blood was collected by puncture of the jugular vein using a 4 mm lancet and collected in a BD Vacutainer collection tube with a gel separator. All blood samples were allowed to clot at room temperature for 45 min and were then centrifuged at 2000 × g for 15 min at 4°C using a fixed angle rotor. The supernatant was collected and stored at −80°C. For all serum samples, the degree of hemolysis was determined by measuring levels of free hemoglobin by spectral analysis using the Nanodrop 1000 (ThermoScientific). Absorbance peaks at 414 nm are indicative of free hemoglobin.

Total RNA isolation

For serum samples, RNA was isolated using the miRNeasy serum/plasma kit (Qiagen) according to the manufacturer's instructions. 50 μl of serum was used as input and total RNA was eluted in 12 μl of RNase-free water. For tumour samples, tumour material was denaturated using guanidinium thiocyanate and then lysed using the TissueLyser II (Qiagen) using stainless steel beads (5 mm) two times two minutes at 20 Hz. RNA was isolated using the miRNeasy mini kit (Qiagen), according to the manufacturer's instructions, and total RNA was eluted in 12 μl of RNAse-free water.

tRNA fragment depletion

tRNA halves were depleted from the RNA samples as described previously (37). In short, 12 μl of RNA, 15 μl of 2× hybridization buffer (Supplementary file S1), 1 μl of tRNA halves capture probes (at a final reaction concentration of 0.5 μM for each probe; Supplementary Table S1) and 2 μl of RNase-free water were incubated at 80°C for 2 min to denature the RNA. The mixture was slow-cooled to 22°C (at 0.1°C/min) and placed on ice to allow for efficient hybridization. Dynabeads Myone Streptavidin C1 (Life Technologies) were washed 3 times using a washing buffer (Supplementary file S1). After washing, beads were prepared for RNA manipulation by washing twice with solution A and once with solution B (Supplementary file S1) and suspended in 2× washing buffer to a final concentration of 5 μg/μl. Next, 30 μl of sample was added to 30 μl of beads and the mixture was incubated for 10 minutes at room temperature with gentle mixing. The mixture was then placed on a magnet for 2 min after which the supernatant, containing the depleted RNA, was collected. The depleted RNA was purified by ethanol precipitation and suspended in 7.5 μl RNase-free water.

Small RNA sequencing

For small RNA library preparation, we used the TruSeq small RNA library preparation kit v2 (Illumina) following manufacturer's instructions with small modifications. After PCR amplification, quality of libraries was assessed using a high sensitivity DNA kit on a Bioanalyzer (Agilent) according to manufacturer's instructions. Size selection was performed using 3% agarose dye-free marker H cassettes on a Pippin Prep (Sage Science) following manufacturer's instructions with a specified collection size range of 125–153 bp. Libraries were further purified and concentrated by ethanol precipitation, resuspended in 10 μl of 10 mM Tris–HCl (pH 8.5) and quantified using qPCR (see further). Based on the qPCR results, equimolar library pools were prepared, quality was assessed as described above and the library was further diluted to 4 nM using 10 mM Tris–HCl (pH 8.5). The pooled library was then sequenced at a final concentration of 1.2 pM on a NextSeq 500 using high output v2 kits (single-end, 75 cycles, Illumina). Raw sequencing data is available in the European Genome-Phenome archive (EGAS00001006678).

For RT-qPCR quantification of sequencing libraries to load equimolar concentrations, 1 μl of EtOH purified library was diluted 1:100 000. 2.5 μl of SsoAdvanced universal SYBR green supermix (Bio-Rad Laboratories) and 0.25 μl of each primer (5 μM) (forward primer: AATGATAC GGCGACCACCGA; reverse primer: CAAGCAGAAG ACGGCATACGA) were combined with 2 μl of diluted library. Reactions were set up in duplicate and performed in a LightCycler 480 (Roche) using the following protocol: enzyme activation at 95°C for 15 min, followed by 44 cycles of 95°C for 5 s, 60°C for 30 s and 72°C for 1 s.

Sequencing data analysis

For the quantification of small RNAs, a dedicated small RNA seq pipeline of Biogazelle (now a CellCarta company) was used. Adaptor trimming was performed using Cutadapt v1.8.1. Reads shorter than 15 bp and those in which no adaptor was found, were discarded. For quality control the FASTX-Toolkit (v0.0.14) was used, a minimum quality score of 20 in at least 80% of bases was applied as a cutoff. The reads were mapped with Bowtie (v1.1.2) without allowing any mismatches. Mapped reads were annotated by matching genomic coordinates of each read with genomic locations of miRNAs (obtained from miRBase, v21) and other small RNAs (obtained from UCSC (human: GRCh37/hg19; mouse: GRCm38/mm10) and Ensembl, v84). As publically available alternatives, we advise the use of miRDeep2 and miRExpress. Further data analysis was performed using RStudio (v0.99.486). Samples with fewer than 0.5 million mapped miRNA reads were omitted. Normalization of miRNA counts and differential expression analysis was performed using the R package DESeq2 (v1.8.2). Species specificity was determined based on the transcript sequence. In the case of perfect sequence conservation between the human and murine transcript, the transcript is annotated with both the human and murine mature miRNA name. Note that the presence of both perfectly conserved and species-specific transcripts of the same mature miRNA can result in multiple annotations.

Filtering hemolysis-associated miRNAs and samples

To identify miRNAs that correlate with hemolysis we determined Pearson's correlation coefficient for the abundance of all miRNA transcripts with the optical density at 414 nm (OD414). A correlation cut-off was determined based on the average correlation coefficient of human-specific miRNAs (mean hsa coefficient + 3 × stdev hsa coefficient), as these transcripts are not expected to be influenced by hemolysis in a murine model system. All miRNA transcripts above the correlation cut-off ($n = 165$) were excluded from differential expression analyses (Supplementary Table S2). In addition, all serum samples with an OD414 value above 1.5 ($n = 4$) were excluded for further analysis (Supplementary Table S3).

RT-qPCR of human serum samples

Serum pools were prepared by combining 40 μl of five individual serum samples, as described previously (25). Total RNA was isolated using the miRNeasy serum/plasma kit (Qiagen) according to the manufacturer's instructions. 200 μl of serum was used as input and total RNA was eluted in 12 μl of RNase-free water. cDNA synthesis was performed using the miScript II RT kit (Qiagen) following manufacturer's instructions with 1.5 μl of RNA as input. cDNA was pre-amplified using the miScript PreAMP PCR kit (Qiagen) following manufacturer's instruction with 10 amplification cycles. For each reaction 5 μl of 11-fold diluted cDNA was combined with 7 μl of RNAse-free water, 5 μl of 5× miScript PreAmp Buffer, 2 μl of HotStarTaq DNA Polymerase, 1 μl of miScript PreAmp Universal Primer (5 μM) and 5 μl of miScript PreAmp Primer Mix (5 μM). Whole miRNome RT-qPCR was performed using miScript miRNA PCR arrays (Qiagen) and the miScript SYBR Green PCR kit (Qiagen). For each reaction 2 μl of 22-fold diluted pre-amplified

cDNA was combined with 1 μl of RNase-free water, 5 μl of 2× QuantiTect SYBR Green PCR Master Mix, 1 μl of 10× Universal Primer (5 μM). Data were normalized using the modified global mean, as implemented in qbase+ qPCR data-analysis software (Biogazelle), and non-detects imputed. All human work was approved by the Ethical Committee of Ghent University Hospital (EC UZG 2012/035).

RESULTS

Differential abundance analysis reveals circulating miRNAs released by tumour cells

In order to identify circulating miRNAs that can be associated with tumour burden, we performed small RNA sequencing on serum samples of nude mice ($n = 25$) 6 days before and 11 days after orthotopic engraftment of human SH-SY5Y cells. Concurrently collected serum samples of mice ($n = 8$) not injected with neuroblastoma tumour cells were used as a negative control (Figure 1). When comparing the abundance profiles before and after tumour cell injection, we found a total of 94 differentially expressed (DE) miRNAs (fold change (FC) >2; P <0.05, Wald test, corrected for multiple testing using Benjamin–Hochberg) (Figure 2A) while in the non-engrafted group we detected six DE miRNAs (Supplementary Table S4A). When comparing serum miRNA abundance between the tumour bearing mice and the non-engrafted mice on both assessed time points, we detected 12 DE miRNA and 61 DE miRNAs (Figure 2B) (Supplementary Table S4B) before and after engraftment respectively. Of note, the serum samples collected on day 2 in the non-engrafted group are grouped with the samples collected on day −6 (Figure 1).

As we expect tumour-associated miRNAs to be both differentially abundant after engraftment between non-engrafted and engrafted mice, we determined the overlap between the DE miRNAs of these respective comparisons. This resulted in a set of 57 miRNAs that are convincingly altered as a result of tumour manifestation (Figure 2C, Supplementary Table S4C). As expected, we find this set of miRNAs to be heavily enriched for human-specific miRNAs ($P < 2.2 \times 10^{-16}$, Pearson's chi-squared test). Out of the 57 miRNAs, 54 miRNAs have a human specific sequence and three miRNAs have a sequence conserved between mice and humans. Considering human-specific miRNAs must have a tumour-cell origin, this must hold true for these DE miRNAs as well.

In addition, we performed small RNA sequencing on the serum of the same mice, collected at later time points, being 15 days (tumour-bearing mice: $n = 8$; tumour-free mice: $n = 7$) and 25 days (tumour-bearing mice: $n = 5$; tumour-free mice: $n = 6$) after engraftment (Figure 1). When we consider the expression profiles of the 57 DE miRNAs in all evaluated time points, we observe a gradual increase in expression in engrafted mice which was not observed in non-engrafted mice, evidenced by an increase in fold change between tumour-bearing and non-engrafted mice over time (Figure 2D). While we must note that the non-engrafted mice at these time points have been treated with either idasanutlin or temsirolimus, we do not expect these miRNAs to be influenced by the treatment as virtually all of them are human-specific (and thus absent in non-engrafted mice).

Serum miRNA abundance recapitulates tumour burden

As we observed a gradual increase in serum abundance of the 57 DE miRNAs over time in tumour-carrying mice, we speculated that the serum expression levels of these miRNAs would correlate with tumour size. Tumour size was measured by luciferase imaging at two different time points (14 days and 23 days post tumour cell injection respectively; Figure 1). Pearson's π-values (= Pearson's ρ × (−$\log_{10}$(P-value)); P-value corrected for multiple testing using Benjamin–Hochberg) between miRNA expression levels in serum (measured 15 days and 25 days after tumour cell injection) and the size of the paired tumour (measured by luciferase imaging 14 days and 23 days post tumour cell injection) were calculated. We found all of the 57 DE miRNAs to significantly correlate with tumour size (Pearson's ρ > 0.3 and adj. $P < 0.05$) and that these 57 miRNAs correlate significantly better with tumour size than other serum miRNAs ($P < 2.2 \times 10^{-16}$, two-sample Kolmogorov–Smirnov test) (Figure 3A, Supplementary Table S5). We found 334 miRNAs to be correlated with tumour size, out of which 278 are human-specific, 51 are conserved between mouse and human and 5 are mouse-specific (Supplementary Table S5). As we expect the 57 DE serum miRNAs to be also expressed in tumour tissue, we performed small RNA sequencing on end-point tumour samples ($n = 13$) (Figure 1). When we rank all detected miRNAs according to their mean expression in the tumour samples, we find that the 57 DE serum miRNAs are amongst the top expressed genes in the tumour (Figure 3B). This indicates that miRNAs with a high expression in the tumour are more likely to be detected as differentially expressed in serum. Next, we compared the expression of these miRNAs in paired tumour-serum samples to determine how faithfully serum expression recapitulates expression in the tumour. In order to do so, we calculated the Pearson π-value between miRNA expression in serum collected 25 days post tumour cell injection and the weighted miRNA expression (tumour miRNA expression x tumour size) in the paired tumour for all miRNAs detected in serum. We found that the 57 DE miRNAs correlated significantly stronger with weighted tumour expression than other miRNAs ($P < 2.2 \times 10^{-16}$, two-sample Kolmogorov–Smirnov test) (Figure 3C) (Supplementary Table S6).

DE miRNAs in serum of human neuroblastoma patients

Ideally, liquid biopsy biomarkers for tumour burden should have a low (or absent) basal expression in healthy children. We therefore determined and compared the expression levels of the 57 DE miRNAs in two serum pools of high-risk neuroblastoma patients and one serum pool of healthy children by RT-qPCR. In addition, to evaluate whether these miRNAs are neuroblastoma or cancer specific, we included serum pools collected from children suffering from sarcoma, rhabdomyosarcoma or nephroblastoma. We considered a miRNA to be upregulated in neuroblastoma if the fold change between neuroblastoma and healthy expression was higher than 4 for all neuroblastoma

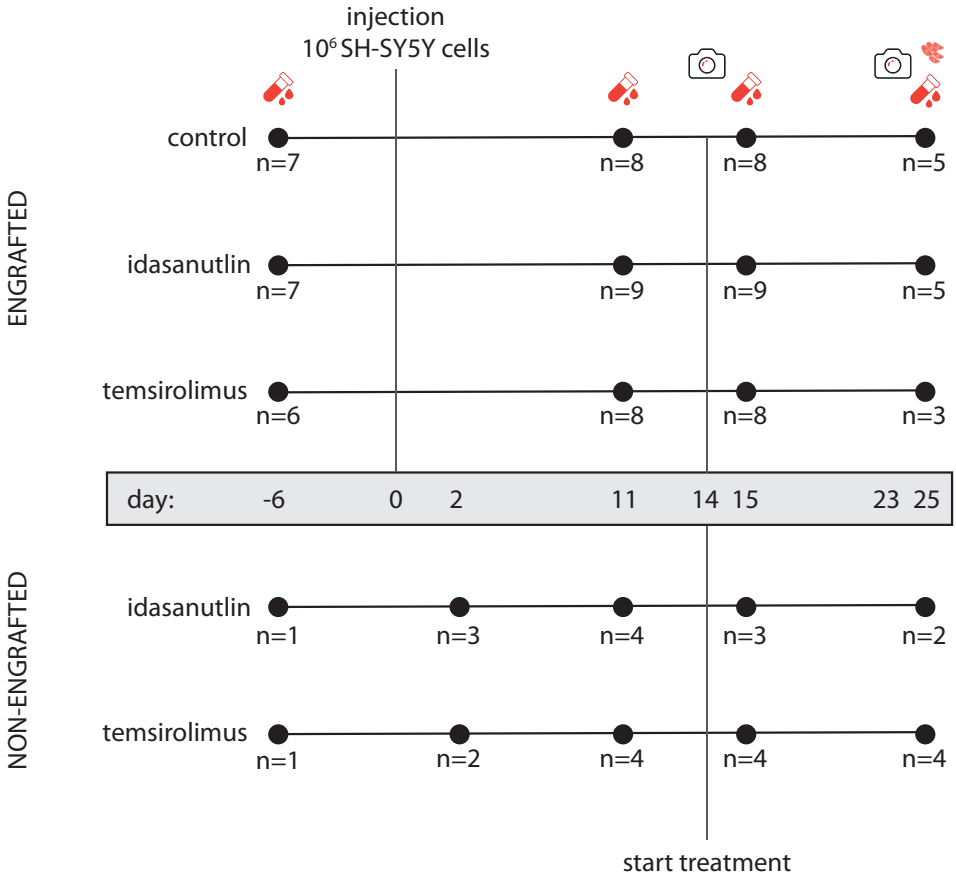

Figure 1. Schematic representation of the study. Numbers represent the amount of mice at each time point for each condition after deduction of samples with high degree of hemolysis and samples with <0.5 million mapped miRNAs. Red collection tubes represent blood collections, red tumour cells represent the collection of tumour material, cameras represent luciferase imaging.

serum pools. Doing so, we found 21 of the 57 DE miRNAs to be upregulated in serum of human neuroblastoma. Some of these miRNAs are putative neuroblastoma specific serum biomarkers (hsa-miR-1269a, hsa-miR-330-3p, hsa-miR-424-3p, hsa-miR-769-5p), while others may be general cancer serum biomarkers (hsa-miR-483-5p) (Figure 4). Details on the serum pooling and clinical characteristics of the patients included in this study were described previously (25).

Circulating miRNAs reflect idasanutlin treatment

As we have demonstrated that tumoural miRNA abundance is, to a certain degree, reflected in the serum, we wondered whether treatment-induced changes in serum miRNA abundance recapitulate expression changes in the tumour as well. Small RNA sequencing was performed on serum collected from tumour-bearing mice 3 days before, 1 day after and 11 days after start of treatment with 30 mg/kg/day idasanutlin, 9 mg/kg/day temsirolimus or vehicle control (n = 9, 9 and 5 for idasanutlin respectively; n = 8, 8 and 3 for temsirolimus respectively; n = 8, 8 and 5 for control respectively; see Figure 1). To identify miRNAs with a differential treatment effect, we performed Wald tests on the difference of the control/treatment expression ratio 3 days before treatment and 1 day and 11 days after start of treatment.

After 1 day of idasanutlin treatment, we identified 50 DE miRNAs and after 11 days of treatment 20 DE miRNAs (fold change (FC) >2; P <0.05, Wald test, corrected for multiple testing using Benjamin–Hochberg) (Supplementary Table S7). We did not find any DE miRNAs upon temsirolimus treatment, in line with a previous report that did not identify any miRNA expression alterations upon temsirolimus monotherapy in melanoma (38). Next, we filtered out murine-specific miRNAs, as they are unlikely to reflect expression changes inside the tumour and only kept miRNAs that have a human annotation. We further filtered results to only keep miRNAs with a significant expression difference both between control and treated samples and before and after treatment (Wald test, P < 0.05, corrected for multiple testing using Benjamin–Hochberg). This resulted

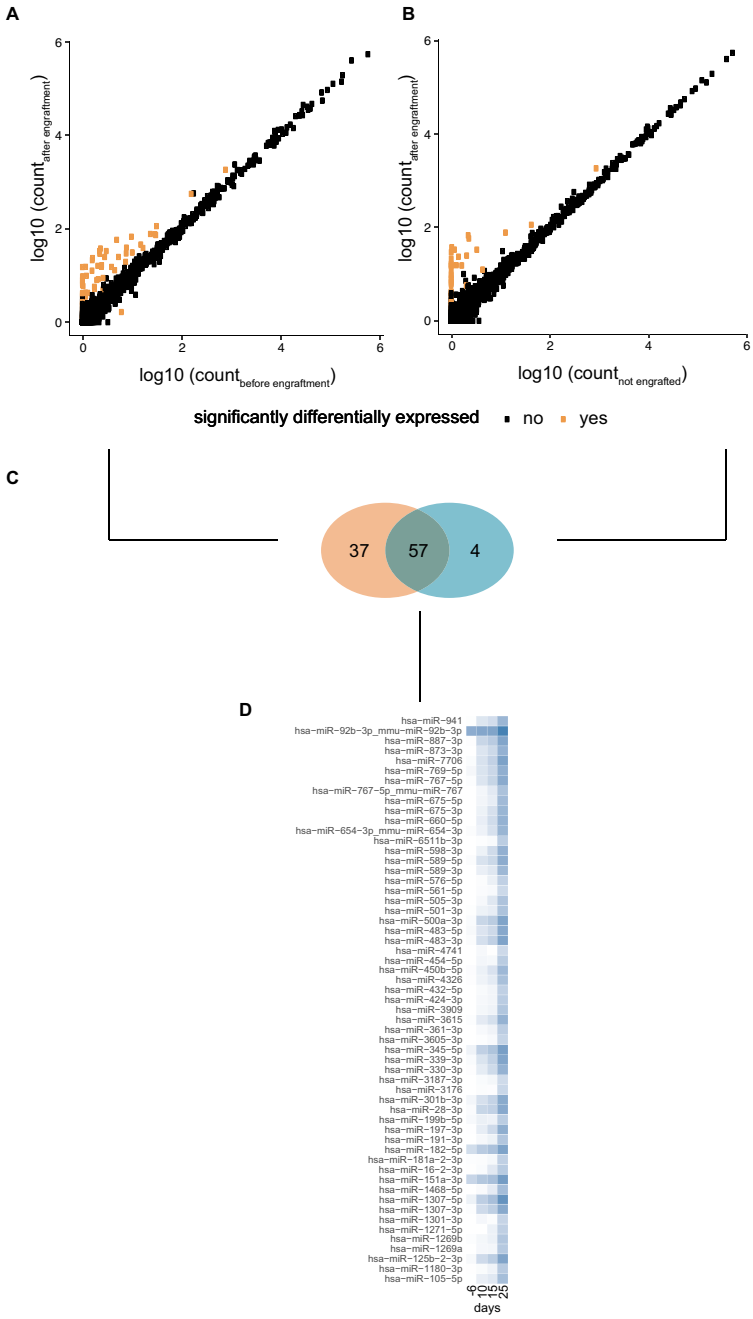

Figure 2. miRNAs differentially expressed in serum of mice carrying orthotopic xenograft tumours of human SH-SY5Y cells. (**A**) miRNA expression levels in the serum of mice 6 days before and 10 days after engraftment with 10^6 human SH-SY5Y cells. 94 miRNAs (in orange) were found differentially expressed between the two conditions ($P < 0.05$ and fold change (FC) >2, Wald test, corrected for multiple testing using Benjamin–Hochberg). (**B**) miRNA expression levels in the serum of mice 11 days after engraftment with 10^6 human SH-SY5Y cells and non-engrafted, control mice. 61 miRNAs (in orange) were found differentially expressed between the two conditions ($P < 0.05$ and FC > 2, Wald test, corrected for multiple testing using Benjamin–Hochberg). (**C**) Overlap between the two groups of differentially expressed miRNAs. 57 miRNAs are differentially expressed in both comparisons. (**D**) Heatmap showing an increasing log2 fold change in serum miRNA expression between mice carrying orthotopic xenografts and non-engrafted mice over time. Time points: −6 = 6 days before engraftment; 11 = 11 days after engraftment; 15 = 15 days after engraftment; 25 = 25 days after engraftment.

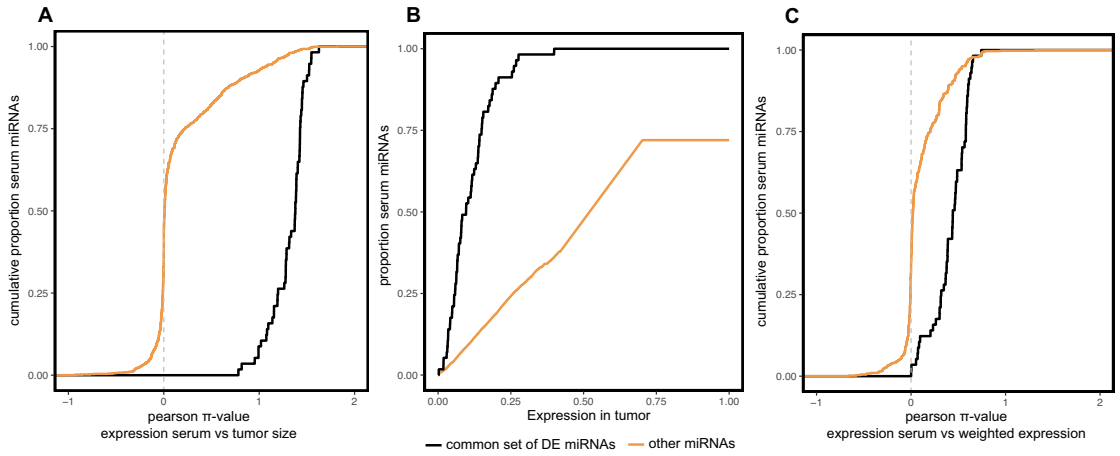

Figure 3. Serum miRNA expression correlates with tumour size. (**A**) Cumulative fraction of serum miRNAs by Pearson π-value (= Pearson's ρ × (–$\log_{10}$(*P*-value)); *P*-value corrected for multiple testing using Benjamin–Hochberg) of the correlation between miRNA serum expression and tumour size (measured by luciferase imaging, 14 days and 23 days after tumour cell injection). The 57 differentially expressed miRNAs (black) correlate significantly better with tumour size than other serum miRNAs (orange) ($P < 2.2 \times 10^{-16}$, Kolmogorov–Smirnov test). (**B**) Cumulative fraction of serum miRNAs ranked by expression in the tumour. The 57 differentially expressed serum miRNAs (black) are much higher expressed in the tumour than other serum miRNAs (orange) ($P < 2.2 \times 10^{-16}$, Kolmogorov–Smirnov test). All 57 serum miRNAs are among the top expressed tumour miRNAs, with half of these serum miRNAs among the top 10% expressed tumour miRNAs. (**C**) Cumulative fraction of serum miRNAs by Pearson π-value of the correlation between miRNA serum expression and weighted tumour expression (tumour size × tumour expression). The 57 differentially expressed miRNAs (black) correlate significantly better with weighted tumour expression than other serum miRNAs (orange) ($P < 2.2 \times 10^{-16}$, Kolmogorov–Smirnov test).

in a total of 31 DE miRNAs (29 up, 2 down) after 1 day of treatment and six DE miRNAs (three up, three down) after 11 days of treatment (Figure 5). It may be possible that the smaller number of detected DE miRNAs after 11 days of treatment (compared to 1 day after treatment) is due to less statistical power as a result of a smaller number of mice in each group.

When examining the expression profiles of these miRNAs in time, we can distinguish some distinctive expression patterns (Figure 5). Amongst the top DE miRNAs after 1 day of idasanutlin treatment are miRNAs of the known p53-regulated miR-143/145 cluster (39,40). Interestingly, this cluster of miRNAs is strongly induced 1 day after treatment but is no longer found differentially expressed 11 days after treatment. On the other hand, after 11 days of idasanutlin treatment, one of the DE miRNAs is miR-34a-5p, a key p53 effector miRNA (41,42).

To further ensure a tumour-driven expression change, we compared miRNA expression levels in end-point tumour samples collected from mice treated with idasanutlin ($n = 5$) and mice treated with vehicle-control ($n = 5$). We find one miRNA to be differentially expressed in serum after 11 days of treatment (fold change (FC) >1.5; P <0.05, Wald test, corrected for multiple testing using Benjamin–Hochberg) and also upregulated in the tumour of the respective idasanutlin-treated mice (fold change (FC) > 1.5; $P < 0.05$, Wald test): hsa-miR-34a-5p/mmu-miR-34a-5p (Figure 6). Interestingly, hsa-miR-34a-5p/mmu-miR-34a-5p was also found upregulated after 1 day of treatment although not significantly ($P = 0.59$). These findings encourage further investigation of hsa-miR-34a-5p/mmu-miR-34a-5p as circulating pharmacodynamic biomarker for p53 activation in neuroblastoma.

DISCUSSION

Novel methods to monitor neuroblastoma progression and response to treatment are highly desired. To this purpose, we longitudinally assessed miRNA abundance in the serum of mice carrying orthotopic xenografts of neuroblastoma and exposed to treatment regimens of idasanutlin and temsirolimus, two clinically relevant small molecule drugs.

Regarding miRNAs associated with tumour burden, we found 57 serum miRNAs to be differentially expressed 10 days after tumour engraftment. Serum abundance of these miRNAs was found to strongly correlate with tumour size, with these miRNAs to be among the top expressed in the tumour, and to also correlate positively with tumoural expression. When evaluating the expression of these miRNAs in the serum of human neuroblastoma patients, we found 21 of these miRNAs to be higher expressed in serum from high-risk neuroblastoma patients compared to children without cancer. A detailed discussion concerning the importance of each of these miRNAs is beyond the scope of this manuscript; we do however like to mention that several of these miRNAs have been described in the context of neuroblastoma. hsa-miR-16-2-3p was found upregulated in MYCN-amplified neuroblastoma tumours as compared to neuroblastoma without MYCN amplification (43). Hsa-miR-92b-3p, hsa-miR-1307-3p, hsa-miR-330-3p and hsa-miR-345-5p for instance are known target genes of the MYCN oncogene often found overexpressed in high-risk neuroblastoma (44,45). Consistent with our observations, miR-191-3p, miR-345-5p, miR-92b-3p, miR-339-3p, miR-483-3p and miR-483-5p have all been reported upregulated in metastatic neuroblastoma compared to primary neuroblastoma (46). Of note, detection of tumoural miRNAs may

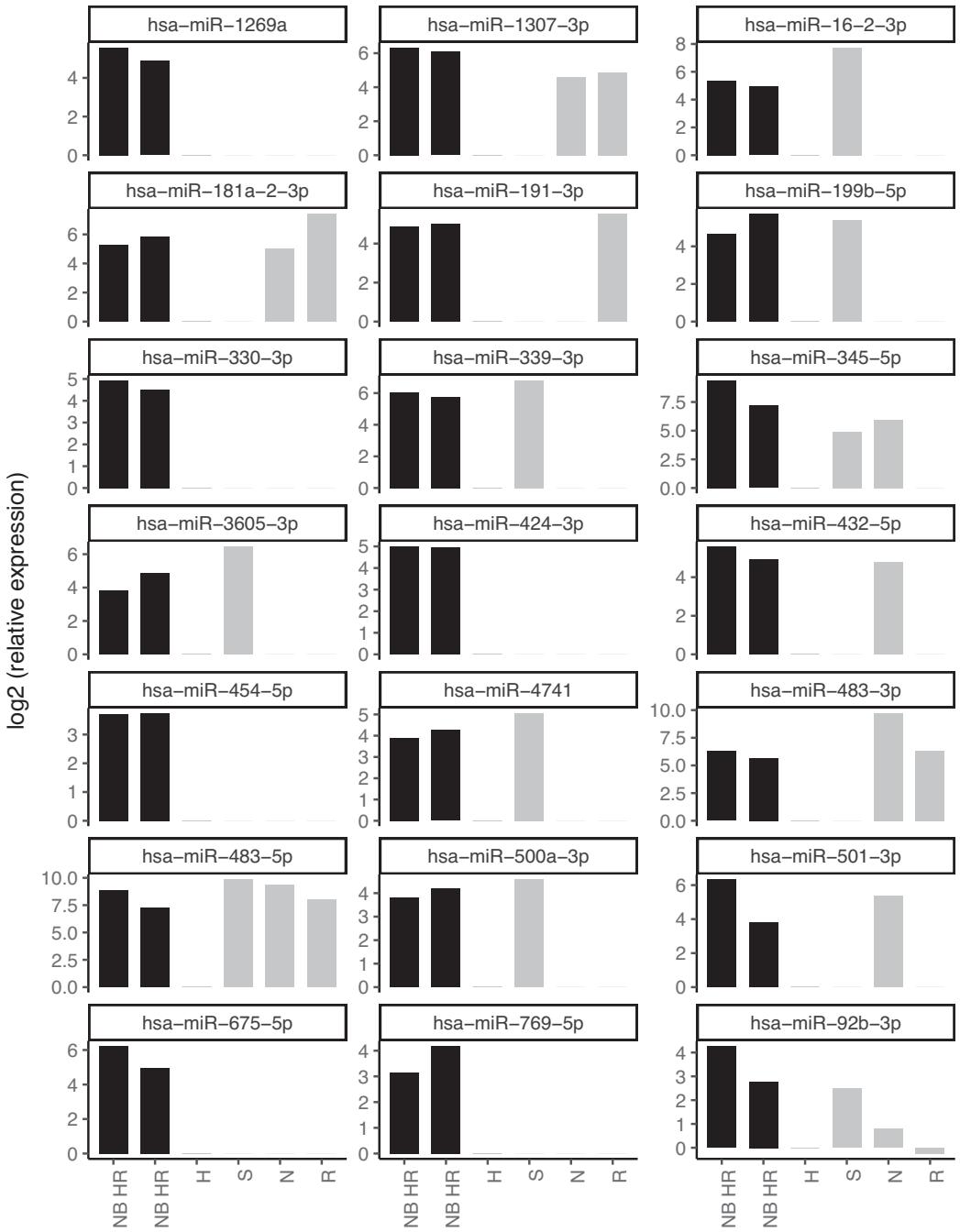

Figure 4. miRNA abundance in human serum. miRNA expression levels in serum pools of high-risk neuroblastoma patients (NB HR), healthy children (H), sarcoma patients (S), nephroblastoma patients (N) and rabdomyosarcoma patients (R) of miRNAs both differentially expressed in the serum of mice carrying orthotopic neuroblastoma xenografts and upregulated in both serum pools of high-risk neuroblastoma patients as compared to healthy serum.

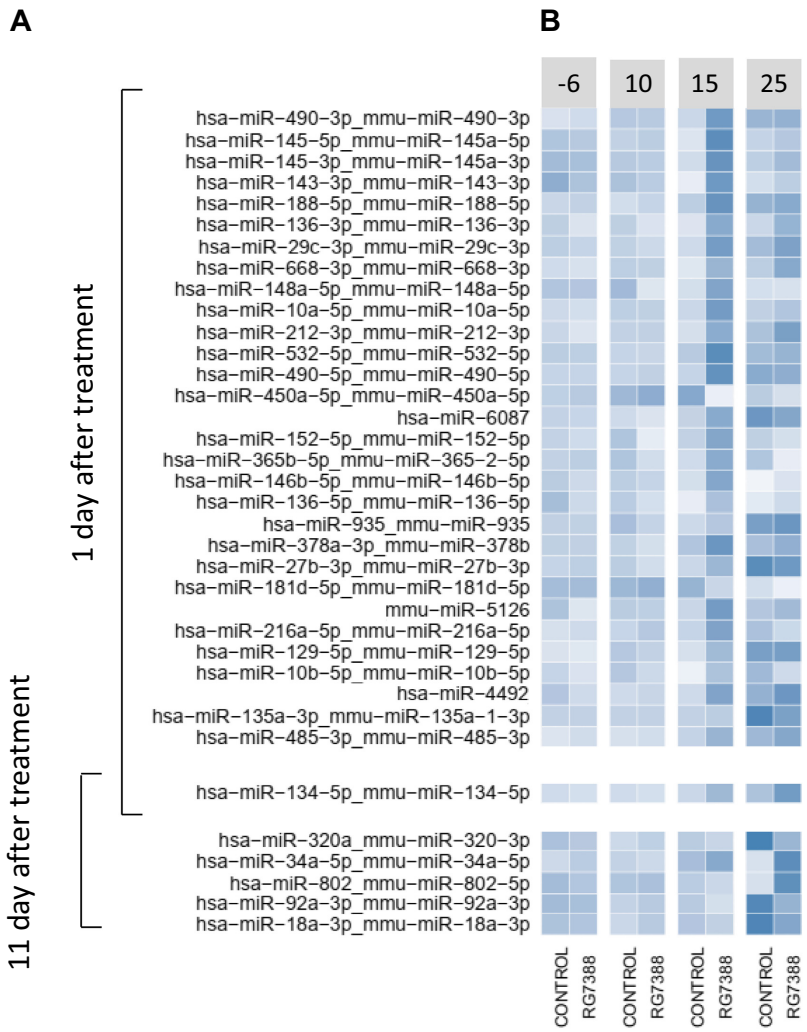

Figure 5. Serum miRNAs responsive to idasanutlin treatment. (**A**) Differentially expressed miRNAs in serum of mice carrying orthotopic xenograft tumours of SH-SY5Y cells after 1 or 11 days of treatment with idasanutlin (30 mg/kg per day), temsirolimus (9 mg/kg/day) or vehicle control ($P < 0.05$ and FC > 2, Wald test, corrected for multiple testing using Benjamin–Hochberg). (**B**) Scaled $\log_2$ expression levels of idasanutlin-responsive miRNAs in serum of mice treated with idasanutlin or vehicle control. Time points: −6 = 6 days before engraftment; 10 = 10 days after engraftment and 3 days before treatment; 15 = 15 days after engraftment and 1 day after start treatment; 25 = 25 days after engraftment and 11 days after start treatment.

depend on the injected cell line, as some microRNAs define distinct human neuroblastoma cell types, such as the adrenergic (e.g. SH-SY5Y) or mesenchymal cells (47). It is currently unknown whether the differentially abundant miRNAs in our study are specific to adrenergic-type neuroblastoma cells or rather reflect the generic neuroblastoma transcriptome irrespective of the cell state. It is of interest to further study this given the link between the mesenchymal cell phenotype and treatment resistance and relapse (48,49). An important issue regarding the use of circulating miRNAs as blood-based biomarkers concerns the cell of origin. As we used small RNA sequencing to quantify miRNA expression levels, we were able to accurately distinguish between murine and human miRNA sequences. As such, we found the majority of upregulated miRNAs to be human-specific, suggesting they are most likely derived from tumour cells. Whether they are actively released by the tumour or enter circulation as a result of breakdown of apoptotic or necrotic tumour cells remains unclear. Unfortunately miRNA profiling of pure extracellular vesicles or exosomes, actively released by tumour cells, is not yet feasible on minute amounts of serum or plasma, as such an approach could allow to more selectively detect tumour-secreted miRNAs.

Besides serum miRNAs associated with tumour burden, an important aim of this study was to identify serum miRNAs that are responsive to treatment. Non-invasive assess-

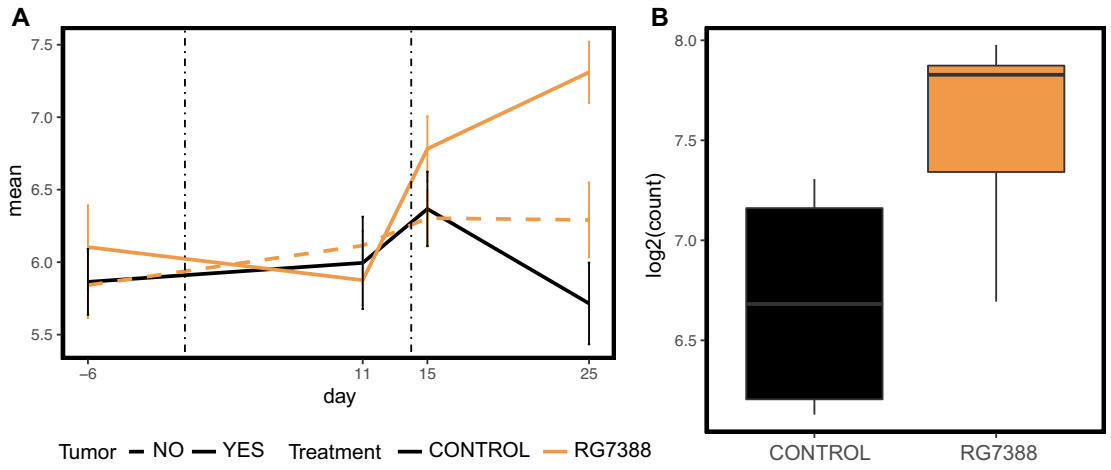

Figure 6. Serum and tumour expression levels of miR-34a-5p. (**A**) Serum expression levels of miR-34a-5p at different time points before and after treatment with idasanutlin (orange) or vehicle control (black). Serum was collected 6 days before engraftment (−6), 11 days after engraftment (11), one day after start of treatment (15) and 11 days after start of treatment (25). Solid lines represent mice carrying orthotopic xenograft tumours of SH-SY5Y cells; dashed lines represent non-engrafted, tumour-free mice. Error bars represent the standard error of the mean. (**B**) Boxplots of the expression levels of miR-34a-5p in tumours collected from mice treated for 11 days with idasanutlin or vehicle control.

ment of drug-induced molecular pathway activation could have clinical utility for patient follow-up. In clinical trials of RG7112, an idasanutlin predecessor, the measurement of serum levels of MIC-1, a secreted p53-inducible protein, has successfully been used in estimating p53 activation (50–52). Given p53 is a known modulator of miRNA expression (40,53,54), assessing p53 activation trough circulating miRNA abundance seemed a plausible scenario. Here, we describe for the first time serum miRNAs that dynamically respond to p53 activation following treatment of engrafted mice with idasanutlin. After only 24 hours of treatment we were able to detect significant induction of expression for 31 miRNAs, including known p53 transcriptional targets such as the miR-143/miR-145 cluster. After 11 days of treatment, we detected six DE miRNAs, including miR-34a-5p, another bona fide p53 response mediator. By comparing treatment-induced changes in serum expression in mice carrying tumours to changes in tumour-free mice and by associating expression changes in serum with changes in the tumour we restricted our analyses to miRNAs of which abundance changes in serum are likely to reflect expression changes in the tumour. This resulted in one miRNA that could potentially function as biomarker for p53 activation, hsa-miR-34a-5p. miR-34a-5p is a known p53-regulated miRNA with potent anti-tumour effects. This miRNA is often found lower expressed in unfavourable neuroblastoma and it has been reported that in neuroblastoma targeted activation of p53 can lead to a potent induction of miR-34a expression in vitro (41,55,56). Interestingly, targeted delivery of miR-34a using anti-GD2 coated nanoparticles has potent anti-tumour effects in vivo in neuroblastoma (57). Whether the same holds true for innately circulating miR-34a-5p, or by extension other p53-regulated miRNAs in circulation, would form an interesting subject of further investigation.

In conclusion, we identified circulating miRNAs that are associated with both human neuroblastoma and murine neuroblastoma xenograft tumour burden and uncovered one miRNA that could potentially be used as non-invasive biomarker for p53 pathway activation. Our findings demonstrate that it is feasible to monitor both tumour burden and treatment response by measuring the levels of circulating miRNAs in serum and that expression changes in the tumour are reflected in serum. The identification of treatment-induced alterations of circulating tumour-related miRNAs is an unprecedented finding that holds promise for liquid biopsies as a tool for miRNA-based monitoring of treatment response in cancer patients.

DATA AVAILABILITY

The dataset supporting the conclusions of this article is available at the European Genome-phenome Archive (EGA – accession ID EGAS00001006678).

SUPPLEMENTARY DATA

Supplementary Data are available at NAR Cancer Online.

ACKNOWLEDGEMENTS

We acknowledge the support by UGent Concerted Research Action BOF-GOA, Stichting tegen Kanker and the Hercules foundation. We gratefully acknowledge Biogazelle for providing access to its small RNA sequencing data analysis pipeline and UGent for the use of the supercomputing infrastructure HPC. Funding for open access charge: BOF-GOA [BOF.GOA.2022.0003.05]. Funding resources did not influence the study design and results.

FUNDING

National Cancer Plan of the Belgian State [Action 29 to A.V.G.]; Kom op tegen Kanker (Stand up to Cancer, the Flemish Cancer Society); Bijzonder Onderzoeksfonds [BOF22/CDV/077]; Research Foundation – Flanders (FWO) [G0B2820N to J.V., LIQUIDHOPE TRANSCAN-2 project, 1803115N/1510813N to T.V.M., 1S07416N to C.E.].

Conflict of interest statement. J.V. is co-founder of Biogazelle, now a CellCarta company, providing human biofluid exRNA sequencing as a global CRO.

REFERENCES

1. Bosse,K.R. and Maris,J.M. (2016) Advances in the translational genomics of neuroblastoma: from improving risk stratification and revealing novel biology to identifying actionable genomic alterations. *Cancer*, **122**, 20–33.
2. Combaret,V., Audoynaud,C., Iacono,I., Favrot,M.-C., Schell,M., Bergeron,C. and Puisieux,A. (2002) Circulating MYCN DNA as a tumor-specific marker in neuroblastoma patients. *Cancer Res.*, **62**, 3646–3648.
3. Combaret,V., Iacono,I., Bellini,A., Bréjon,S., Bernard,V., Marabelle,A., Coze,C., Pierron,G., Lapouble,E., Schleiermacher,G. *et al.* (2015) Detection of tumor ALK status in neuroblastoma patients using peripheral blood. *Cancer Med.*, **4**, 540–550.
4. Chicard,M., Boyault,S., Colmet Daage,L., Richer,W., Gentien,D., Pierron,G., Lapouble,E., Bellini,A., Clement,N., Iacono,I. *et al.* (2016) Genomic copy number profiling using circulating free tumor DNA highlights heterogeneity in neuroblastoma. *Clin. Cancer Res.*, **22**, 5564–5573.
5. Van Roy,N., Van Der Linden,M., Menten,B., Dheedene,A., Vandeputte,C., Van Dorpe,J., Laureys,G., Renard,M., Sante,T., Lammens,T. *et al.* (2017) Shallow whole genome sequencing on circulating cell-free DNA allows reliable noninvasive copy-number profiling in neuroblastoma patients. *Clin. Cancer Res.*, **23**, 6305–6315.
6. Wang,X., Wang,L., Su,Y., Yue,Z., Xing,T., Zhao,W., Zhao,Q., Duan,C., Huang,C., Zhang,D. *et al.* (2018) Plasma cell-free DNA quantification is highly correlated to tumor burden in children with neuroblastoma. *Cancer Med.*, **7**, 3022–3030.
7. Yagyu,S., Iehara,T., Tanaka,S., Gotoh,T., Misawa-Furihata,A., Sugimoto,T., London,W.B., Hogarty,M.D., Teramukai,S., Nakagawara,A. *et al.* (2016) Serum-based quantification of MYCN gene amplification in young patients with neuroblastoma: potential utility as a surrogate biomarker for neuroblastoma. *PLoS One*, **11**, e0161039.
8. Lodrini,M., Sprüssel,A., Astrahantseff,K., Tiburtius,D., Konschak,R., Lode,H.N., Fischer,M., Keilholz,U., Eggert,A. and Deubzer,H.E. (2017) Using droplet digital PCR to analyze MYCN and ALK copy number in plasma from patients with neuroblastoma. *Oncotarget*, **8**, 85234–85251.
9. Chicard,M., Colmet-Daage,L., Clement,N., Danzon,A., Bohec,M., Bernard,V., Baulande,S., Bellini,A., Deveau,P., Pierron,G. *et al.* (2018) Whole-exome sequencing of cell-free DNA reveals temporo-spatial heterogeneity and identifies treatment-resistant clones in neuroblastoma. *Clin. Cancer Res.*, **24**, 939–949.
10. van Zogchel,L.M.J., van Wezel,E.M., van Wijk,J., Stutterheim,J., Bruins,W.S.C., Zappeij-Kannegieter,L., Slager,T.J.E., Schumacher-Kuckelkorn,R., Verly,I.R.N., van der Schoot,C.E. *et al.* (2020) Hypermethylated RASSF1A as circulating tumor DNA marker for disease monitoring in neuroblastoma. *JCO Precis. Oncol.*, **4**, 291–306.
11. Lodrini,M., Graef,J., Thole-Kliesch,T.M., Astrahantseff,K., Sprussel,A., Grimaldi,M., Peitz,C., Linke,R.B., Hollander,J.F., Lankes,E. *et al.* (2022) Targeted analysis of cell-free circulating tumor DNA is suitable for early relapse and actionable target detection in patients with neuroblastoma. *Clin. Cancer Res.*, **28**, 1809–1820.
12. Bosse,K.R., Giudice,A.M., Lane,M.V., McIntyre,B., Schürch,P.M., Pascual-Pasto,G., Buongervino,S.N., Suresh,S., Fitzsimmons,A., Hyman,A. *et al.* (2022) Serial profiling of circulating tumor DNA identifies dynamic evolution of clinically actionable genomic alterations in high-risk neuroblastoma. *Cancer Discov.*, **12**, 2800–2819.
13. Calin,G.A., Sevignani,C., Dumitru,C.D., Hyslop,T., Noch,E., Yendamuri,S., Shimizu,M., Rattan,S., Bullrich,F., Negrini,M. *et al.* (2004) Human microRNA genes are frequently located at fragile sites and genomic regions involved in cancers. *Proc. Natl. Acad. Sci. U.S.A.*, **101**, 2999–3004.
14. Chen,Y. and Stallings,R.L. (2007) Differential patterns of microRNA expression in neuroblastoma are correlated with prognosis, differentiation, and apoptosis. *Cancer Res.*, **67**, 976–983.
15. Mestdagh,P., Fredlund,E., Pattyn,F., Schulte,J.H., Muth,D., Vermeulen,J., Kumps,C., Schlierf,S., De Preter,K., Van Roy,N. *et al.* (2010) MYCN/c-MYC-induced microRNAs repress coding gene networks associated with poor outcome in MYCN/c-MYC-activated tumors. *Oncogene*, **29**, 1394–1404.
16. De Preter,K., Mestdagh,P., Vermeulen,J., Zeka,F., Naranjo,A., Bray,I., Castel,V., Chen,C., Drozynska,E., Eggert,A. *et al.* (2011) miRNA expression profiling enables risk stratification in archived and fresh neuroblastoma tumor samples. *Clin. Cancer Res.*, **17**, 7684–7692.
17. Mitchell,P.S., Parkin,R.K., Kroh,E.M., Fritz,B.R., Wyman,S.K., Pogosova-Agadjanyan,E.L., Peterson,A., Noteboom,J., O'Briant,K.C., Allen,A. *et al.* (2008) Circulating microRNAs as stable blood-based markers for cancer detection. *Proc. Natl. Acad. Sci. U.S.A.*, **105**, 10513–10518.
18. Jin,Y., Wong,Y.S., Goh,B.K.P., Chan,C.Y., Cheow,P.C., Chow,P.K.H., Lim,T.K.H., Goh,G.B.B., Krishnamoorthy,T.L., Kumar,R. *et al.* (2019) Circulating microRNAs as potential diagnostic and prognostic biomarkers in hepatocellular carcinoma. *Sci. Rep.*, **9**, 10464.
19. Lawrie,C.H., Gal,S., Dunlop,H.M., Pushkaran,B., Liggins,A.P., Pulford,K., Banham,A.H., Pezzella,F., Boultwood,J., Wainscoat,J.S. *et al.* (2008) Detection of elevated levels of tumour-associated microRNAs in serum of patients with diffuse large B-cell lymphoma. *Br. J. Haematol.*, **141**, 672–675.
20. Giglio,S., De Nunzio,C., Cirombella,R., Stoppacciaro,A., Faruq,O., Volinia,S., Baldassarre,G., Tubaro,A., Ishii,H., Croce,C.M. *et al.* (2021) A preliminary study of micro-RNAs as minimally invasive biomarkers for the diagnosis of prostate cancer patients. *J. Exp. Clin. Cancer Res.*, **40**, 79.
21. Khan,I.A., Rashid,S., Singh,N., Rashid,S., Singh,V., Gunjan,D., Das,P., Dash,N.R., Pandey,R.M., Chauhan,S.S. *et al.* (2021) Panel of serum miRNAs as potential non-invasive biomarkers for pancreatic ductal adenocarcinoma. *Sci. Rep.*, **11**, 2824.
22. Souza,K.C.B., Evangelista,A.F., Leal,L.F., Souza,C.P., Vieira,R.A., Causin,R.L., Neuber,A.C., Pessoa,D.P., Passos,G.A.S., Reis,R.M.V. *et al.* (2019) Identification of cell-free circulating microRNAs for the detection of early breast cancer and molecular subtyping. *J. Oncol.*, **2019**, 8393769.
23. Murray,M.J., Raby,K.L., Saini,H.K., Bailey,S., Wool,S.V., Tunnacliffe,J.M., Enright,A.J., Nicholson,J.C. and Coleman,N. (2015) Solid tumors of childhood display specific serum microRNA profiles. *Cancer Epidemiol. Biomark. Prev.*, **24**, 350–360.
24. Ramraj,S.K., Aravindan,S., Somasundaram,D.B., Herman,T.S., Natarajan,M. and Aravindan,N. (2016) Serum-circulating miRNAs predict neuroblastoma progression in mouse model of high-risk metastatic disease. *Oncotarget*, **7**, 18605–18619.
25. Zeka,F., Decock,A., Van Goethem,A., Vanderheyden,K., Demuynck,F., Lammens,T., Helsmoortel,H.H., Vermeulen,J., Noguera,R., Berbegall,A.P. *et al.* (2018) Circulating microRNA biomarkers for metastatic disease in neuroblastoma patients. *JCI Insight*, **3**, e97021.
26. Carr-Wilkinson,J., O'Toole,K., Wood,K.M., Challen,C.C., Baker,A.G., Board,J.R., Evans,L., Cole,M., Cheung,N.K.V., Boos,J. *et al.* (2010) High frequency of p53/MDM2/p14ARF pathway abnormalities in relapsed neuroblastoma. *Clin. Cancer Res.*, **16**, 1108–1118.
27. Pugh,T.J., Morozova,O., Attiyeh,E.F., Asgharzadeh,S., Wei,J.S., Auclair,D., Carter,S.L., Cibulskis,K., Hanna,M., Kiezun,A. *et al.* (2013) The genetic landscape of high-risk neuroblastoma. *Nat. Genet.*, **45**, 279–284.
28. Van Maerken,T., Vandesompele,J., Rihani,A., De Paepe,A. and Speleman,F. (2009) Escape from p53-mediated tumor surveillance in neuroblastoma: switching off the p14ARF-MDM2-p53 axis. *Cell Death Differ.*, **16**, 1563–1572.

29. Van Maerken,T., Speleman,F., Vermeulen,J., Lambertz,I., De Clercq,S., De Smet,E., Yigit,N., Coppens,V., Philippé,J., De Paepe,A. *et al.* (2006) Small-molecule MDM2 antagonists as a new therapy concept for neuroblastoma. *Cancer Res.*, **66**, 9646–9655.
30. Van Maerken,T., Ferdinande,L., Taildeman,J., Lambertz,I., Yigit,N., Vercruysse,L., Rihani,A., Michaelis,M., Cinatl,J., Cuvelier,C.A. *et al.* (2009) Antitumor activity of the selective MDM2 antagonist nutlin-3 against chemoresistant neuroblastoma with wild-type p53. *J. Natl. Cancer Inst.*, **101**, 1562–1574.
31. Lakoma,A., Barbieri,E., Agarwal,S., Jackson,J., Chen,Z., Kim,Y., McVay,M., Shohet,J.M. and Kim,E.S. (2015) The MDM2 small-molecule inhibitor RG7388 leads to potent tumor inhibition in p53 wild-type neuroblastoma. *Cell Death Discov.*, **1**, 15026.
32. Chen,L., Rousseau,R.F., Middleton,S.A., Nichols,G.L., Newell,D.R., Lunec,J. and Tweddle,D.A. (2015) Pre-clinical evaluation of the MDM2-p53 antagonist RG7388 alone and in combination with chemotherapy in neuroblastoma. *Oncotarget*, **6**, 10207–10221.
33. Chen,L., Pastorino,F., Berry,P., Bonner,J., Kirk,C., Wood,K.M., Thomas,H.D., Zhao,Y., Daga,A., Veal,G.J. *et al.* (2019) Preclinical evaluation of the first intravenous small molecule MDM2 antagonist alone and in combination with temozolomide in neuroblastoma. *Int. J. Cancer*, **144**, 3146–3159.
34. Johnsen,J.I., Segerström,L., Orrego,A., Elfman,L., Henriksson,M., Kågedal,B., Eksborg,S., Sveinbjörnsson,B. and Kogner,P. (2008) Inhibitors of mammalian target of rapamycin downregulate MYCN protein expression and inhibit neuroblastoma growth in vitro and in vivo. *Oncogene*, **27**, 2910–2922.
35. Agarwal,S., Ghosh,R., Chen,Z., Lakoma,A., Gunaratne,P.H., Kim,E.S. and Shohet,J.M. (2016) Transmembrane adaptor protein PAG1 is a novel tumor suppressor in neuroblastoma. *Oncotarget*, **7**, 24018–24026.
36. Patterson,D.M., Shohet,J.M. and Kim,E.S. (2011) Preclinical models of pediatric solid tumors (neuroblastoma) and their use in drug discovery. *Curr. Protoc. Pharmacol.*, **52**, 14.17.1–14.17.18.
37. Van Goethem,A., Yigit,N., Everaert,C., Moreno-Smith,M., Mus,L.M., Barbieri,E., Speleman,F., Mestdagh,P., Shohet,J., Van Maerken,T. *et al.* (2016) Depletion of tRNA-halves enables effective small RNA sequencing of low-input murine serum samples. *Sci. Rep.*, **6**, 37876.
38. Wagenseller,A.G., Shada,A., D'Auria,K.M., Murphy,C., Sun,D., Molhoek,K.R., Papin,J.A., Dutta,A. and Slingluff,C.L. (2013) MicroRNAs induced in melanoma treated with combination targeted therapy of Temsirolimus and Bevacizumab. *J. Transl. Med.*, **11**, 218.
39. Wang,L., Shi,Z.-M., Jiang,C.-F., Liu,X., Chen,Q.-D., Qian,X., Li,D.-M., Ge,X., Wang,X.-F., Liu,L.-Z. *et al.* (2014) MiR-143 acts as a tumor suppressor by targeting N-RAS and enhances temozolomide-induced apoptosis in glioma. *Oncotarget*, **5**, 5416–5427.
40. Suzuki,H.I., Yamagata,K., Sugimoto,K., Iwamoto,T., Kato,S. and Miyazono,K. (2009) Modulation of microRNA processing by p53. *Nature*, **460**, 529–533.
41. Cole,K.A., Attiyeh,E.F., Mosse,Y.P., Laquaglia,M.J., Diskin,S.J., Brodeur,G.M. and Maris,J.M. (2008) A functional screen identifies miR-34a as a candidate neuroblastoma tumor suppressor gene. *Mol. Cancer Res.*, **6**, 735–742.
42. Raver-Shapira,N., Marciano,E., Meiri,E., Spector,Y., Rosenfeld,N., Moskovits,N., Bentwich,Z. and Oren,M. (2007) Transcriptional activation of miR-34a contributes to p53-mediated apoptosis. *Mol. Cell*, **26**, 731–743.
43. Megiorni,F., Colaiacovo,M., Cialfi,S., McDowell,H.P., Guffanti,A., Camero,S., Felsani,A., Losty,P.D., Pizer,B., Shukla,R. *et al.* (2017) A sketch of known and novel MYCN-associated miRNA networks in neuroblastoma. *Oncol. Rep.*, **38**, 3–20.
44. Mestdagh,P., Boström,A.-K., Impens,F., Fredlund,E., Van Peer,G., de Antonellis,P., von Stedingk,K., Ghesquière,B., Schulte,S., Dews,M. *et al.* (2010) The miR-17-92 microRNA cluster regulates multiple components of the TGF-β pathway in neuroblastoma. *Mol. Cell*, **40**, 762–773.
45. Hsu,C.-L., Chang,H.-Y., Chang,J.-Y., Huang,H.-C. and Juan,H.-F. (2016) Unveiling MYCN regulatory networks in neuroblastoma via integrative analysis of heterogeneous genomics data. *Oncotarget*, **7**, 36293–36310.
46. Guo,J., Dong,Q., Fang,Z., Chen,X., Lu,H., Wang,K., Yin,Y., Cai,X., Zhao,N., Chen,J. *et al.* (2010) Identification of miRNAs that are associated with tumor metastasis in neuroblastoma. *Cancer Biol. Ther.*, **9**, 446–452.
47. Samaraweera,L., Grandinetti,K.B., Huang,R., Spengler,B.A. and Ross,R.A. (2014) MicroRNAs define distinct human neuroblastoma cell phenotypes and regulate their differentiation and tumorigenicity. *BMC Cancer*, **14**, 309.
48. Boeva,V., Louis-Brennetot,C., Peltier,A., Durand,S., Pierre-Eugène,C., Raynal,V., Etchevers,H.C., Thomas,S., Lermine,A., Daudigeos-Dubus,E. *et al.* (2017) Heterogeneity of neuroblastoma cell identity defined by transcriptional circuitries. *Nat. Genet.*, **49**, 1408–1413.
49. van Groningen,T., Koster,J., Valentijn,L.J., Zwijnenburg,D.A., Akogul,N., Hasselt,N.E., Broekmans,M., Haneveld,F., Nowakowska,N.E., Bras,J. *et al.* (2017) Neuroblastoma is composed of two super-enhancer-associated differentiation states. *Nat. Genet.*, **49**, 1261–1266.
50. Patnaik,A., Tolcher,A., Beeram,M., Nemunaitis,J., Weiss,G.J., Bhalla,K., Agrawal,M., Nichols,G., Middleton,S., Beryozkina,A. *et al.* (2015) Clinical pharmacology characterization of RG7112, an MDM2 antagonist, in patients with advanced solid tumors. *Cancer Chemother. Pharmacol.*, **76**, 587–595.
51. Ray-Coquard,I., Blay,J.-Y., Italiano,A., Le Cesne,A., Penel,N., Zhi,J., Heil,F., Rueger,R., Graves,B., Ding,M. *et al.* (2012) Effect of the MDM2 antagonist RG7112 on the P53 pathway in patients with MDM2-amplified, well-differentiated or dedifferentiated liposarcoma: an exploratory proof-of-mechanism study. *Lancet Oncol.*, **13**, 1133–1140.
52. Yang,H., Filipovic,Z., Brown,D., Breit,S.N. and Vassilev,L.T. (2003) Macrophage inhibitory cytokine-1: a novel biomarker for p53 pathway activation. *Mol. Cancer Ther.*, **2**, 1023–1029.
53. Yamakuchi,M., Lotterman,C.D., Bao,C., Hruban,R.H., Karim,B., Mendell,J.T., Huso,D. and Lowenstein,C.J. (2010) P53-induced microRNA-107 inhibits HIF-1 and tumor angiogenesis. *Proc. Natl. Acad. Sci. U.S.A.*, **107**, 6334–6339.
54. Georges,S.A., Biery,M.C., Kim,S.-Y., Schelter,J.M., Guo,J., Chang,A.N., Jackson,A.L., Carleton,M.O., Linsley,P.S., Cleary,M.A. *et al.* (2008) Coordinated regulation of cell cycle transcripts by p53-inducible microRNAs, miR-192 and miR-215. *Cancer Res.*, **68**, 10105–10112.
55. Welch,C., Chen,Y. and Stallings,R.L. (2007) MicroRNA-34a functions as a potential tumor suppressor by inducing apoptosis in neuroblastoma cells. *Oncogene*, **26**, 5017–5022.
56. Rihani,A., Van Goethem,A., Ongenaert,M., De Brouwer,S., Volders,P.-J., Agarwal,S., De Preter,K., Mestdagh,P., Shohet,J., Speleman,F. *et al.* (2015) Genome wide expression profiling of p53 regulated miRNAs in neuroblastoma. *Sci. Rep.*, **5**, 9027.
57. Tivnan,A., Orr,W.S., Gubala,V., Nooney,R., Williams,D.E., McDonagh,C., Prenter,S., Harvey,H., Domingo-Fernández,R., Bray,I.M. *et al.* (2012) Inhibition of neuroblastoma tumor growth by targeted delivery of microRNA-34a using anti-disialoganglioside GD2 coated nanoparticles. *PLoS One*, **7**, e38129.

SUPPLEMENTAL FILE AND TABLES (cf. NAR Cancer Online, https://academic.oup.com/narcancer/article-lookup/doi/10.1093/narcan/zcad002#supplementary-data)

Personal note

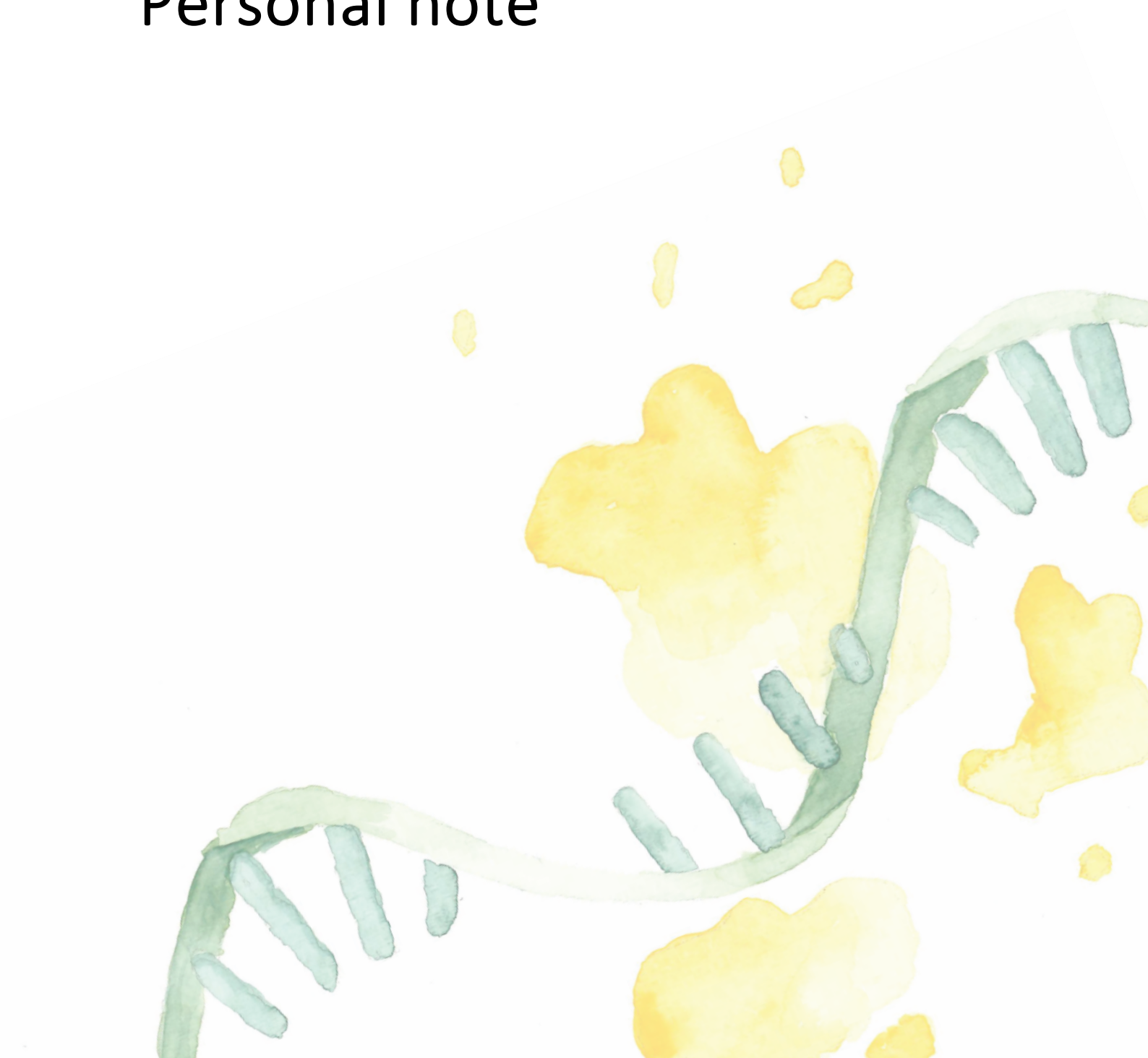

Mijn doctoraatstraject voelde soms als een rit over de kasseien van Roubaix, vol uitdagende hobbels en onverwachte wendingen. De Mont Ventoux beklimmen (zelfs via Bédoin in de hitte met enorme zwermen vliegen) is er niets tegenover. Ik kon deze weg niet alleen afgelegd hebben zonder een aantal mensen die ik hiervoor graag zou willen bedanken.

Bram, Jo en Tom. Ik kon me geen betere supervisors wensen. Jullie verschillende achtergrond zorgde voor een mooi, complementair geheel:

Bram, de clinicus, wiens telefoon nooit zwijgt. Jouw wetenschappelijke en klinische inzichten waren zeer verrijkend. Jij hielp me soms eens de nodige afstand te nemen en stil te staan bij wat het eigenlijke klinische einddoel was van mijn projecten. Daarnaast hoop ik dat ik iets heb opgepikt van jouw skills om projecten op een zeer overtuigende manier neer te schrijven.

Jo, de eeuwige optimist. Ondanks het dikwijls falen van experimenten, bleef je altijd positief en kwam er altijd wel een oplossing uit de bus. Daarnaast kon ik soms volledig vastlopen op experimenten, papers of berekeningen, waarna jij op magische wijze alles ineens heel logisch en vanzelfsprekend kon doen lijken op 10 minuutjes tijd. Ik ben heel dankbaar dat ik in het OncoRNALab werd opgenomen, jij en Pieter zorgen echt voor een fantastische sfeer op het werk.

Tom, de wandelende encyclopedie. Jouw oneindige kennis en expertise was van onschatbare waarde tijdens mijn traject. Ik ben je ook nog steeds heel dankbaar voor het vertrouwen dat je van in het begin in mij had. Je zei me ooit dat ik een doctoraatstraject moest aanvatten vanuit een passie voor wetenschap en geneeskunde. Misschien kon ik me daar toen in 2018 nog geen duidelijk beeld bij vormen. Vandaag kan ik daarentegen met zekerheid zeggen dat jullie die passie in mij hebben aangewakkerd.

The members of the examination committee, thank you for your valuable feedback and interesting discussions.

Kathleen en Hanne, mijn paranimfen, bedankt voor jullie hulp tijdens mijn eindsprint. **Kathleen**, ik ben heel blij dat ik dat hele traject met jou heb mogen doorlopen. We hebben enorm veel plezier gehad samen in het labo en tijdens het schrijven van onze paper, maar waren er ook voor elkaar wanneer we door het bos de bomen niet meer zagen of door de bomen het bos niet meer zagen (spreekwoorden blijven moeilijk). **Hanne**, zo dankbaar dat je ooit voor mijn onderwerp hebt gekozen als masterstudent! Al had je misschien toch liever iets gedaan met TLR agonisten en fibroblasts? Bedankt voor alle hulp en mentale steun, ondanks dat het leven niet altijd een crèmekarre was! Dat die paper waarin we altijd hebben geloofd nu maar snel geaccepteerd wordt!

Justine, bedankt voor je enorme hulp in het labo, maar ook om me altijd op te beuren als het nodig was. Daarnaast ben ik heel blij dat je jouw artistieke talenten hebt losgelaten op de cover van mijn thesis!

Marieke, ik heb zó veel plezier gehad met jou tijdens mijn doctoraat. Op het werk, de lab retreat, onze drinks, de Gentse feesten, altijd ambiance met jou erbij. Bedankt voor alle leuke momenten en de goeie babbels!

Philippe, Ramiro en Jasper V, bedankt voor de Bologna trip, de Italiaanse avond, de pintjes en de toffe babbels!

Anneleen, bedankt om mij zo goed te ontvangen op dag 1 als mijn meter, om altijd klaar te staan met raad als de alleswetende 'ancien', en te helpen om één van de papers tot een goed einde te brengen. Goed dat we dat kleine kamertje in Amsterdam overleefd hebben.

Jasper A, je had gelijk, alles kwam goed! Bedankt om die muis pipeline duizend keer opnieuw te lopen voor mij, maar vooral ook voor alle mentale steun.

Liselot, bedankt voor het beantwoorden van mijn duizenden vragen, zelfs tijdens jouw zwangerschapsverlof (ik kon het niet laten), en jouw hulp met de muisjes.

Jilke, bedankt voor de leuke fietstochtjes, en het opofferen van jouw minimum aan vrije tijd de laatste maanden!

All **previous and current members of the OncoRNALab**, thank you so much for making those last 5 years so memorable. I really enjoyed our lab retreats, drinks, congresses, sports sessions and weekends.

Mijn vrienden en familie, bedankt voor jullie onvoorwaardelijke steun!

César en Oscar, mijn trouwe viervoeters, bedankt voor de oneindige kusjes en knuffeltjes.

Last but not least, **Matthias**, bedankt voor alles! We zijn al meer dan 10 jaar een topteam. Zonder elkaar waren we nooit zo ver geraakt. We waren niet in Thailand, Cambodja, Vietnam, de Filipijnen, Maleisië, Singapore, Jordanië, Marokko of Oeganda geraakt, maar ik was ook niet op het punt geraakt dat ik een doctoraat zou halen. Ik heb het je niet gemakkelijk gemaakt de laatste tijd, en "het werd tijd dat het gedaan was dat doctoraat", awel, het is gedaan! FEEST!!

Cover designed by Justine Nuytens.